A new route for rare-earth free permanent magnets : synthesis, structural and magnetic characterizations of dense assemblies of anisotropic nanoparticles

Evangelia Anagnostopoulou

Université de Toulouse

THÈSE

En vue de l'obtention du

DOCTORAT DE L'UNIVERSITÉ DE TOULOUSE

Délivré par :

Institut National des Sciences Appliquées de Toulouse (INSA de Toulouse)

Présentée et soutenue par :
Evangelia-Eleni Anagnostopoulou
Le **24 juin 2016**

Titre :
A new route for rare-earth free permanent magnets: synthesis, structural and magnetic characterizations of dense assemblies of anisotropic nanoparticles

---

ED SDM : Nano-physique, nano-composants, nano-mesures - COP 00

Unité de recherche :

Laboratoire de Physique et Chimie des Nano-Objets

Directeur(s) de Thèse :

Lise-Marie LACROIX
Guillaume VIAU

Rapporteurs :

Frederic MAZALEYRAT, professeur des universités, ENS Cachan, Paris
Lorette SICARD, maître de conférences, ITODYS, Paris

Autre(s) membre(s) du jury :

Catherine AMIENS, président du jury, LCC, Toulouse
Frederic OTT, chercheur, CEA, LLB, Paris
Manuel Vázquez, professeur des universités, CSIC, Madrid

“We play a game of cards with the nature of the paradox.

In a battle to determine what is possible and what is not”

Science, by S. Vayenas

Acknowledgments

This thesis was prepared at the Institut National des Sciences Appliquées of Toulouse, INSA, and it would not have been accomplished without the help of numerous people.

First and foremost, I would like to gratefully acknowledge my thesis supervisors, Prof. **Guillaume Viau** and Maître de conférences **Lise-Marie Lacroix** for accepting me in their team and introducing me in the amazing world of nanomagnetism and nanochemistry. Despite their busy schedule, their door was always open when I needed their advice. Their academic insights and guidance contributed to my education and personal development, and will surely be invaluable to my career for the years to come.

I express my gratitude to Prof. **Frédéric Mazaleyrat** and Maître de conférences **Lorette Sicard** who accepted to evaluate my thesis. I am very grateful for the interest that they showed for my work, their feedback and for making my thesis examination a very pleasant process via a constructive discussion.

To Prof. **Catherine Amiens**, Prof. **Manuel Vazquez** and researcher **Frédéric Ott** a special thank you for accepting to be part of the jury. I feel very lucky for having been invited at the Laboratoire Léon Brillouin (LLB) at the CEA facilities by Frédéric Ott. Performing and analyzing small angle neutron (SANS) measurements was a very exciting experience during my PhD thesis!

I am very proud having been member of the **REFREEPERMAG team** and having contributed to such a great European project. I had the luck of meeting kind and exceptional scientists, with whom I had helpful conversations and built new friendships. A big thank you to everyone and especially to the researcher A **Dimitrios Niarchos** for the scientific and life advices.

I would like to acknowledge the **European Commission FP7** for funding the REFREEPERMAG (EU NMP3-SL-2012-280670) project and, by extension, my PhD work. I am very grateful for having been able to run costly experiments and participate in international and national conferences.

Of course none of the experiments would be realized without the technical help of **Angélique Gillet**, who was taking care of everything in the lab in order to make it functional and pleasant to work at. Many thanks to **Simon Cayez** for teaching me how to use the TEM and for taking such beautiful SEM images. A big part of my research is accomplished thanks to **Francis Chouzenoux** via the numerous TGA measurements of my samples.

In the LPCNO I had the privilege of being surrounded by great **lab mates**, who made every day enjoyable and memorable. Thank you for your friendship, encouragement and great nights out! Many thanks to my friends **Antonis, Maria**, **Thanasis** and **Fofo** for being always there for me. Finally, I owe an enormous hug and a big thank you to my **Paulo** for his support and capacity to just put up with me!

Everything I have become was shaped by my parents, **Vangelis** and **Mary**. Thank you for raising me with great ethical values, for your immeasurable support, encouragement and love.

Abstract

Permanent magnets have lately become essential to daily life products. This huge market is mostly trusted by **rare earth based- or ferrites based-magnets**. The increasing demand of permanent magnets and the dependence towards China for the rare earths (RE) supply incite important efforts worldwide to develop **next generation magnets** requiring either fewer quantities of RE or even to imagine new technologies based on **RE free magnets**. This thesis investigates the potentiality of a bottom-up approach for the preparation of nanostructured magnets using dense assemblies of Co NRs.

The work was articulated around three main scientific hurdles: - the synthesis of Co NRs, - their alignment into dense assemblies and – iii their further compaction into macroscopic permanent magnets. We demonstrated the up-scaling of the polyol process which, under controlled stirring conditions, yields 5 g of monodisperse cylindrical-like cobalt nanorods. The modification of the nucleating agent allows to tune the size and shape of the NRs. Anhydrous RuCl3 allowed to produce Co NRs with optimized shape, leading to the highest coercivity values measured.

The realization of dense and robust macroscopic magnets was possible via the rods' dispersion in chloroform and its evaporation under a magnetic field of 1 T and ambient conditions. The dense assemblies presented the characteristic square loop with remanence to saturation and squareness equal to 0.99 and 0.96, respectively. The almost perfect squareness along with electron microscopy and small angle neutron scattering (SANS) demonstrated the excellent alignment of the rods within the assembly. Additional information about the inter-rod distance and magnetic domains size could be further determined from SANS measurements under magnetic field. We showed that the magnetic volume fraction of the assembly could be reliably assessed by coupling magnetic and thermogravimetric analysis. Depending on the nanorods' mean diameter and alignment process, magnetic volume fraction in the range of 45 to 55 % were obtained. This allowed a quantitative assessment of the $(BH)_{max}$ values, reaching a maximum of 165 $kJ \cdot m^{-3}$.Preliminary compaction experiments performed on the nanorod assemblies showed that for pressing forces up to 1000 MPa, magnetic volume fraction can be significantly increased (up to 30 %) but optimization are still required to prevent the sintering of the Co NRs and thus the decrease of the coercivity.

This study proves that the bottom-up approach is very promising to get new hard magnetic materials that can compete in the permanent magnet panorama and fill the gap between the ferrites and the NdFeB magnets.

Keywords: nanorods; cobalt; permanent magnets; self-assembly.

Résumé

Les aimants permanents sont devenus essentiels aux produits de notre vie quotidienne. Ce marché est largement dominé par **les aimants à base de terres rares ou de ferrites**. La demande croissante d'aimants permanents et la dépendance des pays européens vis-à-vis de la Chine l'approvisionnement en terres rares incite à d'importants efforts pour développer **une nouvelle génération d'aimants** avec une plus faible quantité de terres rares ou même d'imaginer de nouvelles technologies basées sur des **aimants sans terres rares**. Cette thèse étudie la potentialité d'une approche *« bottom-up»* pour la préparation d'aimants nanostructurés à base d'un assemblage dense de nanobâtonnets de cobalt (Co NBs).

Ce travail s'articule autour de plusieurs problématiques scientifiques: la synthèse de nanobâtonnets de cobalt, leur alignement dans des assemblées denses, la caratérisation magnétique et structurale de ces assemblées et finalement leur compaction en aimant permanent macroscopique. Nous avons démontré la faisabilité d'un changement d'échelle du procédé polyol, avec des conditions d'agitation contrôlées, pour obtenir 5 g de nanobâtonnets de cobalt monodisperse. La modification de l'agent nucléant nous a permis de contrôler la taille et la forme des NBs conduisant à des valeurs élevées de champ coercitif.

La réalisation d'aimants macroscopiques denses et robustes a été possible via la dispersion des bâtonnets dans du chloroforme et son évaporation sous champ magnétique à température ambiante. Des assemblées denses présentant un cycle d'aimantation carré avec une aimantation rémanente pouvant atteindre 99% de l'aimantation à saturation. La fraction volumique magnétique au sein des assemblées a été déterminée par des mesures combinées d'analyse thermogravimétriques, mesures magnétiques et diffusion des neutrons. En fonction du diamètre moyen des nanobâtonnets et du procédé d'alignement, une fraction volumique magnétique comprise entre 45 et 55% a été obtenue. Nous avons ainsi pu estimer la valeur de $(BH)_{max}$, celle-ci a pu atteindre dans le meilleur des cas une valeur de 165 $kJ \cdot m^{-3}$. Des résultats préliminaires sur la compaction d'assemblées de nanobâtonnets montre qu'avec une pression allant jusqu'à 1000 MPa, la fraction volumique magnétique peut être augmenté significativement (jusqu'à 30%) mais des optimisations sont encore nécessaire pour éviter la coalescence des Co NBS diminue le champ coercitif.
Cette étude prouve que l'approche *« bottom-up»* est très prometteuse pour obtenir des nouveaux matériaux magnétiques durs qui peuvent compléter le panorama des aimants permanents et combler le fossé entre les ferrites et les aimants NdFeB.

Mots-clés : nanobâtonnets ; cobalt ; aimants permanents; auto-assemblage

Table of Contents

Chapter III Fabrication & Properties of Dense Assemblies of Cobalt Nanorods

Chapter IV Small Angle Neutron Scattering by cobalt nanorod assemblies

Chapter V Towards macroscopic magnets: Preliminary results on compaction of cobalt nanorods

General Conclusions

Introduction Permanent Magnets

a. What are permanent magnets & their basic characteristics?

The permanent magnets are the key feature of a plethora of applications worldwide. The growing interest and the necessity for these materials stems from their ability to transform attractive or repelling force into mechanical work, to transmit and distribute electric power and to convert mechanical energy into electrical energy. All these allow their use in consumer products, transportation devices, energy storage systems and renewable energy technologies. However, there is an increasing need for small magnets exhibiting large magnetic energy, with low cost and environmentally friendly production, a fact that has been the reason of many researches. In order to deal with these tasks, first let us see what a permanent magnet is and which its basic characteristics are.

A permanent magnet is a material which is initially magnetized and then creates its own persistent magnetic field in a particular volume of space, without the need for continuous electric power and thus no heat generation. The magnetic energy stored in the magnet is not drained away by its use and remains into it indefinitely if it is properly made and handled [1]. Thus, a permanent magnet is nothing else than an energy storage device, whose figure of merit is its energy product, $(BH)_{max}$.

Efficient permanent magnet consists in a material with high remanent inductions (B_r), high saturation magnetization (M_s), square magnetization loop (SQ≈ 1 and M_r/M_s≈ 1) and large coercive field ($H_c^M > M_r/2$) (Figure 1). Processed magnets commercially available are usually prepared following classical metallurgy processes, namely:

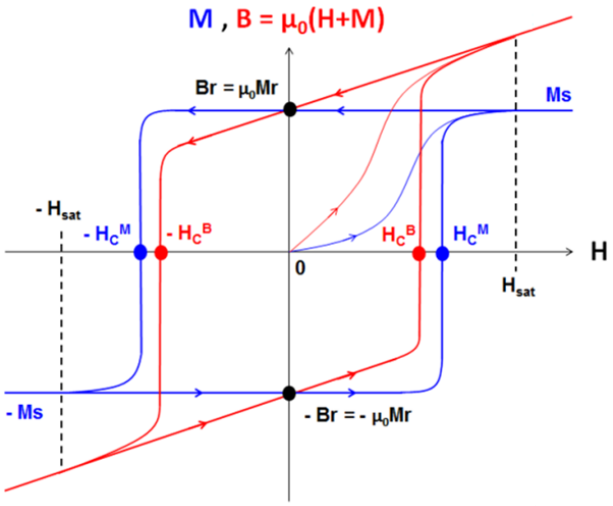

Figure 1. *Magnetization (in blue) and induction (in red) hysteresis cycle. H_C^M, H_C^B : coercive fields, M_r (B_r) : remanent magnetization (resp. induction), M_s: saturation magnetization.*

i) Preparation of an isotropic powder using melt-spinning or ball-milling.

ii) Alignment of the easy axis of all crystallites under an external magnetic field to improve the remanent magnetization (M_R) and the hysteresis loop squareness (SQ). These three steps are mandatory to reach high $(BH)_{max}$ values.

iii) Compaction into a fully dense material to improve the saturation magnetization. This step usually consists in high temperature sintering.

It is arguable that each permanent magnet application is unique and meets different needs, therefore has different requirements. So, when the question of what the basic characteristics of a good permanent magnet are, a single answer cannot be found. Parameters such as temperature stability, flux density, energy product, resistance to demagnetization, physical strength and corrosion, as well as size, weight, raw material cost and availability have to be considered when selecting a material.

b. Applications of permanent magnets

The permanent magnet applications can be classified according to their operation environment, which can be static or dynamic, or by to the form of the delivered magnetic field within the area of the application (uniform or non-uniform, steady or time varying flux density). If we question the permanent magnets' application and the physical effect that is exploited four categories are found (Figure 2) [2], [3]:

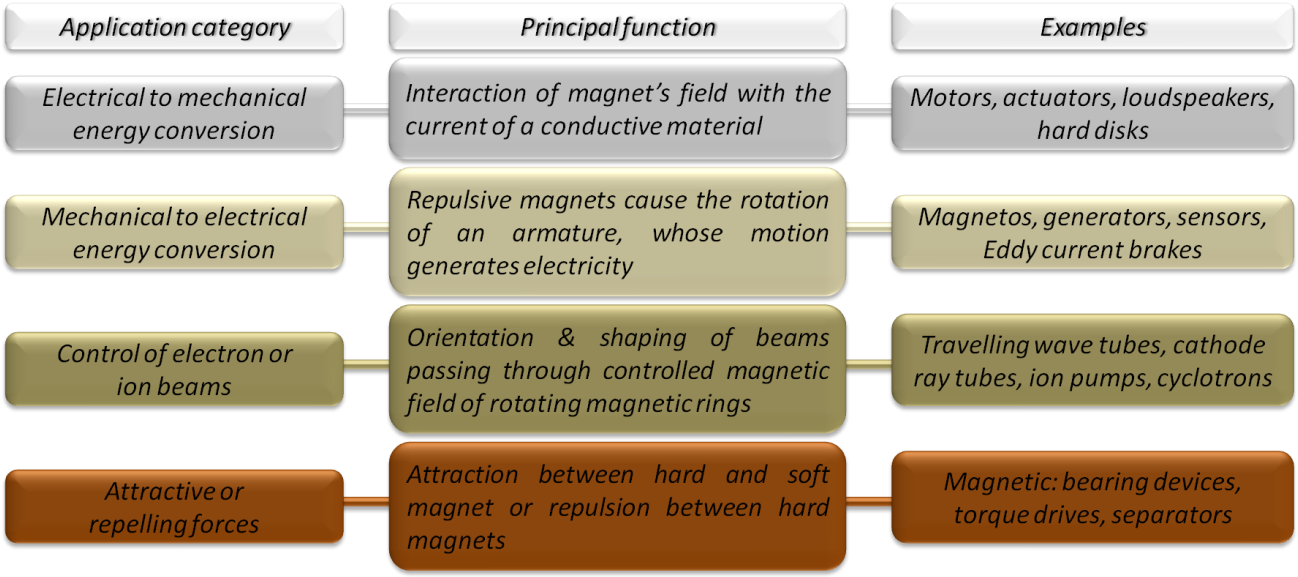

Figure 2. *Categories, principal function and characteristic examples of permanent magnets*

With such a diversity of permanent magnet applications under various working conditions, the demand for their physical and mechanical properties differs. That is why the market of permanent magnet production is equipped with three basic categories where each of them provides certain material types and grades in order to meet the consumer's needs (Figure 3).

c. Commercial magnetic materials

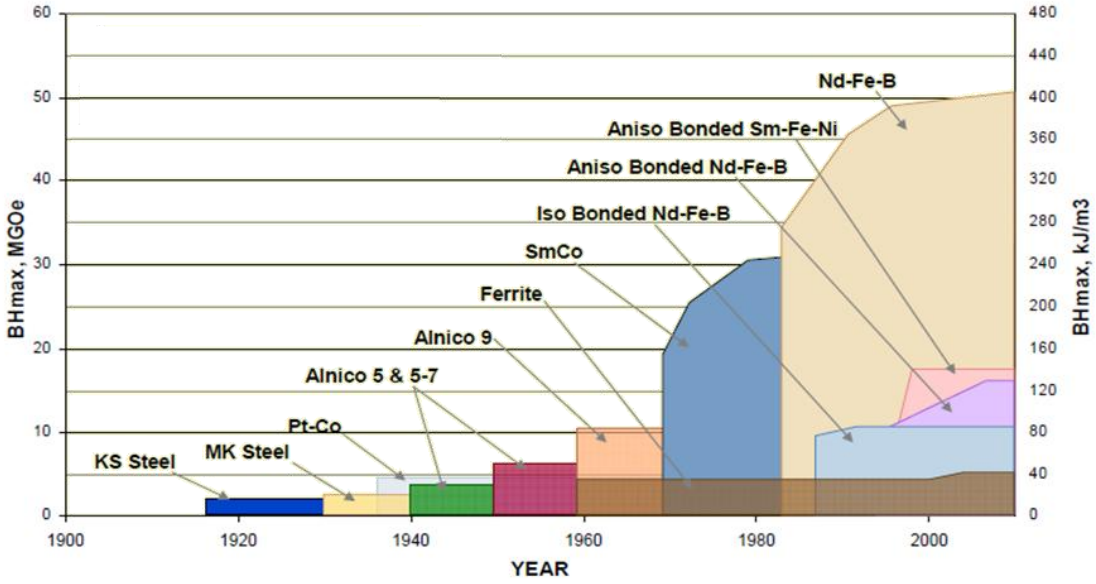

Figure 3. *Commercial permanent magnets and their development through time. (Adapted from [4])*

The origins of the magnetic materials start from Magnesia around 600 B.C., when Thales of Miletus introduced the magnetic properties of the mineral magnetite, Fe_3O_4, or lodestone. Much later, in 1916, the commercialization of the first artificial permanent magnet took place with the invention of the KS steel (a Co-Cr-W alloy), presenting B_r= 0.9 T, H_c= 20 kA/m and $(BH)_{max}$= 7.6 kJ.m^{-3} [11, 12], followed by the improved MK steel (Ni-Al alloy) with H_c=32kA/m. Due to their poor magnetic properties, the steel magnets are now replaced by stronger magnets classified in three categories: (1) Alnico magnets, (2) Ferrites or ceramic magnets and (3) Rare-earth magnets [4], [5], [6], [7]. In the Table 1 a short list of their grades, advantages and disadvantages is provided.

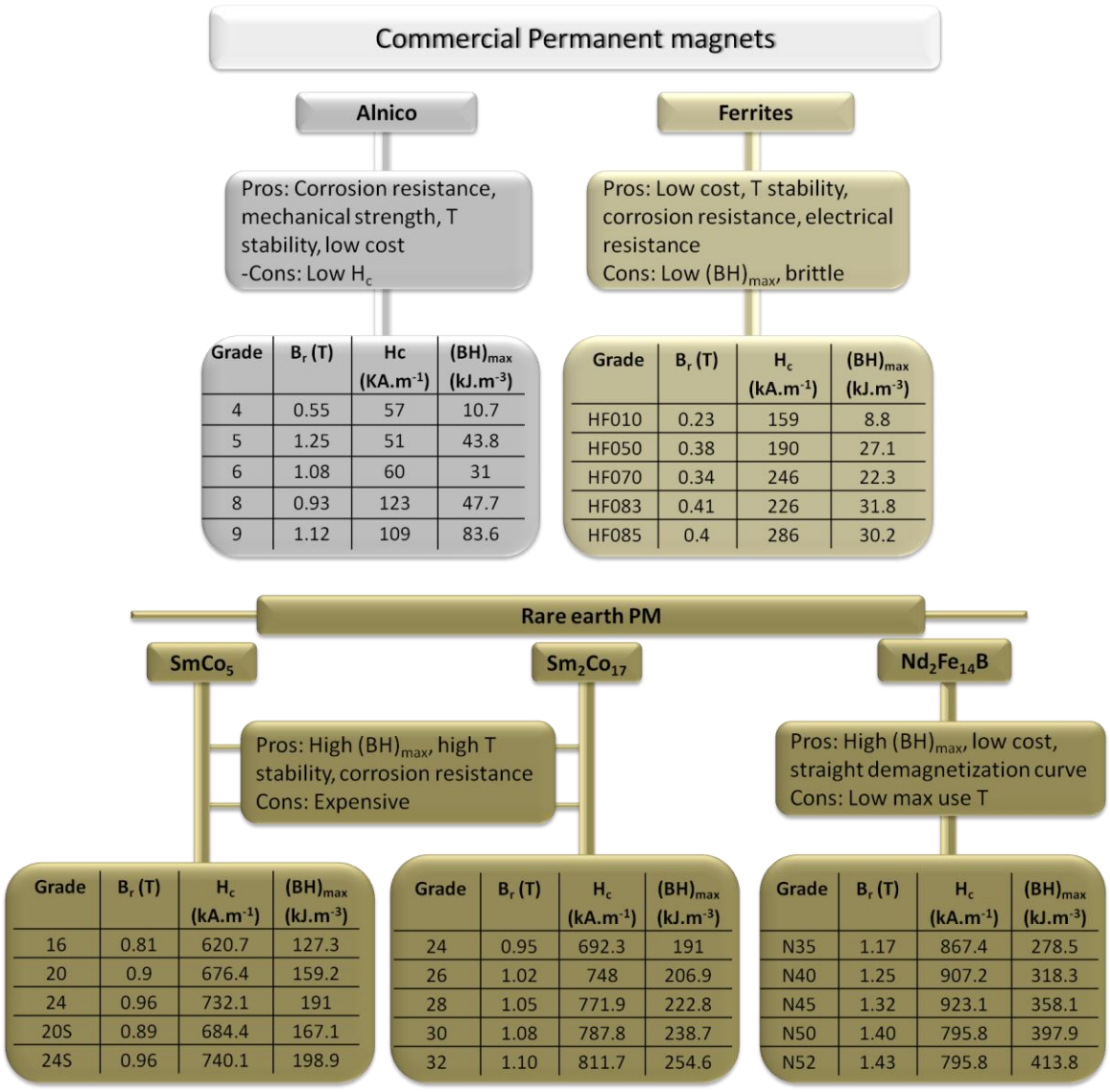

Grade	B_r (T)	Hc ($kA.m^{-1}$)	$(BH)_{max}$ ($kJ.m^{-3}$)
4	0.55	57	10.7
5	1.25	51	43.8
6	1.08	60	31
8	0.93	123	47.7
9	1.12	109	83.6

Grade	B_r (T)	H_c ($kA.m^{-1}$)	$(BH)_{max}$ ($kJ.m^{-3}$)
HF010	0.23	159	8.8
HF050	0.38	190	27.1
HF070	0.34	246	22.3
HF083	0.41	226	31.8
HF085	0.4	286	30.2

Grade	B_r (T)	H_c ($kA.m^{-1}$)	$(BH)_{max}$ ($kJ.m^{-3}$)
16	0.81	620.7	127.3
20	0.9	676.4	159.2
24	0.96	732.1	191
20S	0.89	684.4	167.1
24S	0.96	740.1	198.9

Grade	B_r (T)	H_c ($kA.m^{-1}$)	$(BH)_{max}$ ($kJ.m^{-3}$)
24	0.95	692.3	191
26	1.02	748	206.9
28	1.05	771.9	222.8
30	1.08	787.8	238.7
32	1.10	811.7	254.6

Grade	B_r (T)	H_c ($kA.m^{-1}$)	$(BH)_{max}$ ($kJ.m^{-3}$)
N35	1.17	867.4	278.5
N40	1.25	907.2	318.3
N45	1.32	923.1	358.1
N50	1.40	795.8	397.9
N52	1.43	795.8	413.8

Table 1. *Representative commercial grades of permanent magnets, their pros and cons and their magnetic properties.*

d. Need for rare earth free permanent magnets

The increasing demand of permanent magnets and the dependence towards China for the rare earths (RE) supply incite important efforts worldwide to develop **next generation magnets** requiring either fewer quantities of RE or even to imagine new technologies based on RE free magnets. The stake is not only economic but also ecological since the exploitation of the RE ores is extremely polluting for the environment. These new magnets should exhibit an **energy product** ranging from 100 kJ/m^3 to 200 kJ/m^3, intermediate between ferrites (< 38 kJ/m^3) and rare-earth based magnets (>250 kJ/m^3) properties (Figure 3).

Alternative materials have been intensively sought. Lewis *et al.* distinguished two main routes of research [8]:

(i) The first approach consists of playing with crystal structures in order to find new highly magneto-crystalline compounds such as manganese compounds, iron–nickel, and iron–cobalt borides with tetragonal structures or cobalt carbide Co_2C/Co_3C nanocomposites.

(ii) The second approach consists in exploiting a **nano-structuration to obtain** RE-free magnetic nanocomposites. For that, single domain nanoparticles with a high anisotropy are assembled into dense materials. The recent progress of the **nanochemistry**, which lately yielded nano-crystals with tuneable sizes, shapes and thus physical properties opens the way for such a new approach (Figure 4).

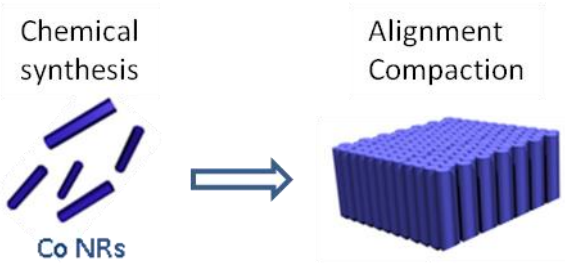

Figure 4. *Schematic view of the bottom-up approach followed during this thesis to yield RE-free permanent magnets using Co nanorods.*

This thesis was conducted in the framework of the *"Rare Earth Free Permanent Magnet"* (REFREEPERMAG, EU-FP7) project, which aimed at developing a new generation of rare earth-free permanent magnets. Amongst the other strategies employed by several European laboratories, we focused our investigation on the fabrication of macroscopic nanostructured permanent magnets based on the dense assembly of cobalt nanorods (NRs). The presented work was carried out in the team of "Nanostructures et Chimie Organométallique" of the Laboratoire de Physique et Chimie des Nano-Objets (LPCNO), which has strong expertise in the bottom-up polyol synthesis of magnetic nanoparticles with various compositions, sizes and shapes. The work was articulated around the synthesis of the Co NRs building blocks and the optimization of their intrinsic properties, their further alignment into assemblies, the characterization of the obtained nanostructured materials and the first attempt of consolidation to obtain permanent magnets. Thus, the manuscript will be divided into 5 chapters.

The Chapter I ***"State of the Art: Magnetism"*** presents characteristic features of nanomagnetism and micromagnetic simulations on single and assembled cobalt nanorods, allowing us to draw the guiding lines for our experimental research.

In the Chapter II ***"Synthesis of Cobalt Nanorods"***, after summarizing the different approaches followed in the literature for the anisotropic growth of Co NRs, we focused our experimental approach to the polyol process aiming at i) developing its up-scaling and ii) obtaining nanorods with the morphology and dimensions suggested by the micromagnetic simulations.

The Chapter III ***"Fabrication and Properties of Dense Assemblies of Cobalt Nanorods"*** will present the protocol we established to fabricate dense cobalt nanorod wafers under an external magnetic field. Factors which affect the alignment quality, and thus the final energy product, were examined such as the intrinsic coercivity, the remanence to saturation ratio, squareness and the magnetic volume fraction. A simple model is introduced allowing shedding lights on the means for the BH_{max} improvement.

The Chapter IV ***"Small Angle Neutron Scattering by Cobalt Nanorod Assemblies"*** describes the structural and magnetic information gained on the assembled Co NRs by means of neutron scattering techniques. Center-to-center nanorod distance and magnetic domain sizes in different states of their magnetization were evaluated, allowing attesting the quality of the nanorods' alignment and their magnetic volume fraction.

Finally, Chapter V ***"Towards Macroscopic Magnets: Preliminary results on compaction of cobalt nanorods"*** presents the first consolidation results performed in collaboration with by Dr. Semih Ener in the team of Pr. Oliver Gutfleish at the Technical University of Darmstadt (TUDA). We will show two different approaches followed for the rods' consolidation i.e. compaction of randomly oriented rods under magnetic field and compaction of pre-aligned nanorod assemblies. The challenge of fabricating a magnet with good mechanical strength and high magnetic volume fraction will be dealt with the use of cold and hot compaction under different applied pressing forces.

Bibliography

[1] B. D. Cullity, *Introduction to Magnetic Materials*, vol. 2012. 2009.

[2] “https://en.wikipedia.org/wiki/Cathode_ray_tube.” .

[3] J. Bradley, “Tech notes,” *Whitmire Pest Manag. Q.*, vol. 13(2), no. December, p. 8, 1994.

[4] S. Constantinides, “Novel Permanent Magnets and Their Uses,” *MRS Proc.*, vol. 577, no. May 1995, 1999.

[5] K. J. Strnat, “Modem Permanent Magnets for Applications in Electro-Technology,” *Proc. IEEE*, vol. 78, no. 6, pp. 923–946, 1990.

[6] “http://www.arnoldmagnetics.com.”

[7] “http://www.stanford-magnets.com.”

[8] L. H. Lewis and F. Jiménez-Villacorta, “Perspectives on Permanent Magnetic Materials for Energy Conversion and Power Generation,” *Metall. Mater. Trans. A*, vol. 44A, no. January, pp. 2–20, 2012.

Chapter I State of the Art: Magnetism

I.1. Magnetic performances of permanent magnets

The following paragraphs are essentially inspired by books of B.D. Cullity & C.D. Graham [1], E. Du Trémolet de Lacheisserie [2] and the viewpoint paper of J.M.D. Coey [3].

The permanent magnets are ferromagnetic materials. These materials can have a magnetic ordering and exhibit a spontaneous magnetization, noted $\overrightarrow{M}$, which is the sum of the magnetic moments of the atoms which compose it per unit volume.

When an external magnetic field, noted $\overrightarrow{H}$, is applied to a ferromagnetic material, the variation of the magnetization presents an irreversibility which results in a hysteresis loop, called "magnetization loop" (Figure I-1, blue curve). Such a cycle is divided into four quadrants:

1st The first quadrant describes the ability of the material to magnetize and maintain its magnetization. On the virgin magnetization curve (starting from the point (H = 0, M = 0)), M increases progressively until the saturation magnetization M_s is reached, all the magnetic moments being aligned along the field direction.
When the magnetic field is released, the magnetization slightly drops, a remanent magnetization M_r is kept for H=0. The material is magnetized and produces its own magnetic field ;

2nd The second quadrant describes the ability of the material to resist to the demagnetization process. When a magnetic field is applied in the opposite direction, the magnetic moments tend to reverse, leading to the reduction of the global magnetization. M falls to zero at the so-called coercive field, noted H_c^M.

3rd & 4th The third and fourth quadrants are generally symmetrical with respect to the origin of the coordinate.

The induction loop $\overrightarrow{B} = \mu_0 (\overrightarrow{M} + \overrightarrow{H})$, also known as flux density, can be deduced from the magnetization loop (Figure 1, red curve). The coercivity associated is H_c^B and usually differs from H_c^M. The remanent induction Br reads: $B_r = \mu_0 M_r$.

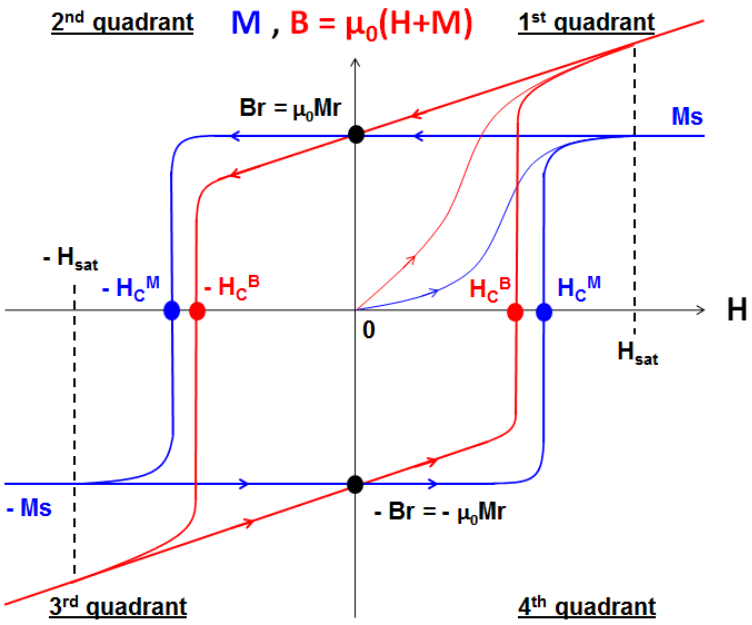

Figure I-1. *Schemes of magnetization (blue curve) and induction loops (red curve) of a permanent magnet.*

The performance of a permanent magnet is evaluated from the second quadrant of the B=f(H) loop (Figure I-2 left curve). Indeed, the so-called energy product (BH), can be estimated as the area below the point of coordinates (H, B). This energy product can be seen as the energy stored in the stray field (H_d) created by the magnet :

$$H_d = -N \times M \qquad \text{(Eq. 1)}$$

Where N is the demagnetization factor, this number depends only on the magnet shape and varies between 0 and 1.

The maximum energy product, noted $(BH)_{max}$, is the real figure of merit of the permanent magnet (Figure I-2 right curve) and enables to define its optimum working point.

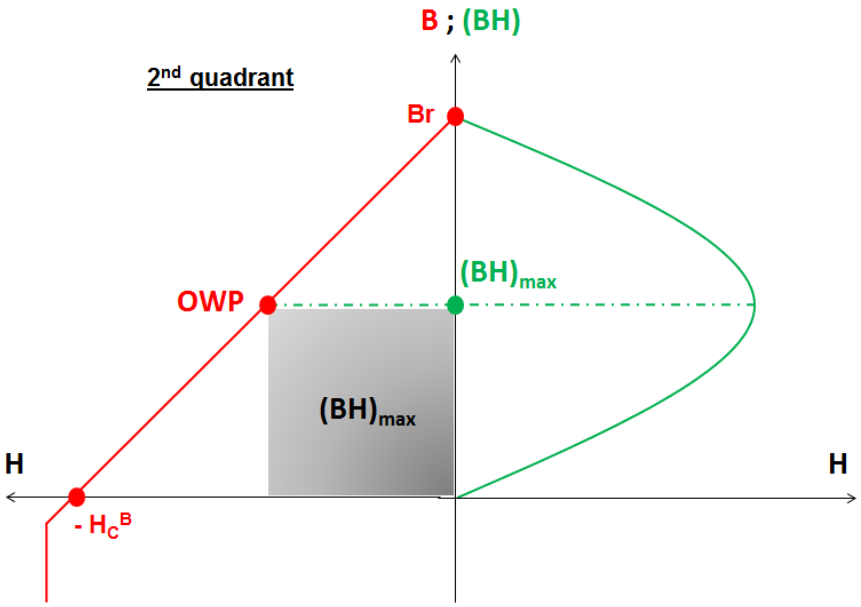

Figure I-2. *Schemes in the second quadrant of the induction loop B=f(H) (red curve) and the associated (BH)=f(H) curve (green curve) allowing to find the optimum working point (OWP) where the rectangular area below the demagnetization curve correspond to the* $(BH)_{max}$ *(grey surface).*

Several parameters affect the magnetic performance of a permanent magnet; though most of them are interconnected we will try to list them independently in a comprehensive order:

(i) The squareness ratio (SQ)

The squareness ratio allows one to compare the experimental magnetization loop with respect to the ideal squared loop expected:

$$SQ = \frac{A}{M_S \cdot H_C^M} \qquad \text{(Eq. 2)}$$

where A is the experimental area below the demagnetization curve M=f(H) and $M_s \cdot H_c^M$ corresponds to the maximum area enclosed in an ideal magnet. The closer the SQ will be to 1, the larger the $(BH)_{max}$ will be (Figure I-3).

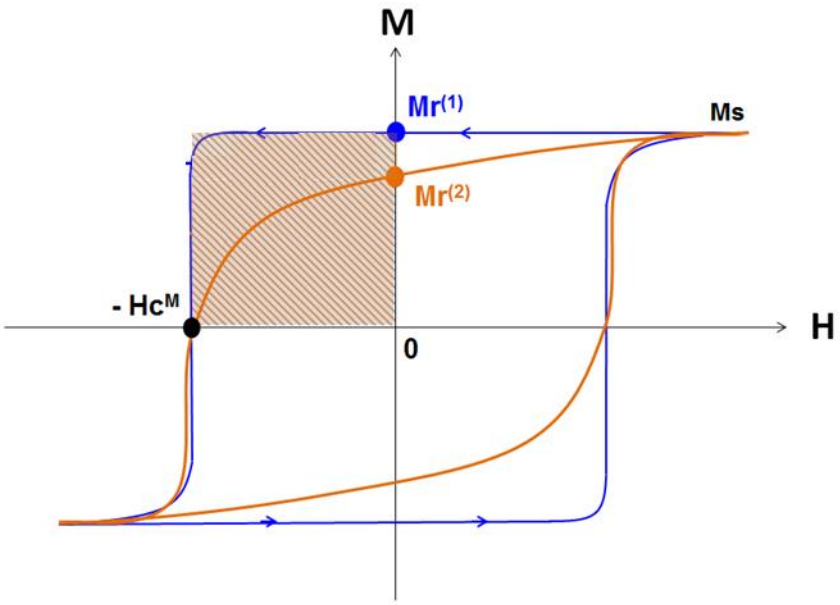

Figure I-3. *Schemes of two magnetization loops with the same values of M_s and H_c^M, but with different values of M_r and M_r/M_s. The blue curve, typically observed for the oriented magnets, exhibits a higher squareness coefficient in the second quadrant, leading to a higher $(BH)_{max}$.*

(ii) The orientation coefficient M_r/M_s

The squareness ratio is related to the well known M_r/M_s ratio, called "orientation coefficient", which gives an indication of the distribution of orientations of the magnetic moments in the material.

In the case of isotropic magnets with random orientation a M_r/M_s = 0.5 is observed. However, if the magnetic moments are aligned in a preferred direction, M_r/M_s tends towards the ideal value of 1 (Figure 3, blue curve), leading to a higher SQ.

(iii) The magnet shape, which affects the demagnetization factor N

If the magnet geometry is optimized, i.e. if the magnet exhibits N = ½ such as in a small cylinder of height roughly equal to its radius, the optimal $(BH)_{max}$, referred to as the maximum energy product $|BH|_{MAX}$ can be reached providing a sufficient coercive fields:

$$|BH|_{MAX} = \frac{B_R^2}{4\mu_0} \qquad \text{(Eq. 3)}$$

(iv) The coercive fields H_c^M and H_c^B

Let us consider a ferromagnetic material with a perfectly rectangular magnetization loop (SQ=1) and an optimized external shape. In such a case, the demagnetization curve of the induction loop is a straight line exhibiting a slope :

$$B = H + \mu_0 B_r. \qquad \text{(Eq. 4)}$$

Two options can then be encountered:

- **$H_c^M \geq B_r/2\mu_0$ (Figure 4a).**

In this ideal case, the maximum energy product can reach the optimal value

$$|BH|_{MAX} = \frac{\mu_0 M_S^2}{4} = \frac{B_r^2}{4\mu_0} \qquad \text{(Eq. 5)}$$

- **$H_c^M < B_r/2\mu_0$ (figure 4b).**

In this case, the maximum energy reads :

$$(BH)_{max} = H_c^B\left(B_r - \mu_0 \cdot H_c^B\right) \qquad \text{(Eq. 6)}$$

The magnet is then limited in coercivity, the $(BH)_{max}$ is far from its optimal value, and the working point is located at the "knee" of the loop. The magnet could be irreversibly demagnetized.

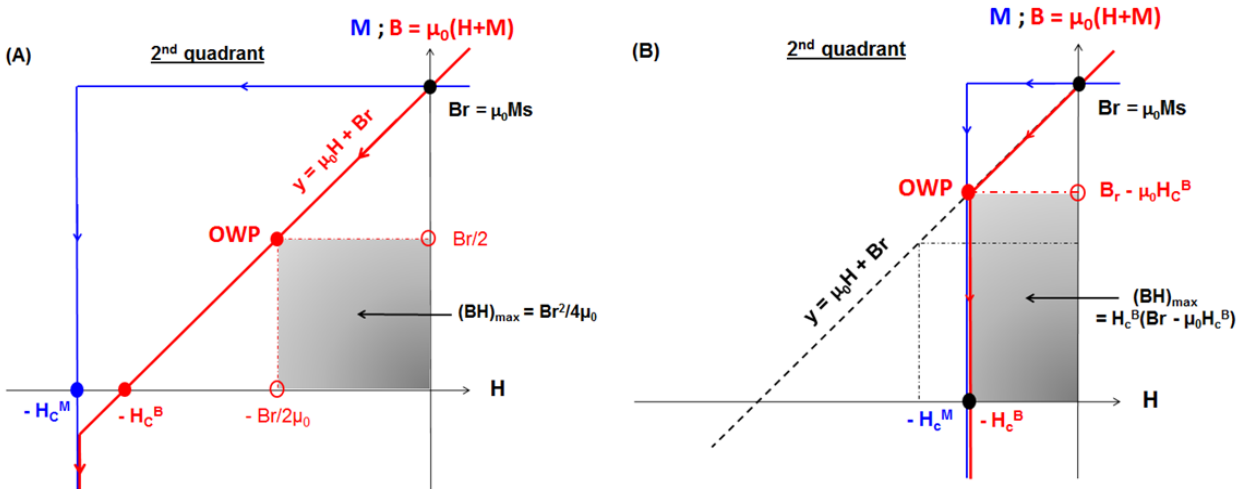

Figure I-4. *Influence of the coercive field on $(BH)_{max}$: schemes of the magnetization loops M=f(H) with a perfectly rectangular shape and with induction loops B=f(H) of ferromagnetic materials with* ***(A)*** *$H_c^M \geq \mu_0 M_r/2$ (ideal case) and* ***(B)*** *$H_c^M < B_r/2\mu_0$. OWP = Optimum working point.*

(v) The saturation magnetization Ms.

Looking at Eq. 3, one can easily understand that the saturation magnetization should be as high as possible to maximize the energy product.

Conclusions:

Based on these different parameters, one can conclude that an efficient permanent magnet consists in a material with high saturation and remanent inductions, square magnetization loop (SQ ≈ 1 and $M_r/M_s \approx 1$), a large coercive field ($H_c^M > B_r/2\mu_0$) and an optimized external shape. Therefore, processed magnets commercially available are usually prepared following classical metallurgy processes:

i) Preparation of an isotropic powder using melt-spinning or ball-milling.
ii) Alignment of the easy axis of all crystallites under an external magnetic field to improve the remanent magnetization and the squareness.
iii) Compaction into a fully dense material to improve the saturation magnetization. This step usually consists in high temperature sintering

These three steps are mandatory to reach high $(BH)_{max}$ values. However, difficulties are encountered when one wants to reduce the size of the final magnet, for instance to prepare sub-centimetric magnets integrated into MEMS. An alternative approach consists in assembling single domain nanoparticles with high anisotropy into dense materials and thus exploits a nano-structuration. The recent progress of the nanochemistry, which lately yielded nano-crystals with tuneable sizes, shapes and thus physical properties, opens great perspective for such magnetic nanocomposites. We will briefly review the main characteristic of nanomagnetism and then develop the potentiality of anisotropic Co rods to elaborate permanent magnets.

I.2 Magnetism of nanoparticles

The books of A.P. Guimarães [4] and B.D. & C.D. Cullity Graham [1] were used to write the following section.

I.2.1 From macroscopic to nanometric scale

a. The different magnetic energies

The configuration of the magnetic moments in materials results from the minimization of the total magnetic energy E_m, defined as the sum of [5]:

$$E_m = E_{ex} + E_{mc} + E_d + E_z \qquad \text{(Eq. 7)}$$

where E_{ex}, E_d, E_{mc} and E_Z represent the exchange, dipolar, magnetocrystalline and Zeeman energies, respectively. These energies will affect the spin configuration as follow:

E_{ex} favors a parallel alignment between magnetic moments. The strength of the coupling is characterized by the exchange constant A. It promotes a uniform magnetized state below the Curie temperature (T_c).

E_{mc} depends on the lattice symmetry and favors some particular crystalline directions, referred to as magnetocrystalline easy-axis. The magnetocrystalline anisotropy constant K_{mc} characterizes its strength.

E_d is the dipolar energy which depends on the nanomagnet shape; it favors the long-axis direction in order to reduce the magnetic flux density. One can define an exchange length, denoted by l_{ex}, above which the dipolar interactions predominates over exchange coupling:

$$\mathrm{l_{ex}} = \sqrt{\frac{2\mathrm{A}}{\mu_0 \mathrm{Ms}^2}} \qquad \text{(Eq. 8)}$$

where μ_0 the vacuum permeability. Generally this length is about a few nm.

E_z is the Zeeman energy and reflects the interaction between the nanomagnets and an external magnetic field.

b. Size effect on spin configurations

At equilibrium, the magnetic configuration adopted, i.e. the orientation of magnetic moment carried by each atom, tends to minimize the energy of the system.

In bulk ferromagnetic materials the competition between different energy sources leads to a division into domains called "Weiss domains" in reference to P.-E. Weiss (Figure I-5).

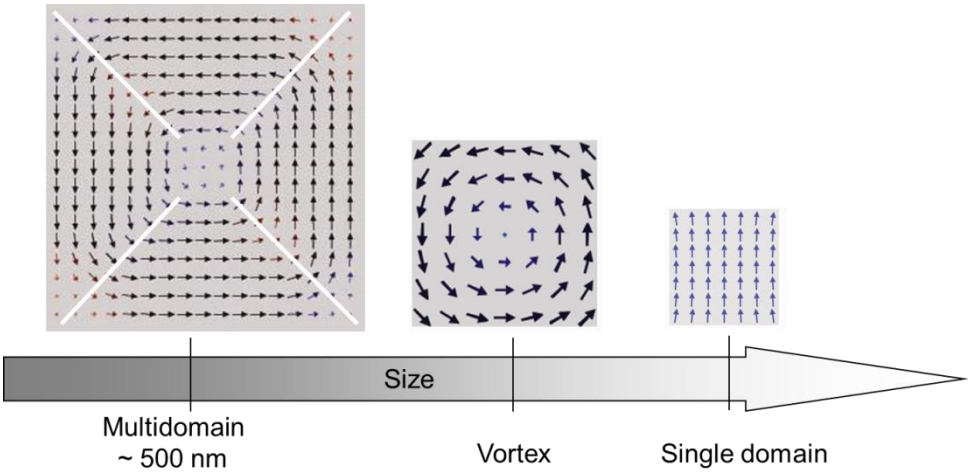

Figure I-5. *Evolution of the magnetic moment configuration as a function of sizes. The transition between the multidomain and single domain configuration occurred through non uniform state such as vortices.*

Between adjacent domains, a transition zone called "Bloch wall" allows the progressive rotation of the magnetic moments. The width of a 180° Bloch wall, denoted δ_B, is determined by the competition between the exchange and the magnetocrystalline anisotropy energies:

$$\delta_B = \pi\sqrt{\frac{A}{K_{mc}}} \qquad \text{(Eq.9)}$$

δ_B can vary from 10 to 100 nm depending on the material.
When the magnet size decreases down to the nanometric dimension, creating a Bloch wall may be energetically unfavorable. Non homogeneous states such as vortices are then observed. For smaller sizes, single domain configurations are finally observed, where all the spins are fairly parallel to each other (Figure I-5). The transition between single domain configuration and vortices is often referred to as the critical single domain size D_{sd}.

This critical size is defined, for spherical particles, as the diameter for which the single domain and two domain configurations are energetically equivalent [6]:

$$D_{SD} = \frac{72\sqrt{A \times K_{mc}}}{\mu_0 M_S^2} \qquad \text{(Eq. 10)}$$

Ferromagnetic nanoparticles (NPs) small enough to exhibit a single domain configuration may have a non-zero magnetization without any applied external magnetic field. This difference in magnetic characteristic between NPs and bulk materials is one of the most noticeable one. One can then assimilate the overall magnetization of a single domain particle to a "macro-spin".

I.2.2 Magnetization reversal in magnetic nanoparticles: Stoner-Wohlfarth Model (SW)

a. The energy barrier KV.

In this model, a single domain particle of volume V with a uniaxial magnetic anisotropy K, i.e. with a single axis of easy magnetization, is considered. The overall magnetization M is the sum of the magnetic moments of each atom (Figure I-6A).

As a first approximation the anisotropy energy, which can arise from the magnetocrystalline or dipolar terms, is calculated as:

$$\mathrm{E_{ani}} = \mathrm{K \cdot V \cdot \sin^2\theta} \qquad \text{(Eq.11)}$$

where θ is the angle between the magnetization $\overrightarrow{\mathrm{M}}$ and the easy axis (Figure 7a).

For θ = 90° E_{ani} is maximum and equals KV (Figure 6b). This value corresponds to an energy barrier that must be overcome to induce the particle magnetization reversal. Depending on the value of this energy barrier in regards to the thermal energy k_BT, two behaviors can be distinguished :

(i) $KV \leq k_BT$: the particle is superparamagnetic. The thermal energy is sufficient to overcome the energy barrier, the magnetization rotates spontaneously to align parallel or antiparallel to the easy axis. Superparamagnetism must be avoided for permanent magnet applications since the mean remanence is zero.

(ii) $KV >> k_BT$: the particle is blocked. The energy barrier may only be overpass by applying a magnetic field H in the opposite direction;

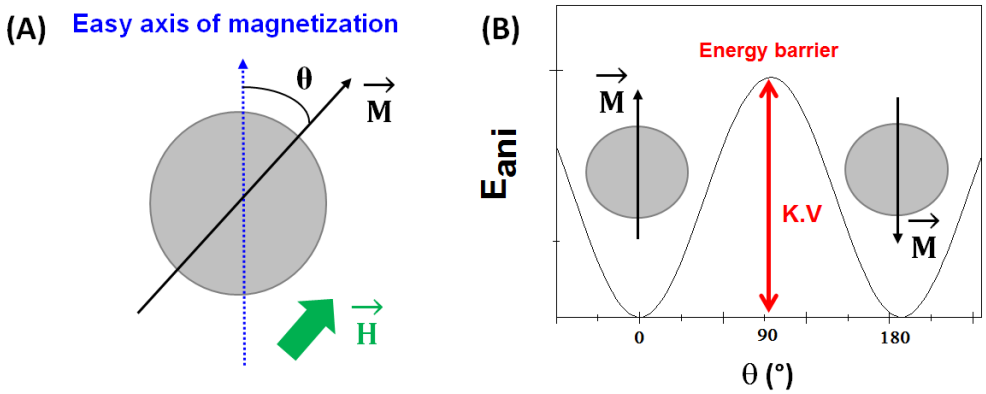

Figure I-6. (A) *Schematic representation of a single domain NP with uniaxial anisotropy. The magnetization $\vec{M}$ is tilted by an angle θ with respect to the magnetization easy axis.* ***(B)*** *Magnetic anisotropy energy as a function of θ.*

b. Impact on the hysteresis loops

The figure I-7a shows the evolution of the hysteresis cycle measured for a single domain NP with uniaxial anisotropy as a function of the angle θ between the easy axis and the applied field directions. The hysteresis loop is perfectly square when the applied field is parallel to the easy axis (θ_0 = 0°), with the coercive field reaching its maximum value, known as the anisotropy field H_K :

$$H_C = H_k = \frac{2K}{M_S} \qquad \text{(Eq. 12)}$$

As the applied field deviates from the particle's easy axis of magnetization, the squareness decreases, ending up to a linear M-H relationship with no hysteresis observed (H_c=0). Finally, the ratio of the magnetization saturation over the remanence magnetization drops from 1 (for θ_0 = 0°) to 0 (for θ_0 = 90°), respectively, indicating that in the second case the sample is no more magnetized.

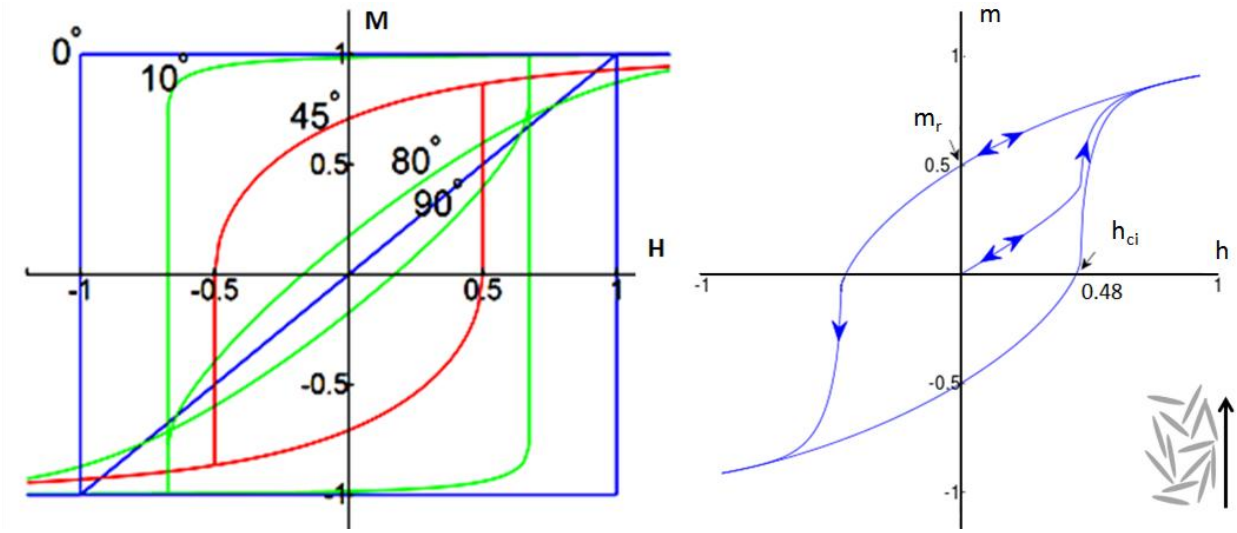

Figure I-7 *Typical M-H curves for the SW model at 0°, 10°,45°,80° and 90° angle of the applied field with respect to the particle long axis (left); M-H loop for an array of randomly oriented single domain particles (right).*

The SW model also examined an array of non interacting particles with a random distribution of anisotropy axes, a model that resembles a real polycrystalline magnet. The hysteresis loop is plotted in the figure I-7b in terms of the reduced variables, $m = M/M_s$ and $h = H/H_K$. The remanence for the array of particles is $m_r = 1/2$ and the coercivity is $h_c = 0.482$.

Thus, in the perspective of preparing efficient permanent magnets from nanoparticles, the alignment will be of crucial importance. Moreover to fully benefit from the remanent magnetization, the coercive field should be as high as possible, the anisotropy constant K should then be maximized according to eq. 12.

I.2.3 Magnetic anisotropy: different sources

The magnetic anisotropy describes the preferential magnetization orientation of a material in one particular direction of space, referred to as the magnetic easy axis direction. Such anisotropy may arise from different sources: the external shape of the magnet (shape anisotropy), the crystal structure of the material (magnetocrystalline anisotropy), the presence of a mechanical stress (magnetostriction anisotropy), the presence of a large surface/volume ratio (surface anisotropy) or the presence of an antiferromagnetic layer at the surface (exchange anisotropy). The permanent magnets presently produced benefits from the two first source of anisotropy that we will further detail.

a. Magnetocrystalline anisotropy

The magnetocrystalline anisotropy tends to align the magnetic moments along certain crystallographic directions of the crystal lattice. It is mainly due to the interaction between the magnetic moment and the crystal lattice through the electric field radiated by the surrounding ions. The intensity of this anisotropy depends on the symmetry of the crystal lattice and on the strength of the spin-orbit coupling.

(i) Lattice symmetry

For high symmetry lattices, such as the cubic ones, the magnetization easy axes are three (in case of <001> easy axis, bcc-iron for example) or four (in case of <111> easy axis, fcc-nickel for example). In contrast, for lattices exhibiting structural anisotropy, such as the hexagonal, orthorhombic, rhombohedral or tetragonal lattices, there is a single magnetization easy axis, generally along the c axis; this is for example the case for hcp-cobalt (Figure I-8A), for the tetragonal platinum-iron alloy (Figure I-8B) and for the intermetallic compound $Nd_2Fe_{14}B$ (Figure I-8C).

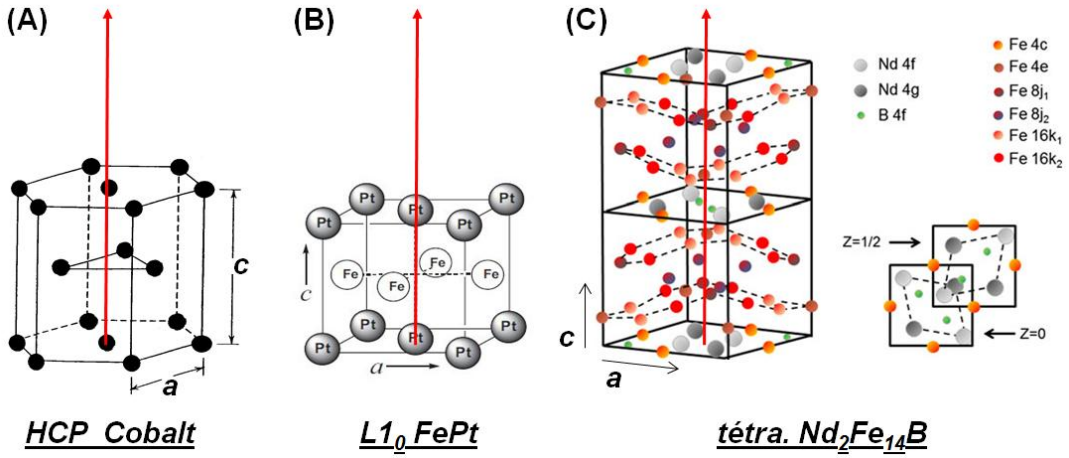

Figure I-8. *Atomic cell of* ***(A)*** *HCP cobalt,* ***(B)*** *tetragonal ($L1_0$) FePt (figures from [9] and* ***(C)*** *tetragonal $Nd_2Fe_{14}B$ (figure from* [7]*). The red arrows denote the magnetization easy axis along the crystallographic c axis.*

(ii) Spin-orbit coupling

The magnetocrystalline anisotropy is strong when the spin-orbit coupling is important. This is the case with rare earth compounds, such as $Nd_2Fe_{14}B$. The combination of these two effects leads to the magnetocrystalline anisotropy and the derived energy:

$$E_{mc} = K_1 sin^2\theta + K_2 sin^4\theta \qquad \text{(Eq. 13)}$$

Where θ represent the angle between the applied field and the easy axis, K_1 and K_2 are the first and second uniaxial anisotropy constants.

Thanks to the combination of lattice symmetry and spin-orbit coupling, $Nd_2Fe_{14}B$ exhibits a very high magnetocrystalline anisotropy constant $K_1 = 4.9\times10^6$ J.m^{-3}. For hcp Co, the anisotropy mostly arises from the lattice symmetry and is thus one order of magnitude below: $K_1 = 4.5\times10^5$ J·m^{-3}.

The effect of such magnetocrystalline anisotropy can be directly observed on the magnetization loop. The evolution of the magnetization as a function of the applied field is reported for hexagonal close pack structure of cobalt (Figure I-9). When the field is applied parallel to the c-axis, the saturation magnetization is very easily reached. This direction is therefore referred to as "easy axis". However, for an applied field perpendicular to the c-axis, known as "hard axis", large fields are mandatory to reached saturation magnetization.

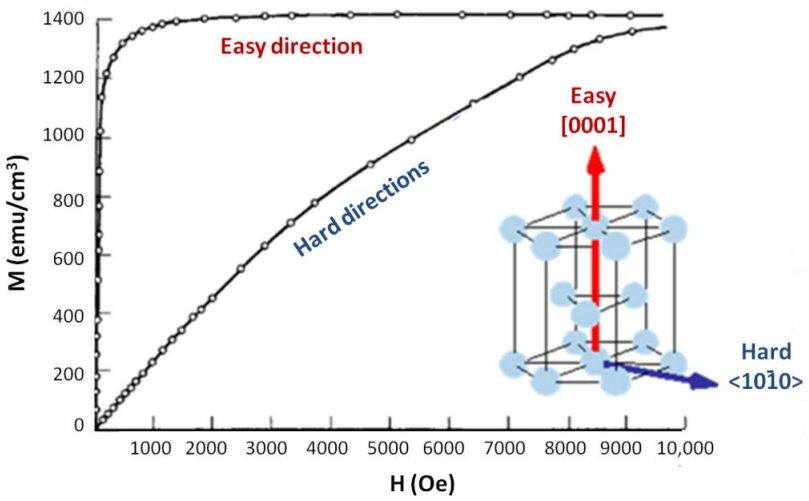

Figure I-9. *Magnetization curves for the hcp structure of Co along its easy and hard axis.*

b. Shape anisotropy

In the magnetized state, i.e. under a saturation field H_{sat}, one can assume that magnetic charges appear at the surface of the material which thus creates a magnetic field in the opposite direction, referred to as demagnetization field H_d (Figure I-10).

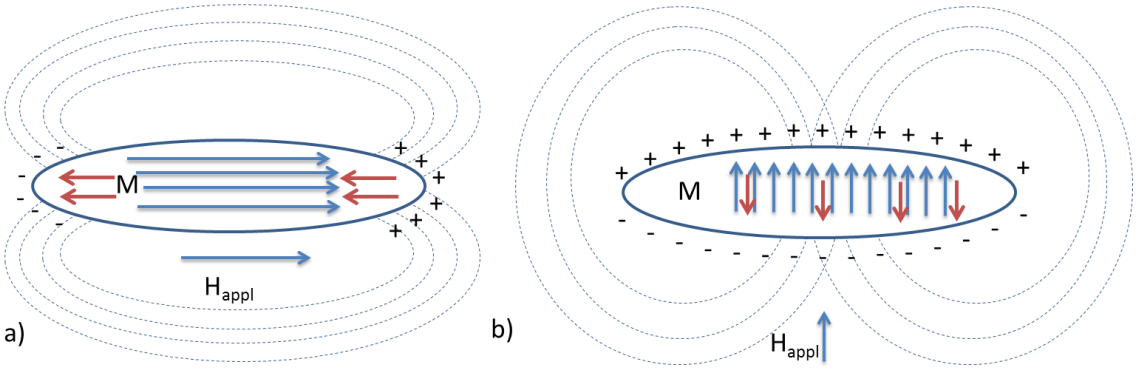

Figure I-10. *Schematic representations of magnetic poles, demagnetizing field H_d (red arrows), magnetization M (blue arrows) in an elongate ferromagnetic grain* ***a)*** *parallel or* ***b)*** *perpendicular to the applied field direction (H_{appl}). (Adapted from* [8]*).*

As previously described, this field varies linearly with the demagnetization factor N (Eq. 1), which is shape dependent. N can be calculated along both axes (Figure I-11), for perfect ellipsoid with circular cross section and high aspect ratio (m= c/a > 10) [9] :

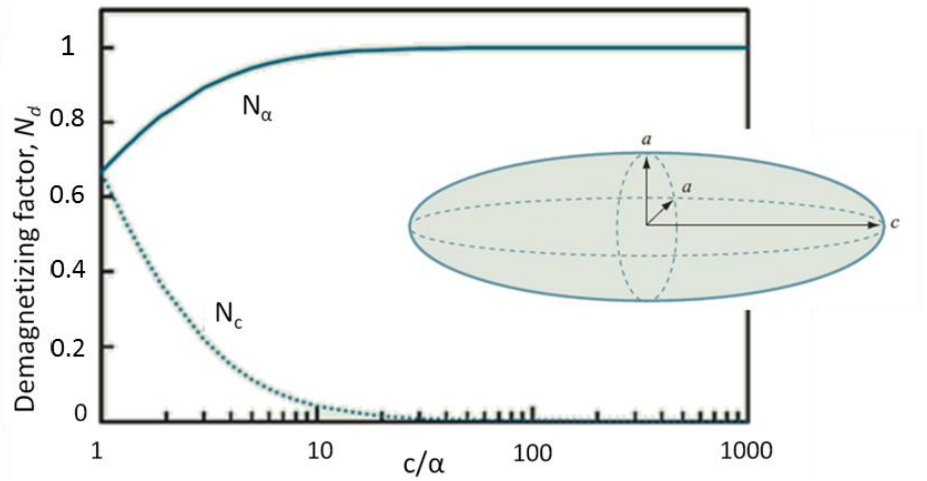

Figure I-11 *Dependence of the demagnetization factor (N) on the aspect ratio c/a. of an ellipsoid. (Adapted from* [9]*).*

For nanowire with aspect ratio higher than 10, the demagnetization factor along the hard axis (perpendicular to the long axis) equals to 2, while the demagnetization factor along the easy axis (parallel to the wire axis) is 0 (Figure I-11). Thus, the shape anisotropy energy of the nanowire is:

$$E_D = \frac{1}{2}\mu_0 N_\alpha M_s^2 - \frac{1}{2}\mu_0 N_c M_s^2 = \frac{1}{2}(N_\alpha - N_c)M_s^2 = \frac{1}{2}\left(\frac{1-3N_c}{2}\right)M_s^2 = \frac{1}{4}\mu_0 M_s^2 \ \ erg.cm^{-3} \qquad \text{(Eq. 14)}$$

The industrial magnets AlNiCo are made up of FeCo needles embedded in a non magnetic AlNi matrix. They take benefit from this shape anisotropy and therefore exhibit a good thermal stability (up to 500°C), the shape anisotropy being less temperature dependent that the magnetocrystalline one.

I.2.4. Summary of ferromagnetism in nanoparticles

In summary, single domain NPs can exhibit high coercivity providing a size and a magnetic anisotropy constant *K* large enough to be blocked at room temperature. This is the first condition to develop permanent magnets based on NPs.

Materials with high K_1 and moderate M_s, such as intermetallic compounds based on rare earth (NdFeB, SmCo) and 3d-5d alloy (FePt, CoPt), may be single domain for sizes up to several hundreds nm and do not exhibit a superparamagnetic behavior down to a few nm (Figure I-12). In contrast, in 3d metals such as cobalt, this size range between the super-paramagnetic behavior (≈ 15 nm) and the division into multi-domain (≈ 100 nm) is much smaller. Thus, in order to obtain high coercivities with 3d ferromagnetic NPs, it is necessary to increase the anisotropy combining shape anisotropy and magnetocrystalline anisotropy. Amongst the different 3d ferromagnetic metals and alloys cobalt crystallizing with the hcp structure exhibits the highest magnetocrystalline anisotropy.

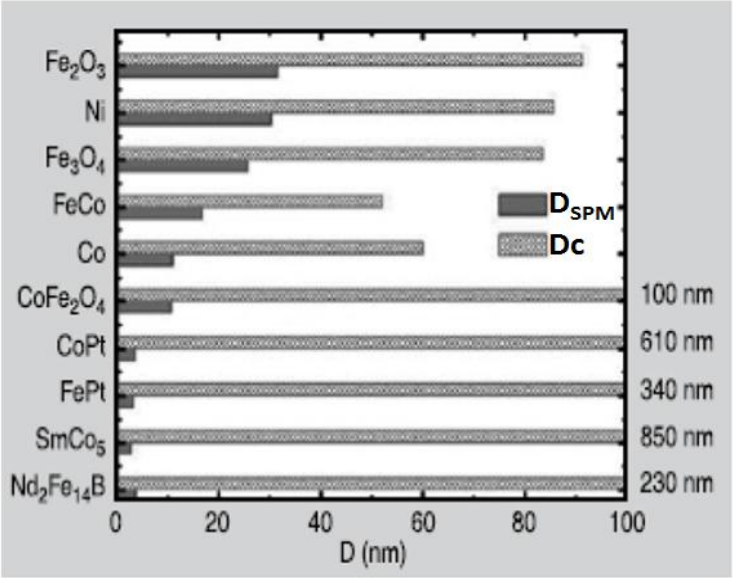

Figure I-12. *Critical sizes at room temperature for spherical particles of different materials: single domain limit (D_c) and super-paramagnetic limit (D_{SPM}). (Adapted from [10]).*

I.3 Towards cobalt nanostructured hard magnetic materials

In previous reports ([11], [12], [13], [14]) monocrystalline and monodispersed Co nanorods and nanowires have been suggested as promising candidates for permanent magnet applications, due to their combined shape and magnetocrystalline anisotropy where the c-axis of their hcp structure is parallel to their long axis (Figure I-13). The sum of these anisotropies corresponds to the internal energy field of these structures:

$$H_{tot} = H_D + H_{ca} \qquad \text{(Eq. 15)}$$

Considering an hcp cobalt nanoparticle, with ellipsoidal shape and infinitive length:

$$H_{tot} = H_D + H_{ca} = 2\pi M_s + k_1/2\pi M_s = 8.9 + 7.3 = 16.2\ kOe \qquad \text{(Eq. 16)}$$

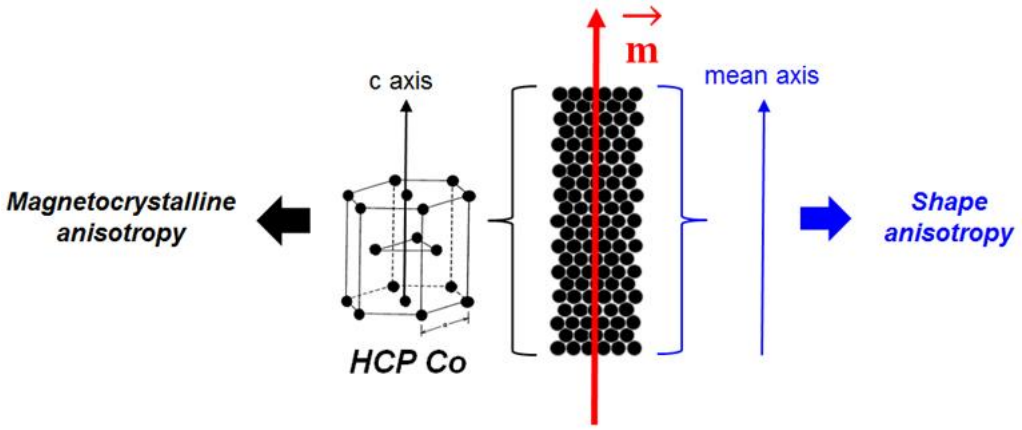

Figure I-13. *Schematic representation of a cobalt rod with the c-axis of the hcp structure and the long axis are in the same direction, resulting by an addition of magnetocrystalline anisotropy and shape anisotropy contributions. The vector m represents the magnetization of the particle.*

Nevertheless, much lower coercive fields were experimentally measured. Since the coercivity of a nanostructure may deviate from its theoretical values, due to its size, shape and the magnetization reversal mode, micromagnetic simulations may provide useful guidelines to improve the properties of individual objects prior to their further compaction.

I.3.1. Optimization of the magnetic properties of individual Co particles

The following section is a compilation of the micromagnetic modeling performed by F. Ott et al. on individual Co nanowires using the finite element code Nmag and the bulk parameters for Co (M_S = 1400 kA/m, A = 2.8x10^{-11} J.m^{-1}, K_1 = 4.1x10^5 J.m^{-3}).

a. Effect of the shape of elongated magnetic particles on the coercive field

Various experimental protocols (e.g. electrodeposition, polyol and organometallic route) or conditions (e.g. heating rate, pH, reducing agent and surfactants) can provide several shapes and sizes of elongated Co nanoparticles, such as cylinders or even diabolos (see chapter II).

F. Ott et al. studied how the exact shape of the magnetic nano-objects influences the coercivity. Real nano-objects could be modelled very precisely, distinction being made between ellipsoids, cylinders with flat tips and cylinders with rounded tips (Figure I-14). The micromagnetic simulations were performed keeping a constant length of L= 100 nm and varying the objects diameter D between 5 and 28 nm [15]. The aspect ratio (AR) was defined as:

$$AR = \frac{L}{D} \qquad \text{(Eq. 17)}$$

The external field was applied at θ= 5.7° with respect to the object's easy axis and the magnetocrystalline anisotropy was neglected (K_1 = 0) to only observe the shape anisotropy.

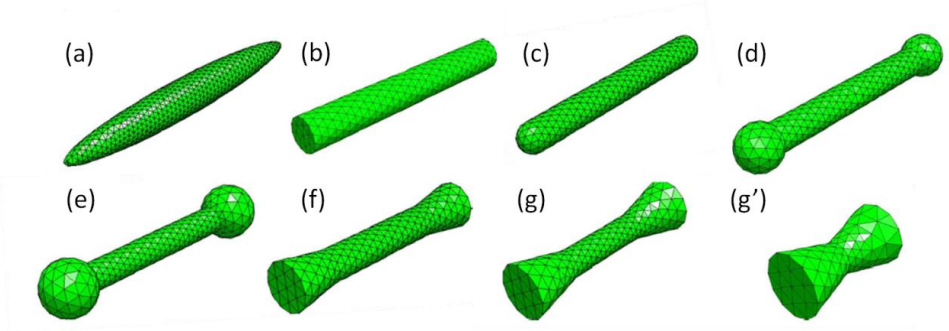

Figure I-14. *Different types of particles models and the corresponding meshes.* ***(a)*** *Ellipsoids,* ***(b)*** *cylinders,* ***(c)*** *capped cylinders,* ***(d)*** *dumbbells with small spherical ending, (dumbbell 1),* ***(e)*** *dumbbells with larger spherical endings (dumbbell 2),* ***(f)*** *cylinders with small cone endings (diabolo 1),* ***(g)*** *cylinders with larger cone endings (diabolo 2), and* ***(g')*** *small diabolos. (Adapted from* [15]*).*

The evolution of the coercive field with the aspect ratio of these objects is summarized in the Figure I-15 and raises various comments:

- Whatever the shape, the coercivity increases with the aspect ratio, due to the reinforcement of the shape anisotropy. However, aspect ratio above 10 barely increases the coercive field.
- The shape control appears to be crucial to increase the coercivity. Significant differences are indeed observed between ellipsoidal particles and cylinders.The coercive field is reduced by about 20% as soon as the shape departs from the perfect ellipsoidal one due to an inhomogeneous demagnetization field. The maximum of the demagnetization field acts as nucleation point for the magnetization reversal.

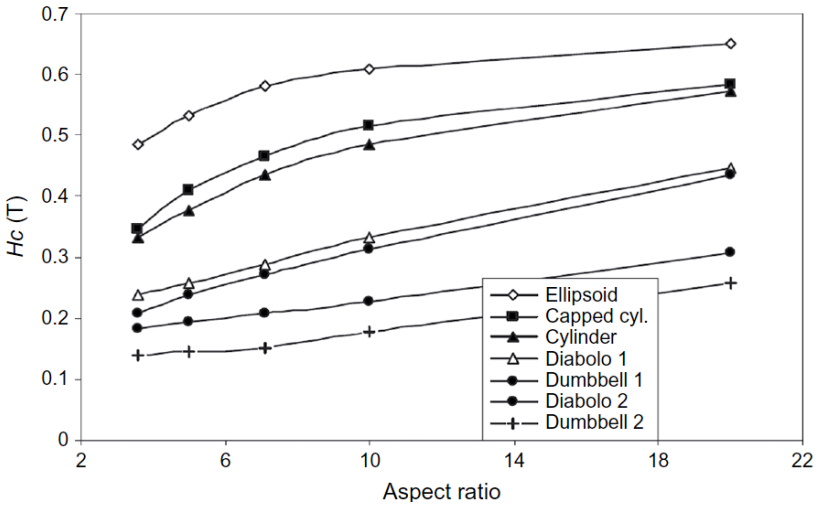

Figure I-15. *Variation of the coercivity of Co anisotropic particles as a function of their aspect ratio for different shapes of objects. The magnetic field is applied at an angle 5.7° with respect to the object long axis. (Adapted from Ott et al.* [15]*).*

b. Mean Diameter and aspect ratio effect of isolated cobalt rod

F. Ott et al. further studied the effect of the mean diameter and aspect ratio of Co nanorods on the coercivity [16]. Both lengths and diameters were varied and the magnetocrystalline anisotropy of Co was used. Figure I-16 summarizes the reported results which are compared with the Stoner-Wohlfarth model (in red) :

- As previously observed, the coercivity increases with the aspect ratio varying from 1 to 8. Above that (AR > 10) there is no significant gain in H_c.
- The coercivity is lower than the Stoner-Wohlfarth model for aspect ratio above 2.
- Small wire diameters (D= 5 nm) lead to higher coercive fields than larger ones.

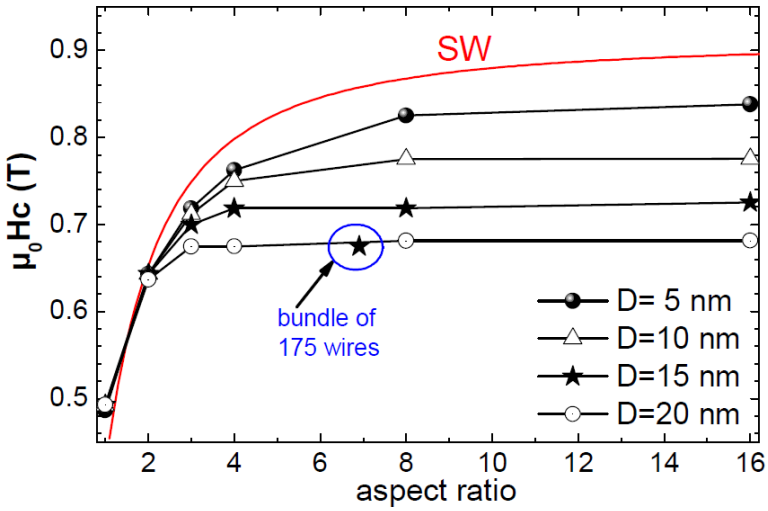

Figure I-16 *Coercivity values of Co cylinders with different diameters D as a function of their aspect ratio. The external field was applied at 22° with respect to the cylinder's axis. The prediction of the Stoner-Wohlfarth (SW) model is plotted as a red continuous line. (Adapted from* [16]*).*

c. Magnetization reversal in Co nanorods

The Stoner-Wohlfarth model is quite often referred when trying to describe the reversal processes in magnetic nanoparticles. Strictly speaking, the Stoner-Wohlfarth (SW) model should only be applied when the rotation of the magnetization in the nanoparticle is coherent, i.e. only in ellipsoidal particles with homogeneous demagnetizing field. Such SW behaviour is nevertheless expected for particles having sizes below a coherent radius defined as:

$$R_{coh,sphere} = \sqrt{24} l_{ex} \qquad \text{for spheres} \qquad \text{(Eq. 18a)}$$

$$R_{coh,cyl} = 3.65 \times l_{ex} \qquad \text{for cylinders} \qquad \text{(Eq. 18b)}$$

In the case of cobalt, this coherent radius can be calculated to be $R_{coh,cyl}$ = 7.5 nm which is on the order of or above the typical radius of the considered Co nanowires.

Reduced coercive fields are however always encountered with Co NRs compared to the Stoner-Wohlfarth model (Figure I-17). To understand this effect, time resolved micromagnetic simulations [16] were studied on two types of Co rods exhibiting diameters smaller (D= 5 nm) and larger (D= 20 nm) than D_{coh}. The detail of the reversal process is illustrated on Figure I-18. Whatever the diameter of the nanowire, the magnetization reversal always proceeds with transverse domain wall propagation:

- For $D > D_{coh}$, the reversal process takes place via a buckling mode and the magnetization becomes inhomogeneous along the wire axis (Figure 17a).
- For $D < D_{coh}$, the reversal does not take place as a fully coherent rotation of the magnetization. A transverse domain wall is accommodated across the nanowire diameter and the reversal takes place through the propagation of such domain wall (Figure I-17b). In the other parts of the nanowire, the magnetization remains parallel to the wire which is a very low energy state. This mechanism, which is different from the fully coherent rotation, is made possible by the fact that the tips of the wire create nucleation points for domain walls.

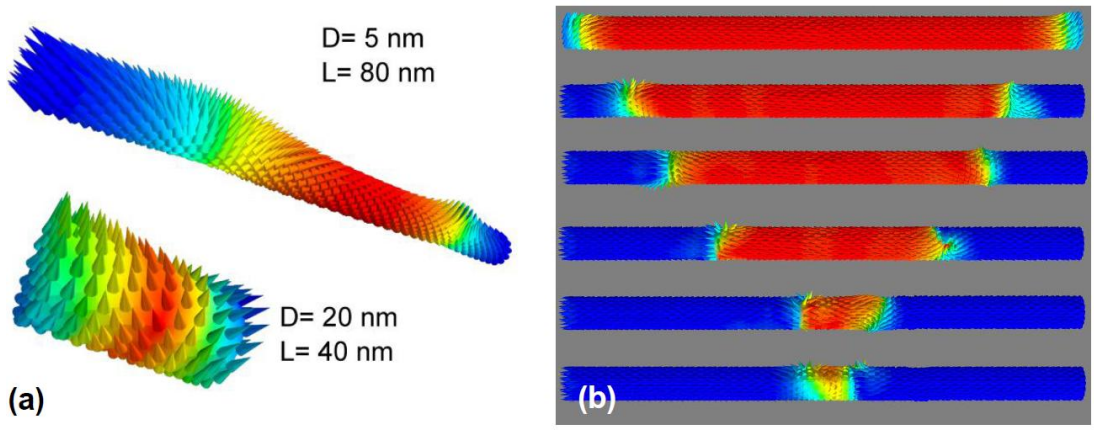

Figure I-17 ***(a)*** *Magnetic states close to the coercivity of Co cylinders with different diameters and aspect ratios. The color variation corresponds to the magnetization component along the cylinder axis. The external field is applied with an angle ψ= 5° relative to the cylinder axis.* ***(b)*** *Magnetic reversal in a Co cylinder with D=20 nm and L= 16D. The color variation corresponds to the magnetization component along the cylinder axis. The reversal proceeds with simultaneous propagation of two domain walls (tail-to-tail and head-to-head) towards the centre following nucleation of reversed domains from the left and the right sides, respectively. The external field is applied with an angle ψ= 5° relative to the cylinder axis. (Adapted from* [16]*).*

d. Conclusions on optimized Co nanorods

The micromagnetic simulations thus provide the following general guidelines to produce high coercivity nanowires: (i) the diameter should be as small as possible, (ii) the aspect ratio does not need to be higher than 10, (iii) the tips of the wires play a key role and should be as rounded as possible to avoid providing a nucleation point.

I.3.2. From nanowires to bulk materials

a. Influence of the degree of alignment

When considering assemblies of nanowires, the alignment of the wires is one of the key parameter [17]. Assemblies of randomly oriented nanowires (black curve, figure I-18) or aligned nanowires (red and blue curves, figure I-18) lead to very different magnetization loops and thus magnetic performances. In the former case, one gets an isotropic material with average properties, while in the aligned case, the properties of the material are enhanced (H_c and M_r) but only in the direction of the wires alignment (blue curve). In the perpendicular direction the properties are fairly poor (red curve). This corresponds to an anisotropic magnet such as aligned AlNiCo.

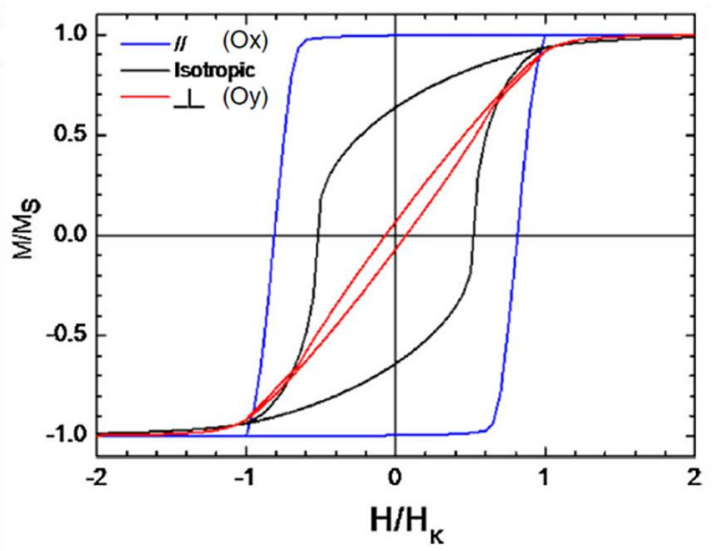

Figure I-18 *Calculated in-plane hysteresis loops of an isotropic (black) and of an aligned sample (blue easy axis, red hard axis). (Adapted from* [17]*).*

b. Influence of the packing density p

(i) Effect on Hc

The effect of the packing motif on the coercivity was simulated by Toson et al. [18] who considered aligned assemblies of Co nanowires (D= 10 nm, L= 100 nm) organized along either a close-pack hexagonal or a squared arrangement (Figures I-19a, b). In both types of assemblies the coercivity decreases with the packing fraction due to the presence of magnetic interactions and demagnetization fields effects (Figure I-19c).

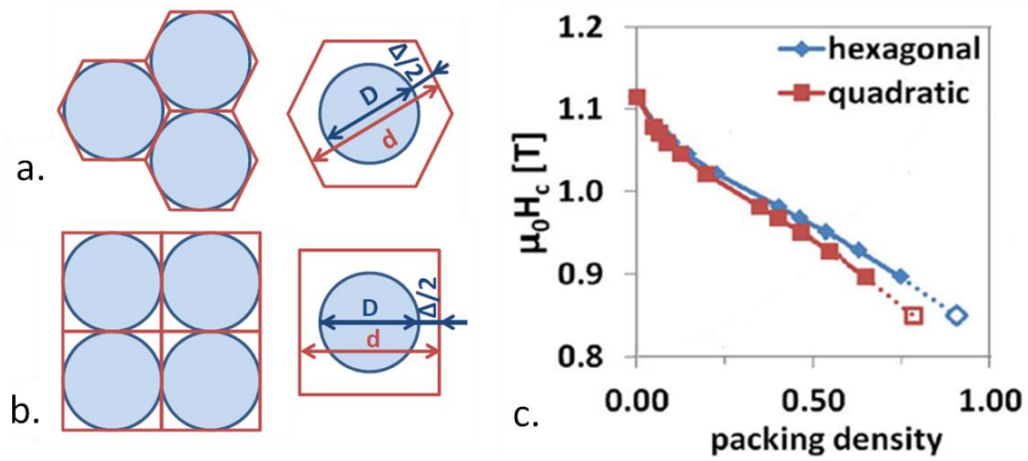

Figure I-19. *Models for perfectly aligned Co nanowires in* ***a.*** *hexagonal and* ***b.*** *quadratic grid, with diameter D and surface-to-surface distance Δ= d – D; c. variation of the coercivity over the packing densities of hexagonal (blue diamonds) and quadratic (red squares) nanowire arrangements. (Adapted from* [18]*).*

(ii) Effect on the $(BH)_{max}$

Micromagnetic calculations were performed on a bundle of nanowires, made of Co or Fe, assembled in rectangular arrays of 19 rows, each of which being composed of nanowires arranged along an hexagonal 2D-lattice [19]. The maximum BH_{max} value could be deduced from the simulated hysteresis cycles. Figure I-20 shows the variation of the energy product of Fe and Co nanowire.

In the case of Fe, there is an optimal packing density above which the energy density decreases. A larger packing fraction increases B_r but decreases H_c due to the dipolar interactions. Above a critical packing fraction the $(BH)_{max}$ becomes limited by the coercivity as previously presented in Figure I-4b.

In the case of Co, high packing fraction is not detrimental because of the large magneto-crystalline anisotropy, thus the $(BH)_{max}$ increases as a function of the packing density and is never limited in coercivity (Figure I-4a). If packing fractions of 0.9 are idealistic values which will not be achievable experimentally, adapted compaction techniques could lead to p = 0.6-0.7. Thus, one can hope that assemblies of Co NRs well aligned and densified could reached $(BH)_{max}$ values in the range 200 – 300 $kJ \cdot m^{-3}$, thus competing with SmCo and bonded NdFeB magnets.

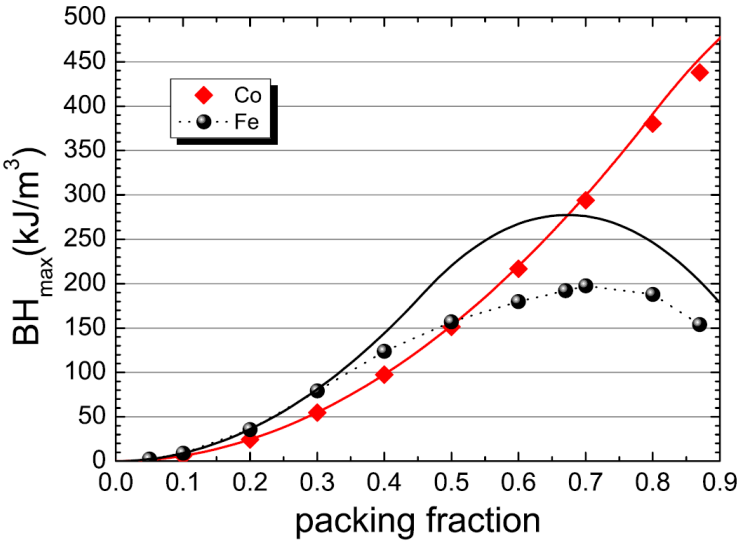

***Figure I-20** : Energy product $(BH)_{max}$ as a function of packing fraction for cobalt (red diamonds) and iron (black circles) nanowires. The continuous lines show the calculations under the assumption of square loops. (Adapted from* [19]*).*

I.4 Conclusions

Cobalt nanorods can be promising candidates for permanent magnet applications, due to their combined shape and magnetocrystalline anisotropy, where the c-axis of their hcp structure is parallel to their long axis.

For the realization of Co based permanent magnet the challenge consists in aligning these NRs into dense parallel assemblies to yield squared induction loop with high saturation and remanent inductions. To fully benefit from high $(BH)_{max}$, large coercivity field are required to satisfy the criterion of $H_c^M > \frac{B_r}{2\mu_0}$.

Important efforts should thus be devoted on the optimization of the Co NRs properties by adjusting the rod shapes, enlarged tips should be strictly avoided while small diameters and intermediate aspect ratio (AR~5-8) should be targeted.

Considering **realistic packing fraction** (0.6<p<0.7), **good alignment** (misalignment angle < 5°) and a **large intrinsic coercivity** of the NRs ($\mu_0 H_C$>0.7T), one could obtain **$(BH)_{max}$ in the range 200-300 kJ.m^{-3}**, far above the AlNiCo and ferrites based magnets.

Bibliography

[1] B. D. Cullity, *Introduction to Magnetic Materials*, vol. 2012. 2009.

[2] É. du T. de Lacheisserie, "Magnetism I – Fundamentals," *Grenoble Sci.*, 2002.

[3] J. Coey, "Permanent magnets: Plugging the gap," *Scr. Mater.*, vol. 67, no. 6, pp. 524–529, 2012.

[4] A. Guimarães, "The Basis of Nanomagnetism," *Princ. Nanomagnetism SE - 1*, pp. 1–20, 2009.

[5] W. F. Brown, "The Fundamental Theorem of Fine-Ferromagnetic-Particle Theory," *J. Appl. Phys.*, vol. 39, no. 2, p. 993, 1968.

[6] C. Kittel, "Physical theory of ferromagnetic domains [37]," *Phys. Rev.*, vol. 79, no. 4, p. 745, 1950.

[7] L. H. Lewis and F. Jiménez-Villacorta, "Perspectives on Permanent Magnetic Materials for Energy Conversion and Power Generation," *Metall. Mater. Trans. A*, vol. 44A, no. January, pp. 2–20, 2012.

[8] J. Degauque, "Magnétisme et matériaux magnétiques : introduction," 1992.

[9] L. Sun, Y. Hao, C.-L. Chien, and P. C. Searson, "Tuning the properties of magnetic nanowires," *IBM J. Res. Dev.*, vol. 49, no. 1, pp. 79–102, 2005.

[10] N. Poudyal and J. Ping Liu, "Advances in nanostructured permanent magnets research," *J. Phys. D--Applied Phys.*, vol. 46, no. 4, p. 43001, 2012.

[11] G. Viau, C. Garcia, T. Maurer, G. Chaboussant, F. Ott, Y. Soumare, and J. Y. Piquemal, "Highly crystalline cobalt nanowires with high coercivity prepared by soft chemistry," *Phys. Status Solidi Appl. Mater. Sci.*, vol. 206, pp. 663–666, 2009.

[12] N. Liakakos, C. Achkar, B. Cormary, J. Harmel, B. Warot-Fonrose, E. Snoeck, B. Chaudret, M. Respaud, K. Soulantica, and T. Blon, "Oriented Metallic Nano-Objects on Crystalline Surfaces by Solution Epitaxial Growth," *ACS Nano*, vol. 9, no. 10, pp. 9665–9677, 2015.

[13] M. Vázquez and L. G. Vivas, "Magnetization reversal in Co-base nanowire arrays," *Phys. Status Solidi Basic Res.*, vol. 248, no. 10, pp. 2368–2381, 2011.

[14] Y. Henry, K. Ounadjela, L. Piraux, S. Dubois, J. M. George, and J. L. Duvail, "Magnetic Anisotropy and Domain Patterns in Electrodepositedcobalt Nanowires," *Eur. Phys. J. B*, vol. 20, pp. 35–54, 2001.

[15] F. Ott, T. Maurer, G. Chaboussant, Y. Soumare, J. Y. Piquemal, and G. Viau, "Effects of the shape of elongated magnetic particles on the coercive field," *J. Appl. Phys.*, vol. 105, no. 1, 2009.

[16] M. Pousthomis, E. Anagnostopoulou, I. Panagiotopoulos, R. Boubekri, W. Fang, F. Ott,

K. A. Atmane, J.-Y. Piquemal, L.-M. Lacroix, and G. Viau, “Localized magnetization reversal processes in cobalt nanorods with different aspect ratios,” *Nano Res.*, 2015.

[17] W. Fang, I. Panagiotopoulos, F. Ott, F. Boué, K. Ait-Atmane, J. Y. Piquemal, G. Viau, and F. Dalmas, “Optimization of the magnetic properties of aligned Co nanowires/polymer composites for the fabrication of permanent magnets,” *J. Nanoparticle Res.*, vol. 16, no. 2, 2014.

[18] P. Toson, W. Wallisch, A. Asali, and J. Fidler, “Modelling of Packed Co Nanorods for Hard Magnetic Applications,” *EPJ Web Conf.*, vol. 75, no. 20 14, pp. 4–7, 2014.

[19] I. Panagiotopoulos, W. Fang, F. Ott, F. Boué, K. Ait-Atmane, J. Y. Piquemal, and G. Viau, “Packing fraction dependence of the coercivity and the energy product in nanowire based permanent magnets,” *J. Appl. Phys.*, vol. 114, no. 14, 2013.

Chapter II Synthesis of Cobalt Nanorods

We saw in the chapter I the potentiality of ferromagnetic nanoparticles exhibiting an anisotropic shape for permanent magnet applications. Among the ferromagnetic metals and alloys, cobalt is probably the most interesting. Indeed in cobalt elongated nanoparticles one could benefit from an addition of the hcp structure magneto-crystalline anisotropy and the shape anisotropy.

In this chapter we will establish first a short state of the art on the synthesis of cobalt nanorods and nanowires. We will describe the main methods that allow the growth of anisotropic cobalt particles focusing on their mean diameter, crystallinity and organization. We have chosen to describe only the bottom-up approaches due to their higher capacity in the control of the nanoparticle shapes. Basically there are two main methods for cobalt rods and wires production. The first ones use a template for the anisotropic growth, while the second ones are called “template free liquid phase syntheses”. Among these latter, we will focus on the polyol process that seemed to be the most appropriate for a large scale production.

In the second part of this chapter we will present our experimental results on cobalt rod synthesis by the polyol process. The final scope was first, to develop an up-scale of the polyol process for the synthesis of cobalt nanorods at large scale and, second, to fabricate nanorods with the morphology and dimensions suggested by the micromagnetic simulations.

II.1. Synthetic methods for the production of cobalt nanorods : State of the art

The bottom-up synthetic approaches are based on the use of molecular precursors (e.g. metal ions or metal complexes) that produce, by a chemical reaction, metal atoms or clusters and eventually metal nanoparticles after a growth step. They are classified in two categories: vapor-phase and liquid-phase reactions. The liquid-phase route is a versatile method that can provide good control of the shape, size and crystallinity of the particles and it can be easily up-scaled.

A great challenge in the liquid-phase methods is the production of anisotropic shapes, especially with metals that exhibit a high surface tension favoring the isotropic shapes. Anisotropic growth is managed through the use of a template (organic, inorganic or biological) or by the presence of ligands in the growth medium that bind selectively to crystallographic facets. These latter methods, like the organometallic route and the polyol process are called template-free methods (Figure II- 1).

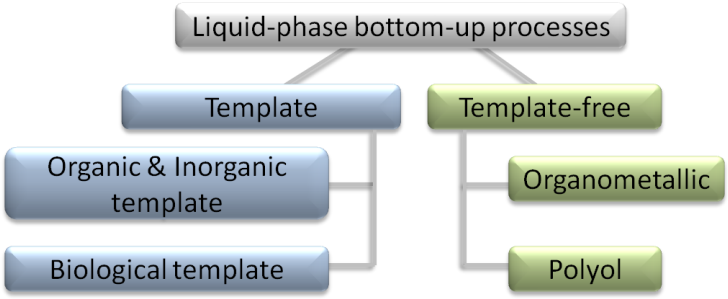

Figure II- 1 *Liquid-phase bottom-up approaches for the synthesis of cobalt anisotropic nanoparticles.*

II.1.1 Electrochemical deposition in nanoporous membrane

Numerous efforts have been directed towards the use of uniaxial porous membranes for the directed growth of parallel assemblies of anisotropic nanoparticles, with the most common being the anodic aluminum oxide (AAO) [1] and the radiation track-etched polycarbonate (TEPC) [2]. The TEPC membranes bear small pores (10 nm) with a random symmetry distribution. The AAO display very uniform pore size with length between 10 nm and 10 µm and diameter from some tens to several hundred of nanometers. The pore cells are hexagonally close-packed arranged forming straight cylindrical channels perpendicular to the surface.

Metal nanowires can be grown in these templates through: i) chemical deposition, ii) chemical vapor deposition or iii) i) electrochemical deposition; the latter being the most common technique for Co nanowires synthesis.

The electrodeposition (ED) of metals consists of an electrochemical process by which metallic ions from an electrolyte are reduced to form a solid deposit in the cathode of an electrochemical cell, according to the general reaction [3]:

$$M^{n+} + n^{e-} \rightarrow M$$

If the reaction is driven out of equilibrium by applying an overpotential, the effective electrodeposition of the metal M starts from the bottom of the template channels, with a bottom-up fashion. Electrochemical deposition processes are commonly carried out in an electrochemical cell such as the one schematized in Figure II- 2, which consists in a working electrode (cathode), where the reduction takes place, a counter electrode, used to close the electric circuit, and a reference electrode, with a stable and well-known electrode potential. In order to obtain the growth of metallic nanowires, the nanoporous membranes must be first modified to become electrically conductive and thus, allow the electrochemical reduction of electrolyte cations. For that reason a thin conductive layer, such as Au, Ag or

Cu, is often deposited on one side of the membrane [4]. The metal deposition into the cylindrical pores is achieved by applying different modes of electrical field to the electrochemical cell including potentiostatic ED [5], galvanostatic ED [6] and their combination called pulsed ED [7].

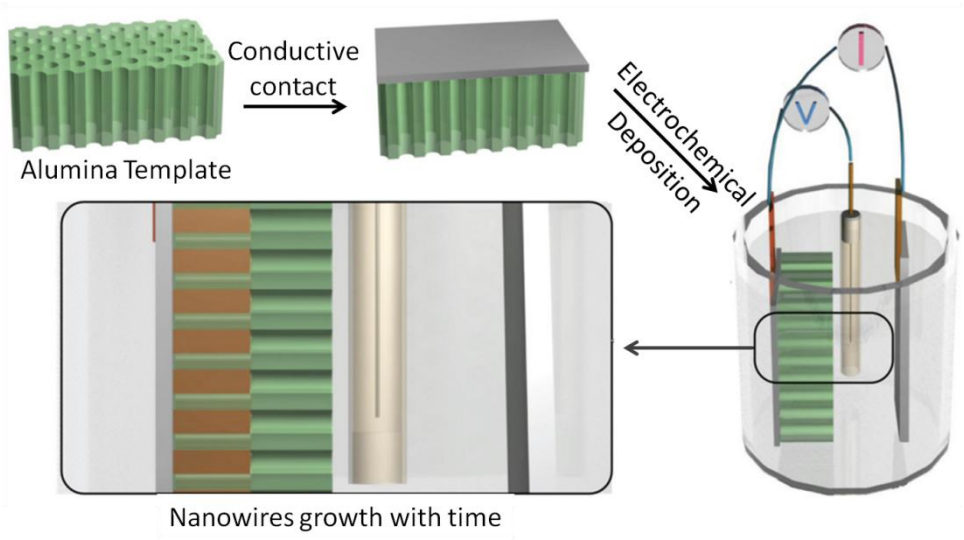

Figure II- 2 *Typical electrochemical deposition process with the use of an alumina template*

The final metal wire diameter is equal to the membrane's pore diameter, while other properties, such as their length, crystal structure and magnetic properties, can be controlled through different experimental parameters including current density, electrolyte pH, working electrode potential and reaction time.

The electrochemical synthesis of magnetic Co nanowires with controlled geometry and magnetic anisotropy was reported by Vivas *et al.* [8]. The nanowires were synthesized via DC electroplating into the pore channels of an AAO membrane. The electrodeposition was carried out using an aqueous electrolyte containing $CoSO_4$ and H_3BO_3 at room temperature, under constant stirring, and at a bias of -1V (versus Ag/AgCl). The wires' length could vary between 3 and 30 µm by monitoring the total charge that passed during deposition and their crystalline structure was tailored through the adjustment of the bath's acidity. The wires grew in the usual bottom-up fashion starting from the Au electrode at the pore bottoms and the average wire length (L). An SEM image of cobalt wires inside the AAO membrane (pore diameter: 50 nm, interpore distance 105 nm and NW length 3 µm) is illustrated at the Figure II- 3a. XRD patterns of Co NWs reveal the hcp structure in all cases, showing strong textures along the [100], [101] and [002] directions depending on the pH (Figure II- 3b). Their corresponding magnetic hysteresis loops are shown in the Figure II- 3c. The [100] texture (pH 3.5) presents a complex anisotropy distribution since there is a strong competition between the shape and magnetocrystalline anisotropy to make the effective magnetic anisotropy parallel and/or perpendicular to the NWs main axis. In the case of the

samples with [101] texture (pH 5.0) is it deduced that the easy magnetic axis is parallel to the wires, despite the non zero H_{ci} values for the perpendicular configuration. Finally, the NWs textured in the [002] direction (pH 6.7) present a strong uniaxial magnetic anisotropy.

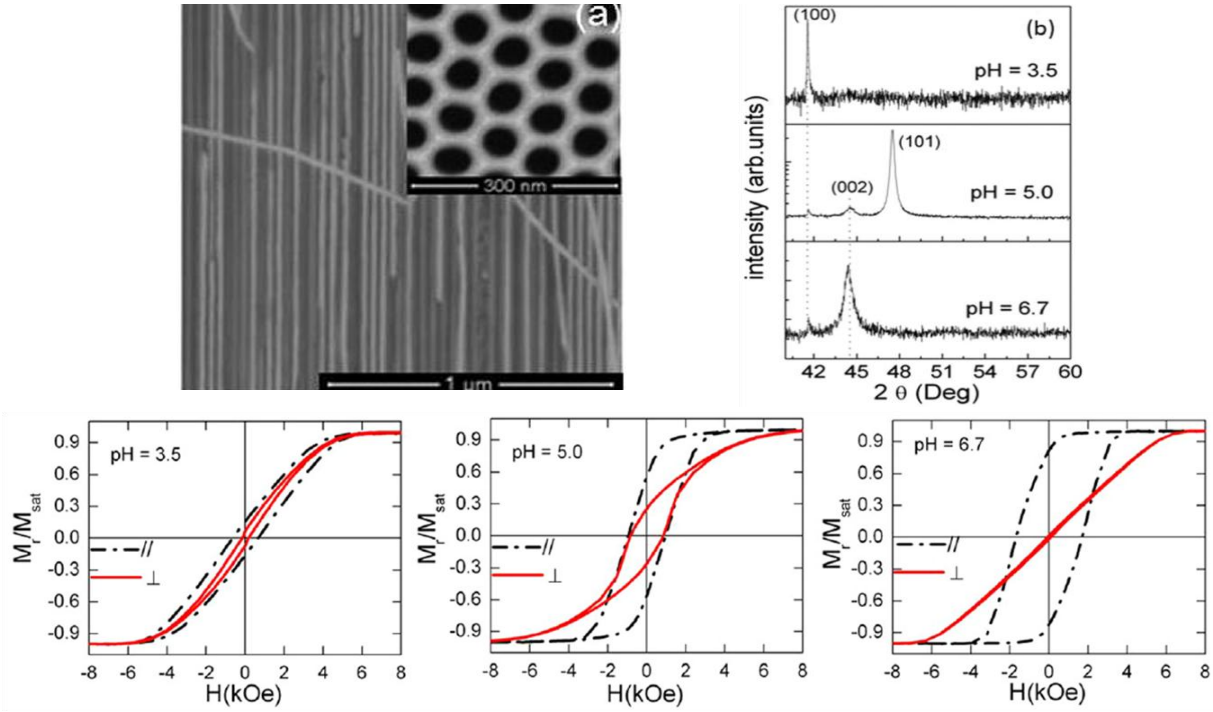

Figure II- 3 a. *Cross-sectional SEM image of anodic aluminum oxide membranes filled with Co nanowires (the inset shows an SEM image of the top of the AAO);* ***b.*** *XRD patterns of the Co nanowires with a hcp structure;* ***c.*** *Normalized hysteresis loops for the applied field parallel (//) and perpendicular (⊥) to the NWs* [8].

Several other groups explored the effect of the Co NWs dimensions and crystal structure on their magnetic properties. For example, Zeng *et al.* [9] synthesized cobalt polycrystalline nanowires of varying dimensions with mean diameter and length ranging between 10 nm ≤ d_m ≤ 20 nm and 100 nm ≤ l_m ≤ 1000 nm. Measurements of cobalt nanowires (d_m = 10 nm, l_m = 400 nm) in an anodic alumina template with the applied field parallel to the wires long axis showed that the coercivity of 2.6 kOe and M_r/M_s= 0.9 is based mainly on the shape anisotropy of the wires, since no preferential orientation of the c-axis was observed. In another case, Henry *et al.* [10] managed to synthesize nanowires with rather good quality of hexagonal compact structure, with the c-axis exhibiting a preferential orientation parallel to the long axis of the wires. For the thinnest obtained wires of d_m = 30 nm, a coercivity of 3 kOe with M_r/M_s= 1 was achieved (figure II-4a, b). The strong effect of the c-axis orientation with respect to the wires' long axis was presented by Liu *et al.* [11]. Even though highly crystalline hcp cobalt nanowires (d_m = 90 nm, l_m = 1 µm) were prepared, the c-axis was perpendicular to their long axis, a fact that led to a decreased H_c of 1.1 kOe. The highest, up to date, reported H_c and M_r/M_s values were reported by Ramazani *et al.* [12], [13] at 4.8 kOe

and 1 respectively, for hcp cobalt nanowires with their c-axis parallel to their long axis and dimensions d_m = 15 nm and l_m= 250 nm (figure II-4c, d) [12], [13].

The table II-1 summarizes the above representative examples including information in the wires' dimensions, crystal structure and magnetic values.

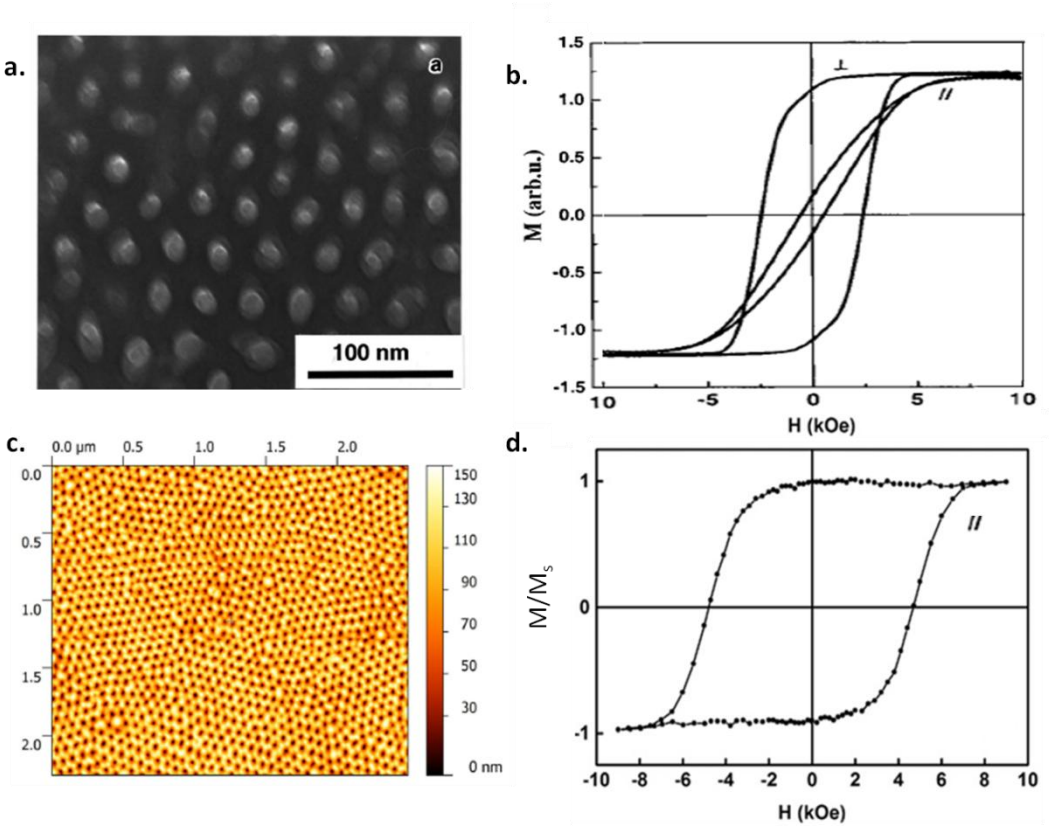

Figure II- 4 a.*TEM of the top view of Co polycrystalline fcc, hcp nanowires in anodic porous alumina, with mean diameter 10 nm and center to center distance of 35 nm and* ***b.*** *their corresponding M(H) loops measured parallel and perpendicular to the wires' long axis;* ***c.*** *AFM photograph of a highly ordered nanoporous template with monocrystalline hcp cobalt nanowires of mean diameter 30 nm and* ***d.*** *their corresponding M(H) loop measured parallel to the wires' long axis.*

D_m (nm)	L_m (nm)	Crystalline phase		c-axis orientation	M_r/M_s		H_c (Oe)		Ref.
					∥	⊥	∥	⊥	
10 ≤ D ≤ 20	10 ≤ L ≤ 10^3	PC	hcp, fcc	Random	0.9	0.12	2600	500	[9]
30 ≤ D ≤ 50	10^3 or 2·10^3	PC	hcp	∥	1	0.05	3000	500	[10]
90	10^3	MC	hcp	⊥	0.7	0.02	1100	15	[11]
35	120	PC	fcc	-	0.20	--	1700	--	[4]
30	10^3	PC	hcp	∥	0.95	0.17	3200	1500	[12]
50	3·10^3	MC	hcp	∥	0.85	≈0	1700	≈0	[8]
15	250	MC	hcp	∥	1	0.09	4800	500	[13]

Table II- 1. *Dimensions, crystal structure and highest magnetic properties of cobalt nanowires prepared via electrodeposition.*

II.1.2 Chemical reduction in liquid phase – General view

The synthesis of metal particles in liquid phase from a metal source is fairly different from the electrodeposition technique previously described. We will first introduce the different chemical species involved and the classical nucleation/growth mechanism invoked in the formation of nanoparticles. Then, the role of the organic surfactants in the anisotropic growth will be further discussed. Among the different approaches one could follow, we will focus on the polyol process and describe several key parameters for the controlled growth of Co nanowires.

a. The different chemical species involved

The chemical reduction usually proceeds through the general equation:

$$Metal\ precursor + surfactants + reducing\ agent \xrightarrow{solvent,T} NPs$$

Metal precursor: These chemical species contain the inorganic elements (Fe, Co, Ni ...) constituting the final NPs. The metal precursors may be either an organometallic complex (i.e. involving metal-carbon or metal-nitrogen bonds), an inorganic complex (including metal-oxygen bonds such as acetylacetonates) or even a metal salt such as halides.
Depending on the precursor chosen, the metal center can have different oxidation states:

- A zero oxidation state like in the metal carbonyls $Co_2(CO)_8$. Thermal energy is then sufficient to break the metal-carbon bond.

- An oxidation state of (+II) or (+III). In these cases the use of a reducing agent (organic molecules, hydrides, H_2 ....) is necessary to form the metal NPs. Thermal energy may also be required.

Solvent: Organic solvents are usually preferred to aqueous solution for the synthesis of magnetic NPs, due to the propensity of ferromagnetic metals to oxidize in water. The solvent ensures a homogeneous mixing of the different chemical species and will act as the medium in which the NPs nucleate and grow.

The polarity of the solvent is generally adapted to the metal precursor used: apolar solvents, such as toluene, mesitylene or ethers are typically used in organometallic syntheses [14], [15], [16], while polar solvents, like polyols, are often preferred with inorganic complexes and metal salts [17], [18].

Stabilizing agent: The sub-coordinated atoms at the NPs surface have very high energy leading to the latter's instability. As a result the NPs tend to aggregate in order to reduce their surface energy. The small size of the nanoparticles can be stabilized by the specific adsorption of molecules at their surface, called stabilizing agent. Surfactants, which combine polar head, which adsorbs at the NPs surface, and a long apolar tail, are often used (Figure II- 5a). In addition to the thermodynamic stabilization of the surface, the presence of long carbon chains around each NP acts as a steric barrier that prevent the particles from coalescing (Figure II- 5b);

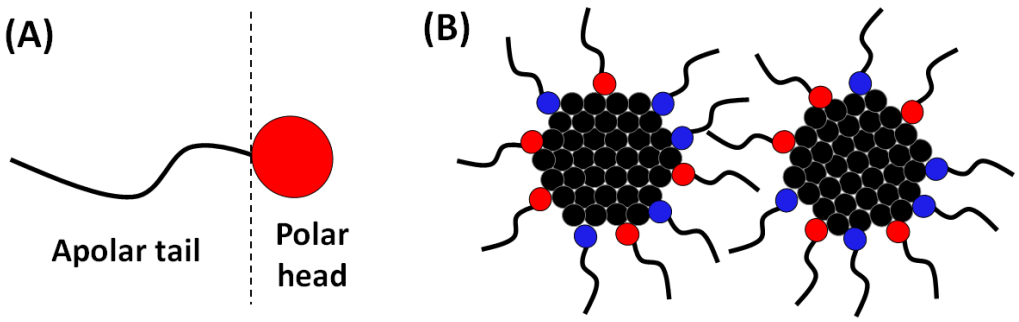

Figure II- 5 *Schematic representations of* ***(A)*** *a surfactant and* ***(B)*** *two NPs stabilized by two types of surfactants at their surface that prevent their agglomeration.*

b. *LaMer's nucleation-growth mechanism*

The synthesis of nanoparticles in liquid phase is a very complex process which has been extensively studied empirically, but for which theoretical predictions are rather limited. One of the most referred mechanism is the LaMer's model, which is based on the thermodynamical stability of small aggregates of atoms [19].

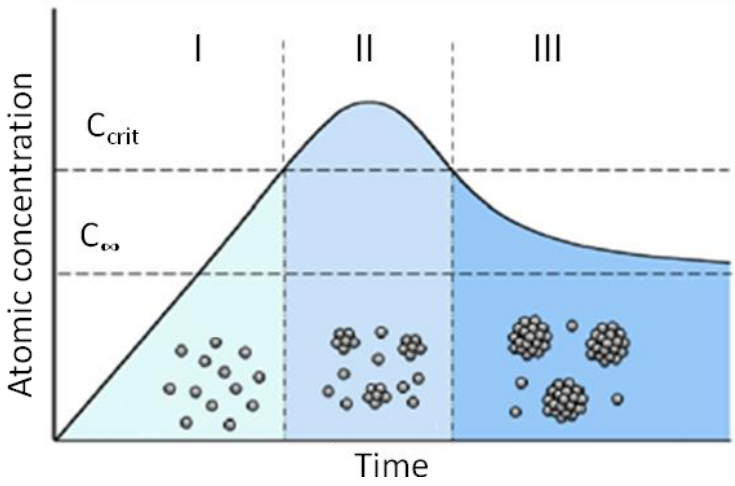

Figure II- 6 *Schematic diagram of LaMer's mechanism*

The Figure II- 6 summarizes the successive steps leading to monodisperse spherical particles according to LaMer's model. In stage I the metal ions, introduced in the medium as metal precursor, are reduced into zerovalent atoms. Their concentration increases with time until it reaches the supersaturation concentration, C_{crit}. Above this concentration the nucleation takes place (stage II), leading to the aggregation of these atoms into small clusters (nuclei). The nuclei will then grow into nanoparticles by further reduction of precursors (step III). In the LaMer's model monodisperse particles are synthesized if the overlap between the nucleation and growth stages is very short (nucleation burst). Generally, the growth step may proceed by single atom addition, coalescence of NPs, or through ripening process, smaller particles being redissolved at the benefit of larger ones. In the framework of the LaMer model the first growth mode is required.

c. *Shape control*

The nucleation and growth model presented above yields nanoparticles with isotropic shapes, such as spheres or cubes. An additional force should be implemented during the reaction to drive an anisotropic growth. Preformed templates, such as the nanoporous membrane used in electrochemical deposition, can be used, leading to a confined growth. Alternatively, the surfactants can impose a growth direction thanks to specific coordination to certain crystallographic facets. These two approaches will be reviewed for Co nanorods liquid phase synthesis.

II.1.3 Template-free synthesis of cobalt nanorods and nanowires

Several approaches can be followed to yield Co NRs using only surfactants as driving force for the anisotropic growth

II.1.3.1 Thermodecomposition route

Puntes *et al.* presented the synthesis of anisotropic magnetic nanoparticles following a thermo-decomposition approach [20]. Briefly, the synthesis consisted in the hot injection of a zerovalent precursor ($Co_2(CO)_8$) in a mixture of tri-octylphosphine oxide (TOPO) oleic acid (OA) and oleylamine (OY), both used as surfactants, in dichlorobenzene (DCB). The fast injection of carbonyl precursor at high temperature (182°C) allows a burst nucleation and yield particles monodispersed in size. With the appropriate surfactant mixture and reaction time (between 1 and 20 min) single crystal hcp cobalt nanodisks were obtained.

The role of the TOPO surfactant in the shape control was stressed and a selective adsorption was invoked. The Figure II- 7 shows TEM images of cobalt nanodisks deposited with or without external magnetic field (1T).

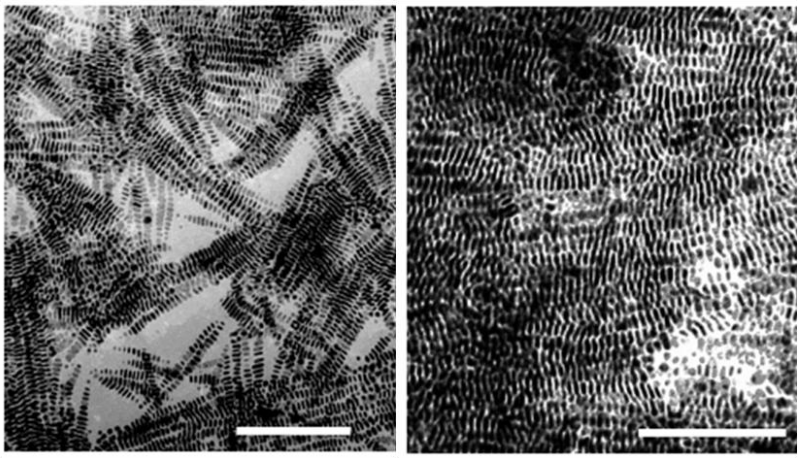

Figure II- 7 *TEM images of cobalt nanodisks self-assembled (left) and deposited under magnetic field (1 T, right). The bar is 100 nm* [20].

II.1.3.2 Organometallic synthesis

Chaudret *et al.* developed the synthesis of cobalt nanowires following an organometallic approach [21]. Cobalt (I) or (II) complexes, $Co(\eta^3\text{-}C_8H_{13})(\eta^4\text{-}C_8H_{12})$ or $Co\{N[Si(CH_3)_3]_2\}_2(THF)$, respectively, were reduced under mild conditions (150°C) in a non polar solvent (anisole or

toluene) using H_2 as reducing agent. In presence of a mixture of lauric acid (C12) and hexadecylamine (C16), hexagonal close-packed (hcp) cobalt nanorods with a mean diameter of 5 nm and a mean length of 85 nm could be obtained (Figure II- 8B). Structural characterization evidenced that the growth direction of these Co rods was along the c axis of the hcp structure.

The influence of the surfactants on the size and shape control was investigated. When the lauric acid was substituted with octanoic acid (C8), an acid with a shorter alkyl chain, the obtained rods were thicker (d= 9 nm) but shorter (l = 33 nm, Figure II- 8A). On the contrary, when stearic acid (C18) was used, the rods obtained were fairly thick (d= 8 nm) and longer (l= 128 nm, Figure II- 8C).

Using Co(II) precursors, similar objects could be obtained, their mean diameter being of 6 nm and their length varying from 45 to 90 nm by modifying the precursor's concentration and the reaction time. The highest measured coercivity (6.5 kOe, with M_r/M_s= 0.84) corresponded to nanorods with d_m= 6 nm and l_m= 90 nm [22]. However, the shorter rods (l_m= 90 nm) demonstrated better alignment with M_r/M_s ratio of 0.91 (Table II-2).

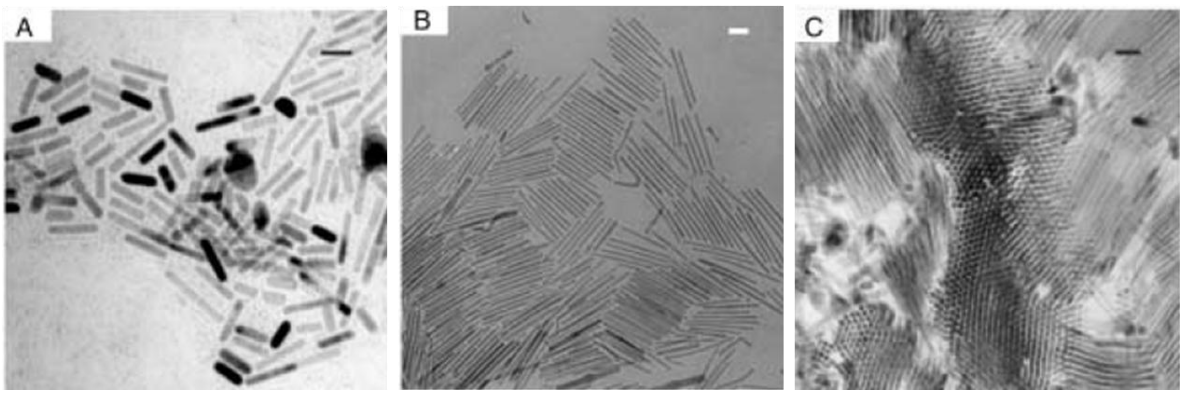

Figure II- 8 *TEM micrographs of nanorods synthesized using hexadecylamine and (A) octanoic acid ; (B) lauric acid and (C) stearic acid. Scale bar: 30 nm [21].*

D_m (nm)	L_m (nm)	Crystalline phase		c-axis orientation	M_r/M_s	H_c (Oe)	Ref.
6	45	MC	hcp	‖	0.91	6200	[22]
6	90	MC	hcp	‖	0.84	6500	

Table II-2 *Dimensions, crystal structure and highest magnetic properties of cobalt nanowires prepared via organometallic synthesis.*

II.1.3.3 Polyol mediated synthesis

The polyol process is a method initially developed by F. Fiévet and coworkers [23] for the synthesis of Ni and Co spherical nanoparticles. It consists in the reduction of inorganic metal salts or complexes in a basic solution of liquid α-diols, like 1,2-ethanediol, 1,2-propanediol and 1,2-butanediol. The advantages of these liquids are multiple: (i) they can easily dissolve the metal salts due to their high polarity, unlike most organic solvents; (ii) they reduce the metal cations; (iii) they possess a high boiling point (190-200° C) and therefore allow reaction at high temperature, and (iv) the polyol synthesis can be adapted for large-scale productions.

Several metals can be prepared by this method ranging from noble metals to magnetic metals such as cobalt, nickel and their alloys [24]. In the case of nickel and cobalt, a general schematic description of the reaction steps involved in the polyol process is presented in the Figure II- 9 [18].

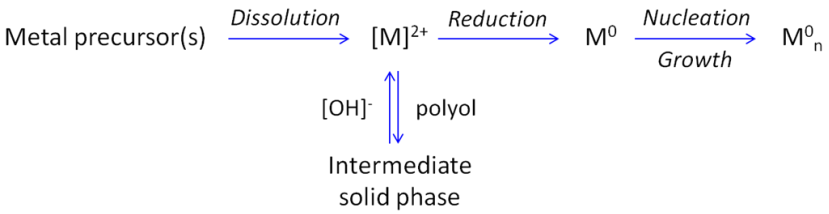

Figure II- 9 *General description of reaction steps involved in the polyol process*

The first step consists in the dissolution of the metal salt thanks to the polyol. As the basic solution is heated, a slightly soluble intermediate phase gradually precipitates. Previous studies stressed on the role of the solid intermediate phase for the formation of monodisperse particles and proposed a reaction mechanism [25]. The solid phase acts as a metal cation reservoir and its dissolution releases gradually metal cations in the solution. These cations can then be reduced to metal atoms. The presence of such a reservoir may help in the separation of the nucleation and growth steps, which is crucial for obtaining particles monodisperse in size.

II.1.3.4 Synthesis of cobalt nanorods via the polyol process

The synthesis of cobalt nanorods via the polyol method was first proposed by Soumare *et al.* [18], [25] and was then studied in detail by Aït Atmane *et al.* [26], [27]. It involves the reduction of a cobalt carboxylate precursor, $Co(C_nH_{2n+1}COO)_2$, at 175°C in a NaOH solution of 1,2-butanediol with the use of $RuCl_3 \cdot xH_2O$ as nucleating agent.

The role of the long carboxylate chain, $C_nH_{2n+1}COO_2$, in the nanorods' synthesis was reported by Soumare *et al.*. They demonstrated that the alkyl chain length influences the particles' morphology and dimensions. Sea-urchin like particles were obtained with cobalt(II) acetate as precursor (C2, Figure II- 10a), while nanorods were observed in presence of cobalt caprate(II) (C9, Figure II- 10 b) and cobalt(II) laurate (C12, Figure II- 10 c). The mean diameter of the nanorods slightly increased with the chain length of the carboxylate precursor evolving from d=13 nm with C9 to d = 15 nm with C12.

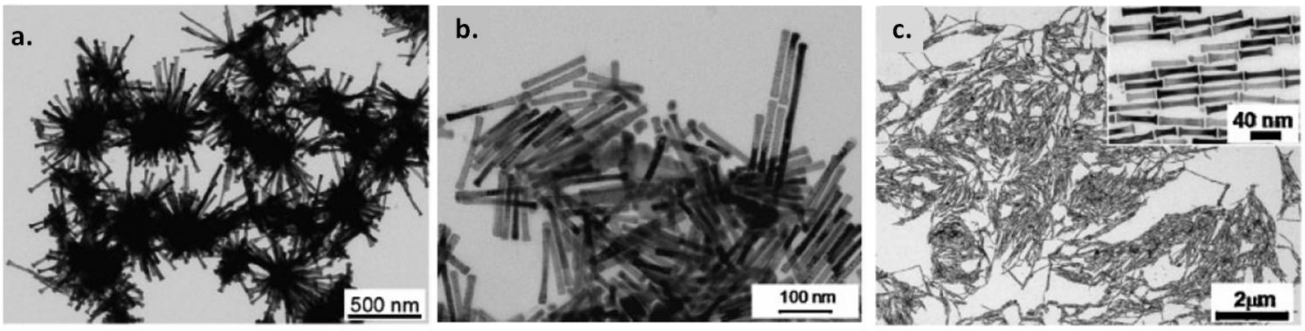

Figure II- 10 *TEM images of Co particles obtained by reducing the following cobalt carboxylates:* ***a)*** *sea-urchin like particles from cobalt acetate;* ***b)*** *nanorods with L_m= 133 nm and D_m= 13 nm from cobalt caprate(C9) and* ***c)*** *nanorods with L_m= 99 nm and D_m= 15 nm from cobalt laurate (C12)* [18].

However the long chain carboxylate was not the only parameter optimized by Soumare and Aït Atmane to control accurately the growth of cobalt rods. We will review the influence of the different experimental parameters for the controlled growth of Co NRs.

a. Effect of the nucleating agent

A factor that has a strong effect in the final particle morphology is the use of a heterogeneous nucleating agent. While in homogeneous nucleation the nuclei are formed uniformly throughout the parent phase, in heterogeneous nucleation a foreign metal precursor first nucleates and then the desired metal atoms assemble upon it (Figure II- 11). The use of a nucleating agent ensures the successful separation of the nucleation and growth step, resulting in monodisperse nanoparticles.

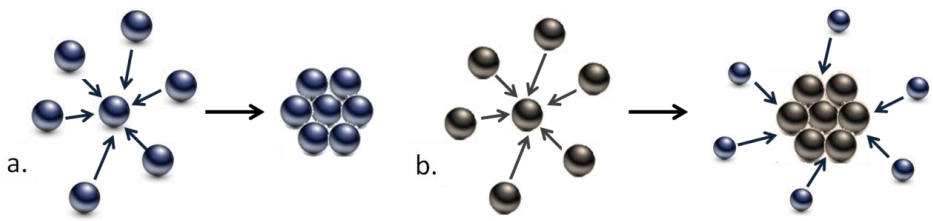

Figure II- 11 a. *Homogeneous and* ***b.*** *Heterogeneous nucleation*

The effect of the nucleating agent on the final shape of the cobalt particles was first reported by Chakroune *et al.* [23] and then by Ung *et al.* [28] for cobalt and cobalt-nickel particles, respectively. But in these two papers isolated rods were not described. The combination of cobalt(II) laurate precursor and an heterogeneous nucleation with ruthenium chloride permitted the formation of isolated cobalt rods.

The importance of the heterogeneous nucleation was illustrated by Bozon-Venduraz *et al.* (figure II-12). When cobalt laurate was reduced in a basic solution of 1,2-butanediol, homogeneous nucleation led to the growth of isotropic polycrystalline sub-micrometric particles (Figure II- 12 a). However, when $RuCl_3 \cdot xH_2O$ was added as a nucleating agent, single crystal nanowires were obtained (Figure II- 12 b).

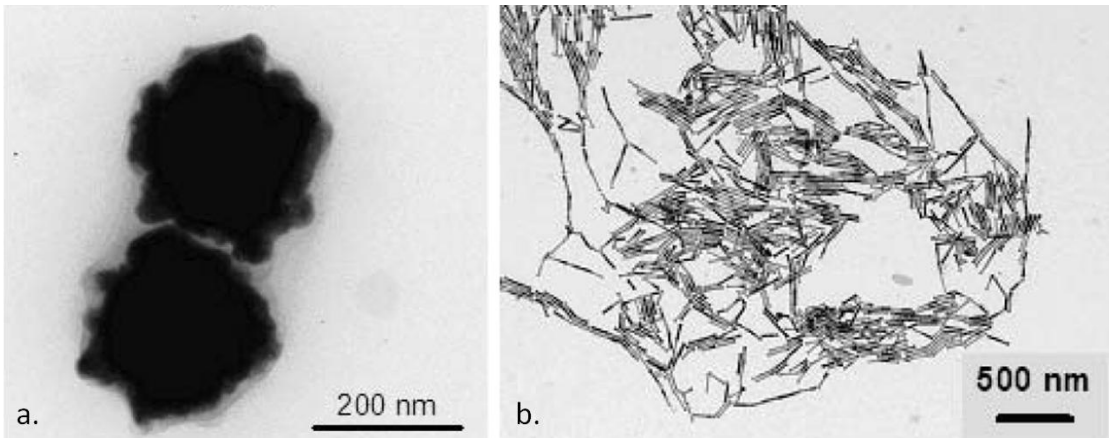

Figure II- 12 a. *Co isotropic particles obtained with homogeneous nucleation;* ***b.*** *Co nanowires obtained through heterogeneous nucleation of* Ru^{III} [29].

b. Effect of the polyol

Aït Atmane *et al.* demonstrated that among different polyols, 1,2-butanediol was the only one into which hcp cobalt nanorods could be obtained (Figure II- 13). Ethyleneglycol and diethyleneglycol results in isotropic cobalt nanoparticles, while 1,2-propanediol yields a diversity of morphologies including platelets, cubic and anisotropic nanoparticles. This effect was attributed to the lower dielectric constant of the 1,2-butanediol (22 $pF \cdot m^{-1}$) compared to ethyleneglycol, 1,2-propanediol and diethyleneglycol with 38, 32 and 32 $pF \cdot m^{-1}$, respectively. Taking into account that the laurate ions remain at the metal surface and in some extent control the cobalt growth, it is not surprising that the best particle shape was obtained in the less polar polyol.

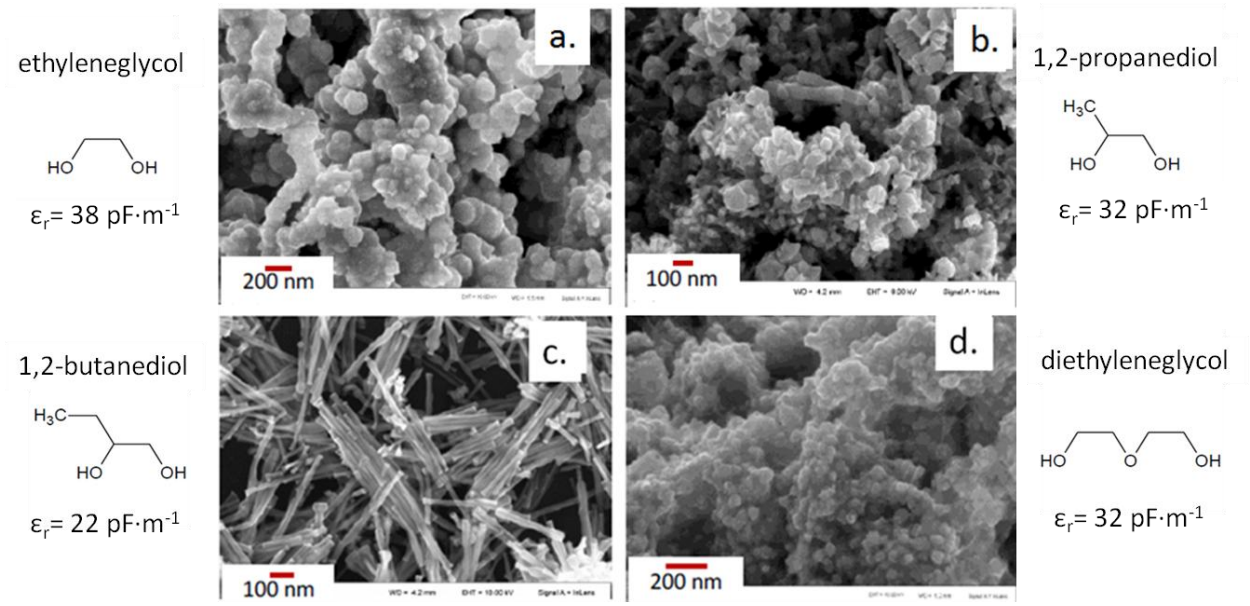

Figure II- 13 *SEM image of cobalt particle synthesized by reduction of cobalt laurate in basic solution of* ***(a)*** *ethyleneglycol;* ***(b)*** *1,2-propanediol;* ***(c)*** *1,2-butanediol and* ***(d)*** *diethyleneglycol* [26].

c. Effect of the medium basicity

According to the general scheme recalled in Figure II- 9, the basicity favors the formation of the solid intermediate phase [18]. Soumare *et al.* showed that the basicity also affects the nature of the intermediate phase formed: high NaOH concentration (0.2 M) leads to a cobalt alkoxide, while for NaOH ≤ 0.10 M a cobalt hydroxyl laurate was formed. Depending on the intermediate phase nature, the final particle shape was modified. TEM examples of the [NaOH] effect are shown in the Figure II- 14. In the range of 0.02 ≤ [NaOH] ≤ 0.10 M cobalt nanorods are obtained. For higher NaOH concentrations, e.g. 0.2 M, only cubic particles are observed.

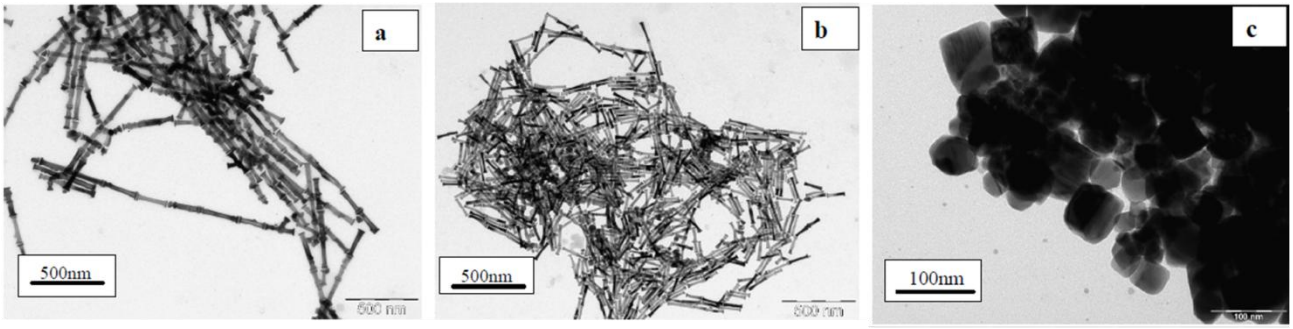

Figure II- 14 *Evolution of morphology in function of the basicity:* ***a.*** *[NaOH]= 0.02 M (L= 220 nm, D= 28 nm);* ***b.*** *[NaOH]= 0.1 M (L= 126 nm, D= 15 nm) and* ***c.*** *[NaOH]= 0.2 M* [18].

d. Growth study

Structural studies by X-ray diffraction and high resolution microscopy showed that the obtained cobalt nanorods crystallize with the hcp structure and that their long axis is parallel to the c-axis of their hcp structure.

In order to have a deeper understanding of the growth mechanism, Aït Atmane followed by electron microscopy the shape of the solid particles formed after different reaction times during the reduction of cobalt laurate in a basic solution of 1,2-butanediol (Eq. II-1) [30].

$$\underset{80\ mM}{Co(C_{11}H_{23}COO)_2} + \underset{75\ mM}{NaOH} + \underset{2\ mM}{RuCl_3 \cdot xH_2O} + \underset{300\ mL}{\text{1,2-butanediol}} \xrightarrow[20\ min]{13°C \cdot min^{-1},\ 175°C} \text{Co NRs} \quad \text{(Eq. II-1)}$$

The Figure II- 15 presents TEM images of solids recovered after different reaction times at 175°C. The black particles are the metal particles and the grey zones correspond to the intermediate solid phase. After 2 min very small metal particles were detected embedded in the intermediate solid phase. Rods were already observed after 4 min (Figure II- 15 b). With time, the intermediate solid phase vanished and the cobalt nanorods' diameter grew from 15 nm (at 5 min of reaction) to 20 nm (at 10 min of reaction), while the mean length for the same time range increased from 180 nm to 275 nm. The process was completed approximately after 15 min at 175°C, leading to cobalt nanorods with small conical tips at their extremities.

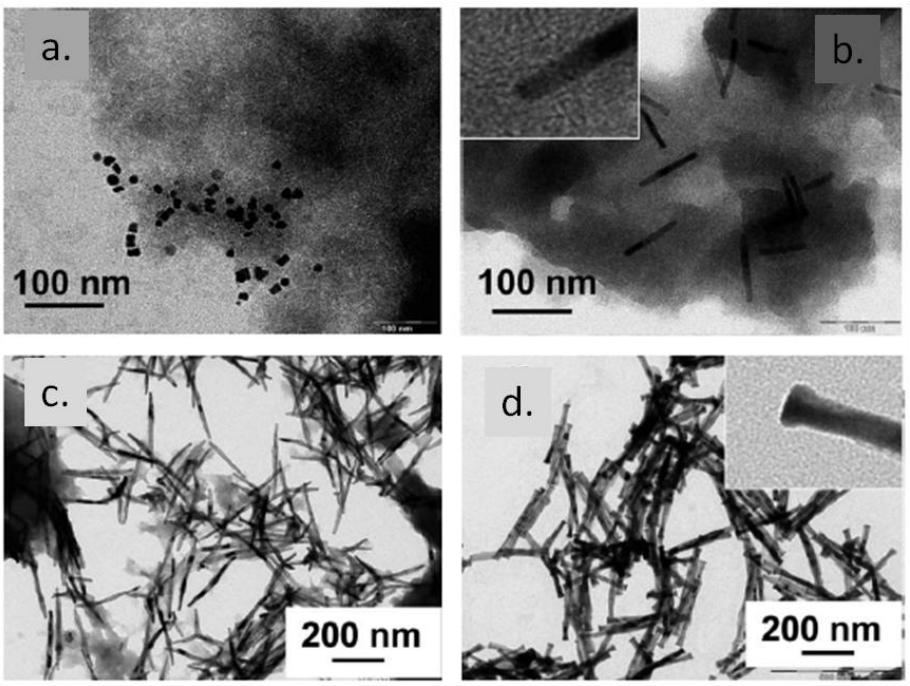

Figure II- 15 *TEM images of solids recovered after different reaction times at 175°C:* ***(a)*** *2 min;* ***(b)*** *4 min;* ***(c)*** *6 min;* ***(d)*** *10 min. Inset: detail of the extremity of a single nanorod* [30].

e. Thermodynamic aspects

For growth under thermodynamic control, the final crystal shape allows to maintain a minimum total interfacial free energy. The shape thus depends on the energy of the crystal's facets, with the most stable ones being favored.

For a liquid phase process, the stability of the different facets is related to the adsorption of the different ions or surfactants present in the medium. According to their nature and their concentration, a metal particle can adopt different shapes.

In order to have an assessment of the adsorption effects at the surface of cobalt particles on the final particle shape, K. Aït Atmane and coworkers undertook a theoretical study using Density Functional Theory calculations (DFT) [30]. In the case of cobalt particles with hexagonal structure, two surfaces were considered: the basal (0001) facets and the lateral $(10\bar{1}0)$ and $(01\bar{1}0)$ facets.

In vacuum and in the absence of any other agent, the lowest surface energy corresponds to the (0001) facet. This means that the close packed (0001) surface is the most stable one and thus the most exposed, favoring the formation of hexagonal-shaped disks. However, in the case of polyol process, where various surfactants are introduced in the medium, their controlled adsorption on the lateral facets can lead to a decrease of the interfacial energy and to the formation of nanorods. On the other hand, if the adsorption of the surfactants is on the basal facets, nanoplatelets or nanodisks will be obtained (Figure II- 16).

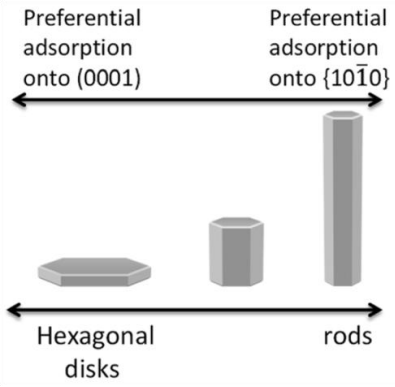

Figure II- 16 *Expected particle shapes as a result of the preferential adsorption of the ligand on the (0001) and {10$\bar{1}$0} surfaces of cobalt hexagonal crystals.*

Two different ligands were considered by Aït Atmane *et al.* [30]: the polyol itself, because it is known that the diol can form metal alkoxydes, and the carboxylate ions.

They showed that the diol has a negligible influence on the crystal shape, due to the fact that its interaction with the cobalt's surface is very weak. Therefore, they assumed that it is the carboxylate chain which can stabilize the lateral surfaces at the expense of the basal ones. In order to quantify this selective adsorption, its adsorption energy, E_{ads}, on the $\{10\bar{1}0\}$ and (0001) plane was calculated.

Considering the simplest form of carboxylate, the acetate (CH_3COO), they showed that the E_{ads} is much higher on the lateral surface $\{10\bar{1}0\}$ than on the close packed (0001). In other words, the acetate is more strongly absorbed on the lateral surface tending to over-stabilize it. On the other hand, this over-stabilization may be compensated due to the fact that there are more adsorption sites per surface unit on the (0001) facets. To calculate this subtle balance, the surface adsorption energies were compared at a given chemical potential of the carboxylate ligand. The Figure II- 17 demonstrates the stability of the (0001) and $\{10\bar{1}0\}$ surfaces as a function of the chemical potential of the acetate: when the chemical potential is between -3.04 and -2.19 eV, the $\{10\bar{1}0\}$ surface is stabilized by the adsorption of the acetate and should lead to the formation of nanorods. For values below -3.04 eV and above -2.19 eV, the (0001) surface is more stable and the formation of nanoplatelets or nanodisks is favored.

Thus, the ligand's chemical potential has to be carefully controlled for a driven formation of anisotropic particles. At a first approximation, the chemical potential of ligands in solution is proportional to their concentration. These theoretical calculations predicted that an increase of laurate concentration could favor a growth perpendicular to the c-axis giving platelets.

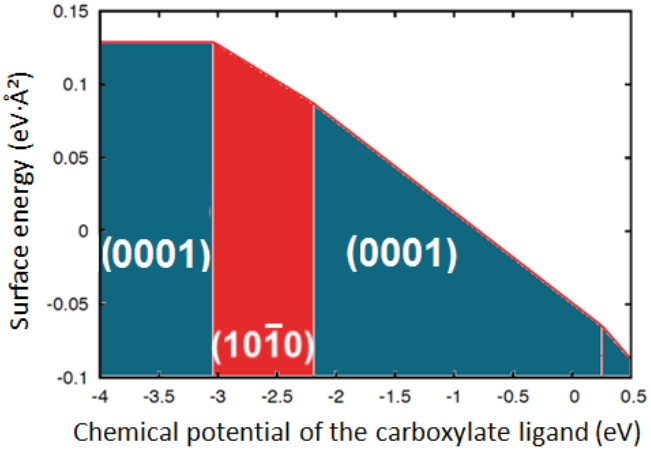

Figure II- 17 *Stability diagram for the cobalt (0001) and (10$\bar{1}$0) surfaces with the CH_3COO ligand* [30].

Two experimental observations seem to confirm the theoretical calculation predictions.

- Without the addition of any laurate, aside from the laurate contained in the Co precursor, cobalt nanorods with small tips in their extremities were obtained. Thus for [laurate] = 0.16 M the $\{10\bar{1}0\}$ are stabilized and nanorods are formed. The release of laurate ions through the dissolution of the solid intermediate phase may explain the enlarged tips, indeed the increasing concentration of laurate ions at the end of the reaction may favor the growth of the (0001) facets.

- The effect of the increased carboxylate concentration was studied experimentally thanks to a progressive increase of the laurate concentration in the medium by addition of sodium laurate.

The transition from the (0001) to the $\{10\bar{1}0\}$ stability zone is visualized in the Figure II- 18, where the rods are replaced by nanorods of shorter length and finally platelets. More precisely, for 0.5 equivalents of $Na(C_{11}H_{23}CO_2)$ added relative to the cobalt precursor, $Co(C_{11}H_{23}CO_2)_2$, ie. for [laurate] = 0.20 M, nanorods with decreased aspect ratio were observed (Figure II- 18 b). The addition of 2 equivalents of $Na(C_{11}H_{23}CO_2)$, i.e. for [laurate] = 0.32 M, led to a significant chemical potential increase, with result the stabilization of the (0001) basal plane and the formation of cobalt platelets (Figure II- 18 c).

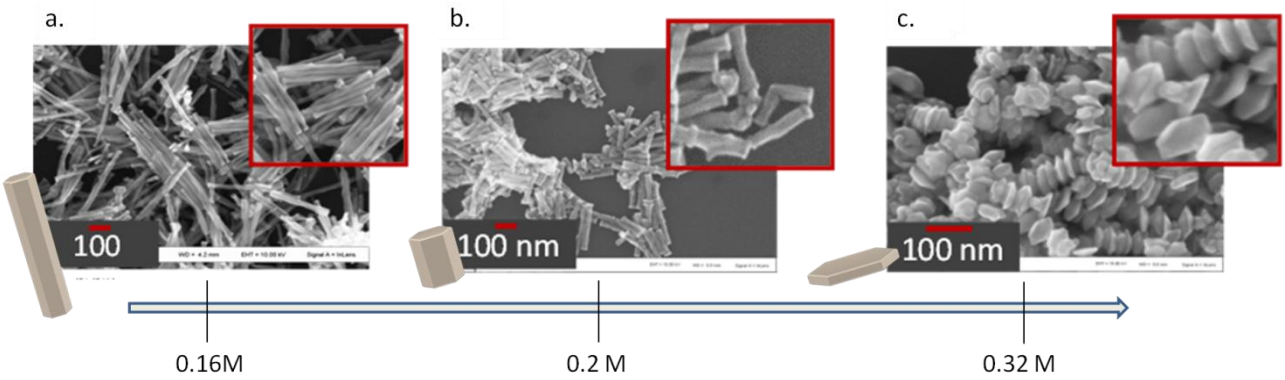

Figure II- 18 *SEM images of cobalt nanoparticles obtained with the system $Co(C_{11}H_{23}CO_2)_2$/NaOH/1,2-butanediol/$RuCl_3 \cdot xH_2O$/$Na(C_{11}H_{23}CO_2)$ for different $Na(C_{11}H_{23}COO)$ equivalents relative to Co(II):* ***(a)*** *0 equiv.;* ***(b)*** *0.5 equiv.; and* ***(c)*** *2 equiv. The concentration indicated on the arrow is the total $C_{11}H_{23}CO_2$ molar concentration. Conditions: [NaOH]= 0.075 M; $Co(C_{11}H_{23}CO_2)_2$= 0.08 M; [Ru]/[Ru + Co]= 2.5%* [30].

f. Kinetic aspects

A kinetically controlled growth is determined by the ratio of the relative growth rates of the different crystal facets. A way to distinguish experimentally kinetically controlled growth from thermodynamically controlled growth is to make syntheses modifying a parameter that can affect the growth rate.

In the case of the polyol process modifying the heating rate could be a way to change the dissolution/reduction of the cobalt monomers and release of the carboxylate ligand from the intermediate solid phase and thus, to modify the overall metal growth rate.

Soumare *et al.* [18] demonstrated the effect of the heating rate on the final particle shape. When the mixture was heated from room temperature up to 175°C a strong effect both on their morphology and structure was observed as a function of the heating rate (Figure II-18):

a) for a heating rate of 7°C·min^{-1} the nanorods exhibited a mean diameter and length of 17 nm and 330 nm, respectively. Tips were observed at their extremities;
b) for 3.5°C·min^{-1} the nanorods exhibited a rough surface, their mean diameter increased up to 35 nm, while their mean length decreased to 140 nm;
c) for 2°C·min^{-1} only hexagonal platelets were produced with a mean diameter of 130 nm.

Moreover, while the rods synthesized with heating rates between 3.5 and 7°C·min^{-1} crystallized with the hcp structure, it is noticeable that the platelets prepared with the lower heating rate, 2°C·min^{-1}, crystallized in a mixture of fcc and hcp phases.

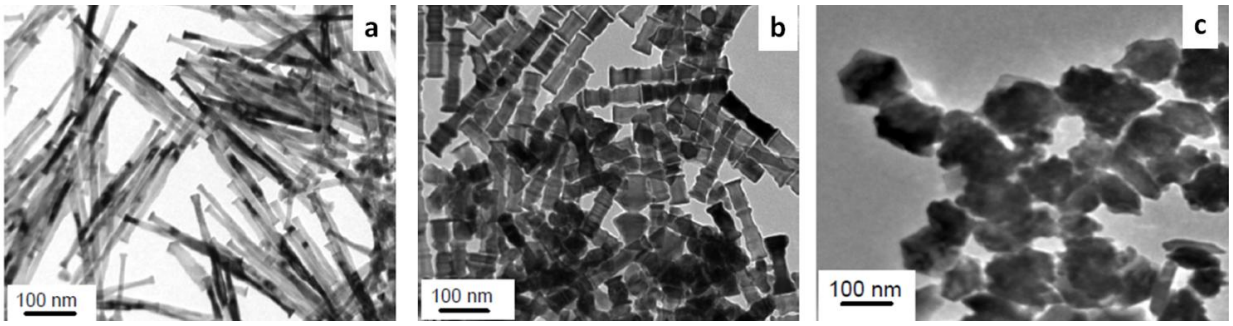

Figure II- 19 *Influence of heating rate in the morphology using Co dodecanoate and [NaOH]= 0.075 M in 1,2-butanediol:* ***a.*** *7°C·min^{-1} (D_m= 17 nm, L_m=330 nm);* ***b.*** *3.5°C·min^{-1} (D_m= 35 nm, L_m=140 nm);* ***c.*** *2°C·min^{-1} (D_m= 130 nm). Reaction conditions: [NaOH]=0.075 M; $Co(C_{11}H_{23}COO)_2$= 0.08 M and [Ru]/[Ru + Co]= 2.5%* [18].

This set of experiments showed that the growth rate is an important parameter for the final shape control. The formation of the cobalt rods in the polyol process is under kinetic control. Nevertheless, the thermodynamic calculations of the adsorption energies presented in the previous section are helpful to understand the growth.

The theoretical calculations and the experiments on the heating rate effect suggested that the $\{10\bar{1}0\}$ facets require less laurate to be stabilized that's why they can grow faster than the (0001) basal planes. In the classical conditions of reduction of cobalt laurate a fast

reaction favors the rods, while a slow reaction let time for the laurate anions to assemble at the surface of the (0001) basal planes favoring the platelet formation.

g. Magnetic properties

The magnetic properties of Co and $Co_{80}Ni_{20}$ nanorods prepared by the polyol process were examined on aligned assemblies by Soumare *et al*. (Table II- 3) [25], [31].

A polymer-bonded sample was produced from $Co_{80}Ni_{20}$ nanowires (d_m=6.8 nm and l_m= 240 nm) through they dispersion in a solution of PMMA and toluene and its solidification under a magnetic field. Room temperature measurements of the M(H) loops along the easy and hard axis of the alignment direction are illustrated in the Figure II- 20. For the measuring field applied along the easy axis, the H_c and M_r/M_s ratio were 4.8 kOe (381 $kA \cdot m^{-1}$) and 0.85, respectively [31], [25].

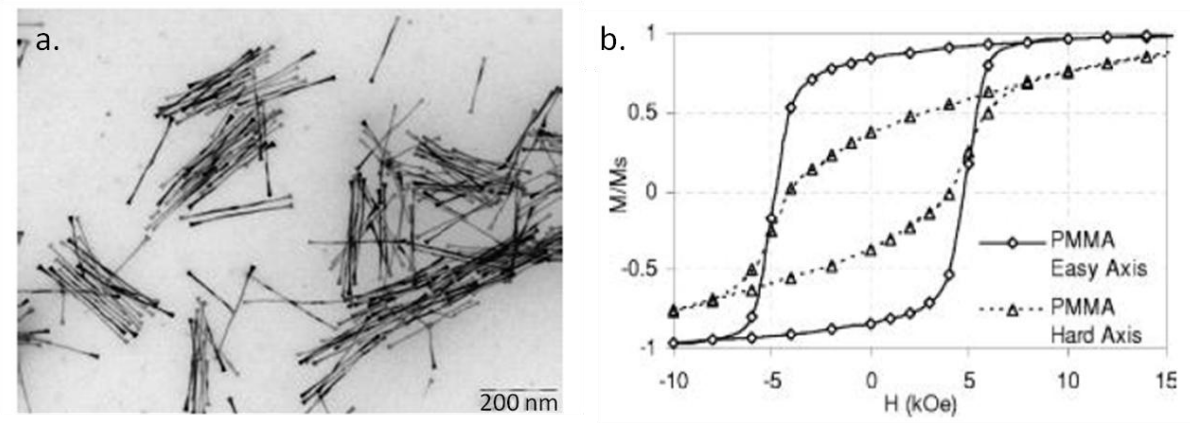

Figure II- 20 *Room temperature hysteresis loops of polymer-bonded $Co_{80}Ni_{20}$ nanowires (l_m = 250 nm, d_m = 7.5 nm) aligned in PMMA and toluene under 1 T* [31], [25].

The ability of Co nanorods (d_m=20 nm, l_m= 200 nm) to align under magnetic was also examined through their dispersion in a solution of toluene deposited on a Si substrate [32]. The magnetization curve at room temperature is shown in the Figure II- 21. A coercivity of 5.5 kOe (437 $kA \cdot m^{-1}$) and a remanence to saturation ratio M_r/M_s = 0.81 were obtained.

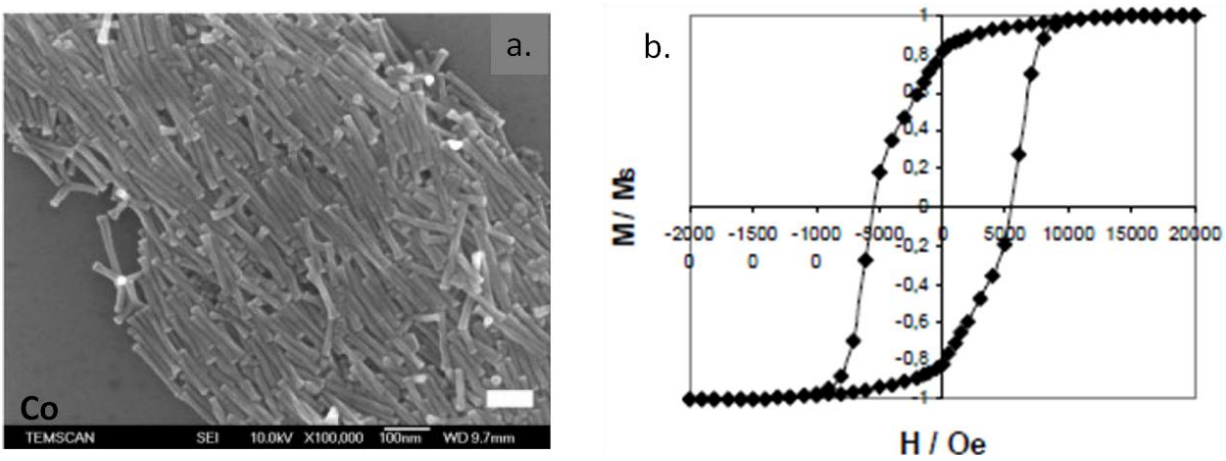

Figure II- 21 a. *SEM image of Co nanowires (l_m = 130 nm, d_m = 13 nm) deposited on Si substrate and aligned under 1 T (scale bar 100 nm) and* ***b.*** *their M(H) loop with the measuring field parallel to the rods' long axes at 300 K* [32].

Despite the high aspect ratio of the $Co_{80}Ni_{20}$ wires their coercivity is lower than the Co rod assemblies. The lower magnetization of the cobalt–nickel alloys is a result of the tips formed at their endings and could be responsible for this phenomenon. Indeed, the magnetic anisotropy related to the particle shape increases with the saturation magnetization (in the case of long ellipsoids, one would expect an ideal coercive field of $M_s/2$).

	D_m (nm)	L_m (nm)	Crystalline phase		M_r/M_s		H_c (Oe)		Ref.
					∥	⊥	∥	⊥	
Co	20	200	MC	hcp	0.87	--	5600	--	[18]
	13	130	MC	hcp	0.81	--	5500	--	[31]
$Co_{80}Ni_{20}$	7.5	250	--	hcp+fcc	0.85		4800		[32]

Table II-3 *Publications on cobalt nanorods presenting the highest magnetic properties to date.*

II.1.4 Conclusions on the different cobalt nanorods and nanowires synthetic routes

Among all synthetic methods, the polyol process was the most appealing for our project. The method was already developed for the production of monodisperse Co nanorods with a mean diameter in the range 10-20 nm. This method is quite easy to carry out since all the reactants are handled in air, it does not require high pressure nor dihydrogen gas. It seemed promising for an up-scale at least at laboratory scale.

The influence of various experimental parameters on the growth mechanism was already studied. A combination of the theoretical and experimental analysis shed light on the

growth mechanism demonstrating the importance of the thermodynamic and kinetic control. From the thermodynamic point of view, the ligands presenting the strongest coordination with the crystal's surfaces are those who define its final shape. The rod formation is attributed to the preferential adsorption of the laurate ions upon the $\{10\bar{1}0\}$ surface and the subsequent addition of the cobalt species on the basal plane. The theoretical calculations predicted an optimum concentration of the gradually dissolved laurate for the rod growth. The kinetics of the dissolution/reduction of the cobalt monomers, as well as ligands, defines the growth mechanism. As far as the nucleation step is concerned, the important role of seeding the medium with Ru^{III} ions for a heterogeneous nucleation was evidenced. A detailed description of the crystallization process of the nuclei is still limited, mostly due to the small size of the seeds consisting of a few tens of atoms.

II.2. Synthesis of cobalt nanorods by the polyol process

II.2.1 Objectives

In this experimental work two objectives were defined:

- the possibility to synthesize in one batch several grams of well-defined cobalt nanorods;
- the possibility of a better shape control of the cobalt nanorods in order to improve the magnetic properties.

Even though the reported polyol process -in low scale- provided nanorods with already good magnetic properties, it is interesting to modify their morphology and dimensions according to those suggested by the micromagnetic simulations. Aspect ratio around 10 and diameter in the range 5-15 nm are desired. The shape of the rod tips is also very important. As a reminder, ellipsoids give the highest coercivity values, with the rounded cylinders and cylinders with flat edges following (Fig. I-15). On the other hand, cylinders with large tips result to a significant decrease of the coercivity.

In the following paragraphs we will focus our study on the nucleation and growth process (Figure II- 22). The influence of several experimental parameters on the growth of cobalt nanorods in liquid polyol has already been reported. On the contrary the nucleation step has been less studied. Based on the fact that the nanorods' size depends on the number of the produced Ru^0 seeds, we will study the effect of the nucleating agent's nature and concentration. Moreover, since the diameter and aspect ratio are defined during the growth process, the dissolution rate of the cobalt ions and carboxylates will be adjusted by the medium's heating rate. An important parameter that has to be taken into account is the homogeneous mass and heat transfer in the system. Thus, the mixing problem including the appropriate selection of impeller and stirring speed has to be considered. Finally, all these parameters should be able to be reproducible in a large scale reactor, respecting the conditions of the low scale synthesis.

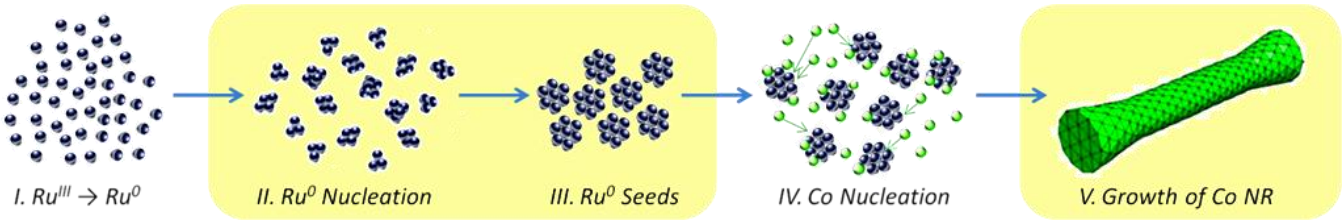

Figure II- 22 *Proposed schematic representation of the nanorods' formation via the polyol mechanism. The highlighted steps are into the scope of examination.*

II.2.2 Experimental details

The experimental protocol followed for the synthesis of cobalt nanorods was the same with the one reported by Soumare *et al.* [18] and involves three steps summarized in

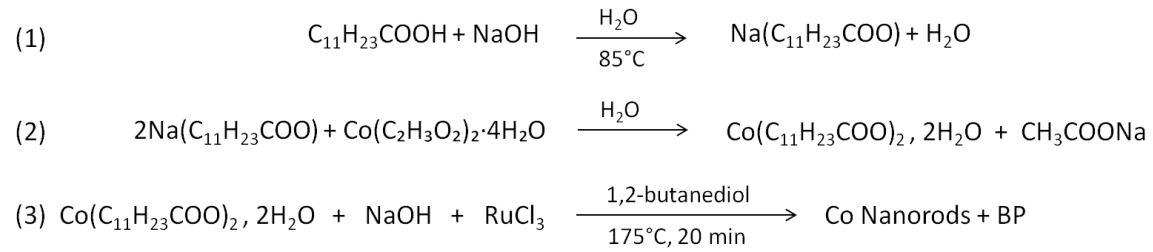

Figure II- 23: (1) the synthesis of sodium laurate, $Na(C_{11}H_{23}CO_2)$, (2) the preparation of the cobalt laurate precursor, $Co(C_{11}H_{23}CO_2)_2$ and (3) the production of cobalt nanorods through the polyol route.

(1) $C_{11}H_{23}COOH + NaOH \xrightarrow[85°C]{H_2O} Na(C_{11}H_{23}COO) + H_2O$
(2) $2Na(C_{11}H_{23}COO) + Co(C_2H_3O_2)_2 \cdot 4H_2O \xrightarrow{H_2O} Co(C_{11}H_{23}COO)_2, 2H_2O + CH_3COONa$
(3) $Co(C_{11}H_{23}COO)_2, 2H_2O + NaOH + RuCl_3 \xrightarrow[175°C, 20 min]{1,2\text{-butanediol}}$ Co Nanorods + BP

Figure II- 23 Experimental protocol for the cobalt nanorods synthesis: (1) Synthesis of sodium laurate, (2) synthesis of Co laurate and (3) synthesis of nanorods. BP are the reaction's byproducts.

In the following we describe, first, the precursor synthesis, then the general protocol for the cobalt rods synthesis and finally the different set-ups for the low and large scale experiments.

II.2.2.1 Precursor synthesis and characterization

Sodium laurate was prepared by mixing equimolar aqueous solutions of lauric acid, $C_{11}H_{23}COOH$, and sodium hydroxide at 85°C until the reactants were dissolved. The mixture was left to cool down at room temperature, resulting in a white solid, which was filtered and then dried in the microwave for 40 min in order to remove the water excess.

For the synthesis of the cobalt laurate precursor, the sodium laurate and 0.5 equivalent, relative to sodium laurate, of cobalt acetate tetra hydrate, $Co(C_2H_3O_2)_2 \cdot 4H_2O$, were dissolved separately in de-ionized water. Afterwards, they were mixed at 12000 rpm with a homogenizer (IKA-T25, Digital Ultra TURRAX) at room temperature for 15 min. A pink fine powder was obtained after removing the water through a normal vacuum filtration setup.

The remaining water was removed by drying the powder in the oven at 50°C. Depending on the drying time, two cobalt laurates could be isolated by this method: a di-hydrated one, $Co(C_{11}H_{23}CO_2)_2$**,** $2H_2O$, already described by Rabu *et al.* [33] and an anhydrous one, $Co(C_{11}H_{23}CO_2)_2$, obtained for longer drying times. The cobalt precursors were characterized by thermogravimetric analysis (TGA) in air from room temperature up to 600°C (Figure II-24).

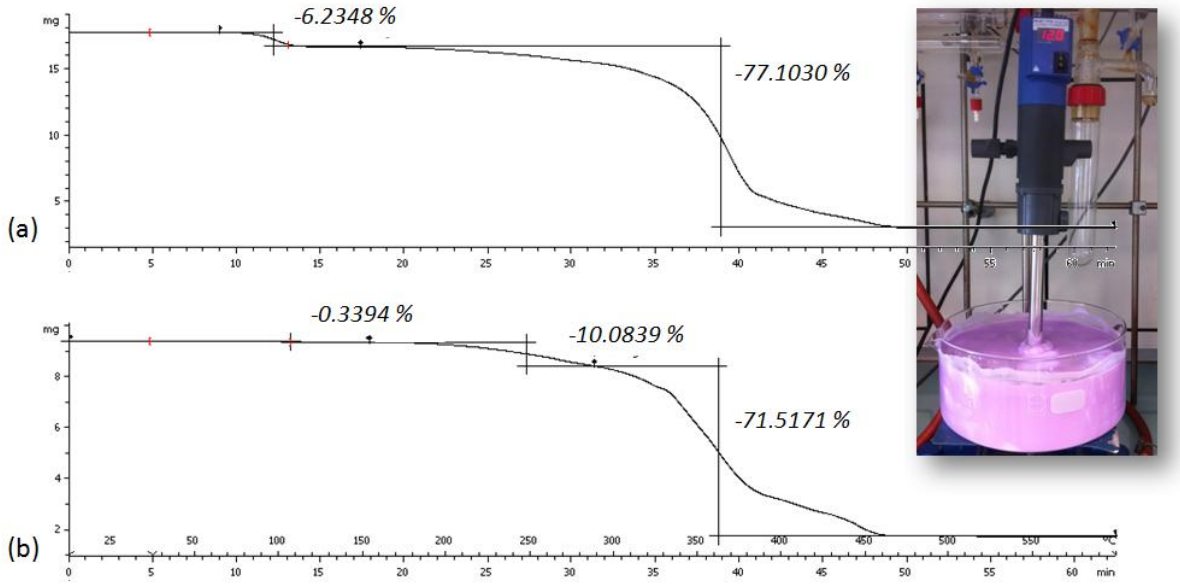

Figure II- 24 *Thermogravimetric analysis of* ***(a)*** *dihydrated and* ***(b)*** *anhydrous cobalt laurate.* ***Inset:*** *Set-up of the cobalt laurate precursor synthesis*

Two mass losses were observed in the TGA of the di-hydrated cobalt laurate (Figure II- 24a):

- a first one of about 6% around 100°C, which corresponds to the loss of water;
- a second mass loss of 76-77 % in the temperature range 200-450°C, which corresponds to the decomposition of the cobalt laurate to Co_3O_4 according to the chemical reaction:

$$Co(C_{11}H_{23}CO_2)_2,\ 2\ H_2O + 205/6\ O_2 \rightarrow CoO_{4/3} + 24\ CO_2 + 25\ H_2O$$

These mass losses are in a good agreement with a di-hydrated cobalt laurate, $Co(C_{11}H_{23}CO_2)_2$**,** $2H_2O$ with molecular mass 493 $g{\cdot}mol^{-1}$.

For such a formula, the first theoretical mass loss corresponding to the two water molecules is:

$$\frac{\Delta m_1}{m} = \frac{36}{493} = 7.3\%$$

While the total mass loss corresponding to the total transformation of the cobalt laurate di-hydrate into $CoO_{4/3}$ is:

$$\frac{\Delta m_{total}}{m} = \frac{493 - 80.2}{493} = 83.7\%$$

very close to the total mass loss measured experimentally, which is comprised between 82% and 83%.

The TGA analysis of the $Co(C_{11}H_{23}CO_2)_2$ compound showed a single weight loss between 79.5 and 82.4% in the temperature range 200-450°C. Taking into account a molecular mass of 457 $g \cdot mol^{-1}$, a theoretical weight loss of 82.2% is expected (Figure II- 24b).

Furthermore, the chemical analysis of the anhydrous cobalt laurate gave a mass content in carbon and hydrogen of 61.2 and 10.6%, respectively. These values are very close to the calculated values of 63 and 10% for the expected formula $Co(C_{11}H_{23}CO_2)_2$.

II.2.2.2 General protocol for cobalt rod synthesis

For the cobalt nanorods synthesis, the anhydrous cobalt precursor and the nucleating agent, $RuCl_3$, were dispersed in a basic solution of 1,2-butanediol with the following concentrations:

- $8 \cdot 10^{-2}$ M of $Co(C_{11}H_{23}CO_2)_2$
- 5.5×10^{-2} M ≤ [NaOH] ≤ 7.5×10^{-2} M
- molar ratio $[RuCl_3]/[Co(C_{11}H_{23}COO)_2]$, referred to from now on as [Ru]/[Co]= 2.5%,.

The mixture was heated from room temperature to 175°C and allowed to react 20 min under mechanical stirring. The mixture turned black at 175°C indicating the cobalt reduction. The cobalt particles were recovered by magnetic separation and were washed twice with absolute ethanol and once with chloroform before characterizations.

All small scale syntheses were carried out in 60 ml of polyol resulting in the formation of 0.27 g of cobalt nanorods, while the large scale production (from a laboratory perspective) was planned to be carried out in 1L of 1,2-butanediol (resulting cobalt nanorods' mass 4.56 g) (see details in Table II-4).

$Co(C_{11}H_{23}COO)_2, 2H_2O$ +	NaOH +	$RuCl_3$	1,2-butanediol, 175°C, 20 min →	Co NRs + BP
Low-scale	*2.36 g*	*0.18 g*	*0.03 g*	*60 mL*	*0.27 g*
Large-scale	*39.4 g*	*3 g*	*0.49 g*	*1000 mL*	*4.56 g*

Table II-4. Details of masses and volumes of reactants and products for a typical low and large scale production of cobalt nanorods by the polyol process.

II.2.2.3 Set-up for low and large scale synthesis

Three different heating set-ups were used for the realization of the cobalt nanorods: a. the microwave, b. the heating mantle and c. the jacketed reactor (Figure II- 25).

Figure II- 25 *Heating set-ups:* ***a.*** *microwave;* ***b.*** *heating mantle;* ***c.*** *jacketed reactor.*

a) The microwave allows heating small and large volume of 1,2-butanediol. Low scale syntheses were performed inside a 250 mL flask. High heating rates (up to 150°C·min^{-1}) can be reached for this volume (60 mL of 1,2-butanediol). This advantage will be used in order to control the final dimensions of the nanorods. However, its strong drawback is the heterogeneous heating, especially if we increase the volume of the flask.
b) The heating mantle offers better temperature homogeneity inside the flask compared to the microwave. Its drawback is the narrow range of heating rates. Thus, the growth control experiments are limited to 10 °C·min^{-1}. Low scale and large scale experiments are made inside 250 mL and 5L spherical flask, respectively.

c) The jacketed reactor's heating system consists in a double glass cylindrical flask with oil circulation. Its equipment prevents any heat losses and allows very homogeneous temperatures inside the reactor, another advantage is the good control of the stirring but the heating rates are rather limited (< 8°C·min^{-1}). The scalability and reproducibility experiments of the polyol process are performed in 1L of 1,2-butanediol in the 3L cylindrical flask.

In these three systems a mechanical stirring of the suspension was preferred to the classical magnetic stirring. The cobalt nanorods are indeed strongly attracted by the magnetic stirrers and it is then difficult to separate them at the end of the reaction.

For the mechanical stirring, two different Teflon impellers were used: an anchor and a propeller, attached to a mechanical stirrer with a speed range from 50 to 2000 rpm (Figure II- 26). The efficiency of these two parameters (stirring speed and impeller's shape) in the mass homogeneity of the mixture will be studied.

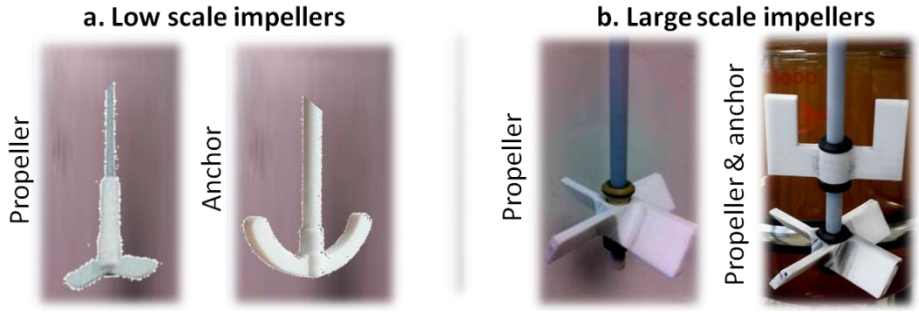

Figure II- 26 *Teflon impellers used for* ***a.*** *low and* ***b.*** *large scale synthesis.*

II.2.2.4 Cobalt nanorods characterization techniques

Transmission Electron Microscopy (TEM)

The cobalt nanorods were characterized by transmission electron microscopy (TEM) using a Jeol JEM 1011 operating at 100 kV. The samples were prepared by drop casting of the solution on a carbon coated copper grid. After the evaporation of the solvent a number of particles remain on the surface of the grid. Prior to observation, the grids were dried under vacuum (10^{-5} Torr).

The rods' mean diameter (D_m) and mean length (L_m) were measured from the image analysis on c.a. 200 rods with the ImageJ software.

X-Ray powder Diffraction (XRD)

The XRD measurements were carried out in a Panalytical Empyrean instrument operating with a Co cathode source. The samples were prepared from dried powder of cobalt nanoparticles. The analysis of the obtained diffractograms was done using Highscore software and the average crystallite size was calculated using the Scherrer equation:

$$L_{(hkil)} = 0.94 \times \frac{\lambda}{B(2\theta)\times\cos\theta} \qquad \text{(Eq. II-1)}$$

where λ is the wavelength of the X-Rays source ($\lambda_{Co\ K\alpha}$= 1.789 Å), B(2θ) is the full width at half maximum of the diffracted beam corrected from the instrumental broadening and 2θ is the diffraction angle of the (hkil) plane.

A. From small scale to large scale synthesis – Results

In this section we describe the scale-up of the polyol process. In all these experiments we have chosen as nucleating agent the hydrated ruthenium chloride $RuCl_3 \cdot xH_2O$ (Sigma Aldrich reference 84050). We anticipated that the main problems for the synthesis of cobalt nanorods at large scale could be:

- the homogeneity of the temperature inside the reactor;
- the control of the stirring conditions.

In this section we will describe, first, the effect of the stirring conditions on the cobalt rods morphology at small scale and then we will compare the cobalt nanorods prepared at large scale using either the heating mantle and a spherical 5L flask or the jacketed reactor.

II.2.3 Effect of the stirring conditions in small scale synthesis

In this study we have performed several syntheses at small scale varying the stirring conditions: the impeller shape and the stirring speed.

The impeller's type, depending on its shape, can provide different flows and consequently, affects the mass homogeneity in the medium. As recently observed by Nassima *et al.* for the polyol synthesis of $Co_{80}Ni_{20}$ nanorods, the selection of the proper stirrer is essential to provide an efficient distribution of the mass in its plane of rotation [34]. By coupling experimental observations with 3D turbulent computational fluid dynamics simulations, they showed that an anchor stirrer provides a higher flow and thus a better mass distribution than a Rushton turbine (Figure II- 27).

The stirring speed can change the growth kinetics. A high stirring speed favors the diffusion of the precursors from the solution towards the particle's surface. The kinetically limiting step of the particle growth in that case is generally the surface reaction. On the contrary, with a low stirring speed the kinetically limiting step of the particle growth is the diffusion of the precursors from the solution towards the particle surface. This second case is generally considered as more favorable for the growth of monodisperse particles.

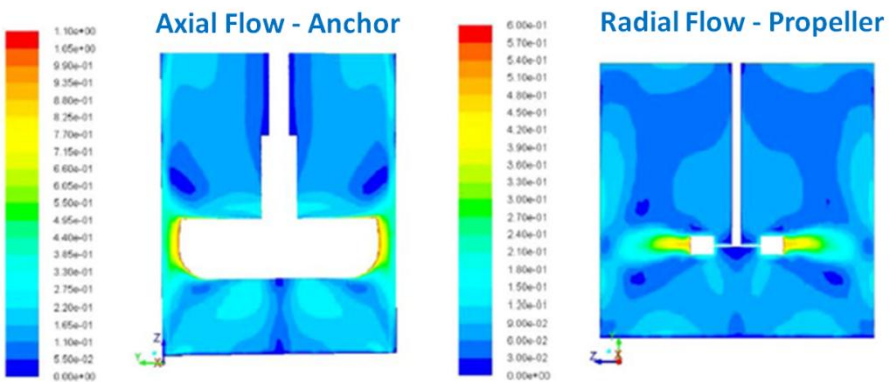

Figure II- 27 *Velocity magnitude in $m \cdot s^{-1}$ depicting the flow features in a vertical (up) and horizontal (down) planes with the use of an anchor (left) and a Rushton turbine (right)* [34].

II.2.3.1 Impeller's shape effect

Two experiments were realized at low scale in the heating mantle set up under typical experimental conditions ($RuCl_3 \cdot xH_2O$ ref. 84050, [Ru]/[Co]=2.5%, [NaOH] = 7.5×10^{-2} M, heating rate 8°C·min^{-1}). The stirring was carried out with (a) a propeller and (b) an anchor. With the propeller, a black mirror covering the interior wall of the flask was observed. On the contrary, no mirror was formed with the use of the anchor shape stirrer. Aliquots from both reactions and a sample from the solid phase mirror were obtained for TEM analysis (Figure II- 28).

The result of the propeller use was cobalt nanorods of d_m= 18±3 nm and l_m= 280±90 nm, in combination with multipods (Figure II- 28a). The precipitated sample formed in the wall of the flask, consists of polydisperse and agglomerated nanorods, multipods and particles with poorly defined shape (Figure II- 28b). On the other hand, the anchor shape stirrer provided monodisperse nanorods with d_m= 16±3 nm and l_m= 225±55 nm, without any multipods or stars observed (Figure II- 28c).

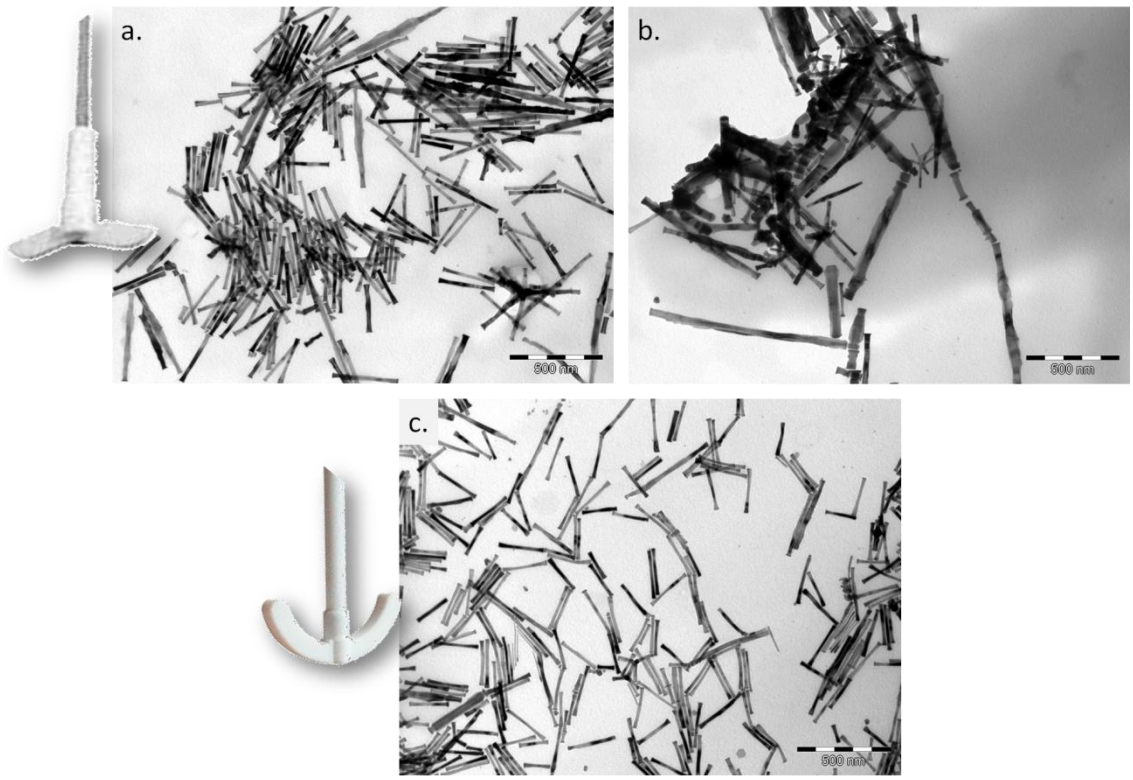

Figure II- 28 *TEM images of cobalt nanorods prepared under the same experimental conditions, but with different stirrers.* ***a.*** *Nanorods resulting from the use of a propeller and* ***b.*** *agglomerated nanorods, multipods and particles with poorly defined shape obtained from the wall of the flask when a propeller was used;* ***c.*** *nanorods recovered after the use of an anchor.*

The mirror on the wall of the flask is a serious drawback for the shape homogeneity of the samples and must be avoided. From our observations we conclude that this mirror appeared when the solid intermediate cobalt phase first deposited on the wall of the flask. An increasing stirring speed permitted to avoid its deposition and the mirror. But as we will see below an increasing stirring speed caused other problems. In conclusion the anchor shape stirrer was preferred in the following experiments.

II.2.3.2 Stirring speed effect

In addition we studied the effect of the stirring speed for the anchor shape stirrer. Four typical low scale reactions using $RuCl_3 \cdot xH_2O$ (ref. 84050) with [NaOH] = 7.5×10^{-2} M and heating rate of $8°C \cdot min^{-1}$ were realized in the heating mantle, under different stirring speeds:

a. 240 rpm, b. 160 rpm and c. 80 rpm

In the Figure II- 29 the TEM images of the recovered nanorods are displayed and their dimensions are summarized in the Table II-5.

As seen the strongest effect of high stirring speed (240 rpm) is the formation of conical tips at the extremities of the nanorods Figure II- 29 a. With the decrease of the stirring rate (160 rpm), the tips are gradually disappearing (Figure II- 29 b). For low mixing speed (80 rpm) the rods appears smoother, their diameter decreases and their aspect ratio increases up to 12 (Figure II- 29 c).

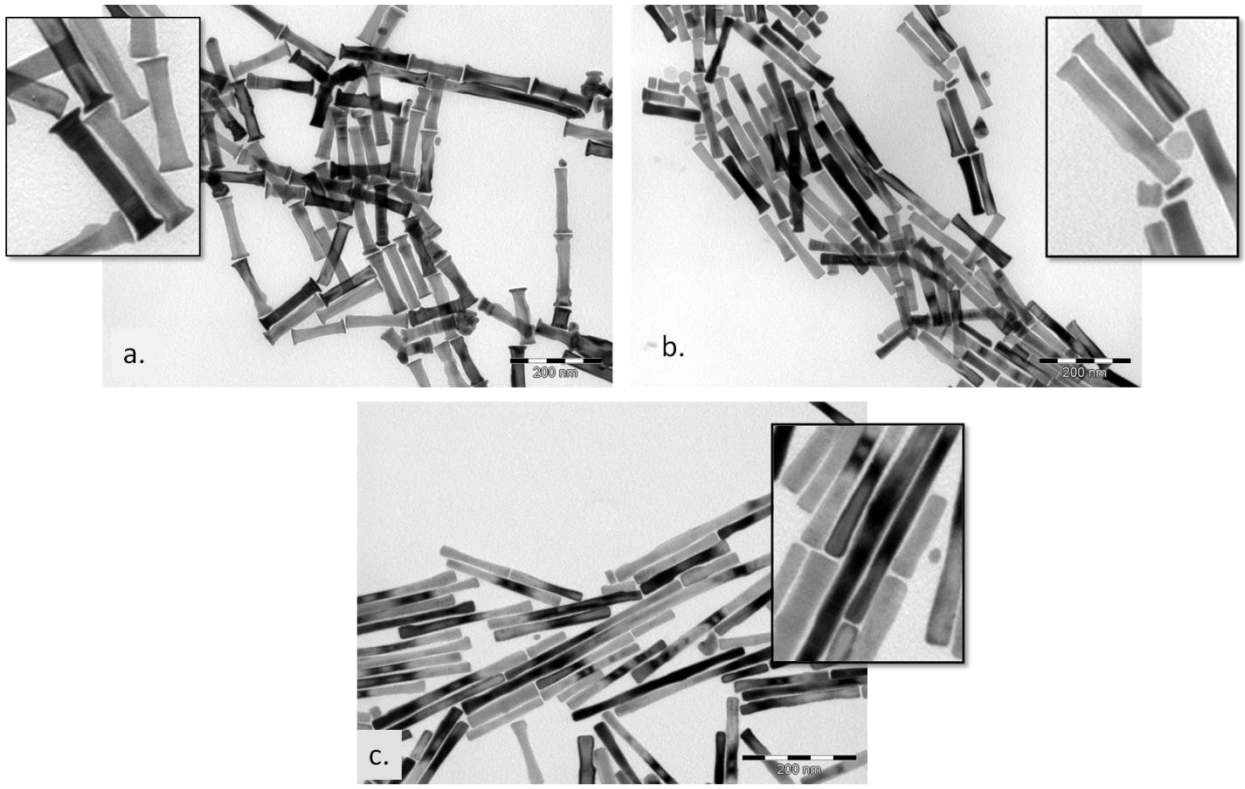

Figure II- 29 *TEM images of cobalt nanorods prepared with different stirring speed:* ***(a)*** *240 rpm;* ***(b)*** *160 rpm;* ***(c)*** *80 rpm. Experimental conditions: 60mL of 1,2-butanediol; $RuCl_3 \cdot xH_2O$ (ref. 84050) [Ru]/[Co] = 2.5%; [NaOH] = 7.5x10^{-2} M; heating rate 8°C·min^{-1}; anchor stirrer.*

	Stirring speed (rpm)	D_m (nm)	L_m (nm)	AR_m
a.	240	24±3	140±38	5.8
b.	160	21±2	110±35	5.2
c.	80	16±2	190±80	12

Table II-5 *Stirring speed effect on the nanorods dimensions.*

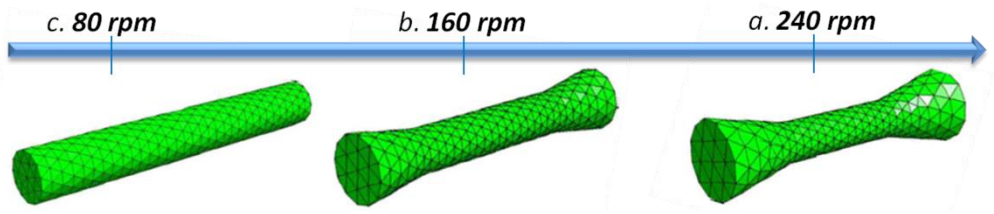

Figure II- 30 *Evolution of conical tips at the rods endings with the stirring speed.*

As far as the magnetic properties are concerned, the simulations presented in chapter I showed that the smooth cylinders with flat endings were more interesting for a high coercivity than the conical tips ending. At small scale the rods obtained with the anchor shape stirrer and with the lower stirring speed were thus the most promising. The challenge was to duplicate these results at larger scale.

II.2.4 Large scale synthesis

For the large scale experiments, we have chosen the heating mantle and the jacketed reactor (Figure II- 25b,c), due to their higher capacity compared to the microwave oven equipment and their better temperature homogeneity.

In all the experiments 1L of 1,2-butanediol was used leading to the production of nearly 5g of Co NRs for each batch. The rest experimental conditions were the same as in the low scale with the use of $RuCl_3 \cdot xH_2O$ (ref. 84050), [Ru]/[Co] = 2.5%, [NaOH] = 7.5×10^{-2} M and heating rate of $8°C \cdot min^{-1}$.

Stirrer shape

We have previously identified the key importance of the stirring on the final shape of the objects. The question is even more predominant due to the large volumes encountered. An anchor impeller combined with a 4-blade propeller was used for the jacketed reactor set-up providing an efficient mass and heat transfer in the horizontal and vertical plane of their rotation level. However, such efficient flowing system could not be found for the heating mantle equipment. Indeed, due to the small concavity of the spherical flask used, it was impossible to insert an anchor whose diameter would be big enough for a sufficient mixing. Thus, only a 4-blade propeller could be used in the heating mantle set-up.

In the case of the heating mantle, a mirror was formed around the flask's wall, due to the inefficient stirring provided by the propeller. In the opposite case, no mirror was observed in the jacketed reactor system. Here again we observed that the homogeneity and regularity

of the stirring produced by the anchor shape stirrer was very important to avoid the nucleation and growth of cobalt particles on the wall of the flask.

Stirring speeds

Three stirring speeds were applied in both set-ups: 160, 90 and 80 rpm. The TEM images of the different cobalt particles are presented in the Figure II- 31 and their dimensions are summarized in the Table II-6.

- We verify once more that high stirring speeds (160 rpm) result in rods with rough surface (Figure II- 31a and d).
- When the mixing rate is decreased at 90 rpm, smooth rods with tips at their extremities are obtained (Figure II- 31 b and e).
- The tips are finally vanishing at 80 rpm (Figure II- 31 c and f), replaced by flat endings.
- Another effect of the decreased stirring, as already observed in the low scale reactions, is that the mean diameter drops (Figure II- 30 a, b and c).

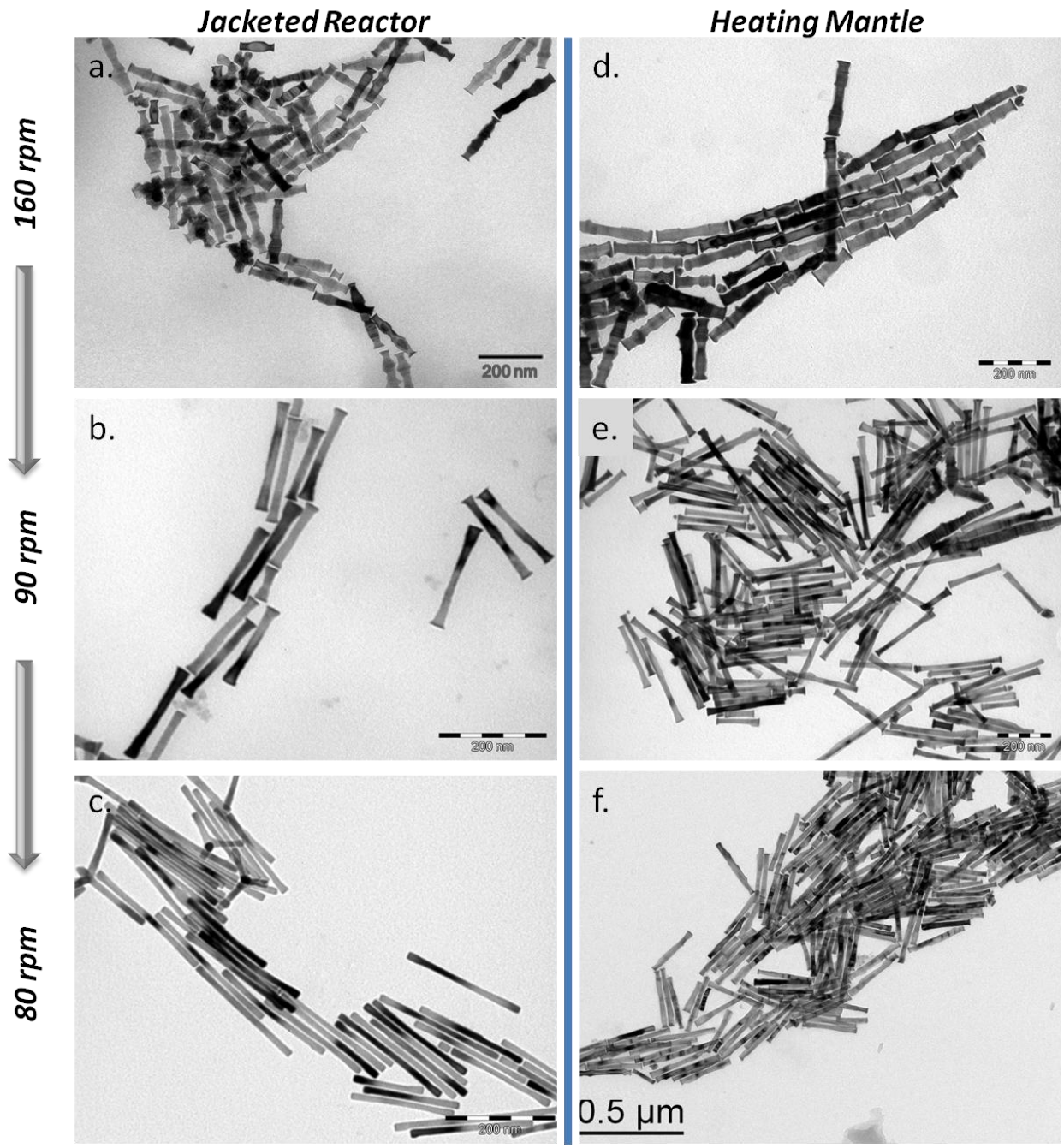

Figure II- 31 *TEM images of cobalt nanorods prepared in 1L of 1,2 butanediol using the jacketed reactor* ***(a-c)*** *or the heating mantle* ***(d-f)*** *with a stirring speed of (a,d) 160 rpm ;(b,e) 90 rpm ; (c,f) 80 rpm.*

		Stirring speed (rpm)	D_m (nm)	L_m (nm)	AR_m
Jack. React.	a.	160	29±5	200±40	6.8
	b.	90	18±2	165±37	9.1
	c.	80	10±1	200±46	18
Heat. Mant.	d.	160	30±7	200±35	6.6
	e.	90	20±2	260±60	13
	f.	80	21±3	260±40	12

Table II-6 *Effect of stirring speed on nanorods dimensions and morphology.*

II.2.5 Conclusions on the large scale synthesis

In conclusion, we have shown in this study that the scale-up of the polyol process at laboratory scale is possible. By controlling the stirring conditions we obtained smooth rods with very regular diameter and a flat tip. The mean diameter around 10 nm is a good compromise for the magnetic properties. Actually the samples prepared in the jacketed reactor with the stirring speed of 80 rpm exhibit a morphology which is even better that most of the rods prepared at low scale before this study.

B. Study on the nucleation step effect - Results

In this section we compare first the results obtained with different seeding procedure and different ruthenium chlorides as nucleating agent and then we focus on different results obtained with the anhydrous ruthenium chloride. The aim was to modify the rods' morphology by varying the nucleation step. All the syntheses were done at low scale.

II.2.6 Effect of the seeding procedure

We studied first the influence of the temperature at which the nucleating agent is injected. We chose as nucleating agent the $RuCl_3 \cdot xH_2O$ (Sigma Aldrich reference 84050). Two experiments were performed using the heating mantle set up.

Both experiments were realized under typical conditions with [NaOH] = 7.5×10^{-2} M and heating rate at $8°C \cdot min^{-1}$. In the first reaction, the $RuCl_3 \cdot xH_2O$ was introduced in the flask at room temperature (25°C) with the rest of the reactants, while in the second case $RuCl_3 \cdot xH_2O$ was previously dissolved in a few mL of 1,2-butanediol at RT and then quickly injected at 175°C following a hot-injection process.

In both experiments, a reaction time of 20 min at 175°C was set. The TEM images of the resulting rods are presented in the Figure II- 32. In the case of $RuCl_3 \cdot xH_2O$ addition at RT, cobalt nanorods of L_m =160±29 nm and D_m = 22±1.6 nm were observed with relatively flat endings. On the contrary, the hot-injected $RuCl_3 \cdot xH_2O$ resulted in dumbbell shaped particles of smaller length (L_m = 94±18 nm) and similar diameter (D_m = 22±3 nm). The mean tip size (Tip_m) was measured in both rods' endings at 39±4 nm.

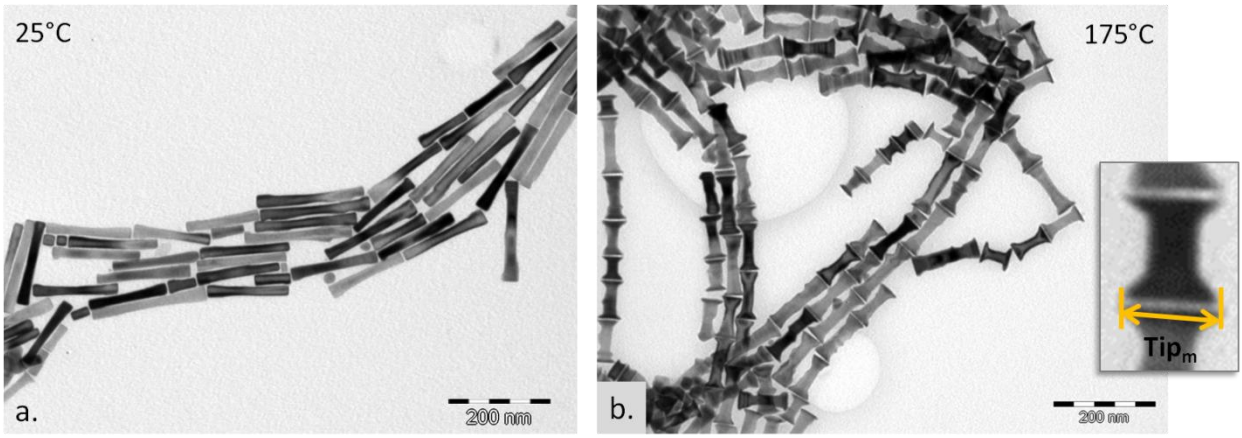

Figure II- 32 *Effect of $RuCl_3 \cdot xH_2O$ seeding procedure:* ***a.*** *typical synthesis with $RuCl_3 \cdot xH_2O$ added at RT resulting in rods of D_m = 22±2 nm and L_m = 160±30 nm;* ***b.*** *hot injection of $RuCl_3 \cdot xH_2O$ at 175°C resulting in dumbbell like particles with D_m = 22±3 nm, L_m = 94±20 nm and tip size Tip_m=39±4 nm.*

Despite a small difference in the mean length, the rods prepared following both procedures exhibit a similar volume. The nucleation process has no strong effect on the number of Ru nuclei that act as seeds for the cobalt growth.

The strong effect of the ruthenium's hot injection appears in the formation of dumbbell-like nanoparticles with tips that can be very large with respect to the central diameter. Surprisingly, the ruthenium injection procedure modifies the growth step. We can imagine that the formation of Ru nuclei occurs at higher temperature with the hot injection procedure. It could lead to a cobalt growth in a medium that contains a higher concentration of free laurate ions, which favors the growth of the (0001) facets.

Whatever the exact mechanism is, the study of which is beyond the scope of our work, we have discarded in the following experiments the hot injection procedure since, as we saw in Chapter I, the large tips contribute to a strong decrease of coercivity.

II.2.7 Effect of the nucleating agent's nature

The possibility to control the nanorods' morphology by varying just the nature of the nucleating agent has been examined. A modification of the nucleation step through a slight change of the nucleating agent's nature could modify the final particle shape and/or size through the production of smaller or bigger cobalt single crystals.

Three different ruthenium chlorides were studied as nucleating agent, two of which were hydrated, $RuCl_3 \cdot xH_2O$, with reference Sigma Aldrich 463779 and 84050, and one anhydrous, $RuCl_3$, with reference Sigma Aldrich 208523.

II.2.7.1 Characterization of the different ruthenium chlorides

In order to have a better understanding in their chemical difference, thermogravimetric analyses of the three ruthenium chlorides were performed in air from room temperature up to 900°C (Figure II- 33).

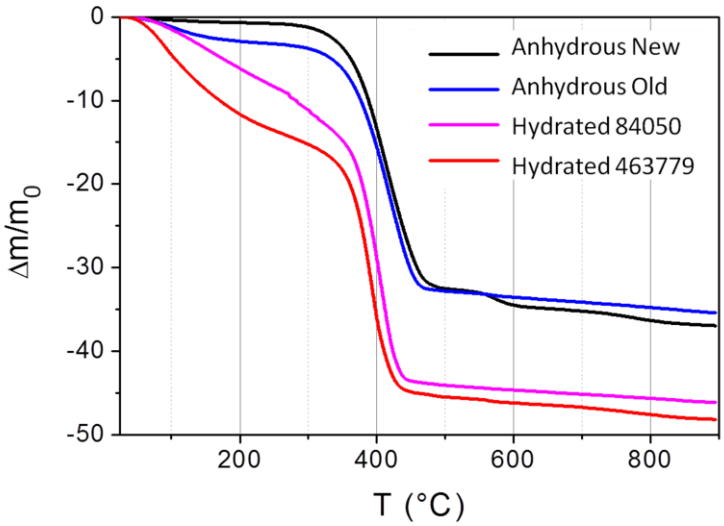

Figure II- 33 *Thermogravimetric analysis of $RuCl_3 \cdot xH_2O$ (ref. 84050, pink line); $RuCl_3 \cdot xH_2O$ (ref. 463779, red line) and $RuCl_3$ (ref. 208523, the black and blue lines correspond to a "new" and "old" sample, respectively).*

The TGA of the anhydrous $RuCl_3$ (ref. 208523) freshly received, noted as "new", and which did not come in contact with air, showed a main weight loss at 400°C, corresponding to its decomposition and oxidation to RuO_2. The total mass loss is 36.5 %, close to the theoretical one calculated for the transformation of the $RuCl_3$ to RuO_2 (Δm/m= 35.9 %). After the exposure of the same batch in air, the TGA curve of the anhydrous $RuCl_3$, referred to as "old", showed a first weight loss at 100°C of about 4 %, prior to the principal weight loss observed at 400°C. The first weight loss corresponds to physisorbed water.

The TGA of the two different $RuCl_3 \cdot xH_2O$ exhibit a continuous weight loss between room temperature and 300°C followed by a steep weight loss at 360°C. The first weight loss is about 7% and 12% for the $RuCl_3 \cdot xH_2O$ 84050 and 463779, respectively (Figure II- 33). The very broad temperature range in which the first weight loss occurs is in agreement with the presence of hydroxychloride complexes such as $Ru(OH)Cl_2$, or oxy-hydroxichlorides in the two hydrated ruthenium chlorides. The amount of these species is more important in the compound ref. 463779 according to the larger weight loss.

Thus, the difference between the TGA of the three $RuCl_3$ in the range 100-300°C is interpreted as the presence of oxy-hydroxy-chlorides in different amount in the two hydrated compounds and its absence in the anhydrous compound.

II.2.7.2 Influence of the ruthenium chloride on the rod morphology

The nucleating agents' effect on the nanorods morphology and size was afterwards determined through a typical experimental set-up in the heating mantle, with [NaOH] = $7.5x10^{-2}$ M and heating rate of 8°C·min^{-1}. Their TEM images are presented in the Figure II-34. The two $RuCl_3 \cdot xH_2O$ with ref. 463779 and ref. 84050, resulted in nanorods with mean diameter and length of D_m = 16±3 nm, L_m = 225±55 nm; and D_m = 22±1.5 nm, L_m = 160±30nm, respectively. The sample of the reaction with the anhydrous $RuCl_3$ was polydisperse with three populations: long rods (D_m = 11.6±1 nm, L_m = 120±40 nm), short and thin rods (D_m = 6±1 nm, L_m = 25±6 nm) and spheres (D_m = 9±3 nm).

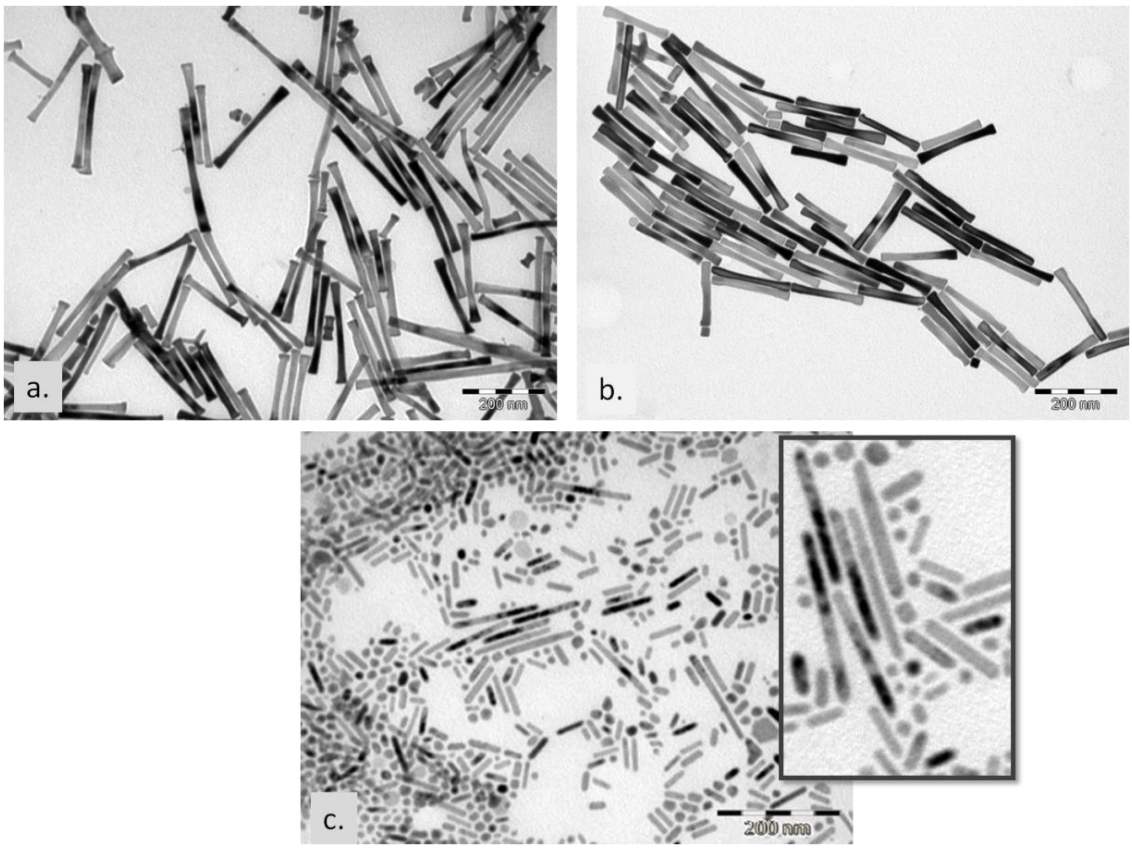

Figure II- 34 *TEM images of cobalt nanorods prepared with* ***(a)*** *$RuCl_3 \cdot xH_2O$ (ref. 463779),* ***(b)*** *$RuCl_3 \cdot xH_2O$ (ref. 84050) and* ***(c)*** *$RuCl_3$ (ref. 208523). Mean diameter, D_m, and mean length, L_m: (a) D_m = 16±3 nm, L_m = 225±55 nm; (b) D_m = 22±2 nm, L_m = 160±30 nm; (c) long rods: D_m = 12±1 nm, L_m = 120±40 nm, short and thin rods: D_m = 6±1 nm, L_m = 25±6 nm and spheres of D_m = 9±3 nm.*

In order to explore the Co NRs size range that one could achieve using these nucleating agents, additional experiments were performed for [NaOH] varying between $5.5x10^{-2}$ - $7.5x10^{-2}$ M. The Table II-7 summarizes the range of dimensions obtained with the different ruthenium chlorides.

The nanorods prepared with $RuCl_3 \cdot xH_2O$ as nucleating agents exhibited a mean diameter in the range 15-25 nm. The length was found in the range 100-300 nm with a slight difference between the two hydrated compounds. In every case the particles prepared with anhydrous $RuCl_3$ were found polydisperse, including long rods, small and very thin rods and small spheres. The main differences with the rods prepared with the $RuCl_3.xH_2O$ are:

- A smaller mean diameter (the rods and the spheres exhibit a diameter always lower than 11 nm);
- The shape of the tips, the rods prepared with the anhydrous ruthenium chloride exhibit a rounded tip, while those prepared with the hydrated ruthenium chloride exhibit a larger tip.

$RuCl_3$ precursor	**D_m (nm)**	**L_m (nm)**
$RuCl_3 \cdot xH_2O$ (ref. 463779)	15-25	200-300
$RuCl_3 \cdot xH_2O$ (ref. 84050)	15-25	100-200
$RuCl_3$ (ref. 208523)	<11	<120

Table II-7 *Summary of nanorods' dimensions obtained with different ruthenium chloride as nucleating agent with [NaOH] in the range $5.5x10^{-2}$ and $7.5x10^{-2}$ M.*

The difference of the particle mean size shows that much more ruthenium nuclei acted as seeds for the cobalt growth when anhydrous ruthenium chloride was introduced. Indeed for given cobalt concentration, an increasing seed number decreases the final particle size. Moreover, the use of the anhydrous $RuCl_3$ provides nanorods with rounded tips in comparison with the two $RuCl_3 \cdot xH_2O$, that produce rods with enlarged tips at their extremities. These rounded tips result in the growth of {10-11} facets in a bigger extend and minimize the extension of the (0001) facets compared to the previous cases (Figure II- 35).

These differences can tentatively be explained by a different reactivity of the ruthenium chlorides. Anhydrous $RuCl_3$ is more reactive than the hydrated compounds; it is reduced faster and produces a very large number of nuclei, explaining the smaller cobalt particle size. This large seeds' number contributes also to an increase of the cobalt growth rate explaining the morphological change. The growth is too fast and thus prevent from an extension of the (0001) facets.

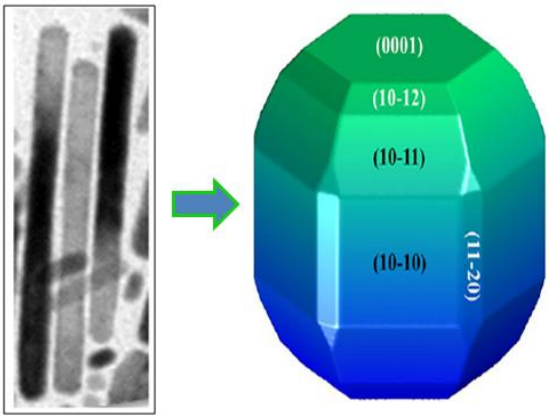

Figure II- 35 *Proposed hcp crystal structure of the rounded tips (image adapted from* [35]*)*

One could link the reactivity of the different ruthenium chlorides with their composition. According to the TGA characterizations, the content of oxy-hydroxy chloride in the different precursors follows the order: $RuCl_3$ ref. 208523 << $RuCl_3 \cdot xH_2O$ ref. 84050 < $RuCl_3 \cdot xH_2O$ ref. 463779. The lower the content of oxy-hydroxy-chloride species in the ruthenium precursor is, the higher the growth rate and the smaller the final particle size gets. The Figure II- 36 presents the suggested difference between the three nucleating precursors and their effect in nucleation and nanoparticles' morphology and dimensions.

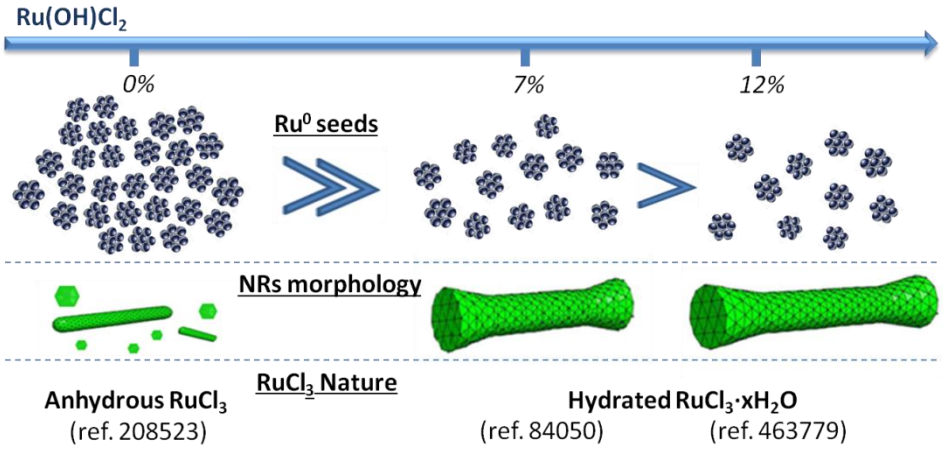

Figure II- 36 *Suggested effect of the $Ru(OH)Cl_2$ content on the Ru^0 nucleation rate and the nanorods' morphology.*

We demonstrate with this set of experiments that it is possible to change the nanorods' dimensions and morphology by varying solely the nature of the nucleating agent. As far as the magnetic properties are concerned, some rods prepared with anhydrous $RuCl_3$ exhibit a shape very close to the ideal ellipsoid described in chapter I. Moreover, the thin diameter should also increase the coercivity (see section I-16). Unfortunately, the particles are polydisperse with a lot a spheres. A clear improvement of the magnetic properties of the samples prepared with anhydrous $RuCl_3$ requires to decrease the polydispersity.

In the next sections we complete the study on the anhydrous $RuCl_3$. The effect of the reduced concentration of the Ru seeds and the increased heating rate on the cobalt nanorods will be examined. In that point, due to the limited heating rates that the heating mantle offers we continued our experimental work in the microwave.

II.2.8 Nucleation with anhydrous RuCl3: Effect of the ratio [Ru]/[Co]

In the aim to obtain solely monodisperse rounded nanorods, without the growth of additional spheres, the nucleation step with anhydrous $RuCl_3$ had to be further controlled. One possible approach is the decrease of the $RuCl_3$ concentration in order to decrease the number of Ru^0 seeds.

The Figure II- 37 shows TEM images obtained for typical reaction conditions in the microwave with [NaOH] = $7.5x10^{-2}$ M, 8°C·min^{-1} and Ru/Co ratio, equal to a. 2.5%, b. 2%, c. 1.5% and d. 1 %.

The first observation is that the decrease of anhydrous $RuCl_3$ concentration does not improve the shape and size distribution. Mixtures of long rods, short and thin rods and spheres are observed in the four cases. The strongest effect of the variation in the $RuCl_3$/$Co(C_{11}H_{23}COO)_2$ concentration is in the nanorods' morphology. The rounded cylinders obtained with 2.5% and 2% are replaced by cylinders with flat edges for 1.5% and 1%. A decreased amount of spherical particle production is also observed when the $RuCl_3$ amount was decreased. These tendencies are represented schematically on the Figure II- 38.

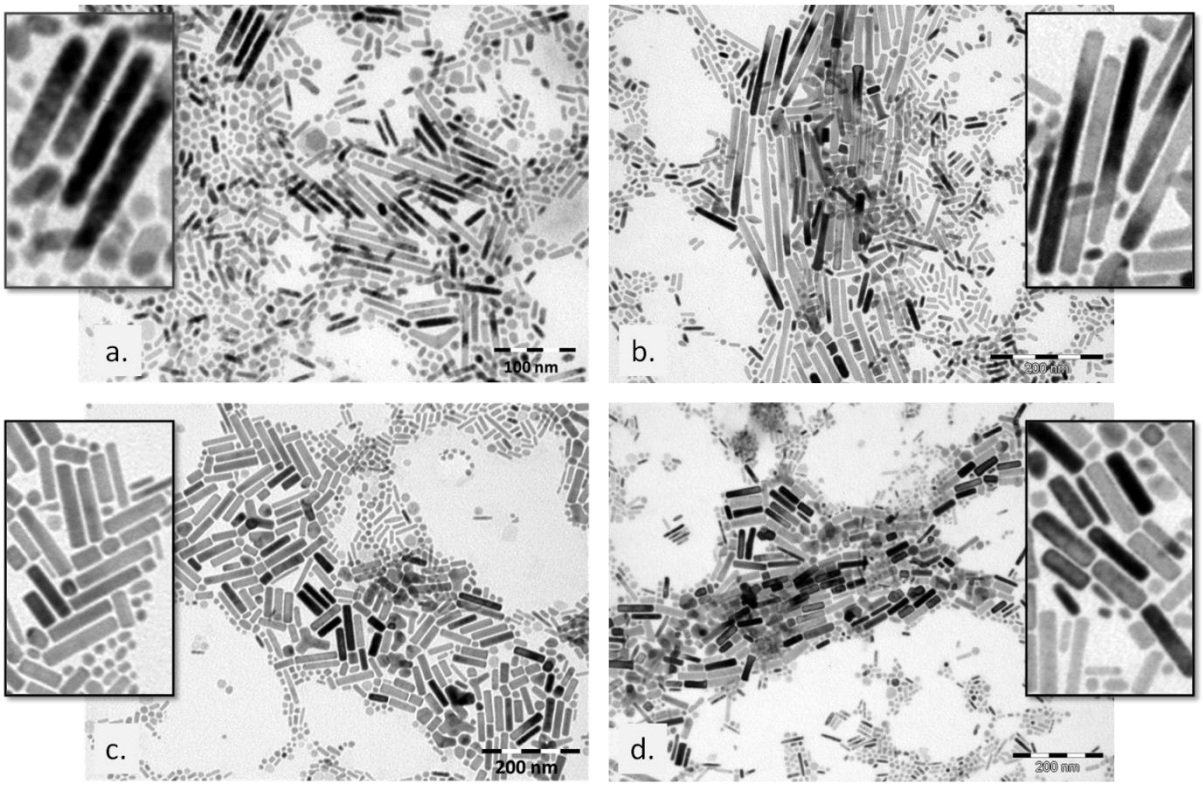

Figure II- 37 *$[RuCl_3]/[Co(C_{11}H_{23}COO)_2]$ effect on the particles' dimension and morphology:* ***a.*** *2.5%;* ***b.*** *2 %;* ***c.*** *1.5%;* ***d.*** *1%.*

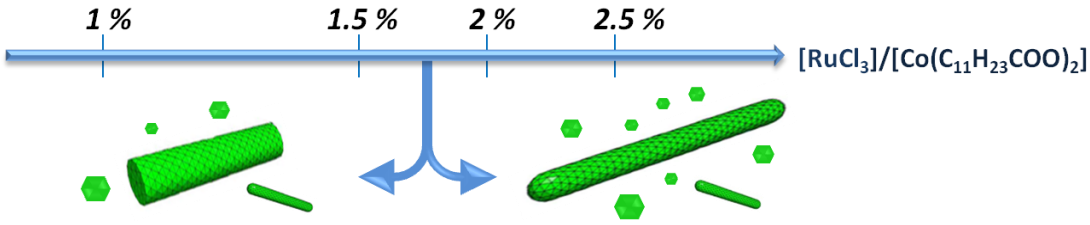

Figure II- 38 *Schematic illustration of the $[RuCl_3]/[Co(C_{11}H_{23}COO)_2]$ limit between rounded and cylindrical nanorods with flat edges.*

Even though the attempt to produce samples with monodisperse rounded cylinders by decreasing the seed number was not successful, we defined the limit of Ru/Co molar ratio (2%) above which the desired rounded ending is obtained.

II.2.9 Nucleation with anhydrous RuCl3: Heating rate effect

Considering that the size and shape polydispersity of the particles is due to a long overlap between the nucleation and growth step, the next approach to favor the synthesis of monodisperse nanorods with anhydrous $RuCl_3$ was to increase the heating rate.

We have interpreted the difference between the anhydrous and the hydrate ruthenium chlorides as a higher ability of the former compound to be reduced in the polyol. The anhydrous $RuCl_3$ produces more seeds in the medium, decreasing the final size of the cobalt particles. The drawback of its higher reactivity is that the ruthenium nuclei are produced at quite low temperature, much below the temperature at which the cobalt starts to grow. The polydispersity of the final cobalt particles is certainly the result of this long nucleation step.

By increasing the heating rate our idea was to reach as fast as possible 175°C, i.e. the temperature at which the cobalt growth can take place. We had the hope to trigger the nucleation step at 175°C in a very short time and come closer to the LaMer conditions.

The reactions were carried out in 60 mL of 1,2-butanediol, with [NaOH] = $5.5x10^{-2}$ M and [Ru]/[Co]= 2.5% under different heating rates: 8, 50 and 150°C·min^{-1} using the microwave. The resulting nanoparticles are illustrated at the Figure II- 39 and their dimensions are summarized in the Table II-8.

The TEM images show that an increase in the heating rate has two effects:

- It leads to a decrease of the rounded cylinders' dimensions (the mean diameter of the rounded cylinders decreased from 11.5 to 8 nm when the heating rate increased from 8 to 150°C·min^{-1});
- It produces also a narrowing of the size distribution and a better shape homogeneity, the proportion of nanospheres is much lower when the heating rate was 150°C·min^{-1}, while long rods together with small spheres were produced with the heating rate of 8°C·min^{-1}.

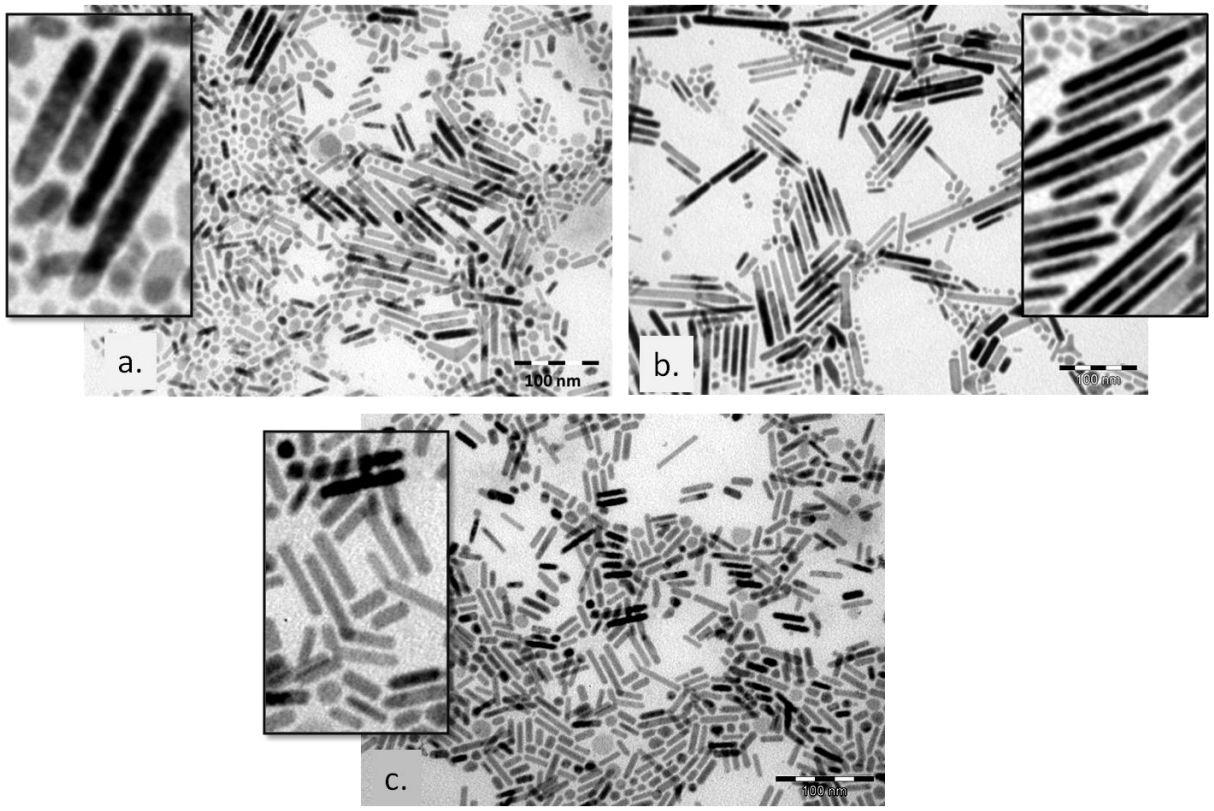

Figure II- 39 *TEM images of the heating rate effect on anhydrous $RuCl_3$:* ***a.*** *8°C·min^{-1};* ***b.*** *50°C·min^{-1};* ***c.*** *150°C·min^{-1}.*

	Heating rate (°C·min^{-1})	**Morphology**	**D_m (nm)**	**L_m (nm)**	**AR_m**
a.	**8°C·min^{-1}**	Nanorods	11.6±1	120±40	10
			6±1	23±6	4.2
		Spheres	9±3	--	--
b.	**50°C·min^{-1}**	Nanorods	8±1.5	70±20	10
			6±1	23±5	4
		Spheres	9±3	--	--
c.	**150°C·min^{-1}**	Nanorods	8±1	26±6	3.2
		Spheres	11±3	--	--

Table II-8 *Nanoparticles' morphologies and dimensions with respect to the applied heating rate.*

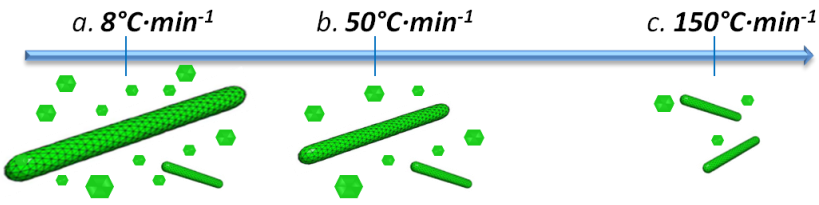

Figure II- 40 *Heating rate effect in the nanorods' size and monodispersity for 8, 50 and 150°C·min^{-1}.*

The combination of a nucleation with 2.5 % of anhydrous ruthenium chloride and a very high heating rate reduced the size distribution as seen at the schematic of Figure II- 40. Nevertheless, the morphology is not fully optimized. Despite the fact that we managed to decrease the population of spheres, it was not possible to avoid totally their formation. One can also observe that the mean aspect ratio decreased to about 3 for the highest heating rate. This smaller shape anisotropy is not favorable for high coercivity.

II.2.10 Conclusions on the nucleation step effect

In this study we have shown that the nature of the ruthenium chloride is a parameter that plays a significant role on the final NR morphology. The rods obtained with the anhydrous ruthenium chloride exhibit a morphology that seems optimized for the hard magnetic properties. Indeed the tips are rounded, the rod shape is closer to an ellipsoid than the shape of the rod obtained when hydrated ruthenium chloride was used as nucleating agent. Unfortunately the rods prepared with anhydrous $RuCl_3$ are polydisperse in length and mixed with spherical particles. By increasing the heating rate we obtained a narrower size distribution but also very small aspect ratio. These results are promising, but a more complete optimization of the rod shape is still necessary.

II.3. Cobalt rods: Characterization by X-ray diffraction

The purpose of the following XRD analysis was to confirm if all cobalt nanorods with different morphologies crystallize in the hcp structure and to correlate their crystallite sizes with the mean length and diameter measured by TEM.

The TEM images of the examined nanorods are presented in the *Figure II- 41*. We have chosen a sample representative of each shape category described in the previous sections: a. smooth rods with flat endings, b. rods with small tips, c. rough rods and d. rods with rounded endings combined with spheres. The Table II-9 summarizes the experimental conditions and set-ups used for their synthesis.

	Morphology	**$RuCl_3$ nature**	**Heating Rate ($°C \cdot min^{-1}$)**	**Scale**	**Set-up**
a.	Smooth NRs	$RuCl_3 \cdot xH_2O$	8	Large	Jacketed Reactor
b.	Small Tips	$RuCl_3 \cdot xH_2O$	8	Large	Heating Mantle
c.	Rough NRs	$RuCl_3 \cdot xH_2O$	8	Large	Heating Mantle
d.	Rounded NRs	$RuCl_3$	150	Small	Microwave oven

Table II-9 *Experimental conditions of different morphologies of cobalt anisotropic samples designated for XRD examination.*

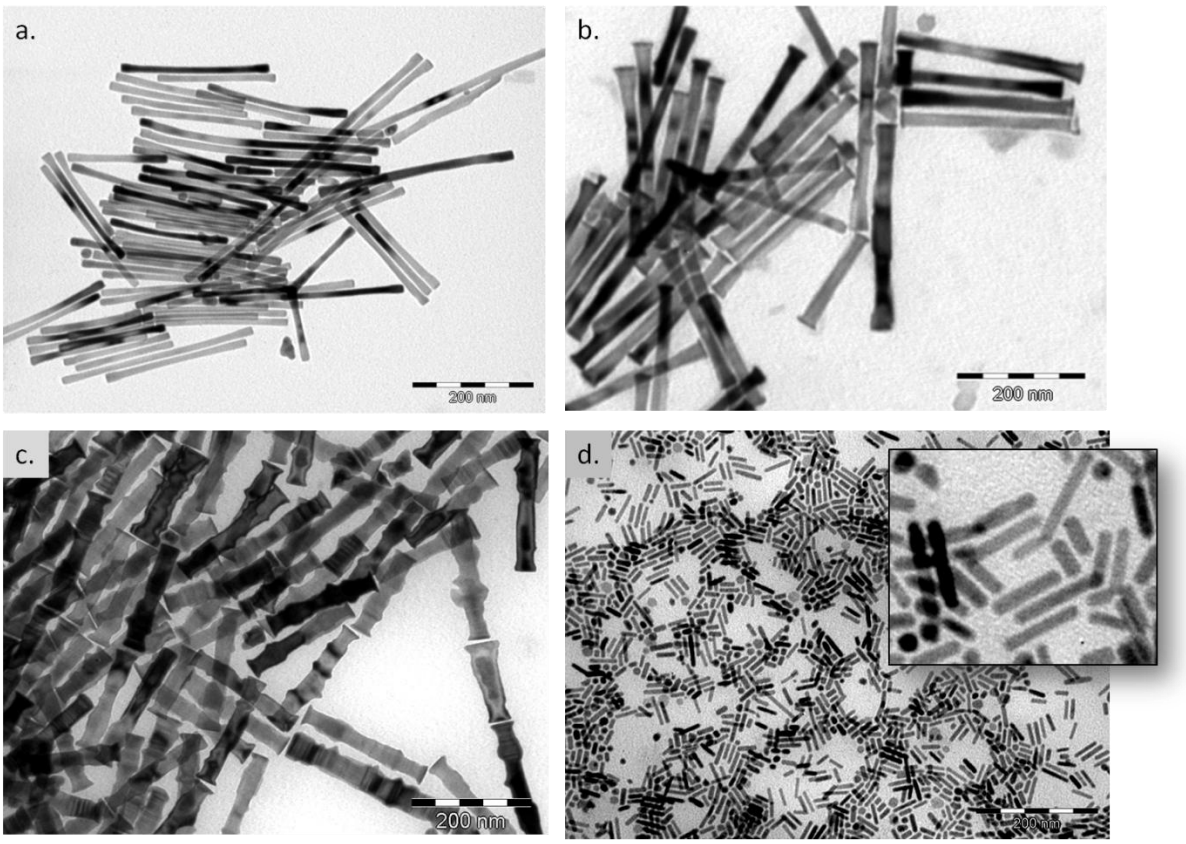

Figure II- 41 *TEM images of cobalt anisotropic particles with various shapes:* ***a.*** *smooth with flat endings;* ***b.*** *smooth with tips at their endings;* ***c.*** *rough; and* ***d.*** *rods with rounded endings and spheres.*

All XRD patterns regardless of the nanorods' smoothness, roughness or shape showed that they crystallize with the hcp structure (*Figure II- 42*). However, in the case of rough rods one can observe a very weak peak at 2θ = 60.7°, which corresponds to the (200) phase of fcc Co. The crystallite sizes calculated for the reflexions (10-10) and (0002), along with the rods' dimensions measured by TEM and the corresponding morphological (L_m/D_m) and structural ($L_{0002}/ L_{10\text{-}10}$) aspect ratios are summarized in the Table II-10.

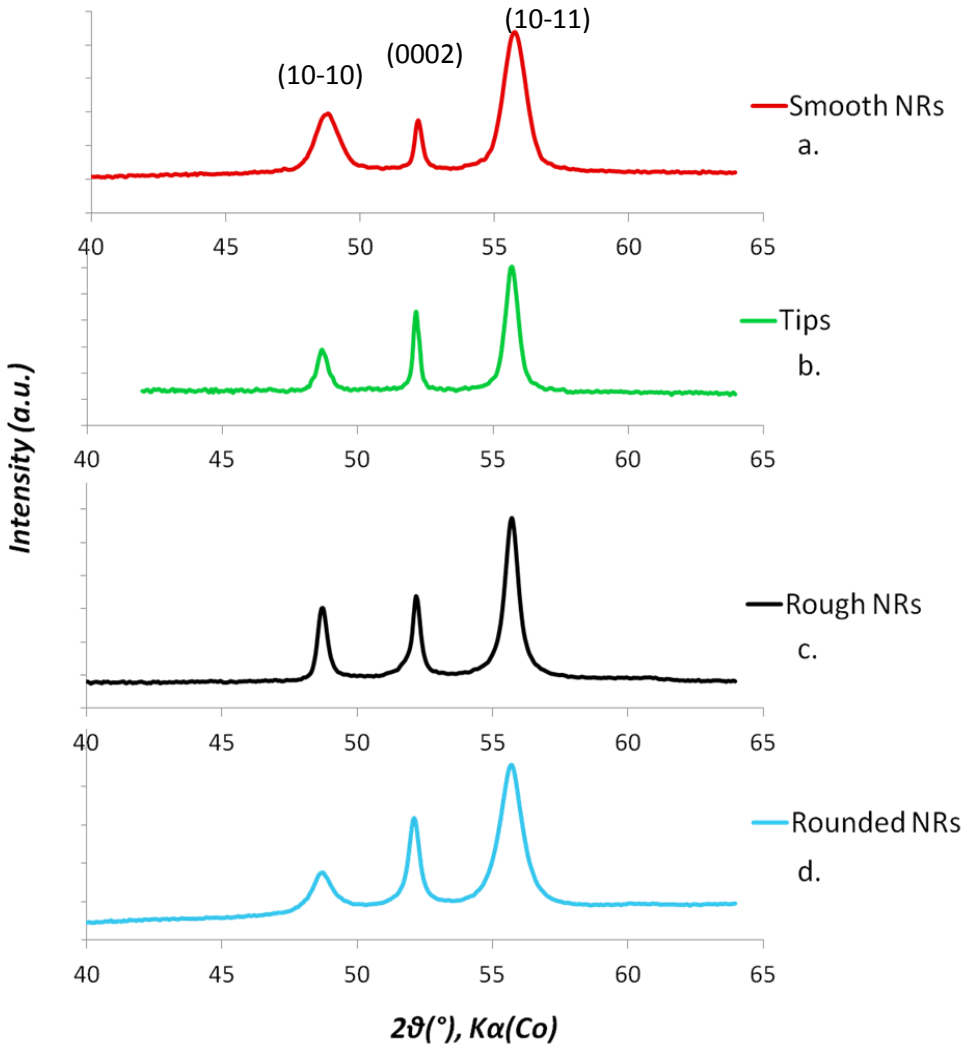

Figure II- 42 *XRD patterns of cobalt anisotropic particles with various shapes:* ***a.*** *smooth with flat endings;* ***b.*** *smooth with tips at their endings;* ***c.*** *rough rods; and* ***d.*** *rods with rounded endings and spheres.*

	Morphology	D_m (nm)	L_m (nm)	L_m/D_m	$L_{10\text{-}10}$ (nm)	L_{0002} (nm)	$L_{0002}/L_{10\text{-}10}$
a.	Smooth NRs	10±1	200±46	20	9	36	4
b.	Small Tips	20±2	260±60	13	19.5	54	2.7
c.	Rough NRs	30±7	200±35	6.6	25	29	1.2
d.	Rounded NRs +spheres	8±1 11±3	26±10	3.2	11.2	21.5	1.9

Table II-10 *Dimensions and crystallite sizes of cobalt anisotropic particles with various shapes:* ***a.*** *smooth with flat endings;* ***b.*** *smooth with tips at their endings;* ***c.*** *rough;* ***d.*** *rounded.*

In the case of smooth nanorods (a) and rods with small tips at their endings (b), the crystallite size $L_{(10\text{-}10)}$ was calculated very close to their mean diameter measured by TEM

revealing a good crystallinity along their diameter. The small difference observed between these values could be due to the presence of a thin oxide shell (≈1 nm). The comparison of $L_{(10\text{-}10)}$ and d_m is more delicate for the samples (c) and (d) because of the broad size distribution in diameter.

Regarding the structural length, $L_{(0002)}$, it was always found much smaller than the morphological, L_m. This difference is attributed in the existence of stacking faults along the c axis of the rods. The structural aspect ratio $L_{0002}/ L_{10\text{-}10}$ is always much lower than the morphological aspect ratio L_m/d_m. The difference is very important for the rough rods.

In the next chapter we will see that the presence of morphological and structural defects have strong consequence on the decrease of the coercivity.

II.4. Conclusions

We demonstrate that the up-scaling of the polyol process for the synthesis of monodisperse and single crystalline cobalt nanorods (up to ≈5 g) is feasible. We show that a homogeneous heat and mass transfer provided by low stirring speed and proper stirring impeller is crucial for the production of the desired nanorods both in small and large scale. More precisely, stirring speed at 80 rpm results in rods with smooth surface and flat edges, while the anchor impeller in small scale (or anchor and propeller in large scale) contributes in obtaining monodisperse in size and population particles.

The effect of the nature of the nucleating agent on the nanorods' morphology has been studied. The rods obtained with the anhydrous ruthenium chloride exhibit a morphology that seems optimized for the hard magnetic properties. Indeed the tips are rounded, the rod shape is closer to an ellipsoid than the shape of the rod obtained when hydrated ruthenium chloride was used as nucleating agent. Though promising, these results should be further extended to allow narrowing the size distribution of the Co NRs while maintaining large aspect ratio.

Bibliography

[1] P. Aranda and J. M. Garcia, “Porous membranes for the preparation of magnetic nanostructures,” *J. Magn. Magn. Mater.*, vol. 249, no. 1–2, pp. 214–219, 2002.

[2] A. Huczko, “Template-based synthesis of nanomaterials,” *Appl. Phys. A*, vol. 70, no. 4, pp. 365–376, 2000.

[3] M. Paunovic and M. Schlesinger, *Fundamentals of Electrochemical Deposition*. New York: John Wiley & Sons Inc., 1998.

[4] M. Vázquez and L. G. Vivas, “Magnetization reversal in Co-base nanowire arrays,” *Phys. Status Solidi Basic Res.*, vol. 248, no. 10, pp. 2368–2381, 2011.

[5] Vega V., Garcia J., Rosa W.O., Vivas L.G., Prida V.M., Hernando B., and Vázquez M., “Magnetic properties of (Fe, Co)-Pd nanowire arrays,” *J Nanosci Nanotechnol.*, vol. 12, no. 9, pp. 7501–4, 2012.

[6] Vega V., Rosa W. O., Garcia J., Sanchez T., Santos J. D., Beron F., Pirota K. R., and Prida V.M., “Template-Assisted CoPd Nanowire Arrays: Magnetic Properties and FORC Analysis,” *J. Nanosci. Nanotechnol.*, vol. 12, no. 6, pp. 4736–4743(8), 2012.

[7] M. Vázquez, K. Pirota, M. Hernández-Vélez, V. M. Prida, D. Navas, R. Sanz, F. Batallán, and J. Velázquez, “Magnetic properties of densely packed arrays of Ni nanowires as a function of their diameter and lattice parameter,” *J. Appl. Phys.*, vol. 95, no. 11 II, pp. 6642–6644, 2004.

[8] L. G. Vivas, J. Escrig, D. G. Trabada, G. A. Badini-Confalonieri, and M. Vazquez, “Magnetic anisotropy in ordered textured Co nanowires,” *Appl. Phys. Lett.*, vol. 100, no. 25, pp. 7–11, 2012.

[9] H. Zeng, M. Zheng, R. Skomski, D. J. Sellmyer, Y. Liu, L. Menon, and S. Bandyopadhyay, “Magnetic properties of self-assembled Co nanowires of varying length and diameter,” *J. Appl. Phys.*, vol. 87, no. 9, p. 4718, 2000.

[10] Y. Henry, K. Ounadjela, L. Piraux, S. Dubois, J. M. George, and J. L. Duvail, “Magnetic Anisotropy and Domain Patterns in Electrodeposited cobalt Nanowires,” *Eur. Phys. J. B*, vol. 20, pp. 35–54, 2001.

[11] Z. Liu, P. C. Chang, C. C. Chang, E. Galaktionov, G. Bergmann, and J. G. Lu, “Shape anisotropy and magnetization modulation in hexagonal cobalt nanowires,” *Adv. Funct. Mater.*, vol. 18, no. 10, pp. 1573–1578, 2008.

[12] A. Ramazani, M. Almasi Kashi, and G. Seyedi, “Crystallinity and magnetic properties of electrodeposited Co nanowires in porous alumina,” *J. Magn. Magn. Mater.*, vol. 324, no. 10, pp. 1826–1831, 2012.

[13] A. Ramazani, M. Almasi Kashi, and A. H. Montazer, “Fabrication of single crystalline, uniaxial single domain Co nanowire arrays with high coercivity,” *J. Appl. Phys.*, vol. 115, no. 11, pp. 0–7, 2014.

[14] S. Sun, “Monodisperse FePt Nanoparticles and Ferromagnetic FePt Nanocrystal Superlattices,” *Science (80).*, vol. 287, no. 5460, pp. 1989–1992, 2000.

[15] D. Ciuculescu, F. Dumestre, M. Comesaña-Hermo, B. Chaudret, M. Spasova, M. Farle, and C. Amiens, “Single-crystalline co nanowires: Synthesis, thermal stability, and carbon coating,” *Chem. Mater.*, vol. 21, no. 17, pp. 3987–3995, 2009.

[16] L.-M. Lacroix, S. Lachaize, A. Falqui, M. Respaud and B. Chaudret, “Iron Nanoparticle Growth in Organic Superstructures,” *J. Am. Chem. Soc.*, vol. 131, no. 2, pp. 549–557, 2009.

[17] B. Jeyadevan, K. Urakawa, A. Hobo, N. Chinnasamy, K. Shinoda, K. Tohji, D. D. J. Djayaprawira, M. Tsunoda, and M. Takahashi, “Direct synthesis of fct-FePt nanoparticles by chemical route,” *Japanese J. Appl. Physics, Part 2 Lett.*, vol. 42, no. 4 A, pp. 23–26, 2003.

[18] Y. Soumare, C. Garcia, T. Maurer, G. Chaboussant, F. Ott, F. Fiévet, J.-Y. Piquemal, and G. Viau, “Kinetically Controlled Synthesis of Hexagonally Close-Packed Cobalt Nanorods with High Magnetic Coercivity,” *Adv. Funct. Mater.*, vol. 19, pp. 1971–1977, 2009.

[19] Guy M., La Mer V. K., “Kinetics of Crystalline Nucleus Formation in Supercooled Liquid Tin” *J. Am. Chem. Soc.*, vol. 74, p. 2323, 1952.

[20] V. F. Puntes, D. Zanchet, C. K. Erdonmez, and A. P. Alivisatos, “Synthesis of hcp-Co nanodisks,” *J. Am. Chem. Soc.*, vol. 124, no. 43, pp. 12874–12880, 2002.

[21] F. Dumestre, B. Chaudret, C. Amiens, M. Respaud, P. Fejes, P. Renaud, and P. Zurcher, “Unprecedented Crystalline Super-Lattices of Monodisperse Cobalt Nanorods,” *Angew. Chemie - Int. Ed.*, vol. 42, no. 42, pp. 5213–5216, 2003.

[22] K. Soulantica, F. Wetz, J. Maynadie, A. Falqui, R. P. Tan, T. Blon, B. Chaudret, and M. Respaud, “Magnetism of single-crystalline Co nanorods,” *Appl. Phys. Lett.*, vol. 95, no. 15, 2009.

[23] N. Chakroune, G. Viau, C. Ricolleau, F. Fiévet-Vincent, and F. Fiévet, “Cobalt-based anisotropic particles prepared by the polyol process,” *J. Mater. Chem.*, vol. 13, pp. 312–318, 2003.

[24] Fiévet F., and Brayner R., *Nanomaterials: A Danger or a Promise? A Chemical and Biological Perspective*. Springer, 2013.

[25] Y. Soumare, “Synthèse et organisation de nanoparticules magnétiques anisotropes par chimie douce. Nouveaux précurseurs pour aimants permanents.,” Universite Paris Diderot (Paris 7), 2008.

[26] K. A. Atmane, “Elaboration de nanoparticules ferromagnétiques par la voie polyol,” Université Paris Diderot, 2012.

[27] K. Atmane, F. Zighem, Y. Soumare, M. Ibrahim, R. Boubekri, T. Maurer, J. Margueritat, J.-Y. Piquemal, F. Ott, G. Chaboussant, F. Schoenstein, N. Jouini, and G. Viau, “High

temperature structural and magnetic properties of cobalt nanorods," *J. Solid State Chem.*, vol. 197, pp. 297–303, 2013.

[28] D. Ung, G. Viau, C. Ricolleau, F. Warmont, P. Gredin, and F. Fiévet, "CoNi nanowires synthesized by heterogeneous nucleation in liquid polyol," *Adv. Mater.*, vol. 17, no. 3, pp. 338–344, 2005.

[29] F. Bozon-Verduraz, F. Fiévet, J.-Y. Piquemal, R. Brayner, K. El Kabouss, Y. Soumare, G. Viau, and G. Shafeev, "Nanoparticles of metal and metal oxides: some peculiar synthesis methods, size and shape control, application to catalysts preparation," *Brazilian J. Phys.*, vol. 39, no. 1a, pp. 134–140, 2009.

[30] K. Atmane, C. Michel, J.-Y. Piquemal, P. Sautet, P. Beaunier, M. Giraud, M. Sicard, S. Nowak, R. Losno, and G. Viau, "Control of the anisotropic shape of cobalt nanorods in the liquid phase: from experiment to theory... and back," *Nanoscale*, vol. 6, pp. 2682–2692, 2014.

[31] T. Maurer, F. Ott, G. Chaboussant, Y. Soumare, J. Y. Piquemal, and G. Viau, "Magnetic nanowires as permanent magnet materials," *Appl. Phys. Lett.*, vol. 91, no. 17, pp. 1–4, 2007.

[32] G. Viau, C. Garcia, T. Maurer, G. Chaboussant, F. Ott, Y. Soumare, and J. Y. Piquemal, "Highly crystalline cobalt nanowires with high coercivity prepared by soft chemistry," *Phys. Status Solidi Appl. Mater. Sci.*, vol. 206, pp. 663–666, 2009.

[33] Rueff J.-M., Masciocchi N., Rabu P., Sironi A., and Skoulios A., "Synthesis, Structure and Magnetism of Homologous Series of Polycrystalline Cobalt Alkane Mono- and Dicarboxylate Soaps," *Chem. – Eur. J.*, vol. 8, pp. 1813–1820, 2002.

[34] Ouar Nassima, Farhat Samir, Mercone Silvana, Zighem Fatih, Schoenstein Frederic, Jouini Noureddine, Hinkov Ivaylo, "Magnetic Nanowire Synthesis: A Chemical Engineering Approach," *IFAC Proc. Vol.*, vol. 61, no. 1, pp. 304–316, 2015.

[35] J. X. Liu, H. Y. Su, D. P. Sun, B. Y. Zhang, and W. X. Li, "Crystallographic dependence of CO activation on cobalt catalysts: HCP versus FCC," *J. Am. Chem. Soc.*, vol. 135, no. 44, pp. 16284–16287, 2013.

Chapter III Fabrication & Properties of Dense Assemblies of Cobalt Nanorods

III. 1 Objectives

The purpose of the present chapter is to prepare dense assemblies of cobalt nanorods obtained by the polyol process. Our task is the rods' parallel arrangement, via the application of an external magnetic field, into a dense and easy to handle macroscopic material. Taking into account the diversity of nanorod morphologies obtained in the previous chapter, we will examine their ability to align and yield the characteristic squared M(H) loop of permanent magnets. Factors which affect the energy product will be examined, the intrinsic coercivity, the remanence to saturation ratio, squareness of the M(H) loop and the magnetic volume fraction. A simple model of the M(H) loop is introduced and applied in simulations where the BH_{max} dependence on squareness and coercivity is examined. Finally, means for the BH_{max} improvement are suggested and preliminary tests are performed.

III. 2 Assembly of Cobalt Nanorods: experimental details

III.2.1 Classification of different nanorod morphologies

Throughout the following experiments two different types of nanorods will be examined, we will classify them according to the nature of their polydispersity, namely:

1. Shape and size polydispersity, in which we distinguish:
   - Smooth rods (Figure III- 1 a). They are monodisperse in diameter, but slightly polydisperse in length;
   - Smooth rods with tips at their endings (Figure III- 1 b);
   - Rough rods (Figure III- 1 c). Their diameter is not constant along the rod length.

2. Population polydispersity, which corresponds to a sample consisting in a combination of:
   - Nanorods and spherical particles (Figure III- 1 d) (prepared with the anhydrous $RuCl_3$);
   - Nanorods and tetrapods (Figure III- 1 e);
   - Nanorods and stars that form aggregates when they are in large amount (obtained from inefficient stirring conditions) (Figure III- 1 f).

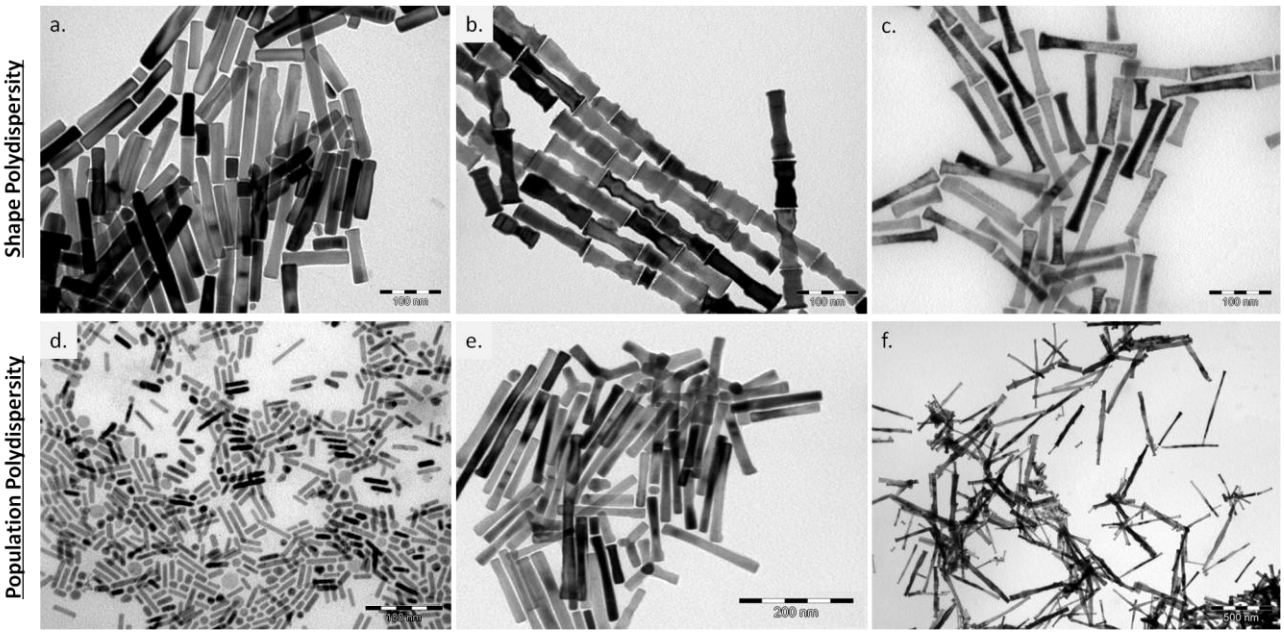

Figure III- 1 *TEM images of the two types of nanorod's polydispersity examined. Shape polydispersity includes rods with* ***a.*** *smooth surface and flat endings,* ***b.*** *rough rods and* ***c.*** *smooth rod with tips; Population polydispersity where the sample is a mixture of:* ***d.*** *rods and spherical nanoparticles; or* ***e.*** *rods and aggregated stars/multipods (****f****).*

III.2.2 Washing procedure

Prior to the alignment, the nanorods' washing is an essential step for the removal of the polyol, where they are dispersed, and the ligands (long alkyl chain carboxylates) surrounding them. Two solvents were used:
- firstly ethanol, to remove the butanediol, and then
- chloroform or toluene, to remove the carboxylate ligands.

We will use the notation R_xA_{yn} which corresponds to rods R of diameter "x", aligned after washing with a solvent "y" ("C" for chloroform or "T" for toluene), for n number of times. As an example, the typical washing process of rods prepared in small scale synthesis was twice with ethanol and once with chloroform, noted as R_xA_{C1}. Additional washings were carried out starting twice with ethanol, and followed by e.g. 10 times with chloroform, noted as A_{C10}, or 4 times with toluene, noted A_{T4}.

For the small scale alignment, 5 mL of the polyol mother liquor, containing 0.047 g of cobalt nanorods, were washed and recovered via magnetic attraction, while for the large scale alignment, 1 g of cobalt nanorods were washed and retrieved with centrifugation, due to the large volume of polyol that had to be removed (≈210 mL). The volume of solvent used

for each washing cycle in the low and large scale batches was ≈20 mL and 200 mL, respectively.

III.2.3 Alignment procedure

After washing, the rods were redispersed in chloroform and sonicated for 20 min before their alignment. The volume of chloroform was 300 µl for small scale experiments and 10 mL for large scale.

Two different moulds were used for the large scale alignments: a Teflon parallelepiped of 5 mm width; and an aluminum discoid of d= 4 cm (Figure III- 2 a, b). The dimensions of the Teflon mould were in agreement with the cavities of the cold and spark plasma sintering (SPS) compaction instruments, which the nanorods were designated for (see Chapter V). All small scale alignments were carried out in a cylindrical mould of d= 1 cm (Figure III- 2 b inset). Since the final step of compaction was planned to be performed under air, no precaution were taken to protect the nanoparticles from oxidation during their washing and alignment process.

In all cases, the suspension was placed in a homogeneous magnetic field of 1T provided by an electromagnet. For the parallelepiped mould the direction of the field was perpendicular to its length (Figure III- 2 c). The chloroform was let to evaporate at room temperature for a few hours (typically 5 h).

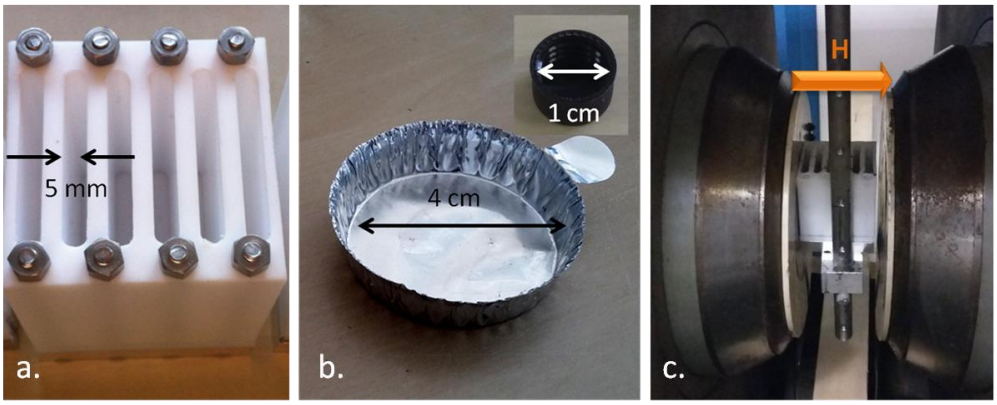

Figure III- 2 a. *Parallelepiped Teflon mould of 5 mm width used for the alignment of the nanorods prior to their compaction;* ***b.*** *Aluminum discoid mould with d= 4 cm. Inset, discoid mould with d= 1 cm;* ***c.*** *Alignment set-up: the applied field (1 T) provided by an electromagnet.*

III. 3 Dense assemblies: observation at macroscopic scale

After the chloroform's evaporation, macroscopic wafers were observed. Their texture varied depending on their washing.

More precisely, small scale alignments prepared with typical washing (A_{C1}) and large scale alignments prepared by additional washings (x10 with chloroform, A_{C10}) resulted in shiny silver assemblies (Figure III- 3 a,b), presenting robustness along the axis parallel to the applied field and flexibility perpendicular to it (Figure III- 3 e). Individual millimeter long needles could be separated from these wafers for further characterizations (Figure III- 3 d). At the opposite, in the case of inefficient washing, e.g. A_{C1} for a large scale alignment, black mat, fragile and cracked wafers were obtained (Figure III- 3 c, f).

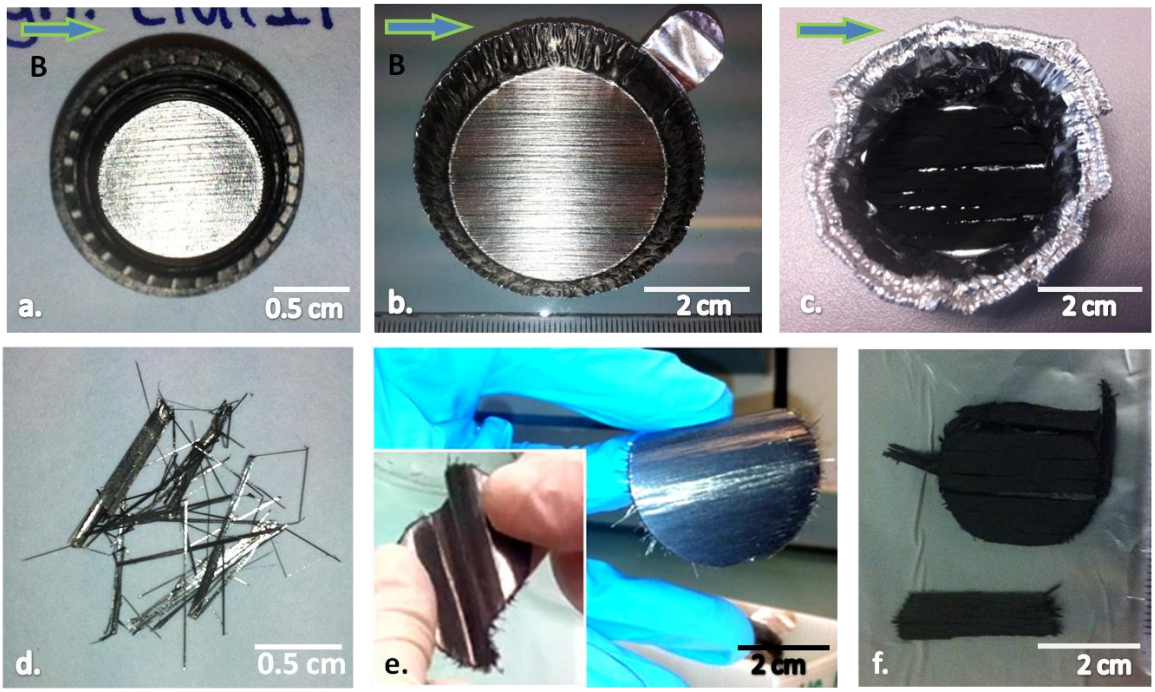

Figure III- 3 *Washing effect on wafers' texture:* ***a.*** *small and* ***b.*** *large scale alignments after effective washings resulting in shiny silver wafers;* ***c.*** *Mat with cracks wafer as a consequence of inefficient nanorod washing. Demonstration of wafers' robustness:* ***d.*** *robust needles;* ***e.*** *Flexibility along the alignment direction;* ***f.*** *fragile wafer due to poor washing.*

III. 4 Dense assemblies: observation at microscopic scale

The rod assemblie were characterized by scanning electron microscopy (FEG-SEM) using a JEOL JSM 6700F. Three different trends in the nanorods' alignment were observed concerning their washing, shape and population polydispersity.

a. Washing effect

SEM images of a needle obtained from a mat wafer such as those presented on Figure III- 3 c,f are presented in the Figure III- 4 a and b. The nanorods (d_m= 31±5 nm, l_m= 240±60 nm) were aligned in a large scale and washed with the typical process (A_{C1}). As a result of the poor washing, the needle's surface is rough, with cracks and exhibits a wavy structure perpendicular to the alignment's direction. The fragility of these wafers can be explained by the fact that the aligned rods form bundles separated with significant distances. The opposite case is presented in the Figure III- 4 c. Similar rods (d_m= 31±4 nm, l_m= 190±35 nm) were prepared for a large scale alignment, but with more efficient washing (A_{C10}). From a macroscopic point of view, the needle's surface is smooth and shinny. On the SEM image, neither cavities nor cracks were noted (Figure III- 4 c). In contrast with the previous case, the rods are assembled closer to each other.

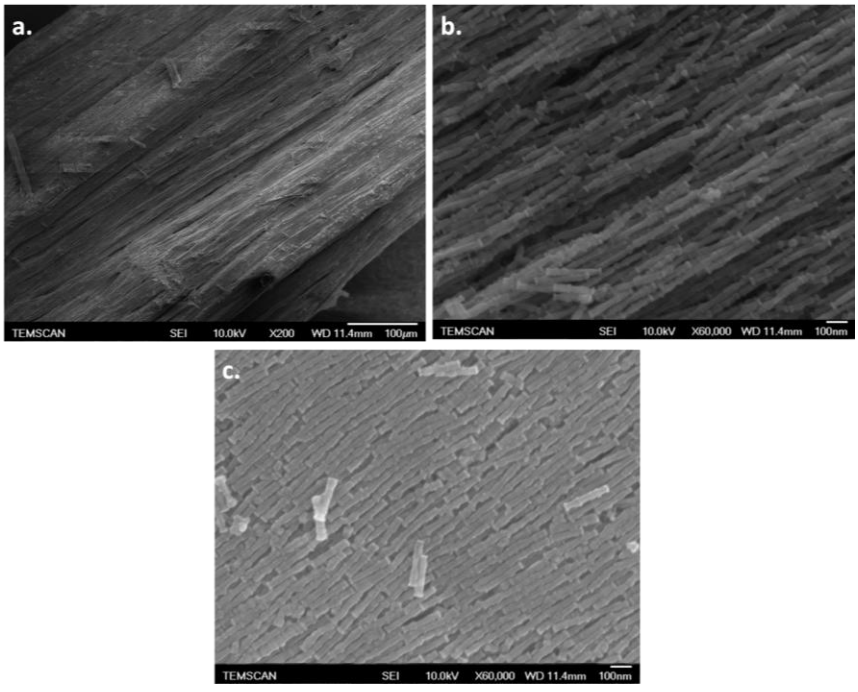

Figure III- 4 *SEM images demonstrating the washing effect on the nanorods' assemblies. Rods washed* ***a.*** *and* ***b.*** *x1 with chloroform; and* ***c.*** *x10 with chloroform.*

b. Effect of stars in alignment quality

The smoothness of the needle's surface can be affected by the sample's population polydispersity. When rods are aligned along with a large amount of stars (Figure III- 5 a, b, c), the needle's surface is rough and with cavities. These cavities are caused by the existence of multipods, which do not present any preferential direction of orientation. The texture of the needle's surface turns to be smoother for a less polydisperse sample, where the concentration of tetrapods is lower (Figure III- 5 d, e, f), and for a monodisperse one where only nanorods are observed (Figure III- 5 g, h, i). In all cases the rods are always aligned with their long axis parallel to the needle's long axis, regardless the existence of stars or tetrapods.

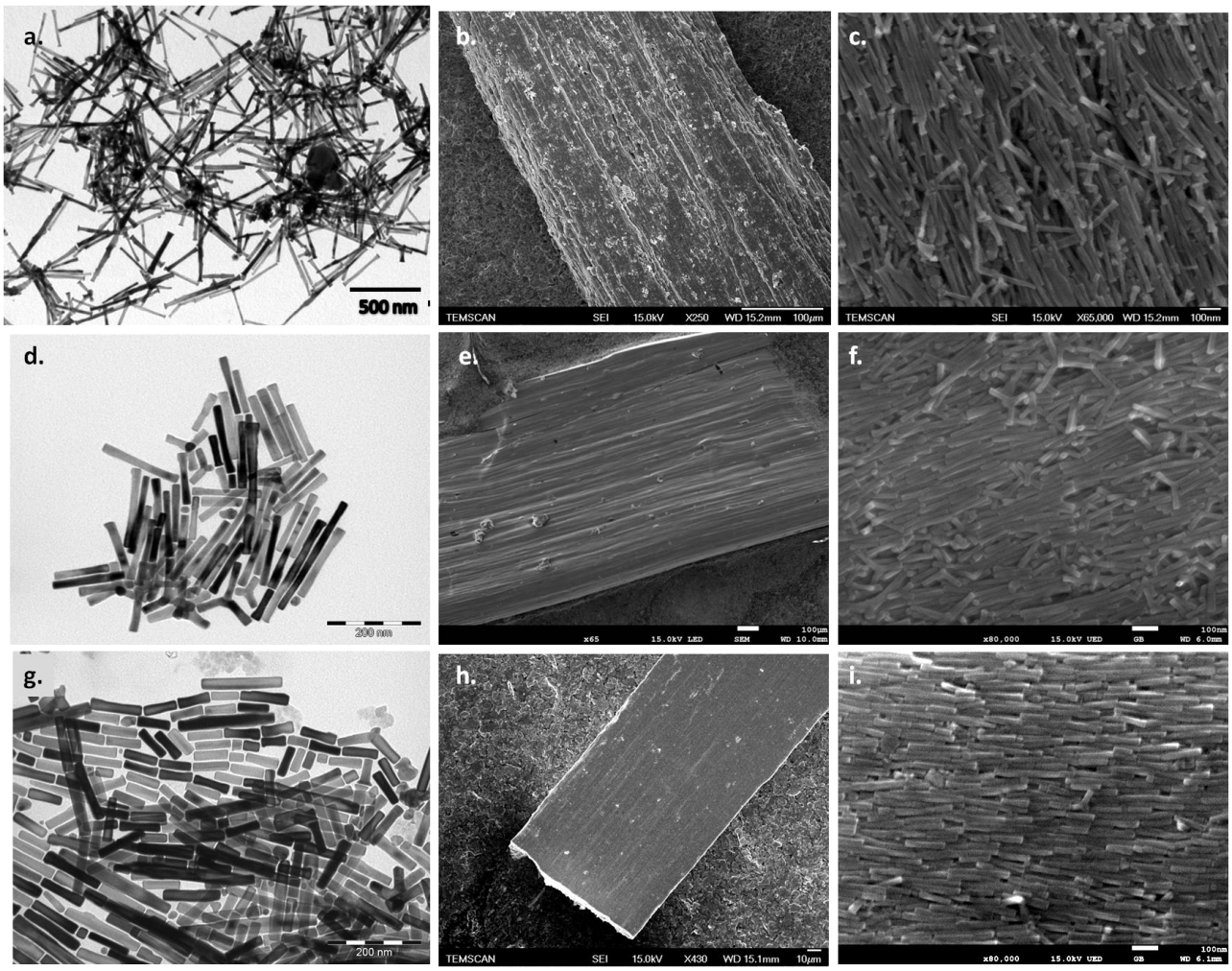

Figure III- 5 TEM(a,d,g) and SEM(b,c,e,f,h,i) *Images demonstrating the effect of multipods in the alignment quality:* ***a, b, c.*** *rods (d_m=20±5 nm; l_m=290±90 nm) combined with big population of stars;* ***d, e, f*** *rods (d_m=17±2 nm; l_m=120±40 nm) combined with small population of tetrapods;* ***g, h, i*** *nanorods (d_m=20±2 nm; l_m=95±40 nm).*

c. Shape polydispersity

The next step consisted in examining whether the nanorods' morphology affects the quality of their alignment. To do so, nanorods with rough surface (d_m=31±4 nm; l_m=190±35 nm), smooth surface with tips (d_m=20±2 nm; l_m=95±20 nm) and smooth surface with flat endings (d_m=21±2 nm; l_m=110±35 nm) were washed with the same protocol (A_{C3}) and aligned in small scale alignments. The Figure III- 6 shows that despite their shape or dimensions, they can all densely align parallel to the applied field.

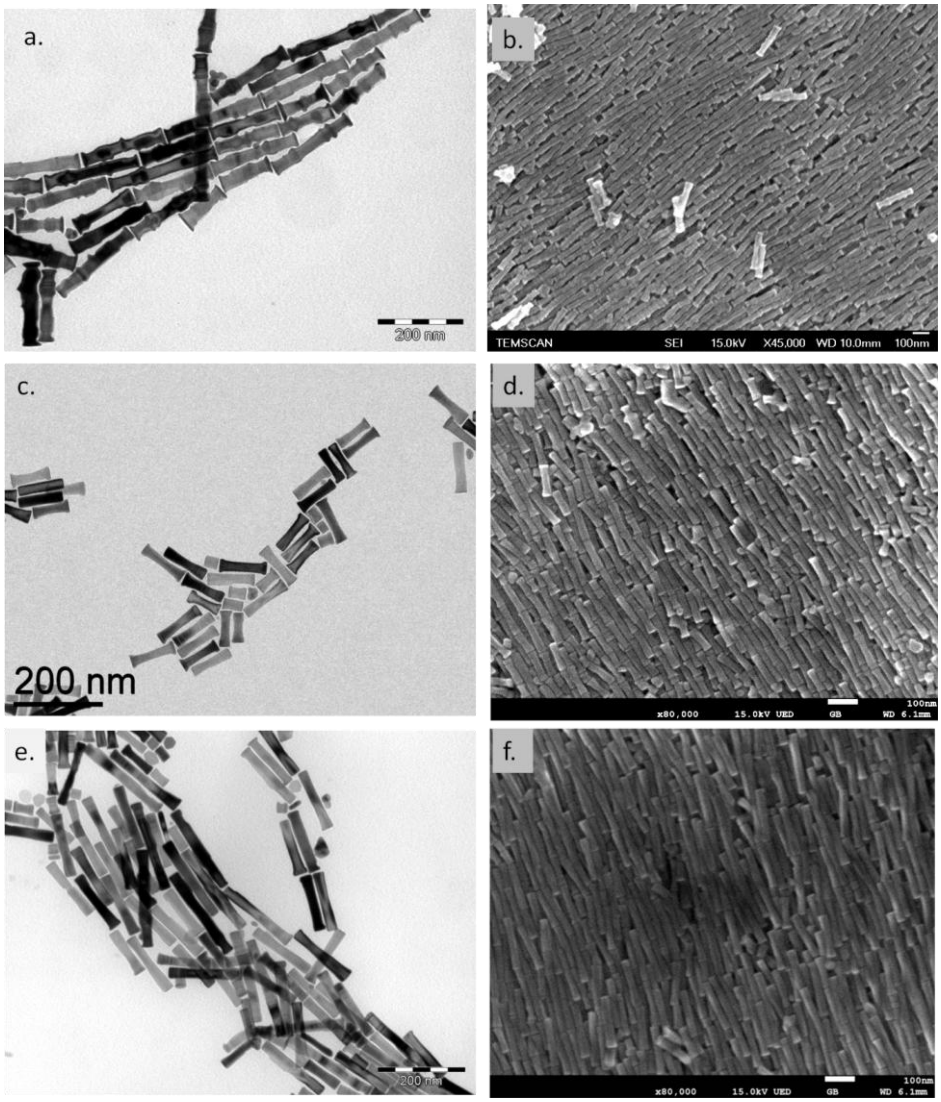

Figure III- 6 *TEM (a, c, e) and SEM (b, d, f) images demonstrating the effect of the sample's morphology on the alignment quality:* ***a.b.*** *rough nanorods (d_m=31±4 nm; l_m=190±35 nm);* ***c.d.*** *rods with tips (d_m=20±2 nm; l_m=95±20 nm);* ***e.f*** *rods with flat endings (d_m=21±2 nm; l_m=110±35 nm).*

III. 5 Hysteresis loop

III.5.1 M(H) loops in parallel and perpendicular configuration

The magnetic properties of individual needles collected in the assemblies were characterized using a Quantum Design Physical Property Measurement System (PPMS) with the Vibrating Sample Magnetometer (VSM) configuration. The M(H) loop was measured at room temperature on small needles of dimensions c.a. 5x0.5x0.1 mm for two configurations of applied field, namely i) parallel and ii) perpendicular to the needle's long axis. Representative M(H) loops for both configurations are shown in the Figure III- 7.

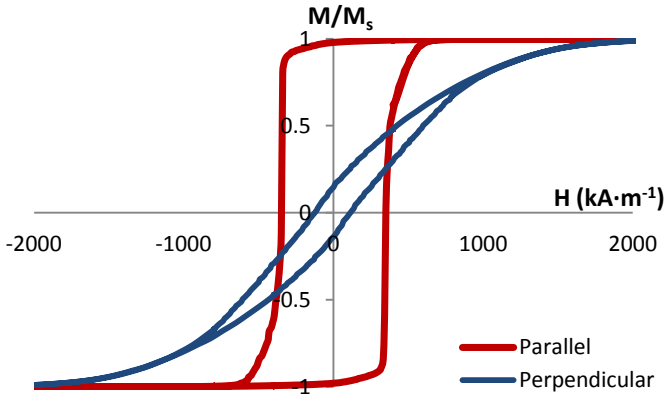

Figure III- 7 M(H) loops for parallel and perpendicular configuration of a magnetic needle along the measuring magnetic field.

When the external magnetic field is applied along the needle's long axis, and consequently along the nanorods' long axis, the measured hysteresis loop is almost squared (red loop in Figure III- 7). As far as the external field is applied perpendicular to the needle's long axis, the loop closes and the field necessary to reach the saturation is much higher (blue loop in Figure III- 7). The different shape of the M(H) loop in parallel and perpendicular configurations are in aggreement with the simulations presented in Chapter I (see section I.3.2).

In the following we will compare the effect of alignment and rod morphology on the shape of the M(H) loop, focusing on the parallel configuration. The values of coercivity as a function of the rod sample will be discussed later (section III-10).

The deviation from a perfectly squared M(H) loop can be assessed by two parameters:

- The orientation coefficient: M_r/M_s. The divergence of M_r/M_s from the ideal value of 1 is due to the nanorods' misorientation, leading to the decrease of the remanence

magnetization value, M_r. In the example of Figure III- 7 M_r/M_s is equal to 0.98 showing a very good easy axis alignment.

- The squareness: SQ. As a reminder, the SQ corresponds to the ratio between the experimental area below the demagnetization curve and the product $|M_s \cdot H_c|$, which corresponds to the maximum area enclosed in an ideal magnet:

$$SQ = \frac{A}{M_S.H_c} \qquad \text{(Eq. III-1)}$$

A SQ value of 1 means that the magnetization reversal of all the nanorods occurs at the same field. A SQ value lower than 1 is due to a broad switching field distribution of the magnetic moments. It can be attributed to:

1. Nanorods misalignment or presence of stars/tetrapods, which do not present any preferential direction of orientation; and/or
2. Presence of morphological defects (large tips, roughness). According to micromagnetic simulations the tips lead to a non coherent magnetization reversal (in a "flower-vortex" state), which promotes the flipping of the magnetization via domain wall propagation in the rest of the rod [1], [2]. Such a non coherent reversal results in a broader switching field distribution and thus in a lower SQ.

In addition, in both cases the dipolar interactions between the defected rods and their neighbors promote the latter's reversal at lower field than their coercive. This results in a non coherent reversal of the whole rod assembly translated by a non squared M(H) loop [3].

In the example of Figure III- 7 the SQ is calculated at 0.93, which is a good value. This shows that all rods reverse at the fairly same value of demagnetizing field.

III.5.2 M(H) loop shape dependence on the nanorods polydispersity

In order to get a more complete idea about the shape and population polydispersity effect on the assemblies' magnetic properties, smooth nanorods (NRs), NRs with cone endings (tips), rough NRs and NRs combined with large population of tetrapods were aligned (Figure III- 8). As seen on the SEM images, the smooth rods, the rods with tips and the rough rods show good alignment with respect to each other (Figure III- 8 a, b, c). However, this is not the case for the sample (d) where the existence of tetrapods prevents from obtaining a full parallel alignment and introduces orientation disorder (Figure III- 8 d).

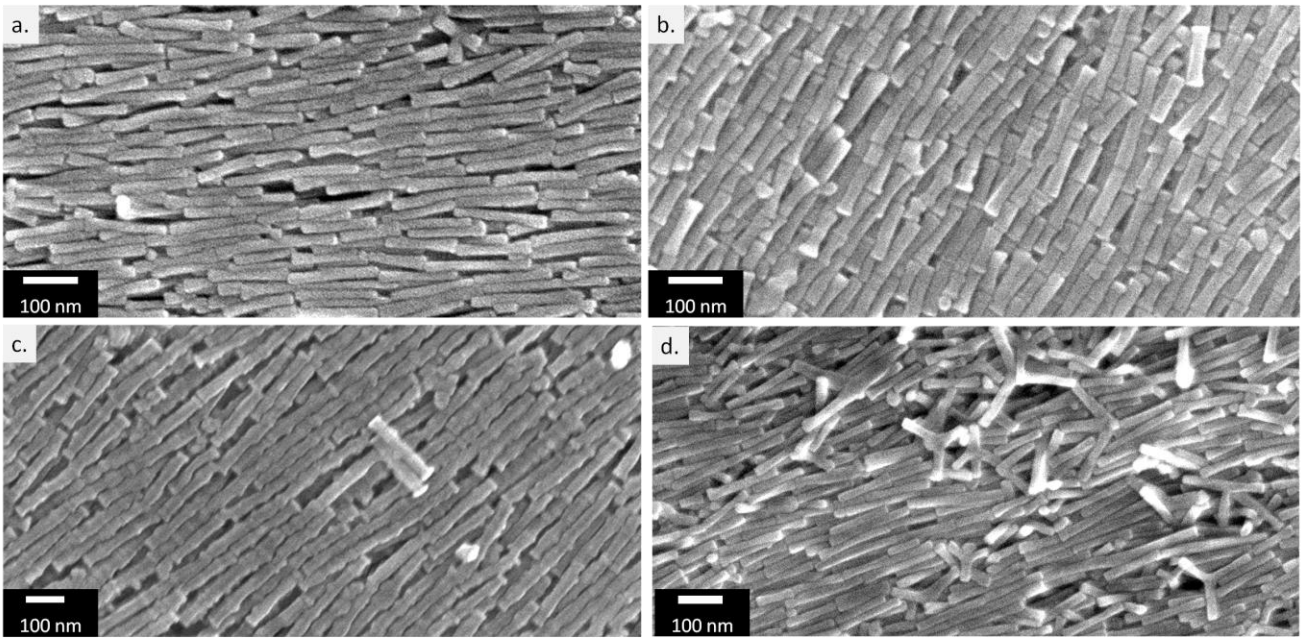

Figure III- 8 *SEM images of aligned magnetic needles from* ***a.*** *smooth NRs (d_m=22±1.5 nm; l_m=166±30 nm);* ***b.*** *NRs with coned endings (d_m=17±2 nm; l_m=123±30 nm);* ***c.*** *rough NRs (d_m=26±4 nm; l_m=102±25 nm) and* ***d.*** *NRs with tetrapods (d_m=24±4 nm; l_m=192±95 nm).*

The M(H) loops of the above samples are presented in the Figure III- 9 and summarized in the Table III- 1.

All M_r/M_s values are above 0.93 which is characteristic of good alignments. However, the comparison of SQ values shows a broader variation from 0.96 to 0.74. Therefore, SQ is a better criterion to compare the quality of a rod alignment along with the magnetization reversal.
In the case of smooth rods the SQ is very high (0.96), meaning that very few defects exist in the assembly. The magnetization reversal occurs at the same field for all rods. The opposite case is observed in the assembly of the polydisperse population sample, where the SQ equals to 0.74. This low value is due to the existence of tetrapods, which first do not present any preferential orientation and secondly act as nucleating points for the reversal of the neighboring nanorods, at lower field than their coercive.

Even if the rods with tips at their endings and the rods with rough surface seemed well aligned on the SEM images their SQ is not so good (0.86 and 0.80, respectively). This practically means that the switching field distribution of the magnetization reversal broadens when the morphology of the nanorods deviates from the ideal one (i.e. smooth cylinders or ellipsoids). Similar effect on the M(H) shape was observed in micromagnetic simulations performed for cobalt nanorods on similar morphologies [1]. They suggest that in the region where the morphological defects are observed the reversal occurs in a non-

coherent fashion, e.g. “flower-vortex” in the case of tips, acting as demagnetizing forces for the magnetization reversal at lower fields.

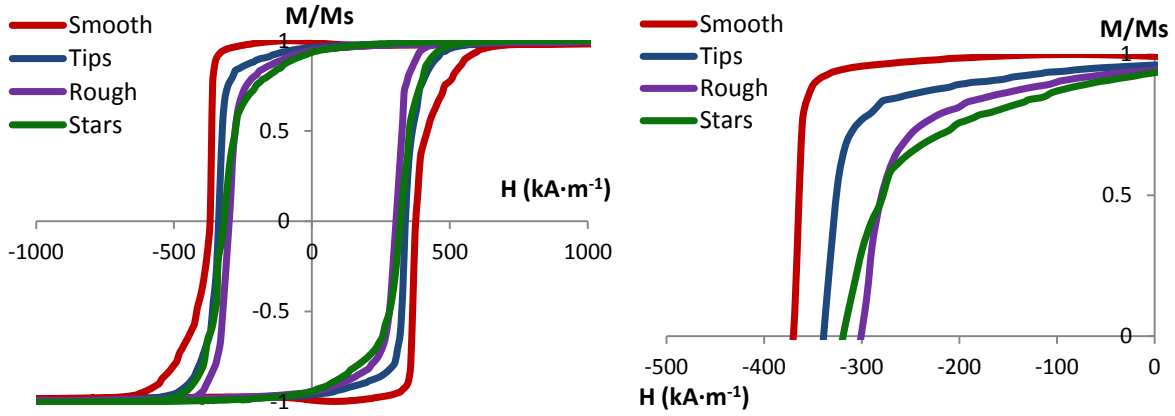

Figure III- 9 *Hysteresis cycle (left) and second quadrant (right) of assemblies comprising of nanorods with different morphologies.*

Poly-dispersity	Morphology	D_m/ L_m nm	SQ	M_r/M_s
Shape	Smooth rods	22/166	0.96	0.99
	Rods with tips	17/123	0.86	0.96
	Rough rods	26/102	0.80	0.97
Population	NRs+Tetrapods	24/192	0.74	0.93

Table III- 1 *Summary of the magnetic properties of assemblies consisting of nanorods with different morphology.*

III.6 Method for B(H) loop extrapolation

In order to plot the B(H) normal loop and calculate the $(BH)_{max}$ from the B×H curve, we had first to determine the magnetic volume fraction, V_M, within the assemblies.
We know that the wafers comprise of nanorods with a Co metal core, cobalt oxide shell around each core and an outer ligand shell, i.e. organic molecules remaining at the rods’ surface and occupying the inter-rod spacing [4]. These organic molecules include the carboxylate ligands, originating from the cobalt precursor, and remaining polyol solvent.

The weight volume fractions of the needles’ components were calculated first, by coupling magnetic and thermogravimetric measurements. The volume fractions of the different components, V_M, V_{CoO} and V_L, were then deduced from these values assuming densities.

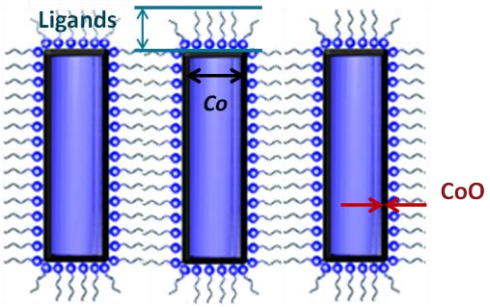

Figure III- 10 Schematic representation of assembled nanorods and their components: Co core, CoO shell and ligands.

III.6.1 Volume fraction assessment

The magnetization of the needles, M_S, was measured by VSM at room temperature on masses larger than 10 mg. Out of this value the magnetic mass fraction could be deduced as follows:

$$\%w(Co)_{metal} = \frac{M_S}{M_{S,Cobalt}} \qquad \text{(Eq. III-2)}$$

with $M_{S,\,Cobalt}$ = 160 emu·g^{-1} the magnetization of bulk cobalt.
For a value M_s= 124.6 emu·g^{-1} (which was measured on rods of d_m= 22 nm and l_m= 166 nm) the weight percentage of the metal cobalt was calculated at 76 %.

The mass fractions of the cobalt oxide shell and ligand outer shell were deduced from thermogravimetric analysis. A sample of mass m_0 was heated in air at 700°C for 2 hours, in order to remove all the organics and to fully oxidize the cobalt core resulting in a mass gain $\Delta m_1>0$. After cooling at room temperature in the thermo-balance, the sample was then heated at 700°C under a mixture of H_2/Ar for 2 hours in order to reduce the cobalt oxide in metal cobalt, resulting in a mass loss $\Delta m_2<0$. The final mass of the sample is m_3 and consists of pure Co metal (Figure III- 11).

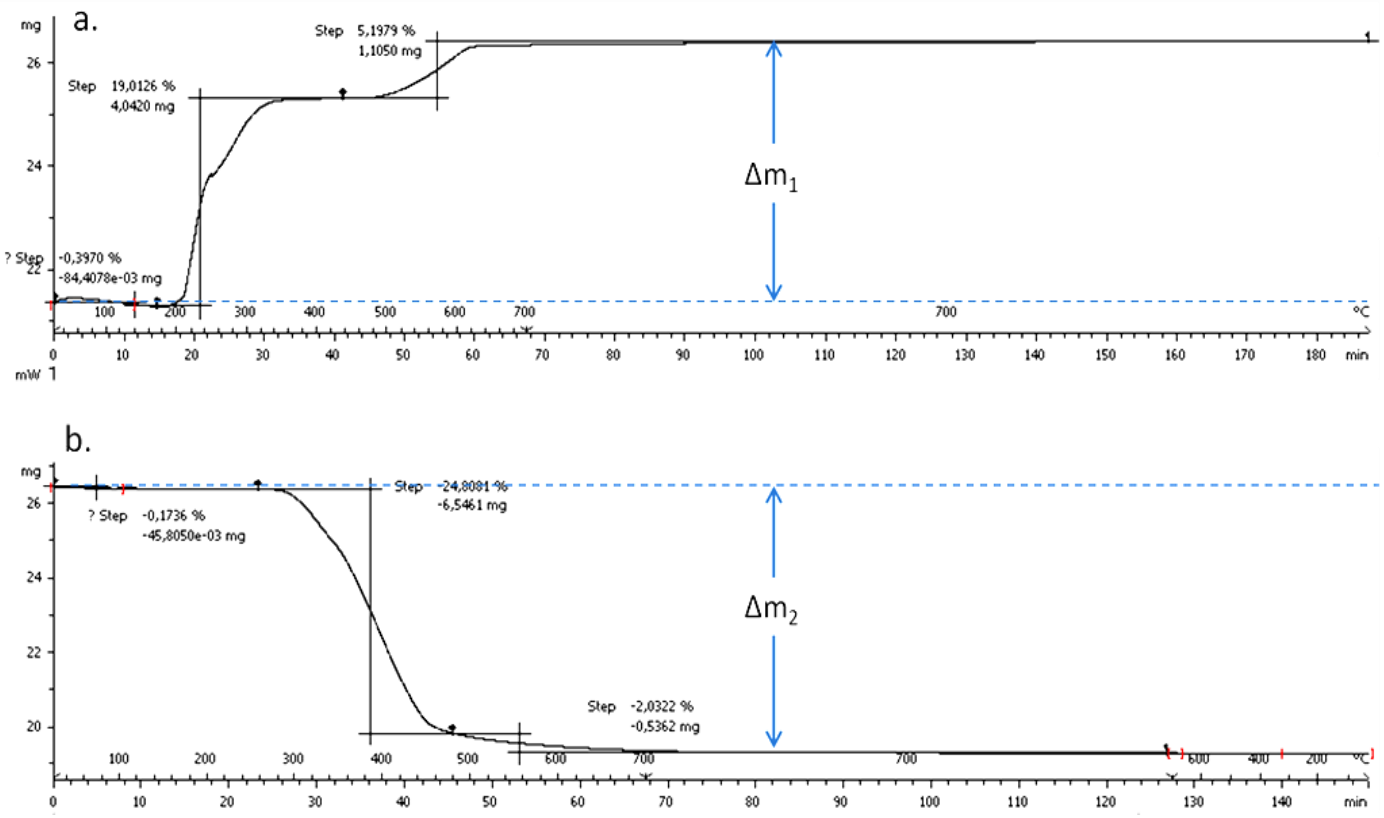

Figure III- 11 *Characteristic TGA result of the magnetic cobalt needles:* ***a.*** *ligands' removal and rods' oxidation;* ***b.*** *reduction of cobalt oxide in metal cobalt.*

The mass fraction of the total Co, *%w(Co_{total})*, i.e. corresponding to the cobalt involved both in the metal core and in the oxide shell, was calculated from Eq. III-3:

$$\%w(Co_{total}) = \frac{m_3}{m_0} = 1 + \frac{\Delta m_1 + \Delta m_2}{m_0} \qquad \text{(Eq. III-3)}$$

This allows deducing the mass fraction of the cobalt involved in the oxide shell:

$$\%w(Co^{II}) = \%w(Co_{total}) - \%w(Co_{metal}) \qquad \text{(Eq. III-4)}$$

Assuming that the cobalt oxide at the surface of the cobalt rods is cobalt monoxide CoO, as previously reported [5], its mass fraction can be calculated from the mass fraction of Co^{II} according to:

$$\%w(CoO) = \%w(Co^{II}) \times \frac{M_{Co} + M_O}{M_{Co}} \qquad \text{(Eq. III-5)}$$

with the molar weight M_{Co}= 58.9 g·mol^{-1} and M_O = 16 g·mol^{-1}. Finally, the mass fraction of the ligands can be obtained by:

$$\%w(L) = 1 - \%w(Co_{metal}) - \%w(CoO) \qquad \text{(Eq. III-6)}$$

The mass fraction of each component in the nanorods' assembly being determined, their volume fraction could be deduced assuming that the density of Co, CoO and ligands are similar to their bulk values, namely ρ_{Co} = 8.9 g·cm^{-3}, ρ_{CoO} =6.4 g·cm^{-3} and ρ_L =0.9 g·cm^{-3}:

$$V_{Co} = \frac{\%w(Co_{metal})/\rho_{Co}}{[\%w(Co_{metal})/\rho_{Co}]+[\%w(CoO)/\rho_{CoO}]+[\%w(L)/\rho_L]} \quad \text{(Eq. III-7)}$$

$$V_{CoO} = \frac{\%w(CoO)/\rho_{CoO}}{[\%w(Co_{metal})/\rho_{Co}]+[\%w(CoO)/\rho_{CoO}]+[\%w(L)/\rho_L]} \quad \text{(Eq. III-8)}$$

$$V_L = \frac{\%w(L)/\rho_L}{[\%w(Co_{metal})/\rho_{Co}]+[\%w(CoO)/\rho_{CoO}]+[\%w(L)/\rho_L]} \quad \text{(Eq. III-9)}$$

In the example presented at the Figure III- 11 the calculated volume fractions were found V_{Co}= 48.7 %, V_{CoO}= 14 % and V_L= 37.3 %. Since the cobalt core is the only component that contributes to the magnetic character of the needle, the magnetic volume fraction is directly V_{Co}=V_M.

The ligand volume fraction of 37.3 % is a result of the rods' washing with the typical protocol (A_{C1}). It is obvious that a decreased V_L leads to higher V_M. A way to achieve that will be presented in section III-7.2.

Finally, considering cylindrical rods with high aspect ratio (i.e. neglecting the tips in the calculations) the thickness of the CoO shell, e, is equal to:

$$e = \frac{d_m}{2} \times \left[1 - \sqrt{\frac{V_{Co}}{V_{Co}+V_{CoO}}}\right] \quad \text{(Eq. III-10)}$$

with d_m the external mean diameter of the rods determined by TEM. For the present example of rods with d_m= 22 nm the CoO shell equals to 1.3 nm, a rather limited thickness in good agreement with previous electron microscope observations on similar cobalt nanorods dried and handled in air [5].

III.6.2 $(BH)_{max}$ calculation

B(H) normal loop can be calculated from the M(H) loop, applying $B=\mu_0(H+M)$. Since M was measured in emu·cm^{-3}, we will convert it in A·m^{-1} units according to:

$$M\ (A\cdot m^{-1}) = \frac{M\ (emu\cdot g^{-1})}{M_S\ (emu\cdot g^{-1})} \times M_{S,bulk}(A\cdot m^{-1}) \times V_M \qquad \text{(Eq. III-11)}$$

where M_{bulk}(cobalt) = 1.42·10^6 A·m^{-1}.

Finally, the product of flux density B and field strength H in the second quadrant, B×H, is plotted versus the flux density and yields a parabola, whose maximum value is the desired energy product, $(BH)_{max}$. As an example, according to the Figure III- 12c, the examined needle can supply a maximum energy of 126.5 kJ·m^{-3}.

The needle's working point (W.P.) is given by the intersection of the B(H) loop and the line passing from the B_d coordinate of the $(BH)_{max}$. In the case presented on Figure III- 12, its position is (-276.8 kA·m^{-1}, 0.457 T).

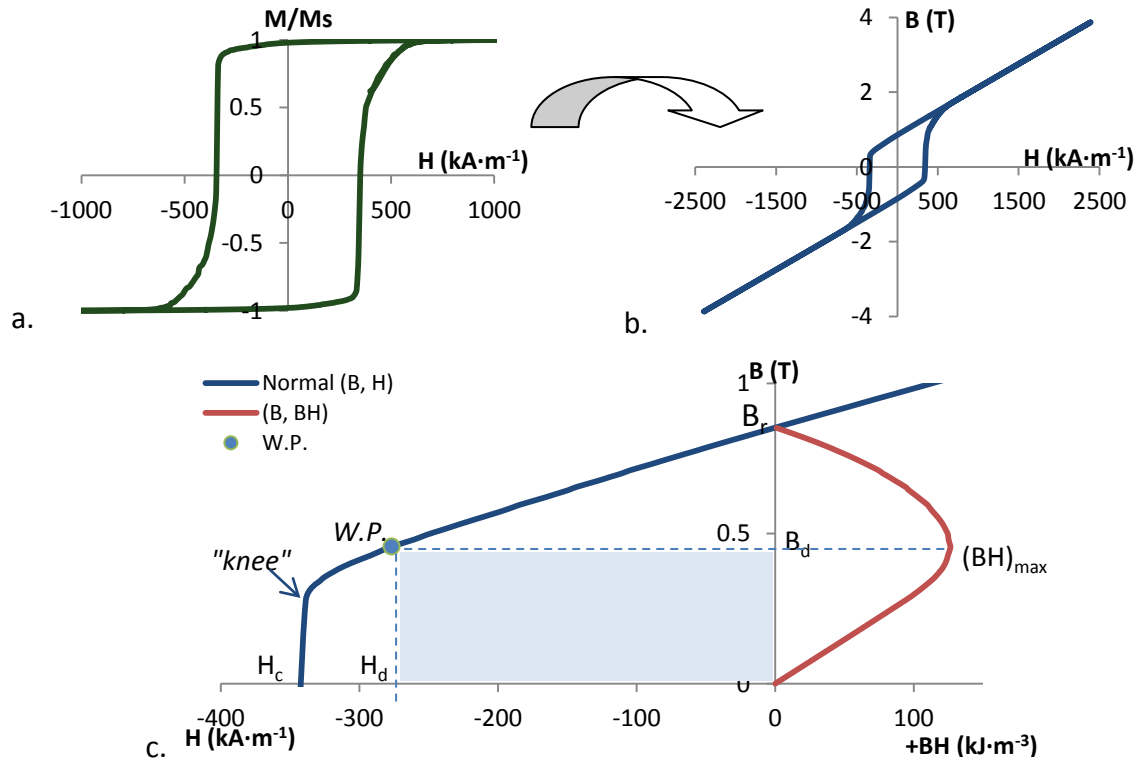

Figure III- 12 a. M(H) loop; **b.** B(H) loop as calculated for a V_M=48.6 %; **c.** second quadrant of the B(H) loop with the energy product and working point.

III.7 Factors that affect the BH_{max}

We have studied the effect of shape/population polydispersity and magnetic volume fraction on the $(BH)_{max}$. We will further detail the role of the washing process (number of cycles, solvent used) in the low and large scale alignments.

III.7.1 Small scale vs Large scale alignment: Importance of washing

The influence of the washing procedure, i.e. in small or large scale, on the V_M, was examined for the same batch of nanorods (d_m= 28 nm, l_m= 190 nm). The low scale sample was washed twice with toluene ($R_{28}A_{T2\text{-}47\ mg}$) while the large scale one was washed four times with toluene ($R_{28}A_{T4\text{-}1g}$). The resulting M(H) and B(H) loops are presented in the Figure III- 13. The volume fractions and magnetic properties are summarized in Table III-2.
Comparing the ligand volume fraction between the two alignments (Table III-2), the small scale sample exhibit a smaller ligand content than the large scale one (25.6% and 35% respectively). Therefore, the 4 washing cycles in the large scale sample is less efficient than the 2 cycles at small scale, due to the lower ratio solvent/powder used. Thus, the number of cycles and the amount of solvent should be adjusted to efficiently remove the ligands.

The SQ of the small scale sample is 0.81, while for the large scale a much lower SQ of 0.57 was obtained. This fact is in agreement with the cracks observed at the large scale wafer surface and can be interpreted by the magnetization reversal occurring at different field for the rods inside the bundle compared to the rods that are surrounding the bundle (see Figure III- 4 b).
Finally, as a result of the low SQ and V_M in the large scale wafer, the $(BH)_{max}$ is calculated at 51 kJ·m^{-3}, half of the $(BH)_{max}$ value from the small scale alignment (106 kJ.m^{-3}).

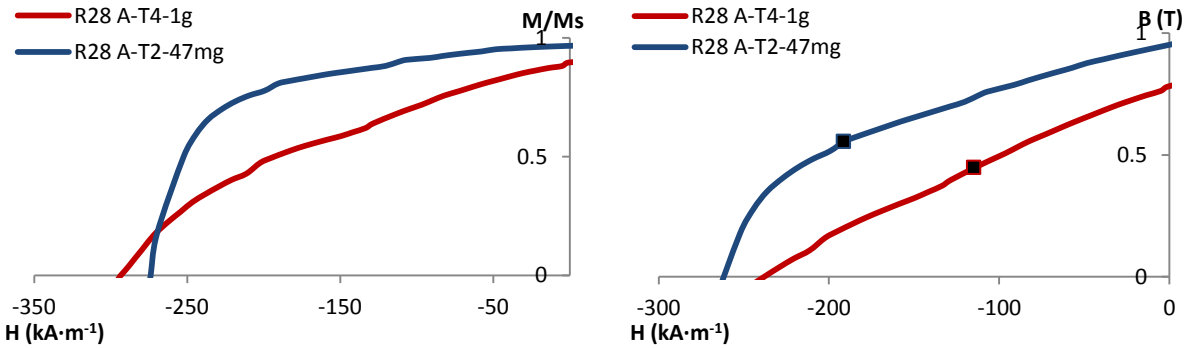

Figure III- 13 *M(H) loop (left) and second quadrant of the corresponding B(H) loops (right) of the assemblies $R_{28}A_{T4\text{-}1g}$ and $R_{28}A_{T2\text{-}47mg}$.*

Sample	V_M %	V_{CoO} %	V_L %	e (CoO) nm	M_r/M_s	SQ	H_{ci} ($kA \cdot m^{-1}$)	B_r (T)	$(BH)_{max}$ ($kJ \cdot m^{-3}$)
$R_{28}A_{T4\text{ - }1g}$ **Large scale**	48.8	15.6	35.6	1.8	0.90	0.57	288	0.78	51
$R_{28}A_{T2\text{ - }47\ mg}$ **Small scale**	55.1	19.3	25.6	1.9	0.96	0.81	276	0.95	106

Table III- 2 *Summary with the washing effect on the chemical and magnetic properties of needles.*

III.7.2 Effect of solvent nature on the BH_{max}: Chloroform vs Toluene

The effect of the washing solvent's nature on the alignment quality and the $(BH)_{max}$ was examined. Efficiency of chloroform and toluene was compared thanks to two different alignments, $R_{22}A_{C1}$ and $R_{22}A_{T1}$, prepared from the same batch of smooth nanorods with mean diameter and length 22 nm and 166 nm. After washing, the rods were redispersed in chloroform suspension and allowed to align in the 1T magnet. The obtained M(H) and B(H) loops with a summary of the chemical and magnetic properties of the obtained assemblies are illustrated at the Figure III- 14 and Table III- 3.

No strong difference on the ligand removal is observed ($V_L \approx$ 37%) resulting in similar values of magnetic volume fraction. The effect of the solvent lays on the alignment quality, where a high degree of misalignment is noted in the case of toluene washing (SQ= 0.79) compared to the chloroform (SQ= 0.93). This is probably due to a partial agglomeration of the rods during their washing, which results in misaligned regions inside the wafer. As a result, the $(BH)_{max}$ in the wafer $R_{22}A_{T1}$ is decreased to 92 $kJ \cdot m^{-3}$ compared to the 126.5 $kJ \cdot m^{-3}$ obtained for chloroform washing (Table III- 3).

Chloroform seems a more appropriate solvent for the rods' washing in order to preserve the stability of the rod suspension. Its efficiency over toluene was also reported by Fang [6] who demonstrated that toluene induced aggregation and precipitation on similar cobalt nanorods.

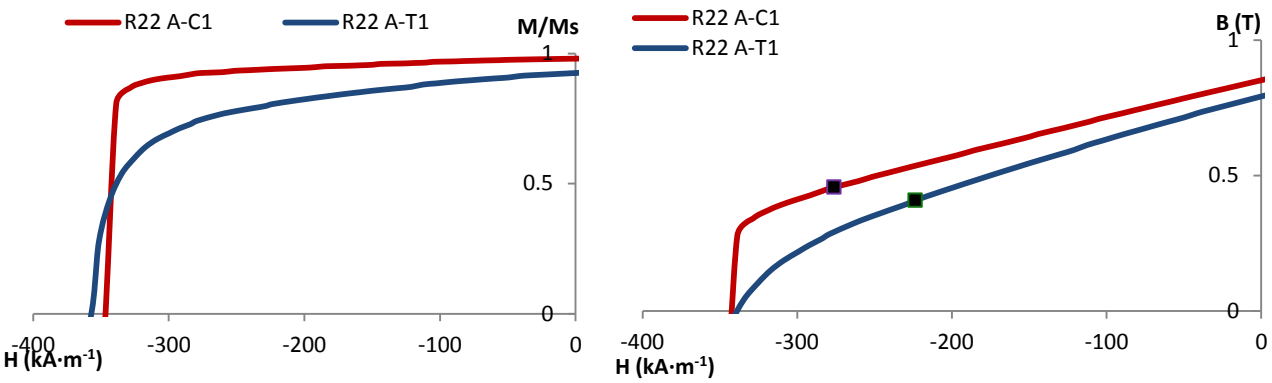

Figure III- 14 *M(H)loop (left) and second quadrant of the corresponding B(H) loops (right) of the assemblies $R_{22}A_{C1}$ and $R_{22}A_{T1}$ comprising of the same nanorods but different alignment process.*

Sample	V_M %	V_{CoO} %	V_L %	e (CoO) nm	M_r/M_s	SQ	H_{ci} (kA·m^{-1})	B_r (T)	$(BH)_{max}$ (kJ·m^{-3})
$R_{22}A_{T1}$	47.9	15.2	36.9	1.4	0.92	0.79	360	0.79	92
$R_{22}A_{C1}$	48.7	14.0	37.3	1.3	0.98	0.93	350	0.85	126.5

Table III- 3 *Summary on the solvent washing effect on the chemical and magnetic properties of needles: toluene ($R_{22}A_{T1}$) and chloroform ($R_{22}A_{C1}$).*

III.7.3 Effect of the V_M on the BH_{max}

While the nature of the washing solvent did matter we also investigate the effect of the number of washing on the ligands removal and thus on the magnetic performance. Starting from the same batch of smooth nanorods (d_m= 22 nm, l_m= 166 nm) 1 or 10 washing with chloroform were performed, $R_{22}A_{C1}$ and $R_{22}A_{C10}$,. The obtained M(H) and B(H) loops with a summary of the chemical and magnetic properties of the densely packed assemblies obtained are illustrated at the Figure III- 15 and Table III- 4.

When the number of chloroform washings is increased from 1 ($R_{22}A_{C1}$) to 10 ($R_{22}A_{C10}$), a strong effect is observed in the V_L which drops from 37.3 % to 33.6 %, thus leading to the increase of V_M (from 48.7% to 54.4 %). In both samples the CoO shell range is around 1.2 nm, a value that is in good agreement with previous electron microscope observations on similar cobalt nanorods [5].

In addition with an increasing V_M, the almost perfect rod alignment of M_r/M_s at 0.99 and the narrow switching field distribution with SQ= 0.96 leads to $(BH)_{max}$= 166.8 kJ·m^{-3}. This is the highest value over all the dense assemblies that we have prepared in this work.

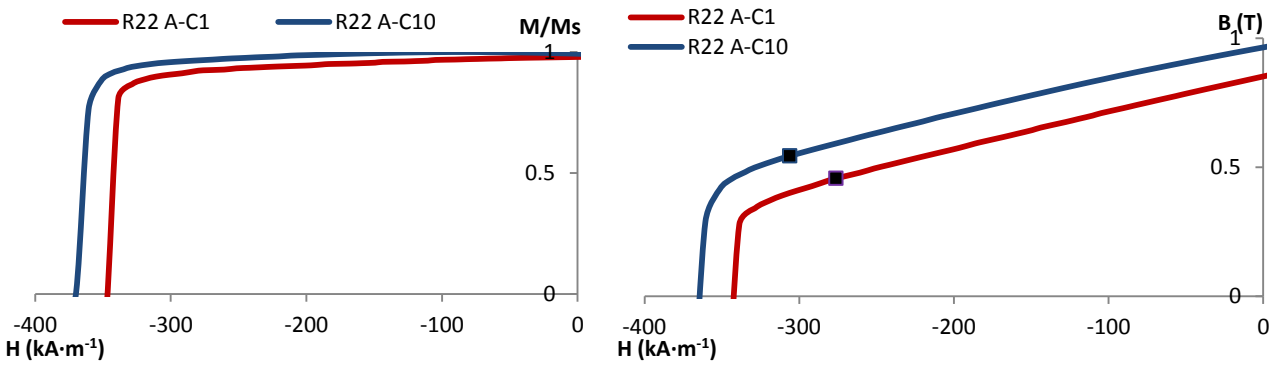

Figure III- 15 *M(H) loop (left) and second quadrant of the corresponding B(H) loops (right) of the assemblies $R_{22}A_{C1}$ and $R_{22}A_{C10}$ comprising of the same nanorods but different alignment process.*

Sample	V_M %	V_{CoO} %	V_L %	e (CoO) nm	M_r/M_s	SQ	H_{ci} (kA·m^{-1})	B_r (T)	$(BH)_{max}$ (kJ·m^{-3})
$R_{22}A_{C1}$	48.7	14.0	37.3	1.3	0.98	0.93	350	0.85	126.5
$R_{22}A_{C10}$	54.4	12.0	33.6	1.1	0.99	0.96	375	0.96	166.8

Table III- 4 *Summary on the washing effect on the chemical and magnetic properties of needles.*

III.7.4 Effect of M(H) loop squareness on BH_{max}

The previous experiments showed the importance of magnetic volume fraction on the $(BH)_{max}$ of an assembly. In the aim to evaluate in what extend the SQ affects the $(BH)_{max}$, we have compared three different samples, not optimized, which presented the same V_M = 48.3%. These samples consist of smooth nanorods with flat endings, rough nanorod and smooth nanorods combined with a small population of tetrapods and were washed in different conditions.

They are noted as $R_{22}A_{C1}$, $R_{28}A_{T4}$ and $R_{24}A_{T4}$, respectively. Due to non-optimized washing or shape distribution, the SQ varied from 0.57 to 0.93, while all wafers presented M_r/M_s higher than 0.90, showing once again that the M_r/M_s is not a good criterion to assess the quality of the alignment.

Different $(BH)_{max}$, were calculated for these three samples. The smooth rods, with the highest SQ (0.93) achieved 125 kJ·m^{-3}, followed by the sample obtained from a population polydispersity (82 kJ·m^{-3}) and finally the rough rods with 51 kJ·m^{-3}.

We can conclude that for a given magnetic volume fraction, the squareness of the M(H) loop is an important criterion to achieve high $(BH)_{max}$. A decrease of SQ of less than 40% lead

to a $(BH)_{max}$ loss of 60%. The quality of the alignment and/or the quality of the rod sample morphology are thus very important to prepare magnets with high performance.

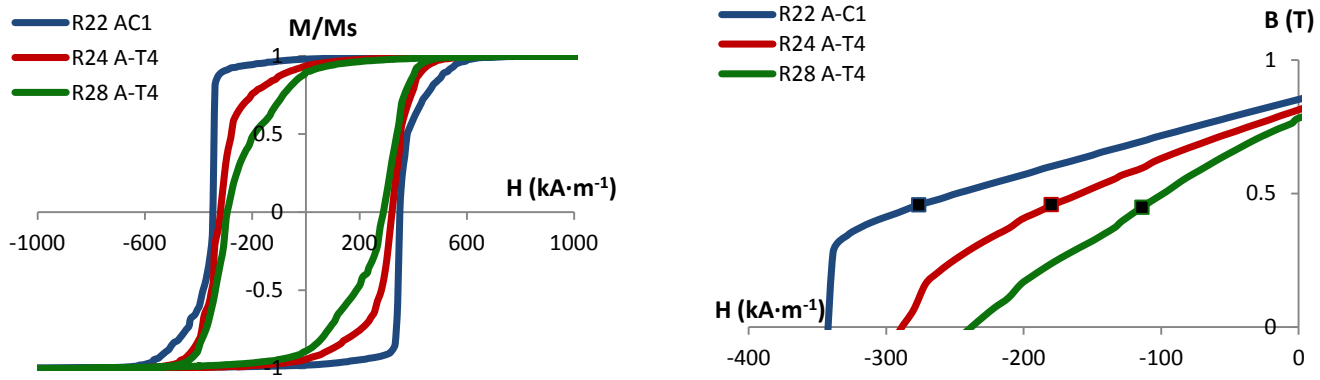

Figure III- 16 *M(H) loop (left) and second quadrant of the corresponding B(H) loops (right) of the assemblies $R_{22}A_{C1}$, $R_{24}A_{T4}$ and $R_{28}A_{T4}$ comprising of smooth rods, rods with tetrapods and rough nanorods, respectively.*

Sample		D_m/L_m (nm)	V_M %	V_{CoO} %	V_L %	e (nm)	SQ	M_r/M_s	H_{ci} (kA/m)	B_r (T)	$(BH)_{max}$ (kJ/m^3)
Smooth NR	$R_{22}A_{C1}$	22/166	48.7	14.0	37.3	1.3	0.93	0.98	350	0.85	125
Tetrapods+NR	$R_{24}A_{T4}$	24/190	48.7	11.0	40.3	1.2	0.74	0.92	320	0.80	82
Rough NR	$R_{28}A_{T4\,;\,1\,g}$	28/190	48.8	15.6	35.6	1.8	0.57	0.90	288	0.78	51

Table III- 5 *Summary on the chemical and magnetic properties of the assemblies $R_{22}A_{C1}$, $R_{24}A_{T4}$ and $R_{28}A_{T4}$ that exhibits the same magnetic volume fraction but different squareness of the M(H) loop*

III.7.5 Summary on BH_{max}

We demonstrated that it is possible to align cobalt nanorods and obtain a robust and dense macroscopic permanent magnet. Several remarks can be drawn from the parametric study we performed:

1. Nanorods with flat endings result in the highest SQ in comparison with other rods with morphological defects (tips at their edges, existence of tetrapods and surface roughness).
2. When a large amount of nanorods is handled (>1 g), a large volume of solvent and/or higher number of washings should be used to yield assemblies without cracks and voids.
3. Chloroform is a more appropriate washing solvent than toluene, since it avoids the rods' precipitation and aggregation.

When high V_M (e.g. 54%) is combined with high M(H) squareness (e.g. 0.96) $(BH)_{max}$ as high as 167 $kJ{\cdot}m^{-3}$ can be obtained.

III. 8 Discussion

III.8.1 Model of B(H) loops

The above results show that the highest $(BH)_{max}$ is obtained for samples that combine high V_M and very large SQ. The energy product of a sample exhibiting a perfectly squared magnetization curve M(H) is:

$$(BH)_{max} = B_R^2/4\mu_0 \quad \text{if} \quad \mu_0 H_{ci} \geq B_R/2 \quad \text{(Eq. III-12)}$$

$$(BH)_{max} = H_{ci}(B_R - \mu_0 H_{ci}) \quad \text{if} \quad \mu_0 H_{ci} < B_R/2 \quad \text{(Eq. III-13)}$$

In order to describe the effect of partial order (SQ < 1) in the rod assembly we consider schematically a linear variation of the magnetization in the second quadrant of the M(H) loop as follows:

$$M = M_R + \alpha H \quad \text{(Eq. III-14)}$$

with α the slope of the M(H) loop at remanence (Figure III- 17). The parameter α can be deduced from the squareness defined above by:

$$\alpha = \frac{2M_R(1-SQ)}{H_{ci}} \quad \text{(Eq. III-15)}$$

α is comprised between 0 and M_R/H_{ci}, α = 0 for a perfect parallel orientation and α > 0 characterizing a degree of disorder in the assembly.

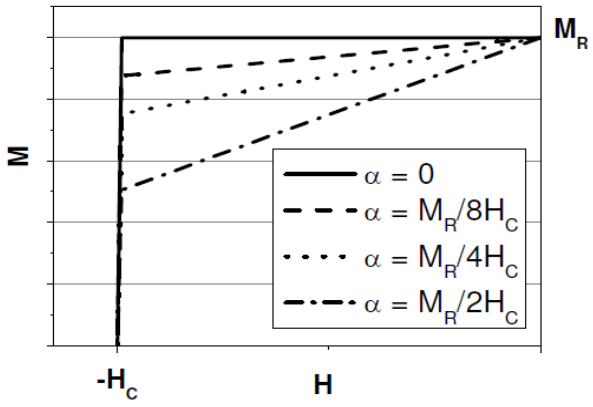

Figure III- 17 *Second quadrant of model M(H) loops with $M = M_R + \alpha H$ for different value of the slope α. The squareness of the four loops is 1, 0.9375, 0.875 and 0.75.*

For such M(H) loops the energy product can be written as:

$$(BH)_{max} = \frac{B_R^2}{4\mu_0(1+a)} \quad \text{if} \quad \mu_0 H_{ci} \geq \frac{B_R}{2(1+a)} \quad \text{(Eq. III-16)}$$

$$(BH)_{max} = H_{ci}[B_R - \mu_0(1+a)H_{ci}] \quad \text{if} \quad \mu_0 H_{ci} < \frac{B_R}{2(1+a)} \quad \text{(Eq. III-17)}$$

For a magnetic volume fraction V_M, in the assembly the remanence is:

$$B_R = V_M \times B_{Cobulk} \quad \text{(Eq. III-18)}$$

with B_{Cobulk} = 1.79 T. So, in the case of coercivity higher than the critical field $\frac{B_R}{2(1+a)}$ the energy product becomes:

$$(BH)_{max} = \frac{B_{Cobulk}^2}{4\mu_0} \times \left[\frac{V_M^2}{(1+a)}\right] \quad \text{(Eq. III-19)}$$

The magnetic field and induction of the working point are respectively:

$$\boldsymbol{H_d = -\frac{B_R}{2\mu_0(1+a)}} \quad \textbf{(Eq. III-20 a) and}$$

$$\boldsymbol{B_d = \frac{B_R}{2}} \quad \textbf{(Eq. III-20 b)}$$

We will now examine if the suggested model applies to the nanorod assemblies previously presented. In order to do so, we first calculate the α value according to Eq. III-15 and then compare the critical field $B_R/2(1+\alpha)$ with the coercivity (Table III- 6).

All of the assemblies exhibit a coercivity higher than the critical field $B_R/2(1+\alpha)$ meaning that the assemblies performance is not limited by the coercivity. In that case the experimental $(BH)_{max}$ has to be compared with the formula of the Eq. III-19 and the position of the working point with the Eq. III-20. For given conditions of V_M, SQ and M_r/M_s the experimental values are very close to those given by our simple model (Table III-6).

	B_R (T)	M_R (kA·m^{-1})	$\mu_0 H_{ci}$ (T)	V_M %	SQ	α	$\frac{B_R}{2(1+a)}$	$(BH)_{max}^{th.}$ (kJ·m^{-3})	$(BH)_{max}^{exp.}$ (kJ·m^{-3})
$R_{22}A_{T1}$	0.79	628	0.452	47.9	0.79	0.73	0.228	84	92
$R_{22}A_{C10}$	0.96	763	0.475	54.4	0.96	0.16	0.413	162	166.8
$R_{22}A_{C1}$	0.85	670	0.439	48.7	0.93	0.27	0.334	119	125
$R_{24}A_{T4}$	0.80	636	0.402	48.7	0.74	1.03	0.197	75	82
$R_{28}A_{T4\ ;\ 1\ g}$	0.78	620	0.362	48.8	0.57	1.85	0.136	53	51
$R_{28}A_{T2\ ;\ 47\ mg}$	0.95	755	0.348	55.1	0.81	1.03	0.234	95	106

Table III- 6 *Calculation of theoretical $(BH)_{max}$ for different nanorod dense assemblies.*

Eq. III-19 predicts that the energy product varies as an inverse function of (1+ α) and as a quadratic function of V_M : $(BH)_{max} \propto V_M^2/(1+\alpha)$. To demonstrate this dependence we plotted the experimental $(BH)_{max}$ versus the $V_M^2/(1+\alpha)$ (Figure III-18). The slope of the linear fit is 670 kJ·m^{-3}, very close to $\frac{B_{Cobulk}^2}{4\mu_0}$= 638 kJ·m^{-3} as expected from Eq. III-19, showing that our simple model applies quite well.

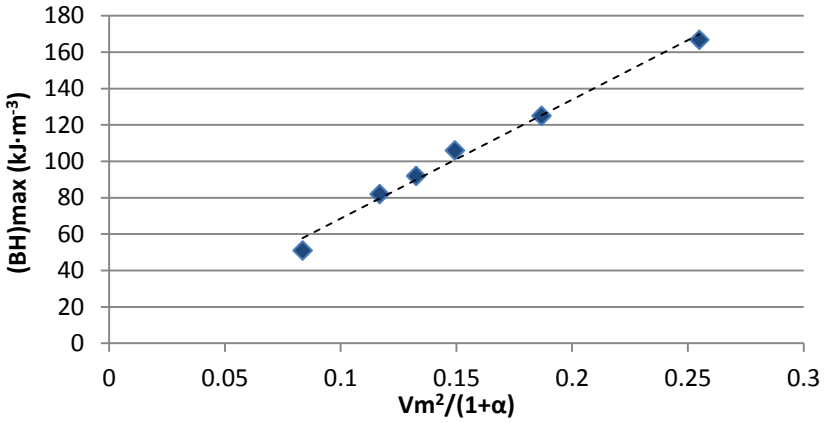

Figure III- 18 *Experimental energy product vs $V_M^2/(1+\alpha)$ with V_M the magnetic volume fraction and α the slope of the model M(H) curve at remanence (dashed line: linear fit).*

III.8.2 Defining the V_M limits where BH_{max} is coercivity limited

In our model we defined the critical field where the $(BH)_{max}$ value depends on the H_{ci} according to:

$$(BH)_{max} = \frac{B_R^2}{4\mu_0(1+a)} \quad \text{if} \quad \mu_0 H_{ci} \geq \frac{B_R}{2(1+a)} \qquad \text{(Eq. III-16)}$$

$$(BH)_{max} = H_{ci}[B_R - \mu_0(1+a)H_{ci}] \quad \text{if} \quad \mu_0 H_{ci} < \frac{B_R}{2(1+a)} \qquad \text{(Eq. III-17)}$$

The critical value $\frac{B_R}{2(1+a)}$ depends on two parameters: the squareness (which affects α) and V_M (which affects B_R). In order to examine the behavior of the working point under varying SQ and V_M we selected two nanorod dense assemblies, $R_{22}A_{T4}$ and $R_{22}A_{C10}$, from the same batch of rods (d_m= 22 nm, l_m= 166 nm) and with different SQ at 0.83 and 0.96, respectively (Figure III- 19 and Table III- 7). Additional M(H) and B(H) loops were plotted from the experimental ones (Figure III- 19) for increasing and decreasing magnetic volume fractions in the range of 10 – 90 %. The simulated B(H) loops are presented on Figure III- 20, and the corresponding $(BH)_{max}$ are plotted in Figure III- 21.

We considered that the H_C was independent from the volume fraction and equal to the one measured experimentally (Table III- 7). Even though we know from Chapter I that the H_c decreases when V_M increases, our assumption of keeping H_C constant will not change the tendency.

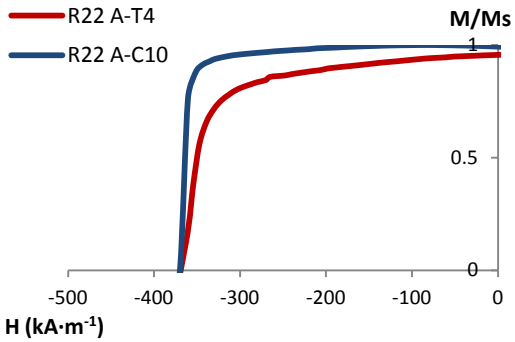

Figure III- 19 *Second quadrant of the M(H) loops of the nanorod assemblies $R_{22}A_{T4}$ and $R_{22}A_{C1}$.*

	d/l (nm)	SQ	M_r/M_s	H_{ci} (kA·m^{-1})
$R_{22}A_{T4}$	22/166	0.83	0.96	355
$R_{22}A_{C10}$	22/166	0.96	0.99	375

Table III- 7 *Characteristics of the cobalt nanorod assemblies $R_{22}A_{T4}$ and $R_{22}A_{C1}$.*

For the assembly $R_{22}A_{T4}$ (SQ= 0.83) the $(BH)_{max}$ variation with V_M can be separated in two regions:

1. 0 % ≤ V_M ≤ 49 %: the $(BH)_{max}$ presents a quadratic growth with the V_M according to the equation III-16 (Figure III-21). The working point's position shifts gradually towards the "knee" according to the equation III-20 (Figure III-20). In this V_M range the $(BH)_{max}$ is not limited by the H_{ci}.
2. 49 % < V_M ≤ 90 %: the $(BH)_{max}$ increases linearly with the V_M and is limited by the H_{ci} of the assembly (Figure III-21). The distance of the working point from the "knee" is constant and its position depends only on the remanent induction increase.
3. The position of the working point is also affected by the V_M, since for values below 49 % it follows the Eq. III-20 b where $B_d = \frac{B_R}{2}$, while above that limit $B_d > \frac{B_R}{2}$. As an example for V_M= 20 % the B_R= 0.34 T and B_d= 0.17 T, thus the factor 0.5 is well observed, while for V_M= 90 % the B_R= 1.54 T and B_d= 0.96 T>0.5B_R.The same behavior is observed in the assembly $R_{22}A_{C10}$ (SQ= 0.96) but the $(BH)_{max}$ is limited by the H_{ci} only for V_M above 66 % (Figure III-20 and 21).

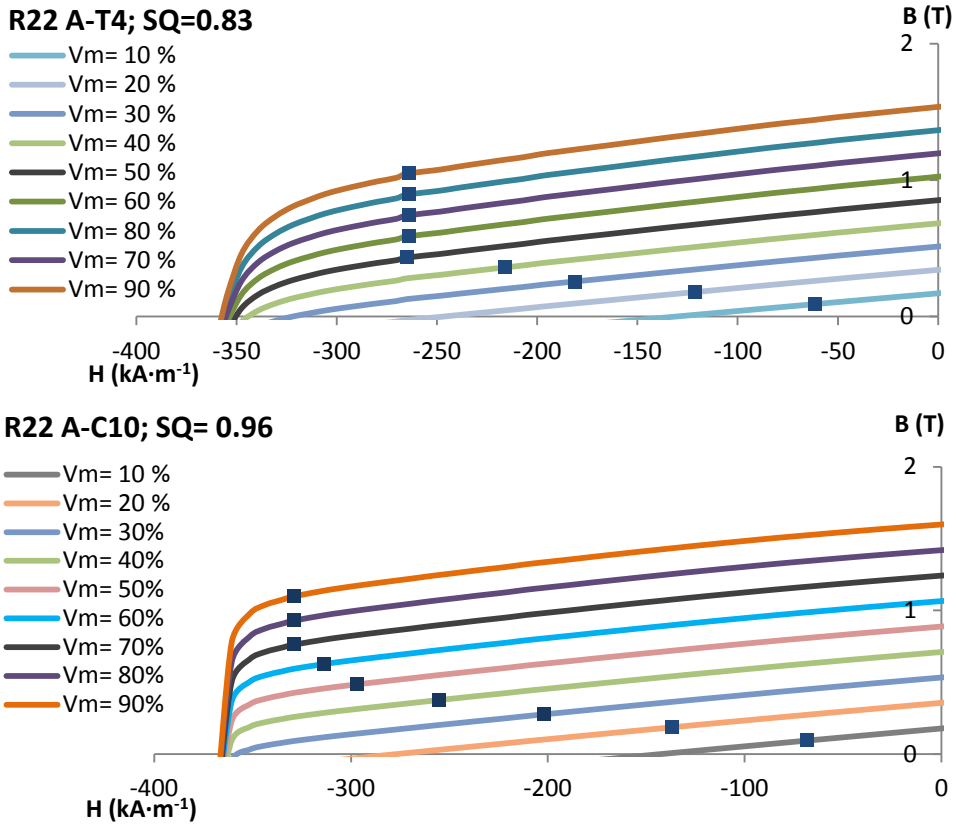

Figure III- 20 *B(H) loops of the assemblies $R_{22}A_{T4}$ and $R_{22}A_{C1}$ with SQ= 0.83 and 0.96 correspondingly simulated for 10 % ≤ V_M ≤ 90 %.*

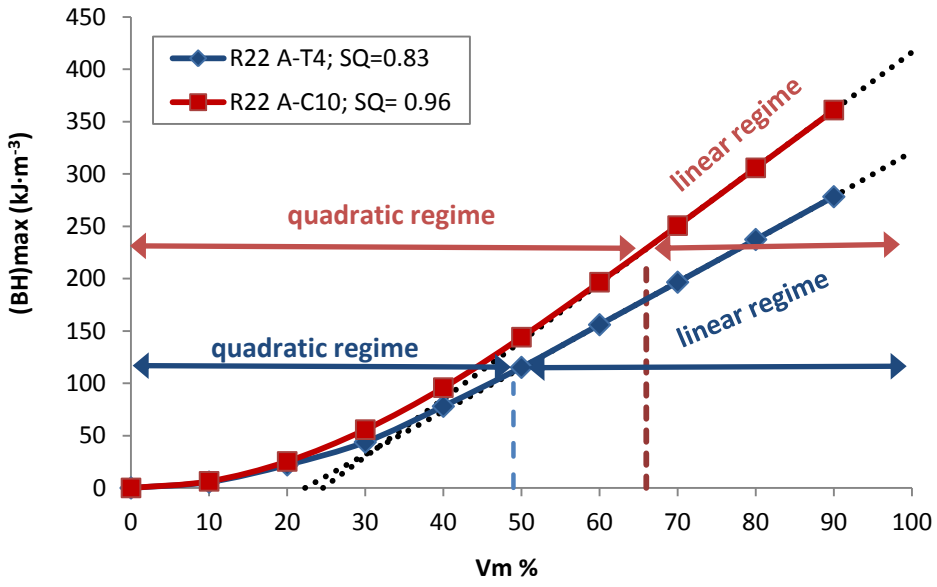

Figure III- 21 *$(BH)_{max}$ dependence on the V_M for the assemblies $R_{22}A_{T4}$ and $R_{22}A_{C1}$ with SQ 0.83 and 0.96, respectively.*

This simulation shows that:

1. If we want to increase V_M while remaining in the quadratic regime, the H_{ci} has to be increased accordingly; and

2. Co nanorod assemblies with high SQ present a higher capacity for $(BH)_{max}$ increase compared to those of similar H_{ci} but lower SQ.

III.8.3 $(BH)_{max}$ and "knee" dependence on H_{ci}

In order to examine the effect of increasing the coercivity on the shape of the B(H) loop, an assembly, $R_{22}A_{C1}$, comprising of cylindrical nanorods (D_m= 22 nm, L_m= 166 nm) with H_{ci} = 350 kA·m^{-1}(or $\mu_0 H_{ci}$ = 0.44 T), SQ= 0.93, M_r/M_s= 0.98 and V_M=48 %, was chosen for simulations. Taking as reference the experimental M(H) and B(H) loops (green loops in Figure III- 22), we simulated additional ones considering the following coercivities: 430, 509 and 588 kA·m^{-1} (or $\mu_0 H_{ci}$ = 0.54, 0.64 and 0.74 T) (Figure III- 22). The resulting $(BH)_{max}$ values are reported in the Table III- 8.

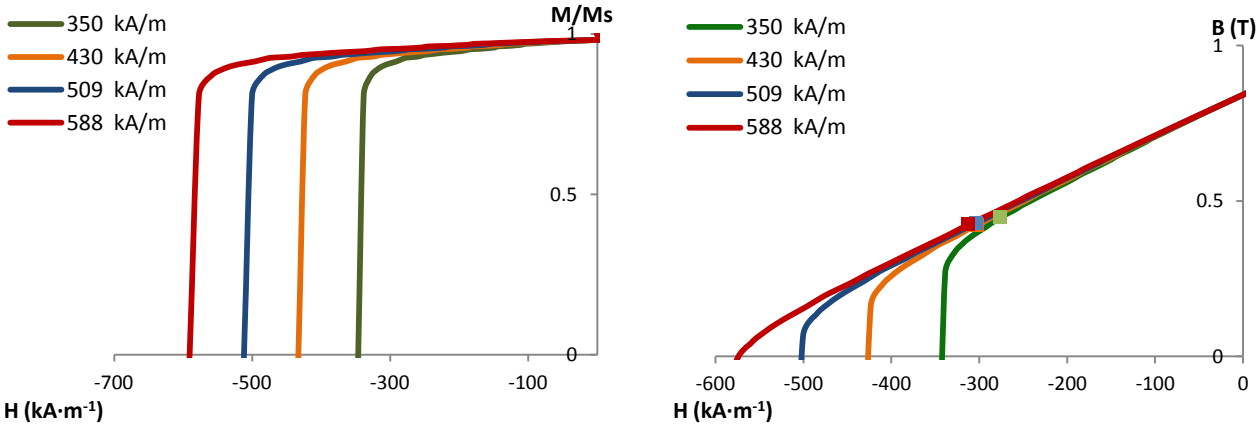

***Figure III- 22 S**imulation of M(H) and B(H) loops of assemblies consisting of the same cylindrical nanorods with a volume fraction of 48 % with H_{ci} equal to 350, 430, 509, 588 kA·m^{-1}.*

$\mu_0 H_{ci}$ (T)	H_{ci} (kA·m^{-1})	$(BH)_{max}$ (kJ·m^{-3})
0.44	350	124
0.54	430	128
0.64	509	130
0.74	588	132

***Table III- 8** Magnetic properties of the same cylindrical nanorods simulated with different.*

There is no effect of the H_{ci} on the $(BH)_{max}$ for the selected conditions: for an increase of 240 $kA \cdot m^{-1}$ (increase of $\mu_0 H_{ci}$ of 0.3 T) the $(BH)_{max}$ raises only by 6 %. Indeed in that case the (BH)max was never limited by the H_{ci} due to a fairly low VM (48%)

In that case, the H_{ci} only affects the working point position and the B(H) loop shape. Since the working point depends only on the B_R, i.e. V_M, its position remained stable in all cases and equal to 0.84 T. But the higher the H_{ci} gets the more the "knee" fades away from the working point. Thus, for coercivity as high as 0.74 T the assembly becomes more stable towards demagnetizing forces.

In order to examine the advantages of high H_{ci} on the magnetic properties of a nanorod assembly, we simulated the above examples of rods with $\mu_0 H_{ci}$ 0.44 T and 0.74 T for V_M between 10 – 90 % (Figure III- 23, Figure III- 24). In these cases, H_{ci} limitations are expected.

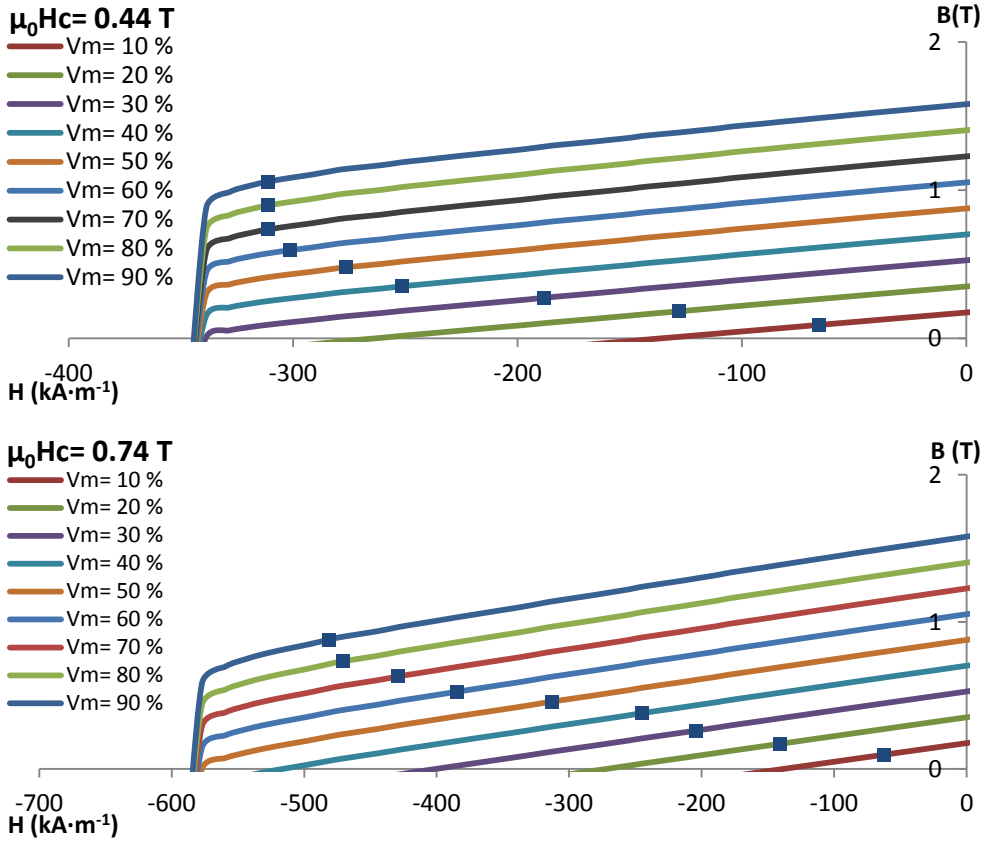

Figure III- 23 *B(H) loops of the rod assemblies with $\mu_0 H_{ci}$ 0.44 T and 0.74 T simulated for 10 % ≤ V_M ≤ 90 %.*

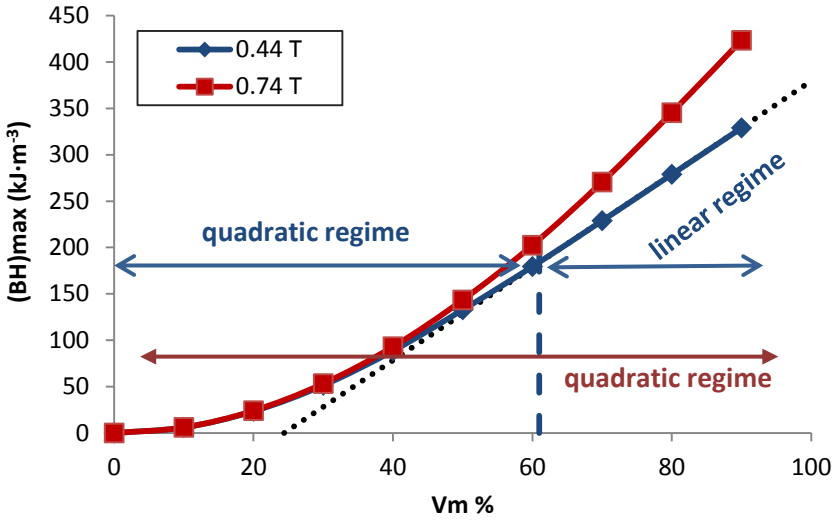

Figure III- 24 *$(BH)_{max}$ dependence on the V_M for assemblies with $\mu_0 H_{ci}$ 0.44 T and 0.74 T simulated for 10 % ≤ V_M ≤ 90 %.*

For the assembly with $\mu_0 H_{ci}$= 0.74 T the energy product increases for all volume fractions quadratically, meaning that it is not H_{ci} limited. On the opposite case of lower $\mu_0 H_{ci}$ (0.44 T) the behavior of the energy product is limited by the coercivity for V_M > 61 %.

The above simulations suggest that nanorods of high H_{ci} have to be used in order to benefit from the increased V_M. Another advantage emerging from the use of rods with high H_{ci} is the fact that the "knee" appears at higher packing fractions compared to rods with lower H_{ci}.

III.9 $(BH)_{max}$ dependence on oxidation and inter-rod distance

The best assembly described in the present thesis exhibited a squareness SQ = 0.96 and M_r/M_s = 0.99, showing that there is quasi no more room to improve the alignment quality. A series of simulations presenting possible ways for the $(BH)_{max}$ improvement are going to be discussed.

We demonstrated experimentally that in order to increase the magnetic volume fraction several washings have to be performed to decrease V_L. Another possible way to achieve a high magnetic volume fraction is to avoid the rods' oxidation or to use shorter carboxylate ligands. Considering a perfectly aligned hexagonal array of nanorods (Figure III- 25a) with mean diameter, d_m, separated from each other by a distance L (center-to-center rod distance D= d_m+L), which corresponds to the ligand shell, and exhibiting a CoO shell of thickness, e, the V_M equals to:

$$V_M = \frac{\pi(d_{TEM}-2e)^2}{4D^2 \sin 60^\circ} \qquad \text{(Eq. III-21)}$$

According to that equation we simulated the V_M evolution for nanorods with diameter in the range of 7-35 nm and we considered the following cases: rods with e= 1.2 nm and ligand shell L= 3.5 nm (blue line); b. rods with e= 0 nm and L= 3.5 nm (red line) and c. rods with e= 0 nm and L= 2 nm (green line) (Figure III- 25b).

For diameters in the range of 10-20 nm the oxidation decreases dramatically V_M (blue line, Figure III- 25b). High magnetic volume fractions of 60 % and 65 % are expected for non-oxidized rods of diameter 15 and 20 nm, respectively, while only 42 % and 51 % is expected for the oxidized ones. A significant increase of V_M could also be reached by lowering the organic amount. With non-oxidized rods separated by a ligand shell of only 2 nm, V_M could reach 70 % and 75 % for 15 and 20 nm rods, respectively.

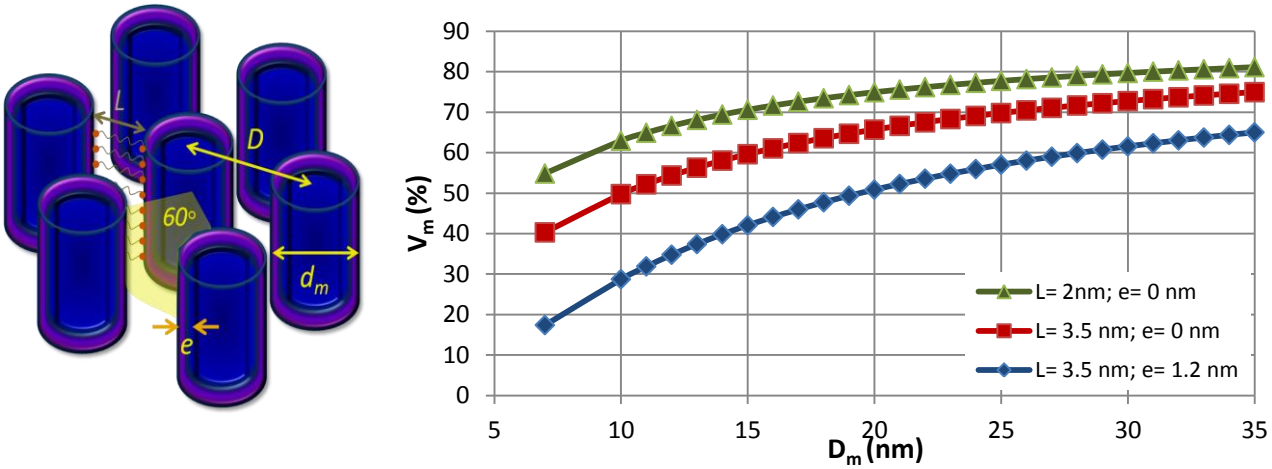

Figure III- 25 a. *Model of perfectly aligned hexagonal array of cobalt nanorods separated from a distance L by ligands, with mean diameter d, CoO shell, e, and center-to-center distance D;* ***b.*** *Magnetic volume fraction in relation to D_m for rods separated by a ligand shell of 3.5 nm with: e= 1.2 nm (blue line) and e= 0 nm (red line) and ligand shell of 2 nm with e= 0 nm (green line).*

The effect of oxidation and inter-rod spacing on the energy product is even more important on the $(BH)_{max}$ since it varies as the square of the magnetic volume fraction (if the coercivity is high enough according to the eq. III-16). According to the Eq. III-16 a V_M in the range 60 % – 75 % could lead to $(BH)_{max}$ values from 230 to 360 kJ·m^{-3}, providing a perfectly squared hysteresis loop and from 180 to 280 kJ·m^{-3} for a more realistic squareness of 0.93 (α = 0.27). Such energy product would require $\mu_0 H_{Ci}$ higher than $B_R/2$, i.e. above 0.54 T or 0.67 T for a magnetic volume fraction of 60 % or 75 %, respectively.

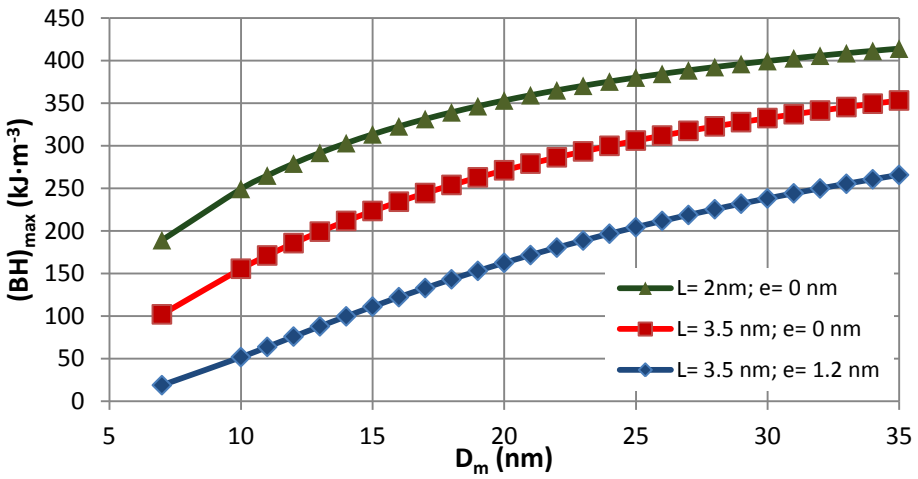

Figure III- 26 *Energy product of perfectly aligned hexagonal arrays of cobalt nanorods of mean diameter d, separated by a ligand shell of 3.5 nm and e= 1.2 nm (blue line); e= 0 nm (red line) and ligand shell 2 nm with e= 0 nm (green line).*

III.10 Coercivity of cobalt nanorod assemblies

In the section III.8.3 we demonstrated the importance of obtaining the highest H_{ci} possible in order to make possible a $(BH)_{max}$ increase concomitantly to a V_M increase. In this section we will describe the results on the coercivity of our cobalt nanorods.

Different factors influence the H_{ci} of a nanorod assembly:

- The intrinsic property of the nanorods, diameter and aspect ratio, shape of the tips , population polydispersity;
- The quality of the alignment;
- The dipolar interactions related to the magnetic volume fraction.

We will present first the influence of the dilution by a comparison between nanorods diluted in a polymer or in a dense assembly. Then, we will compare the coercivities of dense assemblies prepared with nanorods of various mean diameter and aspect ratio, and finally of monodisperse and polydisperse samples.

III.10.1 Experimental procedure : Dispersion in PVP

For the preparation of a nanorod solution in a polymer matrix, $4.7 \cdot 10^{-3}$ g of cobalt nanorods were washed twice with ethanol, once with chloroform and redispersed in chloroform. 1 g of polyvinylpyrrolidone (PVP) was dissolved in chloroform, sonicated for 3 min and mixed with the nanorods. A well dispersed solution containing $4.7 \cdot 10^{-3}$ wt. % of cobalt rods was

ready for alignment after 20 min of sonication. If randomly oriented rods in PVP matrix were desired, the mixture was heated with a gun so the chloroform evaporated and a grey foam was obtained. The foam was then grinded into powder and encapsulated in the VSM capsule for additional measurements. The powder was easily redispersed in chloroform and was used for alignment purposes. The nanorods with PVP remained well dispersed in chloroform and did not precipitate for several minutes after their sonication.

III.10.2 Influence of dilution in H_c

We performed magnetic measurements on randomly oriented and aligned rods (d_m=17.5 nm and l_m=120 nm) diluted in PVP. The diluted alignment resulted in a robust semi-transparent film were black regions could be detected parallel to the applied field (Figure III-27 a, b).
For comparison reasons, an additional dense alignment without PVP of the same rods was performed at small scale. This dense alignment exhibited the typical shiny structure with V_M calculated at 41 %.

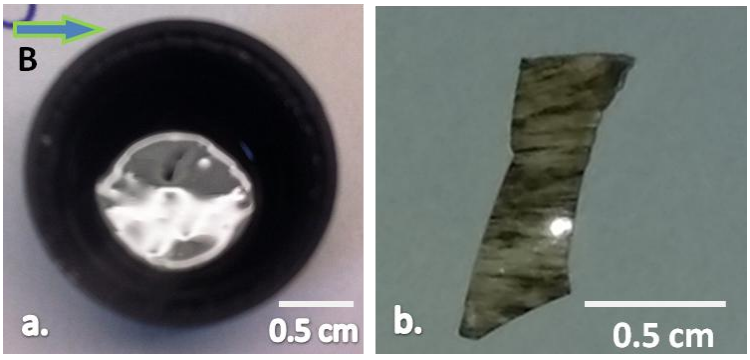

Figure III- 27 a. *Low scale alignment in PVP matrix;* ***b.*** *Film of parallel arrays of cobalt nanorods (V_{rods}= 0.1 %) embedded in PVP.*

The M(H) loops of the diluted rods in PVP with randomly distributed or aligned easy axis directons are presented in the Figure III- 28 and compared with dense assemblies. Depending on the rods' orientation and on the alignment medium, their magnetic properties differ as summarized in Table III- 9.

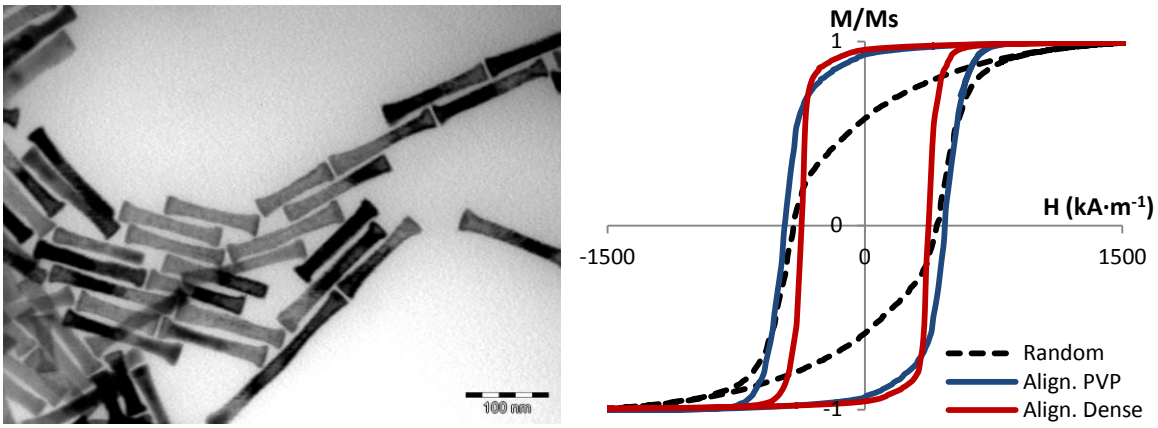

Figure III- 28 *TEM image of nanorods with d_m=17.5 nm and l_m=120 nm (left); and M(H) loops of the same rods randomly oriented and aligned densely and diluted (PVP and tetracosane) assemblies.*

NR Arrangement	M_r/M_s	SQ	H_c (kA·m^{-1})
Random PVP	0.57	--	416
Diluted Alignment PVP	0.93	0.73	466
Dense Alignment	0.96	0.85	370

Table III- 9 *Magnetic measurements of nanorods randomly oriented and aligned in dense and diluted assemblies.*

For randomly oriented rods in PVP, one gets an isotropic material with a random distribution of anisotropy axes, M_r/M_s is close to 0.5 (0.57 in the present case). The H_{ci} equals to 416 kA·m^{-1}. The assembly's magnetic properties improve for the diluted alignment in PVP where the M_r/M_s and H_c increase to 0.93 and 466 kA·m^{-1}. These results are in agreement with the simulations of a similar nanorod assembly presented in the Chapter I (section I.3.2 a).

Dense assembly yields the highest M_r/M_s and SQ as a result of easier nanorod alignment due to the absence of PVP. Nevertheless, it is noticeable that the H_{ci} of the densely packed aligned rods, 370 kA·m^{-1}, is lower than that of the diluted aligned sample (466 kA·m^{-1}). The coercivity decreases by more than 20%. This difference may be attributed to stronger dipolar interactions in the dense assembly. On the Figure III-29 is recalled the variation of coercivity in regular arrays of cobalt nanorods calculated by Toson et. al. [7]. These calculations predicted the decrease of coercivity with increasing packing fraction. Nevertheless, the relative decreasing of Hc between p=0 (isolated rod) and p=0.4 is only of 10% (Figure III-29). Panagiotopoulos et al. calculated also the coercivity of cobalt nanorods assemblies with different packing fraction [8]. In this case a similar coercivity loss of about 10% was also predicted between p = 0 and p = 0.4. If we consider the aligned diluted sample in PVP as a sample with p = 0 (which is probably not the case, because of the bundles), our experimental coercivity loss is two times larger than the predicted loss.

The comprehension of such a difference between our experience and the modeling would require a more detailed study, and will be performed in a near future.

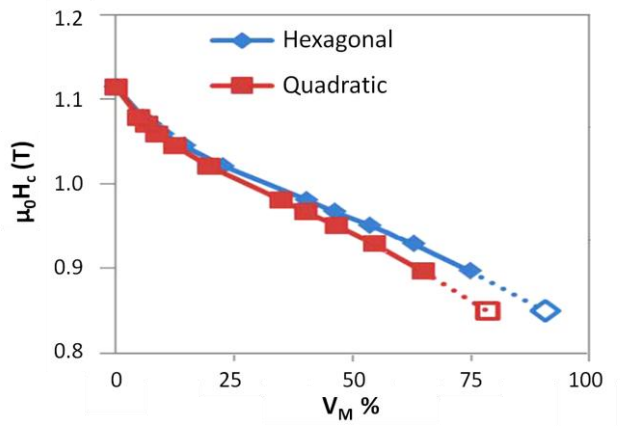

Figure III-29 *Coercivities over the packing densities of regularly aligned (hexagonal: blue diamonds, quadratic: red squares) nanorods (D_m= 10 nm and L_m= 100 nm)* [7].

III.10.3 Coercivity dependence on nanorod dimensions for dense alignments

The next question that rises is which nanorod dimensions provide the higher H_{ci}. That problem was already examined through micromagnetic simulations in single rods by Ott *et al.* [9] (see Chapter I.3.1), who showed that H_{ci} increases when the mean diameter decreases. In order to validate this conclusion for a dense assembly of cobalt rods, we selected small scale assemblies comprising of smooth rods with mean diameter in the range of 10 – 29 nm. Their washing process was performed under similar conditions so that the assemblies' magnetic volume fraction varied in the range between 40-50%.

On the figure III-30 is plotted the coercivity of the assemblies as a function of the rod mean diameter (the mean aspect ratio and the remanence to saturation ratio are also given for each sample). The thinner the rods, the higher the H_{ci} gets. Also for assemblies with the same rod mean diameter the highest H_{ci} belongs to the rods with the highest mean aspect ratio a fact that is due to the enhanced shape anisotropy.

Thus, in the dense assemblies we find again the effect of the mean diameter on the coercivity previously observed on diluted rods. The micromagnetic simulations predict that for diameter in the range 5-30 nm the magnetization reversal occurs in the same fashion independently of the rods' diameter, i.e. nucleation at one of their tips and propagation of a domain wall. The increase of coercivity when the diameter decreases is due to a higher difficulty for the magnetization reversal to nucleate since the volume of the tip becomes smaller.

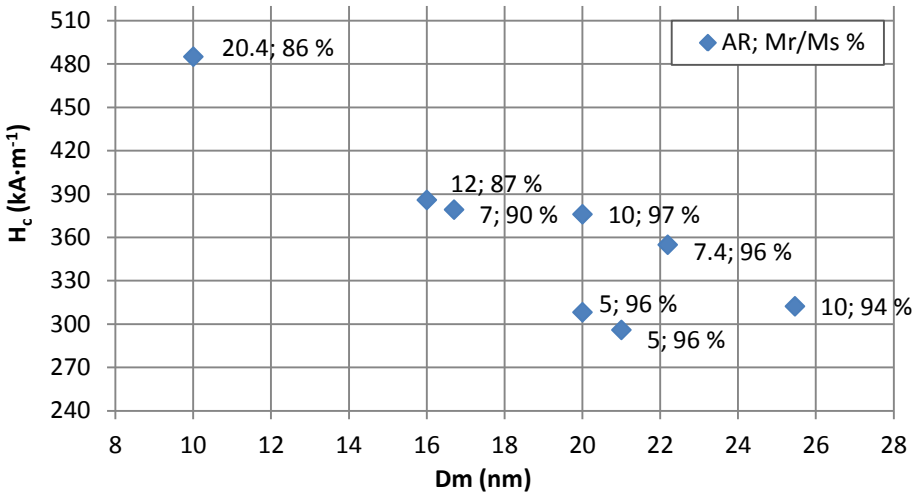

Figure III- 30 *Coercivity of aligned assemblies of densely packed Co smooth nanorods vs. mean diameter D_m ; (aspect ratio, AR, and remanence to saturation ratio, M_R/M_S, are given for each sample).*

III.10.4 H_c dependence on the nanorods' polydispersity

In order to get a more complete idea about the shape and population polydispersity effect on the assemblies' coercivity, nanorods with almost the same mean diameter but comprising different populations were aligned in small scale: a. NRs with smooth surface and flat endings, b. NRs with cone endings (tips) and c. NRs combined with tetrapods (Figure III- 31).

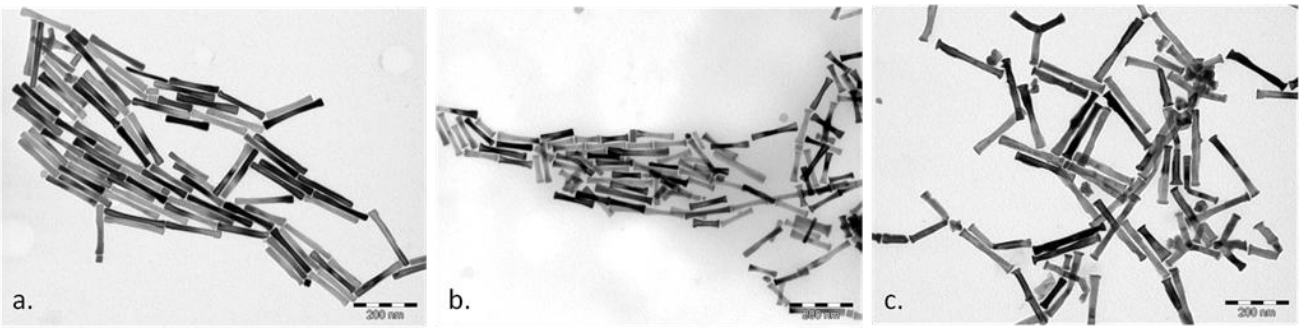

Figure III- 31 *TEM images of selected samples for the study of their morphological or population polydispersity effect on the H_{ci}:* ***a.*** *NRs with smooth surface and flat endings (d_m= 22 nm, l_m= 166 nm),* ***b.*** *NRs with cone endings (d_m= 18 nm, l_m= 120 nm),* ***c.*** *NRs (d_m= 22 nm, l_m= 190 nm) combined with tetrapods.*

The resulting alignments were of similar V_M, in the range of 51 – 54 %. The M(H) loops of the above samples are presented in the Figure III- 32 and summarized in the Table III- 10.

Even though the rods with flat endings are thicker (d_m= 22 nm) than those with the tips (d_m= 18 nm), they present higher H_{ci}, showing that the tips enlargement have stronger effect than the diameter. It is consistent with a magnetization reversal that nucleates at the rod tips. The same observation is also presented in the micromagnetic simulations in the Chapter I (section I.3.1 a).

Regarding the rods combined with tetrapods, no micromagnetic simulations were done on tetrapods but we can reasonably expect a lower coercivity than for the rods. Moreover, the larger distribution of the easy axis orientation due to the disorder induced by the shape polydispersity will also contribute to the decrease of H_{ci}.

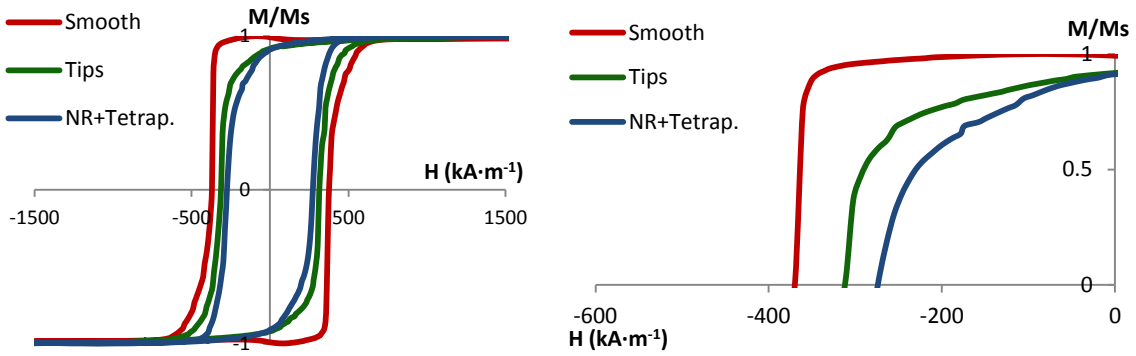

Figure III- 32 *M(H) loop (left) and its second quadrant (right) of assemblies comprising of nanorods with different morphologies.*

Poly-dispersity	Morphology	D_m/ L_m nm	AR_m	V_M %	H_{ci} (kA·m^{-1})
Shape	Smooth	22/166	7.5	54	375
	Tips	18/120	6.6	53	313
Population	NR + Tetrapods	22/190	8.6	51	272

Table III- 10 *Coercivity values of assemblies consisting of nanorods with different morphology.*

III. 11 Experimental optimization

Before closing this chapter, we will examine two ways of improving the magnetic performances of the rod dense assemblies by :
- increasing H_{ci} playing on the rod morphology
- increasing V_M avoiding the rod oxidation.

III.11.1 Improvement with rods of high coercivity

All the nanorods presented above were prepared with $RuCl_3 \cdot xH_2O$ as nucleating agent. We will now examine the capacity of the rods resulting from the use of the anhydrous $RuCl_3$ to yield high H_{ci} values. In chapter II we have showed the interest of the anhydrous chloride as nucleating agent for the synthesis of thin rods with rounded tips.

We have performed a small scale alignment of a sample prepared with anhydrous $RuCl_3$. The sample comprised rods of mean diameter d_m= 8 nm and mean length l_m= 42 nm and rounded endings, combined with spherical particles (d_m= 11 nm). The TEM image of the particles and the SEM of the aligned structure (R_8A_{T4}) are illustrated in the Figure III- 33. The M(H) loop of the assembly R_8A_{T4} is plotted on figure III-34a.

Our first comment is that the coercivity of the assembly (H_C= 518 $kA \cdot m^{-1}$) is higher than all the values reported before (Figure III-30). The high H_C value can be attributed to the small rod diameter despite the presence of spheres in the samples.

The second comment concerns the particular shape of the M(H) loop. A good level of alignment can be seen on the M(H) loop, where the M_r/M_s equals to 0.95 (Figure III- 34). Nevertheless, the shape of the M(H) loop deviates from that presented in all above experiments: it has an intense inclination meaning that the switching field distribution of the particles is very broad. This can be attributed to:

- The easier reversal of the spherical particles (since they do not present shape anisotropy), the M(H) is an average of all the contributions; and
- The dipolar interactions between the spheres and the rods resulting to the magnetization reversal of the rods at lower field.

The magnetic volume fraction, oxide shell and ligand volume fraction of the assembly R_8A_{T4} are summarized in the Table III-11. Despite the regular washing procedure followed, the magnetic volume fraction was only V_M = 25 %. On the opposite, the V_{CoO} was measured at 16 %, corresponding to CoO shell of 0.9 nm, a value that is consistent with the previously

presented results.The high content of organics did not allow the acquisition of good SEM image at high magnification (Figure III- 33 b).

The B(H) loop of the assembly R_8A_{T4} was plotted taking into account the V_M (Figure III-34b). As a result of the low V_M and low SQ, the $(BH)_{max}$ and B_r were measured at 26 kJ·m^{-3} and 0.42 T, respectively.

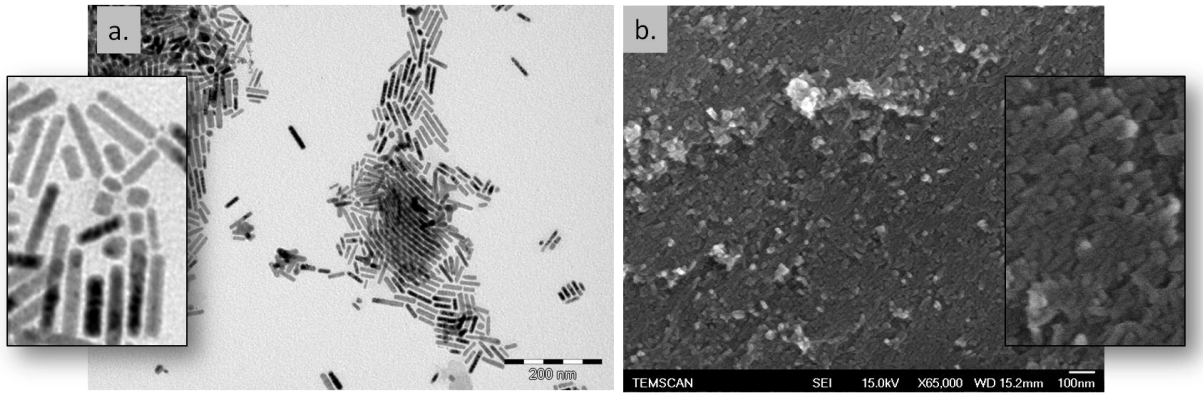

Figure III- 33 *Polydisperse nanorods with rounded edges combined with spheres:* ***a.*** *TEM and* ***b.*** *SEM images after their alignment.*

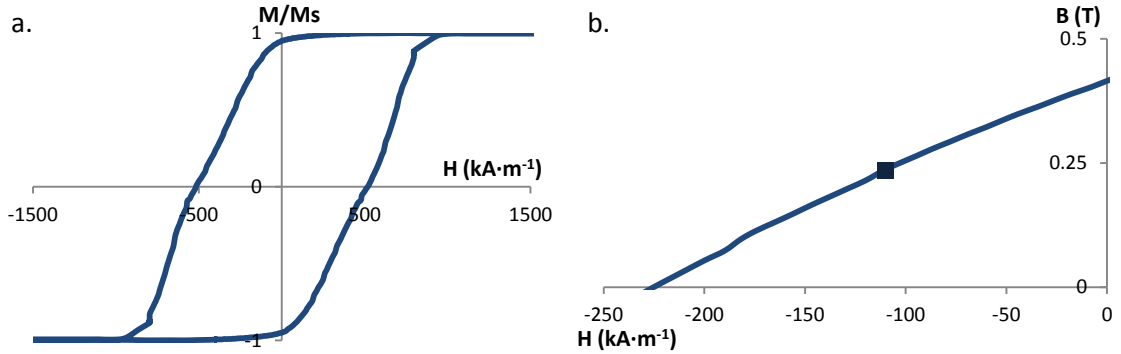

Figure III- 34 *SEM of rounded nanorods combined with spherical particles aligned under 1 T (a) and second quadrant of their B(H) loop (b).*

D_m/L_m (nm)	V_M %	V_{CoO} %	V_L %	SQ	M_r/M_s	H_{ci} (kA·m^{-1})	B_r (T)	$(BH)_{max}$ (kJ·m^{-3})
8/42	25	16	59	0.54	0.95	518	0.416	26

Table III- 11 *Volume fractions and magnetic characteristics of an assembly of polydisperse rods with rounded endings.*

The decreasing of the mean diameter allowed increasing the coercivity of the assembly. Nevertheless, in order to increase the $(BH)_{max}$ with such rods two improvements are necessary:

- efficient washing should be found to decrease the ligand amount;

- small spheres should be removed by efficient centrifugation or filtration processes.

III.11.2 Alignment of nanorods in controlled atmosphere

In the section III.9.1 we suggested that the reduction of the oxide shell results in higher V_M. In order to achieve that, we developed an alignment protocol under controlled atmosphere.

The nanorods are well preserved from oxidation as long as they remain in their polyol solution. However, their manipulation under air during washing and alignment procedure result in a CoO shell of 1-2 nm. Thus, in order to prevent oxidation, washing and alignment process were performed under Ar. Nanorods of d_m= 17 nm and l_m= 300 nm, were washed twice with degassed toluene under Ar atmosphere and dispersed in degassed chloroform in a mould of d= 1 cm. The mould was placed inside a Schlenk tube, which was stabilized in between the electromagnet's coils through a hollow non-magnetic base (Figure III- 35 b). The chloroform was evaporated under reduced atmosphere combining cold trapping and a diaphragm pump (Figure III- 35 a).

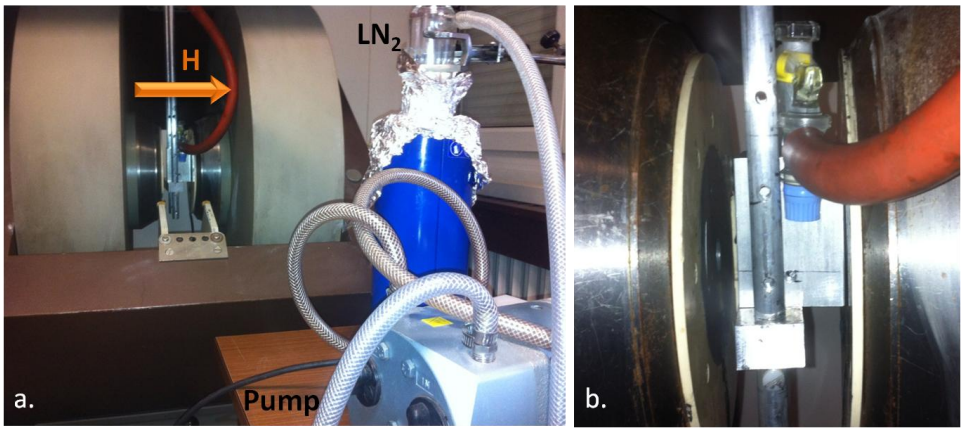

Figure III- 35 ***a.*** *Set-up for alignment under vacuum;* ***b.*** *close-up of the schlenk inside the non-magnetic metallic base. The nanorods' solution is located at the center of the field.*

The obtained alignment was then kept in a glovebox under Ar atmosphere. VSM samples were prepared in the glove bow to lower the air exposure. Measurements were performed on a needle fixed on the quartz of the VSM holder and protected from air with scotch tape. Low temperature measurements after magnetic field cooling were performed to detect the presence of exchange bias and compared with a similar sample prepared under air from rods with d_m= 17.5 nm, l_m=120 nm, exhibiting e_{CoO}=1.4 nm.

At that point, it has to be noted that an extensive study at low temperature measurements was performed for similar cobalt nanorods in powder by Maurer *et al.* [10]. Thus our study

was only limited to the detection of exchange bias phenomena in order to verify if our alignment protocol protects the rods from oxidation.

We define the exchange bias and coercive field from the two intersections of the hysteresis loop with the H axis referred to as H_- and H_+:

$$H_{EB} = \frac{H_+ + H_-}{2} \qquad \text{(Eq. III-22)}$$

$$H_C = \frac{H_+ - H_-}{2} \qquad \text{(Eq. III-23)}$$

In the Figure III- 36 are illustrated the hysteresis loops measured at 10 K and 300 K after field cooling at 3 T of the sample handled in the glovebox and the sample handled in air. The corresponding H_{ci} and H_{EB} values are shown in the Table III- 12. In the case of the aligned under vacuum rods, the exchange bias observed are not significant (H_{EB}= -0.35 kA·m^{-1}), confirming that we had indeed no oxidation or a very limited thin CoO shell. The case is opposite for the rods dried in air where a higher H_{EB} is observed equal to -53 kA·m^{-1}. Similar value of -61 kA·m^{-1} was reported by Maurer *et al.* for Co/CoO cobalt nanorods with d_m= 13 nm and CoO shell 1.2 nm [10].

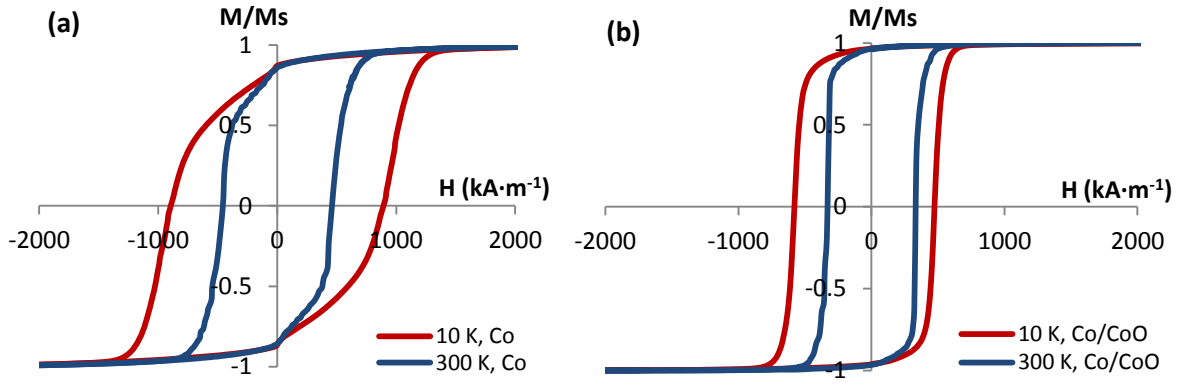

Figure III- 36 *Temperature dependence of the coercive field and the exchange-bias field for non-oxidized (a) and oxidized cylindrical rods of d_m= 17.4 nm (b).*

T (K)	Co		Co/CoO	
	H_{ci} (kA·m^{-1})	H_{EB} (kA·m^{-1})	H_{ci} (kA·m^{-1})	H_{EB} (kA·m^{-1})
10	711	-0.35	526	-53
300	365	--	331	--

Table III- 12 *Exchange bias and coercive field of Co and Co/CoO nanorod assemblies.*

Another way to define the existence of CoO shell is via the combination of VSM and TGA measurements, for the calculation of the M_s and the CoO shell thickness. Both confirm our relatively successful try to protect the nanorods from oxidation during the alignment procedure (Table III- 13). As a result of the nanorods' treatment under Ar, the V_M increased to 59%, which is the highest value obtained during our experimental work and promising for obtaining $(BH)_{max}$ higher than 200 $kJ \cdot m^{-3}$ according to the simulations in Figure III- 26. Unfortunately, the alignment was not perfect and the squareness was low (see the shape of the M(H) loop of figure III-36a).

Sample	D_m/ L_m Nm	V_M %	V_{CoO} %	V_L %	e (nm)	M_s ($emu \cdot g^{-1}$)
Co	17/290	59	5.6	35.4	0.3	142
Co/CoO	17.4/123	41	17	42	1.4	114

Table III- 13 *Volume fractions, magnetization saturation and CoO shell measured for the Co and Co/CoO rod assemblies from TGA and VSM measurements.*

III.12 Conclusions

In this chapter we studied the feasibility to fabricate rare-earth free permanent magnets comprised exclusively of cobalt nanorods.

We developed a protocol according to which cobalt nanorods align in dense assemblies at small (0.047 g) and large (1 g) scale. These assemblies exhibit robustness along the alignment axis and flexibility perpendicular to it. We showed how to extrapolate the B(H) loop out of the measured M(H) loop and how to calculate the assembly's $(BH)_{max}$, which varied $(BH)_{max}$ in the range of 25 – 167 $kJ \cdot m^{-3}$.

Through the use of different alignment procedures and nanorods of varying shape and population polydispersity we could define the following conditions to obtain high $(BH)_{max}$:
1. Quality of alignment (M_r/M_s). Chloroform seems the best solvent to prevent the rods' aggregation and precipitation before and during their alignment. Regardless their shape or population polydispersity, the obtained M_r/M_s was mostly above 0.90, with the highest value (0.99) corresponding to population monodisperse rods of flat endings.
2. Squared M(H) loop. The SQ criterion is very sensitive to the rods' morphological characteristics, since any defects result in a broad switching field distribution. The maximum obtained SQ equals to 0.96 and corresponds to population monodisperse rods of flat endings.
3. High V_M. Repetitive washings ensures an efficient removal of ligands leading to V_M values between 45 – 55 %.

A simple model was introduced to shed light on the $(BH)_{max}$ evolution with the B_R (or V_M), SQ and H_{ci}. To avoid any coercivity limitation, nanorods presenting $\mu_0 H_c \geq \frac{B_R}{2(1+a)}$ (where α is the slope of the M(H) loop at remanence) should be used. Amongst all different rods prepared by the polyol process, we show that the highest H_c belongs to the finest rods, d_m= 8 nm, with rounded endings (518 $kA \cdot m^{-1}$), followed by rods with mean diameter of 10 nm and flat endings (485 $kA \cdot m^{-1}$). Such very thin rods requires however to further improve the washing and alignment procedure to reach high volume fraction. In parallel, preliminary experiments show that alignment of non-oxidized Co NRs can be obtained, confirming that $(BH)_{max}$ up to 250 $kJ \cdot m^{-3}$ is a realistic target within a near future.

Bibliography

[1] F. Ott, T. Maurer, G. Chaboussant, Y. Soumare, J. Y. Piquemal, and G. Viau, "Effects of the shape of elongated magnetic particles on the coercive field," *J. Appl. Phys.*, vol. 105, no. 1, 2009.

[2] M. Pousthomis, E. Anagnostopoulou, I. Panagiotopoulos, R. Boubekri, W. Fang, F. Ott, K. A. Atmane, J. Y. Piquemal, L. M. Lacroix, and G. Viau, "Localized magnetization reversal processes in cobalt nanorods with different aspect ratios," *Nano Res.*, vol. 8, no. 7, pp. 2231–2241, 2015.

[3] T. Maurer, F. Zighem, W. Fang, F. Ott, G. Chaboussant, Y. Soumare, K. A. Atmane, J. Y. Piquemal, and G. Viau, "Dipolar interactions in magnetic nanowire aggregates," *J. Appl. Phys.*, vol. 110, no. 12, 2011.

[4] K. Atmane, C. Michel, J.-Y. Piquemal, P. Sautet, P. Beaunier, M. Giraud, M. Sicard, S. Nowak, R. Losno, and G. Viau, "Control of the anisotropic shape of cobalt nanorods in the liquid phase: from experiment to theory... and back," *Nanoscale*, vol. 6, pp. 2682–2692, 2014.

[5] T. Maurer, F. Zighem, F. Ott, G. Chaboussant, G. André, Y. Soumare, J. Y. Piquemal, G. Viau, and C. Gatel, "Exchange bias in Co/CoO core-shell nanowires: Role of antiferromagnetic superparamagnetic fluctuations," *Phys. Rev. B - Condens. Matter Mater. Phys.*, vol. 80, no. 6, pp. 1–9, 2009.

[6] W. Fang, "Elaboration de matériaux composites nanofils magnétiques / polymères pour la fabrication d ' aimants permanents," UNIVERSITE PARIS-SUD XI ÉCOLE DOCTORALE : Chimie de Paris Sud, 2013.

[7] P. Toson, W. Wallisch, A. Asali, and J. Fidler, "Modelling of Packed Co Nanorods for Hard Magnetic Applications," *EPJ Web Conf.*, vol. 75, no. 20 14, pp. 4–7, 2014.

[8] I. Panagiotopoulos, W. Fang, F. Ott, F. Boué, K. Ait-Atmane, J. Y. Piquemal, and G. Viau, "Packing fraction dependence of the coercivity and the energy product in nanowire based permanent magnets," *J. Appl. Phys.*, vol. 114, no. 14, 2013.

[9] F. Ott, J.-Y. Piquemal, and G. Viau, "High-Aspect-Ratio Nanoparticles: Growth, Assembly, and Magnetic Properties," in *Magnetic Structures of 2D and 3D Nanoparticles: Properties and Applications*, J.-C. Levy, Ed. Pan Stanford, 2016, pp. 213–255.

[10] T. Maurer, F. Ott, G. Chaboussant, Y. Soumare, J. Y. Piquemal, and G. Viau, "Magnetic nanowires as permanent magnet materials," *Appl. Phys. Lett.*, vol. 91, no. 17, pp. 1–4, 2007.

Chapter IV Small Angle Neutron Scattering by cobalt nanorod assemblies

IV.1 Generalities

Small angle X-ray scattering (SAXS) and small angle neutron scattering (SANS) are scattering experiments ideal for characterizing nanostructures. They are non-destructive methods, meaning that the sample can be used afterwards for additional characterization. SAXS experiments are more common because X-ray source are available at laboratory scale or in synchrotron facilities. However, the use of neutrons brings some advantages over the X-rays especially when it comes to the characterization of magnetic materials. Besides, neutrons allow study rather thick samples (up to 1mm) compared to x-rays.
The neutron's wavelength is given by:

$$\lambda = \frac{h}{mv} \qquad \text{(Eq. IV-1)}$$

where h is Planck's constant, m is the mass of the neutron equal to 1.674928×10^{-27} kg and v its velocity. For SANS experiments λ is comprised between 2 Å and 20 Å depending on the experimental set-up. This wavelength range allows to characterize tiny objects with characteristic lengths in the range 1-100 nm such as nanoparticles, polymers or large bio-molecules.

- While X-rays interact with the electron cloud resulting in a cross section of interaction which is mainly dependent on the atomic number Z, the neutrons are uncharged particles capable of interacting with the nuclei. Thus, the neutrons are very penetrating and can be used to probe the bulk properties of samples with thickness of several millimeters. Moreover, due to their magnetic moment (spin) the neutrons can interact with the spin and orbital magnetic moments of atoms bearing unpaired electrons, giving rise to magnetic scattering.
- The interaction of atoms with neutrons is characterized by the cross section σ, or by the scattering length, b, which is related to the cross section by $\sigma = 4\pi b^2$. The cross section varies irregularly with the atomic number Z of the atoms contrarily to the interaction cross section of X-ray that increases with Z. The scattering length is a complex number, the imaginary part being related to the neutron absorption (C, Al and Si exhibit a very weak absorption cross section while Cd used for neutron mask exhibit a very high absorption cross section). The real part of the scattering length contains an elastic coherent scattering that give rise to structural information in matter and an incoherent one that increases the background signal (H atoms present a strong incoherent cross section that may be detrimental for a good signal).

- SANS pattern of colloids or granular nanomaterials will give information on their structural properties provided a good scattering contrast between the dispersed phase and the matrix.
- The interaction of neutron with magnetic moments will probe information on the magnetic structure at many different length scales, from Å (determination of magnetic structure at the atomic scale for a diffraction experiment) to nm (information on the magnetic domain sizes and other spatial variations of the magnetization density) [1].

IV.2 Geometry of SANS

The schematic representation of a small-angle scattering experiment is presented in Figure IV- 1. In an ideal case, the neutron beam can be viewed as an assembly of particles flying in parallel directions at a same speed. It can be described by a planar monochromatic wave described by a wave vector $\vec{k}_i$ of magnitude $k = 2\pi/\lambda$.

In SANS we consider only the elastic interaction between the neutrons and the sample: the direction of the scattered wave $\vec{k}_S$ changes but the magnitude is constant (k_i = k_s). The scattering wave-vector $\vec{q}$ is the difference between the incident and scattered wave vectors:

$$\vec{q} = \overrightarrow{k_s} - \overrightarrow{k_i} \qquad \text{(Eq. IV-3)}$$

The angle between the incident and scattered wave-vector is 2θ. The magnitude of q (expressed in $Å^{-1}$) is related to the scattering angle θ by

$$q = \frac{4\pi}{\lambda} sin\theta \qquad \text{(Eq. IV-4)}$$

A scattering wave- vector *q* is related to a distance in real space by the relation [2]:

$$q = \frac{2\pi}{D} \qquad \text{(Eq. IV-5)}$$

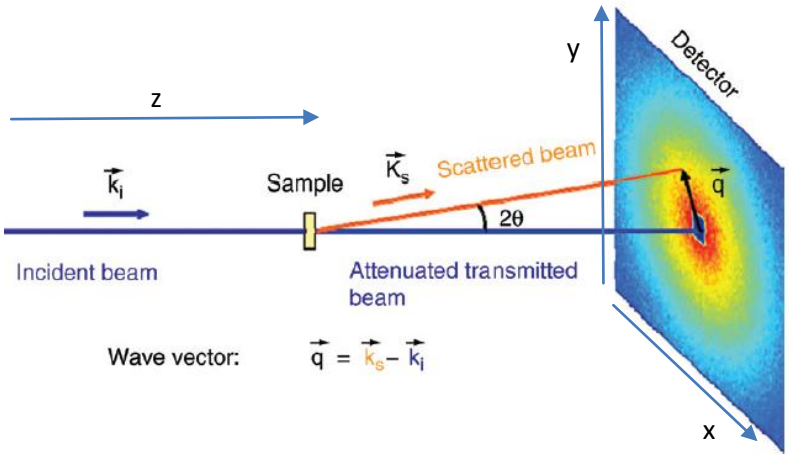

Figure IV- 1 *Schematic representation of a scattering experiment and representation of the scattering wave-vector* $\vec{q}$ *in the detector plane [3].*

It is important to have in mind that in a small angle experiment the angle θ is very small (1-2°) and so the scattering vector $\vec{q}$ can be considered perpendicular to $\vec{k}_i$. Hence a distance on the flat detector plane can be converted with a very good accuracy into a *q* value with simple algebra.

IV.3 SANS on dense nanorod assemblies

The scattering intensity of ferromagnetic particles (p), dispersed in a matrix (m) as a function of the scattering vector q is the product of two terms, namely a form factor *F* and a structure factor *S*:

$$I(q) = N[F_N(q) + F_M(q)]^2 S(q) \qquad \text{(Eq. IV-6)}$$

where N is the number of particles per volume unit, $F_N(q)$ is the nuclear form factor, $F_M(q)$ the magnetic form factor related to the magnetization of the particles and $S(q)$ the structure factor which depends on the spatial correlations between the particles [4].

The nuclear form factor $F_N(q)$ contains the information about the shape of the scattering object. It depends on the nuclear scattering length density contrast $\Delta\rho$, between the particles and the matrix, and on the geometrical form factor of the particles $F_{geo}(q)$ related to the shape of the particles.

In the case of particles of volume V_p with a scattering length density (SLD) ρ_p dispersed in a medium with SLD ρ_{med}, the nuclear form factor $F_N(q)$ of the particles is expressed as:

$$F_N(\vec{q}) = (\rho_p - \rho_m) \int_{V_p} e^{-i\vec{q}.\vec{r}} d\vec{r} = (\Delta\rho) F_{geo}(\vec{q}) \qquad \text{(Eq. IV-7)}$$

with $F_{geo}(q)$ being the geometrical form factor of the particle which is simply the Fourier transform of the object volume.
The scattering length density of the particle is defined as:

$$\rho_p = \frac{N_A}{M} \rho b \qquad \text{(Eq. IV-8)}$$

Where N_A is the Avogadro number, ρ the density, M the molar weight and b the scattering length of the nuclei in the particle.

Equation IV-7 shows that a SLD contrast between the particles and the matrix is necessary to have a scattering intensity.

For cobalt, considering the density ρ_{Co} = 8.9 g.cm^{-3}, a molar weight M_{Co}=58.9 g.mol^{-1} and a coherent scattering length b_{Co} = 2.5 10^{-15} m, we calculate the SLD ρ_{Co} =2.26 10^{-6} Å^{-2}.
For the matrix we consider only the ligand laurate of formula $C_{12}H_{23}O_2$. Therefore, considering a density ρ_L=0.9 g·cm^{-3}, a molar weight M_L= 170 g.mol^{-1} and a coherent scattering length $b_m = 12b_C + 23b_H + 2b_O$, with b_H= -3.74 10^{-15} m; b_C= 6.65 10^{-15} m ; b_O = 5.80 10^{-15} m, we calculate a SLD ρ_m = 0.14 10^{-6} Å^{-2}.

Thus, in the particular case of cobalt rods embedded in a matrix of laurate ligand the SLD contrast can be estimated to $\Delta\rho$ = 2.12 10^{-6} Å^{-2}.

For particles with cylindrical shape (radius R and length L) [5] $F_{geo,cyl}(\vec{q})$ can be written as :

$$F_{geo,cyl}(\vec{q}) = V_p \frac{2J_1(q_\perp R)}{q_\perp R} \cdot \frac{sin\left(\frac{1}{2}q_\parallel L\right)}{\frac{1}{2}q_\parallel L} \qquad \text{(Eq. IV-9)}$$

where $J_1$is the first-order Bessel function, $q_\parallel$ and $q_\perp$are respectively the projections of the scattering wave-vector $\vec{q}$ parallel and perpendicular to the nanorod long axis.
Let α be the angle between the cylinder axis and the scattering vector $\vec{q}$: $q_\perp = q.sin\alpha$ and $q_\parallel = q.cos\alpha$

When the cylinder is perpendicular to the incident wave-vector $\overrightarrow{k_i}$, the scattering vector $\vec{q}$ and the cylinder are in the same plane, the geometrical form factor simplifies as the form factor of a parallelepiped:

$$F_{geo,cyl}(\vec{q}) = V_p \left[\frac{sin(q_\perp R)}{q_\perp R}\right]\left[\frac{sin\left(\frac{1}{2}q_\parallel L\right)}{\frac{1}{2}q_\parallel L}\right] \qquad \text{(Eq. IV-10)}$$

For monodisperse particles the scattering intensity due to the nuclei is generally written given as:

$$I_N(q) = NV_p^2(\Delta\rho)^2P(q)S(q) = \Phi_pV_p(\Delta\rho)^2F^2(q)S(q) \qquad \text{(Eq. IV-11)}$$

where Φ is the particles volume fraction of all defined as: $\Phi = \frac{NV_p}{V}$

The Figure IV- 2 shows the form factor $|F(q)|^2$ for a rod parallel or perpendicular to the incident beam [6].

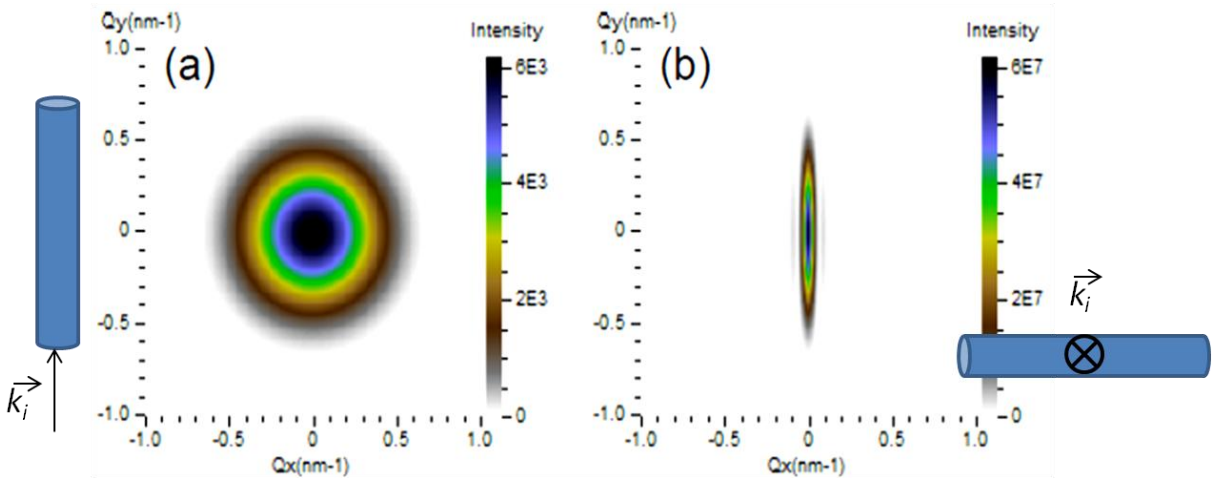

Figure IV- 2 *Simulations of the factor* $\boldsymbol{V_p^2P(q)}$ *performed via the spectraprocessor software for a nanowire with* d_m*= 10 nm and* L_m*= 100 nm depending on its orientation to the incident beam (a) the rod long axis and* $\overrightarrow{\boldsymbol{k_i}}$ *are parallel to z ; (b) the rod long axis is in the (x,y) plane and parallel to x while* $\overrightarrow{\boldsymbol{k_i}}$ *is along z [6].*

In the perpendicular configuration ($\overrightarrow{k_i}$ *is along z and rod long axis along x) the SANS pattern is* is strongly anisotropic with a scattering intensity that falls rapidly to zero in the x direction (Figure IV-2b). The anisotropy is well explained by the equation IV-10. The figure below illustrates that the cardinal sin function decreases much faster for the rod length L_m= 100 nm than for rod diameter D_m= 10 nm.

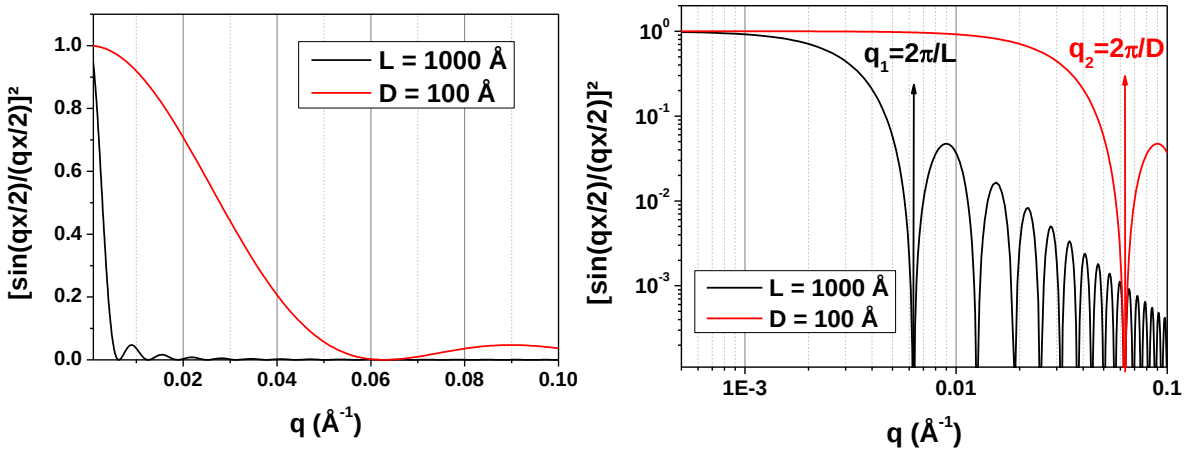

Figure IV- 3 *Dependence of the function* $\left[\frac{sin\left(\frac{1}{2}qx\right)}{\frac{1}{2}qx}\right]^2$ *for the rod dimension x=L= 1000Å and x=D=100 Å.*

For an assembly of rods randomly oriented, the integral of the geometrical factor of a cylinder over all possible orientations with respect to the direction of the scattering vector q gives the curve plotted on Figure IV- 4 with a q^{-1} law in the intermediate range of q and a plateau at very small q.

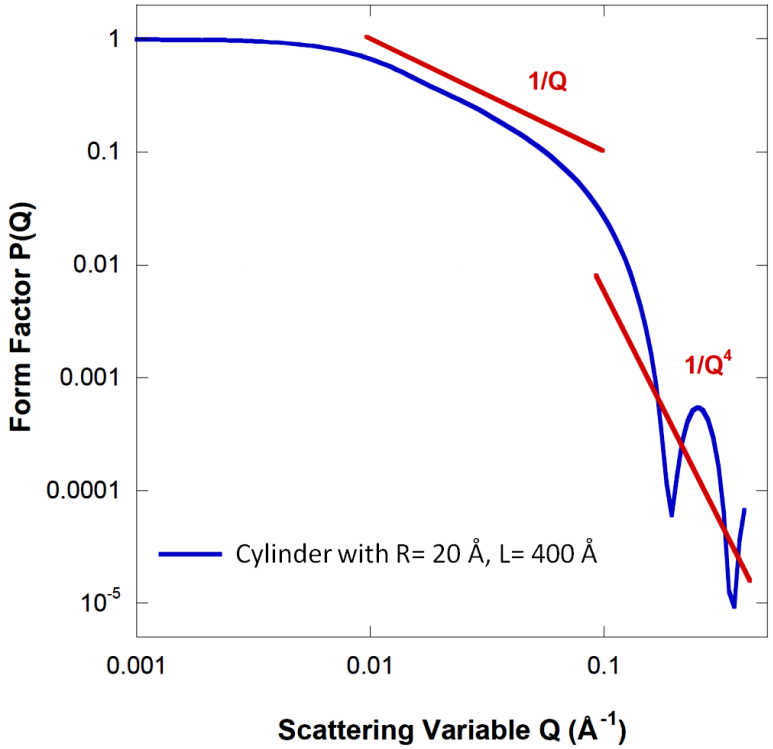

Figure IV- 4 *Example of an average form factor of cylinder over all the orientation of the long axis with respect to the scattering vector q [7].*

The same calculations for flat objects (platelets) give a curve with a q^{-2} variation in the intermediate q range. And more generally for objects with a fractal dimension α the scattering intensity is expected to follow a $q^{-\alpha}$ law in the intermediate *q* range.

The **magnetic form factor** $F_M(\vec{q})$ for a magnetic particle of volume V_p is expressed as:

$$F_M(\vec{q}) = \int_{V_p} \Delta\rho_M \, e^{i\vec{q}\vec{r}} d\vec{r} \qquad \text{(Eq. IV-12)}$$

where $\Delta\rho_M = \rho_M - \rho_{M,matrix}$, with ρ_M and $\rho_{M,matrix}$ the magnetic SLD of the particle and the matrix, respectively. By analogy with the nuclear SLD, the magnetic SLD for an assembly of identical magnetic atoms can be written as :

$$\rho_M = \frac{e^2\gamma}{2mc^2} \sum_i c_i M_i^{\perp} \qquad \text{(Eq. IV-13)}$$

with c_i atomic concentration, $M_i^{\perp}$ the component of the magnetic moment perpendicular to the scattering vector expressed in Bohr magneton and the ratio $\frac{e^2\gamma}{2mc^2}$ = 2.7 10^{-15} m.
In case of a non-magnetic matrix ($\rho_{M,matrix}$= 0) and if the magnetization inside the particle is uniform we can write :

$$F_M(\vec{q}) = \rho_M \int_{V_M} e^{i\vec{q}\vec{r}} d\vec{r} = \rho_M F_{geo}(\vec{q}) \qquad \text{(Eq. IV-14)}$$

with $F_{geo}(\vec{q})$ the geometrical factor which is identical to the one used for the nuclear form factor.
Considering a cobalt particle the atomic concentration is $c = \frac{N_A \rho_{Co}}{M_{Co}}$ = 9.02 10^{22} at.cm^{-3} and the magnetic moment per atom is 1.7 μ_B. From these values we can calculate:

$\rho_M(Co)$=0.902 10^{23}×1.7×2.7 10^{-13} = 4.1 10^{10} cm^{-2} = 4.1 10^{-6} Å^{-2}.

The magnetic form factor is related to the nuclear form factor by the equation:

$$F_M(\vec{q}) = \frac{\rho_M}{\Delta\rho}\frac{V_M}{V_P} F_N(\vec{q}) = \chi(q) F_N(\vec{q}) \qquad \text{(Eq. IV-15)}$$

with V_M the magnetic volume of the particle and V_P the nuclear volume of the particle.
If we neglect the cobalt oxide layer ($V_M \approx V_P$) there is approximately a factor 2 between the magnetic form factor and the nuclear form factor.

Of course this relationship is true only if the magnetization of the cobalt rod is fully saturated. The situation is more complex for intermediate state, for instance when the nucleation reversal starts at one end of the rod as predicted by micromagnetic simulations (Chapter I). In this case, the geometrical form factor cannot be used anymore since the magnetic structure is different from the nuclear structure.

One important point to keep in mind is that the magnetic interaction of neutrons is limited to the component of the magnetization perpendicular to the scattering vector $\vec{q}$. The magnetic scattered intensity is thus related to the magnetic form factor as $I(q) = 2 \sin^2(\alpha) |F_M(q)|^2 S(q)$ where α is the angle between the magnetization and the scattering vector $\vec{q}$. So, for a fully magnetized rod along the easy axis: the neutrons will be essentially scattered in the direction perpendicular to the rods. The magnetic contrast for two configurations $\overrightarrow{k_i}$ parallel and perpendicular to the rod long axis is given on the Figure IV- 5 [6]. Note the strong angular dependence of the scattered neutrons on the Figure IV-5b.

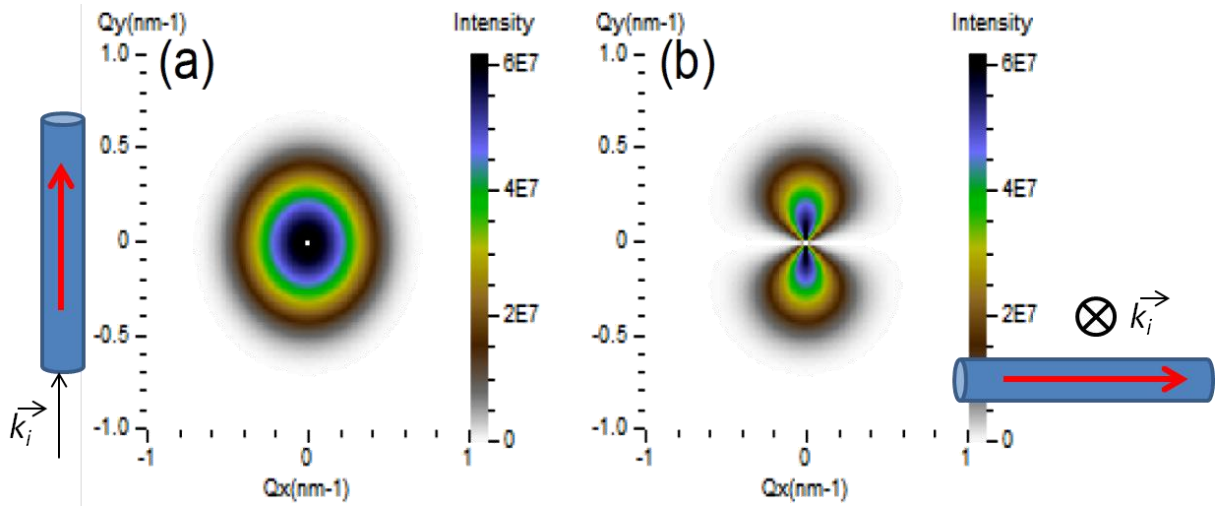

Figure IV- 5 *Simulations of the magnetic intensity contrast* $\left(\boldsymbol{F_M(q)}\right)^2$ *calculated for a rod (*d_m*= 10 nm and* L_m*= 100 nm) performed via the spectraprocessor software depending on its orientation to the incident beam (a) rod long axis and magnetization along z parallel to* $\overrightarrow{\boldsymbol{k_i}}$ *; (b) rod long and magnetization parallel to x while* $\overrightarrow{\boldsymbol{k_i}}$ *is along z [6].*

The **structure factor S(q)** describes the interference of neutrons scattered from different objects and consequently, it is dependent on the degree of local order in the sample. If we examine a very dilute solution of nanoparticles, the system can be seen as the combination of independent particles and so S(q) tends towards one. On the contrary, for concentrated assembly this factor will deviate from 1 and can be determined by several models. However, the determination of S(q) for such concentrated assemblies of particles, though highly interesting for our study, is beyond our thesis objectives. In the following we will limit

ourselves to say that in a dense particle assembly S(q) presents a maximum (correlation peak) out of which we can define the particle center-to-center distance, D_m.

IV.4 SANS experimental set-up

SANS measurements were performed with the PAXY spectrometer at the Laboratoire Léon Brillouin (LLB), at CEA Saclay.

The basic layout of the SANS instrument is illustrated in the Figure IV- 6. Non polarized neutrons are generated from a cold source and are guided to the spectrometer. A velocity mechanical selector allows selecting their wavelength between 4 Å and 20 Å (in our experiment λ was set at 5 Å). Then the beam passes through an attenuator, which decreases the neutrons' intensity in order to protect the detector from being burnt. The neutron beam is focused on the final target by a series of guide tubes and colliminators. The scattered beam is guided to a 2D detector (64*64 cm^2) within a vacuum chamber, preventing scattering from air. The sample-detector distance can vary from 0.8 m to 5 m and in the present case it was adjusted at 2 m, giving access to the q range of 0.005 $Å^{-1}$ < q < 0.06 $Å^{-1}$, which corresponds to the characteristic length-scale range in the real space 10.4 nm < D < 125 nm. At the detector's center is located a beam stop (made of cadmium) in order to absorb the neutrons that are not scattered and thus prevent the detector from being saturated. Like that the measured signal corresponds only to the scattered neutrons, which are finally translated in an array of digital pixels, representing a 2D pattern.

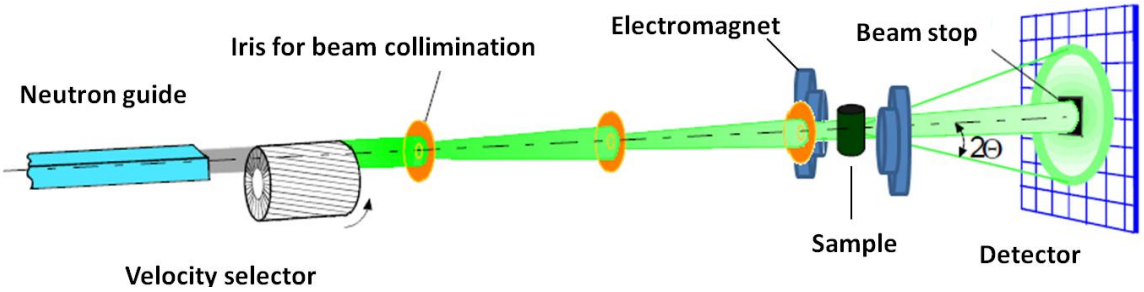

Figure IV- 6 *Schematic layout of a classical SANS facility at a continuous neutron source [ETH Practicum].*

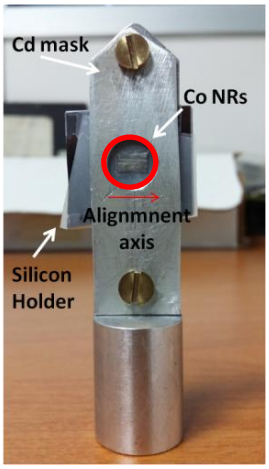

Figure IV- 7
Sample upon holder

The characterized samples were films of cobalt nanorod assemblies prepared according to the protocol presented in the Chapter III (section III.2.3). As a reminder the rods were dispersed in a solution of chloroform inside a Teflon parallelepiped mould and aligned under 1 T. After the chloroform's evaporation thin films with thickness of ≈ 0.2 mm and dimensions 5 mm x 4 mm were obtained. For the SANS measurements the wafer was stabilized between an aluminum foil and a scotch tape upon a silicon substrate. Both aluminum and silicon are transparent to neutrons, making them suitable materials for the SANS measurements. To only illuminate the sample, a cadmium mask frames the sample (Figure IV- 7).

Finally an electromagnet located at the height of the sample's position could provide magnetic fields up to 1.6 T during the SANS measurements able to scan the hysteresis cycle of the sample magnetize the sample. An typical acquisition of a 2D SANS pattern takes about 15 min; All measurements were carried out at room temperature.

IV.5 Dense nanorod assemblies – Data processing

The SANS data were analyzed with the use of the software package, GRASP, developed by C. Dewhurst [8]. GRASP is able to represent the 2D image of the diffraction pattern on the detector. During the analysis the following points have to be considered:

1. Subtraction of the background signal (The scotch tape + silicon was measured separately without any sample). It was necessary to use scotch tape to make sure that the magnetic needles would not move when high magnetic field would be applied (especially perpendicular to the needles)

2. Calculation of the corrected scattered intensity. The corrected data is the result of the foreground minus the two background components taking into account the sample transmission. *GRASP* calculates this in the following manner for each element of the pixelated multi-detector data: where $I_{Corrected}$ is the sample scattering corrected for background scattering, electronic noise, sample and empty cell transmission (i.e. attenuation effects) and other background effects. I_S is the measured scattering from the sample and holder. I_{Bck} is the measured background scattering from the sample holder. I_{Cd} is the "electronic" background and T_s and T_e are the sample and empty cell transmissions measured for each sample:

$$I_{corrected} = \frac{1}{T_s T_{Bck}}(I_s - I_{Cd}) - \frac{1}{T_{Bck}}(I_{Bck} - I_{Cd}) \qquad \text{(Eq. IV-16)}$$

This process allows the comparison of the scattering intensities, between different configurations and samples.

3. Determination of the beam center. A non accurate position of the beam center can cause a shift of the I(q) distribution and thus wrong D values.

4. Masking of the beam trap, which is the central part of the scattering Figure IV- 8 a, in order to hide any extra scattering around it.

Once the various instrumental and background effects have been removed, a 2D scattering is presented as $\mathrm{I}(\mathrm{q})$. It is then necessary to translate the 2D pattern in a 1D plot, which is also expected to be anisotropic (Figure IV- 8 b). For that reason, an angular sector of 20-30° was defined across the parallel and perpendicular signal of the pattern to give the total (nuclear and magnetic) scattering intensity, *I*, vs. scattering vector, *q*. We define as $I_q^{\perp}$ and $I_q^{\parallel}$ the intensities scattered from the rods perpendicular and parallel to their alignment direction.

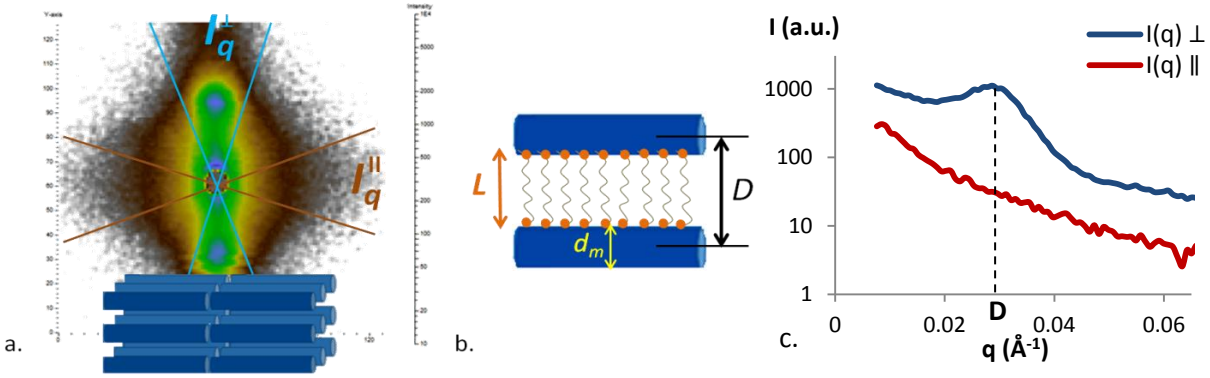

Figure IV- 8 a. *Normalized scattering spectra of dense cobalt nanorod assemblies (the sample's surface is perpendicular to the incident beam);* ***b.*** *Nanorod center-to-center distance, D;* ***c.*** *Normalized intensity as a function of the norm of the scattering wave vector q in lin-log scale.*

IV.6 SANS in zero field: Structural characterization of cobalt nanorod assemblies

In this section we will describe the SANS measurements on dense nanorod assemblies performed under zero field. With neutron scattering our objective was to get more information on the structural properties of the assemblies such as a measurement of the mean distance between the rods and their alignment quality. For practical reasons, the assemblies are referred to as R_i, where '"i" is the mean diameter in nm of the nanorods.

IV.6.1 Samples description

We selected three assemblies of rods with differences in their mean diameter, alignment quality and packing density (V_M). In the Figure IV- 9 are given the TEM images of the rods before alignment, SEM images of the dense assemblies that were measured by SANS and the corresponding hysteresis loops with the measuring field applied parallel to the alignment axis. Their morphological characteristics are summarized as follows:

- The $R_{17.4}$ and $R_{18.4}$: assemblies comprise of rods with similar diameter, smooth surface and tips at their endings Figure IV- 9 a, d).
- The $R_{30.0}$: assembly comprises of rods with larger diameter and rough surface (Figure IV- 9 g).

Their coercivity, M_R/M_S, squareness were measured from their M(H) loop. The magnetic volume fraction, V_M, and the thickness of the oxide shell, e, were determined from saturation magnetization and thermogravimetric analyses as explained in the Chapter III. The morphological data of the rods, the structural and magnetic characteristics of the assemblies are summarized in the Table IV- 1.

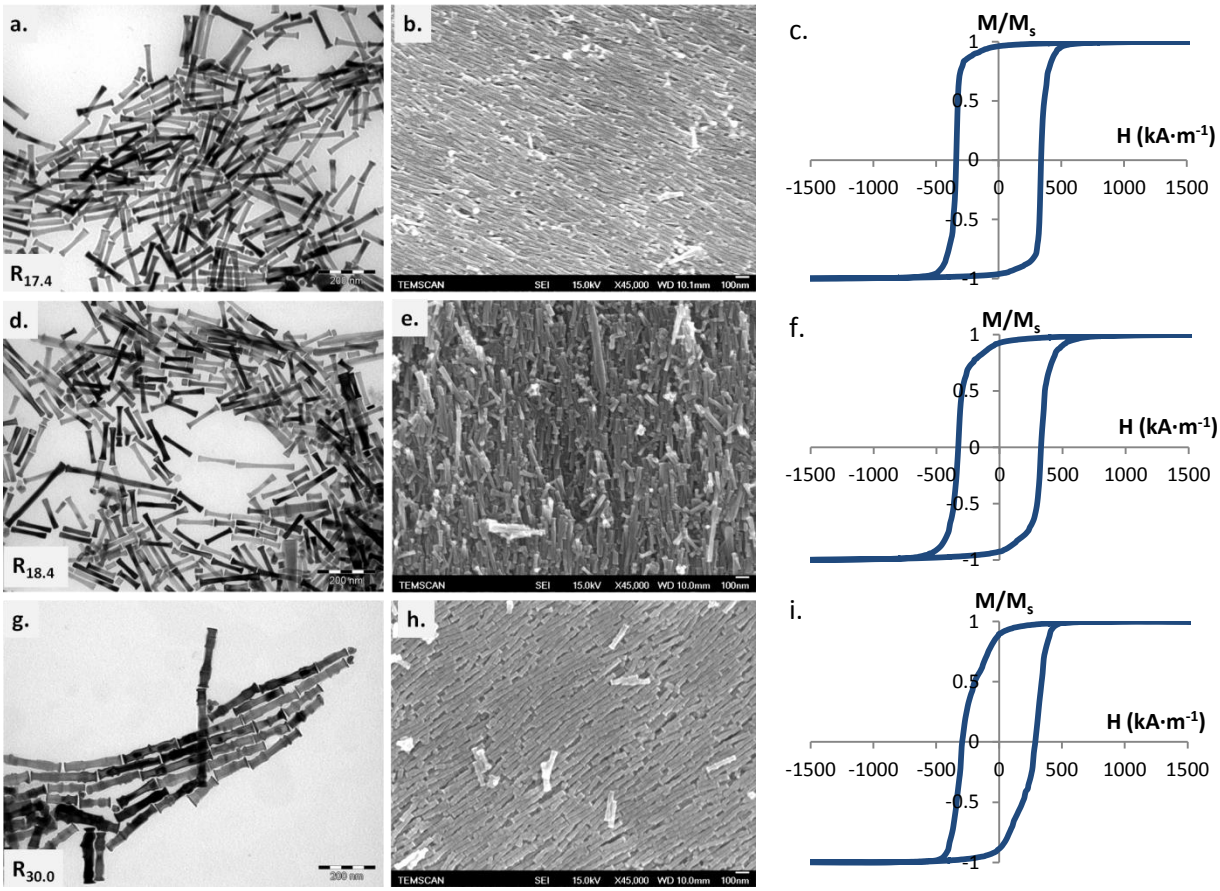

Figure IV- 9 ***(a)*** *TEM image of nanorods with d_m= 17.4 ± 2 nm and l_m= 120 ± 30 nm ;* ***(b)*** *SEM image of their alignment and* ***(c)*** *corresponding M(H) loop measured with the applied field parallel to the*

alignment ; ***(d)*** *TEM image of nanorods with d_m= 18.4 ± 3 nm and l_m= 120 ± 55 nm ;* ***(e)*** *SEM image of their alignment and* ***(f)*** *corresponding M(H) loop measured with the applied field parallel to the alignment.* ***(g)*** *TEM image of nanorods with d_m= 30.0 ± 6nm and l_m= 190 ± 40 nm ;* ***(h)*** *SEM image of their alignment and* ***(i)*** *corresponding M(H) loop with the applied field parallel to the alignment.*

Sample	d_m (nm)	l_m (nm)	e (nm)	H_{ci} ($kA \cdot m^{-1}$)	M_r/M_s	SQ	V_M %
$R_{17.4}$	17.4 ± 2	120 ± 30	1.5	338	0.96	0.86	40.6
$R_{18.4}$	18.4 ± 3	120 ± 55	1.0	337	0.93	0.73	52.0
$R_{30.0}$	30.0 ± 6	190 ± 40	1.8	289	0.90	0.57	48.8

Table IV- 1 *Morphological and magnetic characteristics of the assemblies $R_{17.4}$, $R_{187.4}$ and $R_{31.3}$, where: d_m and l_m is the rods' mean diameter and length;* ***e*** *the CoO shell thickness; H_{ci} the coercivity measured with the applied field parallel to the rods' alignment direction; M_r/M_s the orientation coefficient;* ***SQ*** *the squareness and V_M the magnetic volume fraction.*

For the three assemblies the M_r/Ms ratio is higher than 0.93. It means that at the remanence the magnetic moment of the cobalt rods are still parallel to the long axis. As a consequence the nuclear form factor and the magnetic form factor will contribute both to a strong scattering intensity perpendicular to the rods.

IV.6.2 Influence of the rod mean diameter on the SANS pattern

The normalized 2D patterns of the assemblies $R_{17.4}$, $R_{18.4}$ and $R_{30.0}$ are presented in the Figure IV- 10 a, b, c.

The SANS patterns are all anisotropic, with the intensity scattered perpendicularly to the rods much more intense than parallel to the alignment. The $I^{\parallel}(q)$ and $I^{\perp}(q)$ curves were obtained by integration in parallel and perpendicular directions with an angle of 30°. They are plotted in Figure IV- 10 d, e, f. In all cases we can see that $I^{\perp}(q)$ is much higher than $I^{\parallel}(q)$. This is in good agreement with a SANS pattern of an oriented assembly of anisotropic particles. As we saw in the previous section for nanorod mean length 100 nm $I^{\parallel}(q)$ decreases very fast to zero when q increases, due to the particular form and magnetic factors of cylinders.

On the $I^{\perp}(q)$ curves a well-defined peak can be observed in the case of $R_{17.4}$ and $R_{18.4}$, and two peaks in the case of $R_{30.0}$. These peaks are due to the structure factor and indicate a spatial correlation between the rods and their magnetic moments (rods are in the remanent state but each rod is assumed to be fully saturated) in the assemblies. At a first

approximation the q position of the correlation peak provides a measure of the mean center-to-center distance between the rods, D_m, according to:

$$q_{\perp max} = \frac{2\pi}{D_m} \qquad \text{(Eq. IV-17)}$$

As a result of the SANS measuring in the reciprocal space, the bigger the nanorod's diameter is, the larger the correlation distance between the rods becomes, and thus the $q_{\perp max}$ is found in lower values.

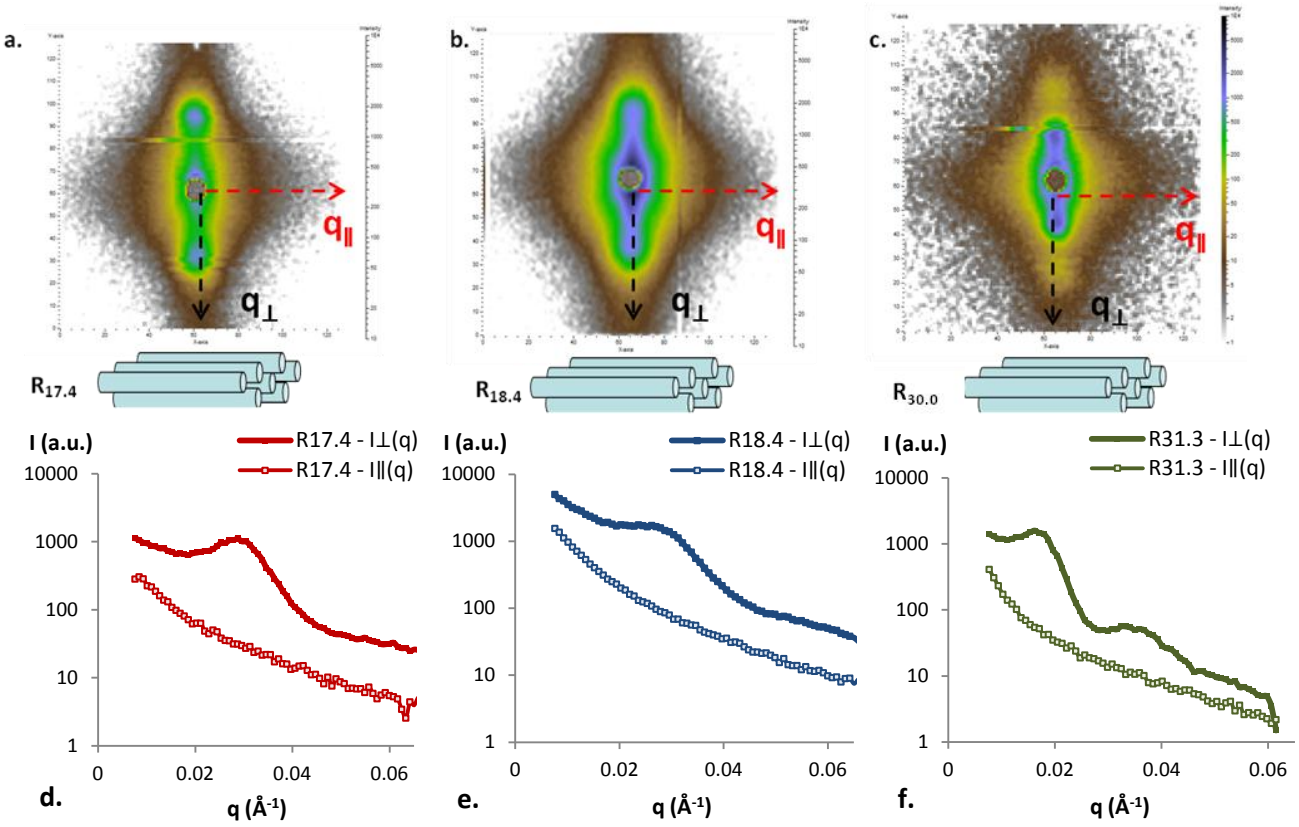

Figure IV- 10 *Normalized scattering spectra on the PAXY spectrometer of the dense cobalt nanorod assemblies:* ***a.*** *$R_{17.4}$,* ***b.*** *$R_{18.4}$ and* ***c.*** *$R_{31.3}$; Normalized intensities as a function of the scattering wave vector q in lin-log scale:* ***d.*** *$R_{17.4}$,* ***e.*** *$R_{18.4}$ and* ***f.*** *$R_{30.0}$.*

Since the baseline is increasing in the region where the maximum correlation peak is observed (Figure IV- 10 d-f) the exact value of $q_{\perp max}$ cannot be defined precisely. To compensate the baseline we chose to plot the anisotropic scattering ratio, $I_{\perp}(q)/ I_{\parallel}(q)$, versus q (Figure IV- 11).

The $q_{\perp max}$ values were found equal to 0.017 Å^{-1}, 0.028 Å^{-1} and 0.029 Å^{-1} for the samples $R_{30.0}$, $R_{18.4}$ and $R_{17.4}$, respectively. These values correspond to mean distances D_m of 36 nm, 21.9 and 21.2 nm. Taking into account the mean rod diameter measured by TEM we can

calculate the mean spacing between rods due to the ligands from: $L_m = D_m - d_m$. We found L_m values of 6 nm, 3.5 nm and 3.7 nm for the samples $R_{30.0}$, $R_{18.4}$ and $R_{17.4}$, respectively. All these values are summarized in Table IV-2.

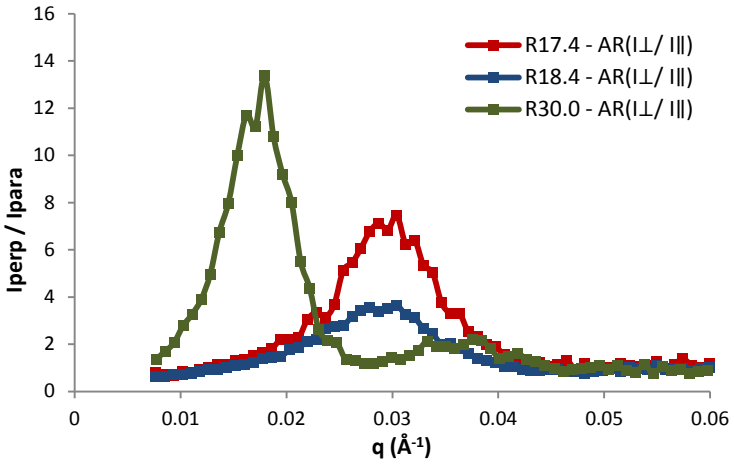

Figure IV- 11 *Anisotropic scattering ratio intensity versus the wave vector q of the assemblies*

Sample	d_m (nm)	$q_{\perp max}$ ($Å^{-1}$)	D_m (nm)	L_m (nm)
$R_{17.4}$	17.4	0.029	21.2	3.7
$R_{30.0}$	30.0	0.017	36.0	6
$R_{18.4}$	18.4	0.028	21.9	3.5

Table IV- 2 *Characteristic lengths of the assemblies $R_{17.4}$, $R_{18.4}$ and $R_{30.0}$: d_m mean diameter of the rods , D_m mean center to center rod distance calculated from $q_{\perp max}$ and L_m mean ligand length between the rods.*

In order to compare the magnetic volume fraction calculated by TGA and magnetic measurements, as it was described in chapter III, with our SANS results, we have considered rods aligned in a perfectly hexagonal array, like in the Figure IV- 12. In that case considering very high aspect ratio we can calculate V_M as:

$$V_M^{SANS} = \frac{\pi(d_{TEM}-2e)^2}{4D_m^2 \sin 60^\circ} \qquad \text{(Eq. IV-18)}$$

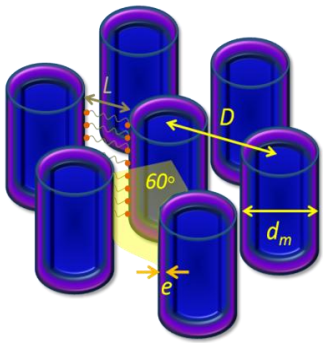

Figure IV- 12 *Hexagonal array of Co NRs.*

where e is the thickness of the CoO shell deduced from TGA and VSM measurements (see also Chapter III, section III.6.1).

In the Table IV- 2 are compared the magnetic volume fractions measured from TGA and from SANS for the three assemblies. In the case of the samples $R_{17.4}$ and $R_{18.4}$ the two V_M are

very close; while in the case of the $R_{30.0}$ the volume fraction deviates due to the nanorods' roughness.

Sample	d_m (nm)	e (nm)	D_m (nm)	V_M^{TGA} (%)	V_M^{SANS} (%)
$R_{17.4}$	17.4	1.5	21.2	40.6	41.8
$R_{18.4}$	18.4	1.0	21.9	52.0	50.5
$R_{30.0}$	30.0	1.8	36.0	47.7	56.8

Table IV- 3 *Characteristic lengths of the assemblies $R_{17.4}$, $R_{18.4}$ and $R_{30.0}$: **d_m** mean diameter of the rods, **e** thickness of the CoO shell, **D_m** mean center to center rod distance calculated from $q_{\perp max}$, V_M^{TGA} deduced from TGA and V_M^{SANS} deduced from SANS measurements.*

IV.6.3 Influence of the rod organization on the SANS pattern

The maximum of the anisotropic scattering ratio, $I_\perp(q)/ I_\parallel(q)$, varies from one sample to another (Figure IV- 11). The highest $[I_\perp(q)/ I_\parallel(q)]_{max}$ = 13.4 is observed for the sample $R_{31.3}$, followed by $R_{17.4}$ and $R_{18.4}$ with $[I_\perp(q)/ I_\parallel(q)]_{max}$ equal to 7.5 and 3.5, respectively.

This highest contrast for the assembly $R_{31.3}$ is due to the rods' larger volume. Indeed, the form factor of the rods is proportional to their volume, so to the square of their diameter, and the scattered intensity is proportional to the square of the form factor (Eq. IV-11). A factor 2 on the diameter will be traduced by a factor 8 on the intensity.

The other parameter that can have an effect on the $[I_\perp(q)/ I_\parallel(q)]_{max}$ ratio is the quality of the rod alignment. The correlation peak is expected to be more intense with the best alignment. The relatively similar mean rod diameter of the assemblies $R_{18.4}$ and $R_{17.4}$ allows us to conclude that the sample $R_{17.4}$ presents better alignment than $R_{18.4}$. This is in good agreement with the measured squareness of the hysteresis loop. The comparison with SQ and $[I_\perp(q)/ I_\parallel(q)]_{max}$ values are summarized in Table IV-4.

Sample	d_m (nm)	SQ	$[I_\perp(q)/ I_\parallel(q)]_{max}$
$R_{17.4}$	17.4	0.86	7.5
$R_{18.4}$	18.4	0.75	3.5

Table IV- 4 *Characteristic lengths of the assemblies $R_{17.4}$ and $R_{18.4}$: d_m mean diameter of the rods , **D_m** mean center to center rod distance calculated from $q_{\perp max}$ and **L_m** mean ligand length between the*

rods. The ***SQ*** *and* $[I_{\perp}(q)/ I_{/\!/}(q)]_{max}$ *presented as means for the evaluation of the rods' alignment quality.*

IV.7 Magnetization reversal in cobalt nanorod assemblies – SANS under applied field

In the SANS measurements described in the previous section the intensity scattered perpendicular to the rods was a sum of the nuclear and magnetic contributions. In the present section we will go further varying the magnetic state of the nanorods thanks to an external magnetic field.

The cobalt nanorod assemblies were installed on the substrate with the rods parallel or perpendicular to the external field. In both cases the rods were perpendicular to the incident beam. Based on the fact that the nuclear contribution does not depend on the external field, while the magnetic cross section is field-dependent, this experiment should make possible to separate the nuclear from the magnetic scattering intensity. The purpose was to examine the magnetization reversal process and to obtain information on characteristic magnetic length scales, i.e. magnetic domains.

IV.7.1 Experimental details

The PAXY set-up includes an electromagnet providing a maximum field of 1.6 T perpendicular to the neutron beam. The rod assembly was fixed in the (x,y) plane (Figure IV-13).

Figure IV- 13 *Photograph of the experimental set-up showing the sample holder centered in between the coils of the electromagnet. The magnetic field was applied perpendicular to the neutron beam.*

SANS experiments were performed for two different orientations. First, the rods direction was vertical (along y), in this case the magnetic field was applied perpendicular to the rods,

notation $H_{\perp}$. Then the assembly was rotated by 90° to have the applied field parallel to the rods, noted $H_{\parallel}$. The Figure IV- 14 and Figure IV- 15 illustrate the experimental set-up for the two orientations.

In both cases the rods were saturated at -1.6 T and then the field's value was varied over two quadrants of the hysteresis loop.

For the perpendicular orientation (Figure IV- 14) the rods were magnetized at -1.6 T and then SANS measurements were carried out from 0 to +1.6 T and from 1.6 T back to 0 T, with step of 0.4 T and duration for each measurement 15 min. Unfortunately, the provided field from the electromagnet was not sufficient to reach full saturation of the rods (see Figure IV- 14 b.) but allowed to reach the reversible region.

The obtained data were normalized according to the protocol presented in the section IV.2.4. From the 2D patterns we deduced the scattered intensities perpendicular and parallel to the rods' long axis, $\left(I_{H_{\perp}}^{\perp}\right)$ and $\left(I_{H_{\perp}}^{\parallel}\right)$ respectively. In order to simplify the notations we will name them $A = I_{H_{\perp}}^{\perp}$ and $B = I_{H_{\perp}}^{\parallel}$.

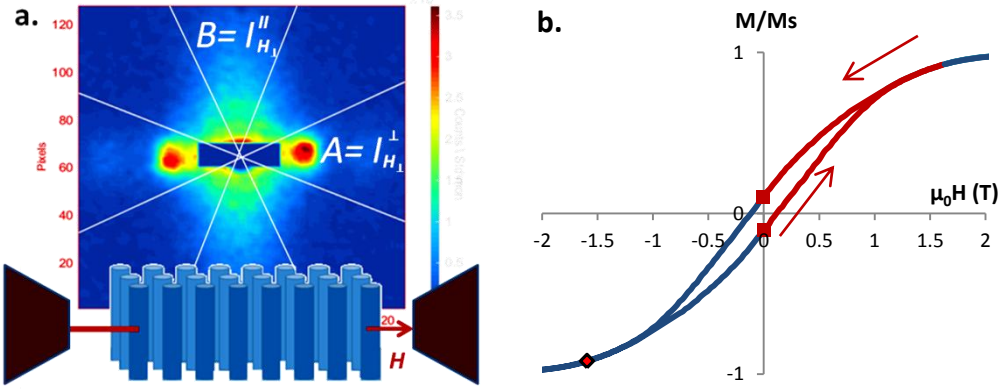

Figure IV- 14 *Experimental set-up of SANS under magnetic field: (a) field applied perpendicular to the rods' alignment direction, $H_{\perp}$; (b) Characteristic hysteresis loop measured in perpendicular to the rods' alignment direction. The red diamonds and squares indicate the saturation applied field (-1.6 T) before the SANS experiment and the starting/ending fields of the measurement.*

For the parallel orientation (Figure IV- 15) the rods were saturated at -1.6 T and the SANS measurements were carried out from 0 to + 0.59 T (with a step of 0.03 T and a duration of 15 min for each pattern) to include the coercivity, and then up to 1.6 T (t= 1 h).

The obtained data were normalized according to the protocol presented in the section IV.2.4. From the 2D patterns were deduced the scattered intensities perpendicular and parallel to the rods' long axis, $\left(I_{H_{\parallel}}^{\perp}\right)$ and $\left(I_{H_{\parallel}}^{\parallel}\right)$, respectively. For practical reasons we will name them $C = I_{H_{\parallel}}^{\perp}$ and $D = I_{H_{\parallel}}^{\parallel}$ (Figure IV- 15 b).

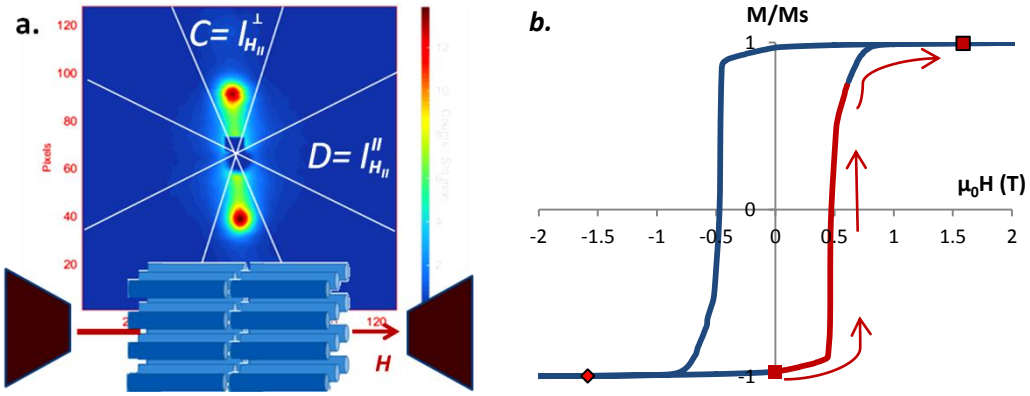

Figure IV- 15 *Experimental set-up of SANS under magnetic field:* ***a.*** *field applied parallel to the rods' alignment direction, $H_{//}$;* ***b.*** *characteristic hysteresis loop measured in parallel to the rods' alignment direction. The red diamonds and squares indicate the saturation applied field (-1.6 T) before the SANS experiment and the starting/ending fields of the measurement.*

IV.7.2 Sample description

The sample analyzed by SANS under magnetic field was a nanorod assembly, noted $R_{20.4}$, comprised of Co NRs with smooth surface and flat endings, d_m= 20.4 ± 2 nm and l_m= 94 ± 40 nm. In the Figure IV- 16 are illustrated a TEM image of the pre-aligned nanorods, the SEM image of their assembly and its hysteresis loop, where the measuring field was applied parallel and perpendicular to the rods' alignment axis. The magnetic volume fraction and the CoO shell thickness were deduced from the TGA and VSM measurements. All the magnetic and structural characteristics of the sample are summarized in the Table IV- 5 and Table IV- 6.

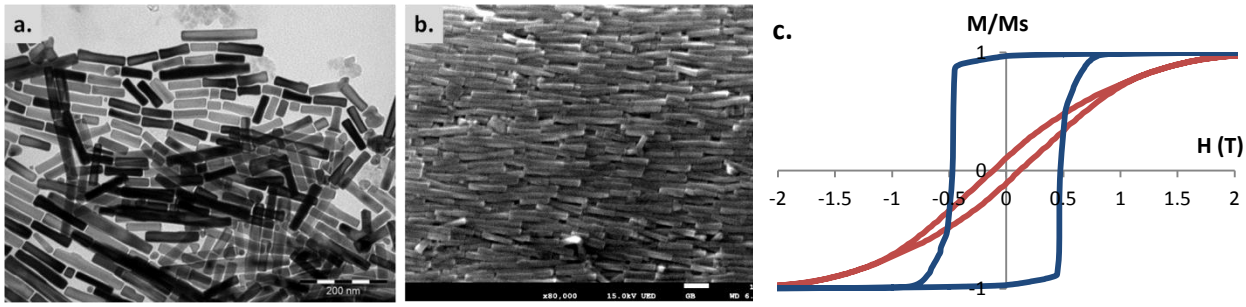

Figure IV- 16 a. *TEM image of the cobalt nanorods of d_m= 20.4 ± 2 nm and l_m= 94 ± 40 nm;* ***b.*** *SEM image of their aligned assembly, $R_{20.4}$;* ***c.*** *M(H) loops measured in parallel and perpendicular to their alignment axis.*

Sample	d_m (nm)	l_m (nm)	e (nm)	V_M (%)
$R_{20.4}$	20.4	94	0.9	46.2

Table IV- 5 *Morphological characteristics of the assembly $R_{20.4}$ where: **d_m** and **l_m** is the rods' mean diameter and length; **e** the CoO shell thickness and **V_M** the magnetic volume fraction of their assembly.*

	H_{ci} (kA·m^{-1})	$\mu_0 H_{ci}$ (T)	M_r/M_s	SQ
H ∥ NRs	376	0.47	0.97	0.91
H ⊥ NRs	74	0.05	0.15	--

Table IV- 6 *Magnetic characteristics of the assembly $R_{20.4}$ measured in the VSM with the applied field in parallel, **H // NRs**, and perpendicular, **H ⊥ NRs**, to the rods' alignment direction. Where **H_{ci}** is the coercivity measured from the corresponding M(H) loops; **M_r/M_s** the orientation coefficient and **SQ** the squareness.*

IV.7.3 SANS results

IV.7.3.1 Perpendicular orientation

The Figure IV- 21 shows the evolution of the normalized 2D scattered intensity, $I_{H_\perp}$, after saturation at -1.6 T, at different magnetic fields from 0 to +1.6 T and back to 0 T. All patterns are anisotropic with the intensity perpendicular to the rods more intense than the parallel one.

The Figure IV- 17 shows the evolution of the intensity profile perpendicular to the rods, $A = I_{H_\perp}^{\perp}$, with the increasing magnetic fields and the Figure IV- 18 the intensity profile parallel to the rods long axis, $B = I_{H_\perp}^{\parallel}$, for the same fields. One can clearly see that in the whole q range the A decreases progressively when the magnetic field is increased from 0 T to 1.6 T, while at the opposite B increases when H is increased (except at very small q).

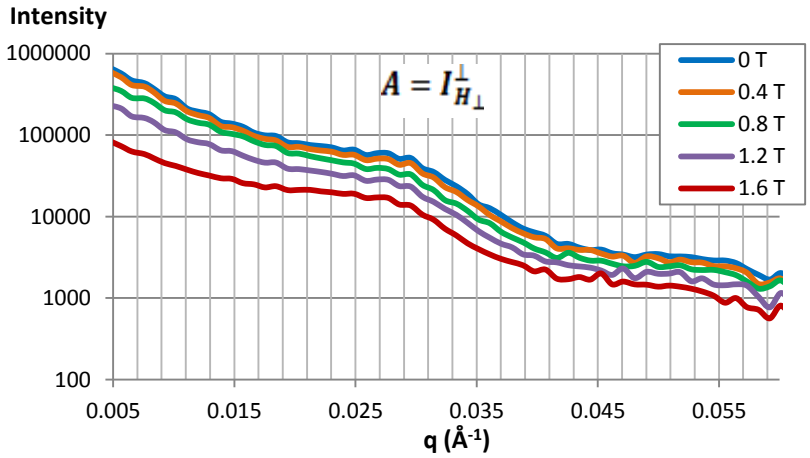

Figure IV- 17 *Evolution with the applied perpendicular field of the scattering intensity perpendicular to the rods.*

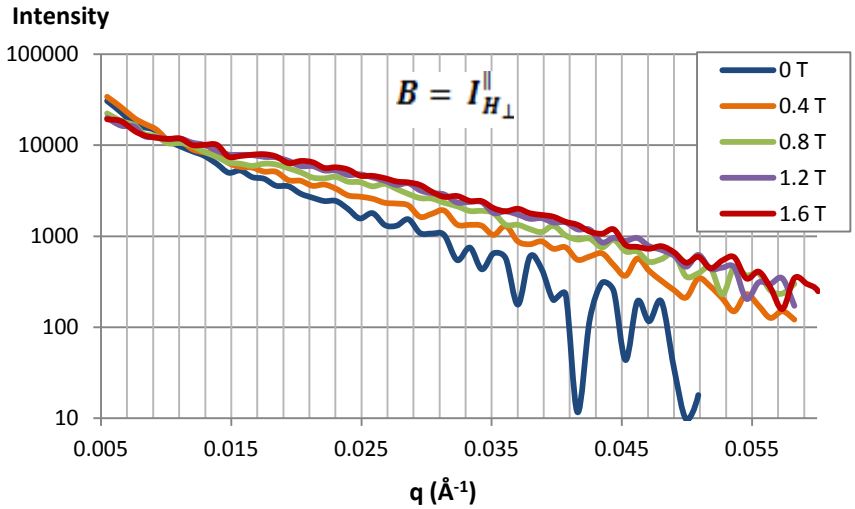

Figure IV- 18 *Evolution with the applied perpendicular field of the magnetic scattering intensity parallel to the rods*

In the Figure IV- 19 and Figure IV- 20 are compared A and B at 0 T, and A and B at 1.6 T, respectively.

- There is a very high contrast between the A and B at 0 T. After being saturated at -1.6 T along the hard axis the external magnetic field is switched off, so the magnetic moments flipped to the easy axis which is the rods' long axis (Figure IV- 19 b). In this remanent state the magnetization in the B direction is almost zero. As a consequence the contributions of both nuclear and magnetic form factor give a strong perpendicular scattering intensity (A), much higher than the parallel one (B).
- When H is increased from 0 to 1.6 T the magnetic moment tends to orient in the field's direction. As a consequence the A intensity decreases because it loses progressively the magnetic scattering. Note that the difference of intensity between A(0 T) and A(1.6 T) is quasi one order of magnitude at small q. At the opposite, when H is increased the B intensity gains the magnetic scattering.

- Even if the saturation is not reached at 1.6 T we considered on the sketch of Figure IV-20 b the ideal case where the magnetic moments are perpendicular to the rods' long axis. At 1.6 T the intensity scattered along A is due to the nuclear form factor only, while the intensity scattered along B is due to the magnetic form factor.

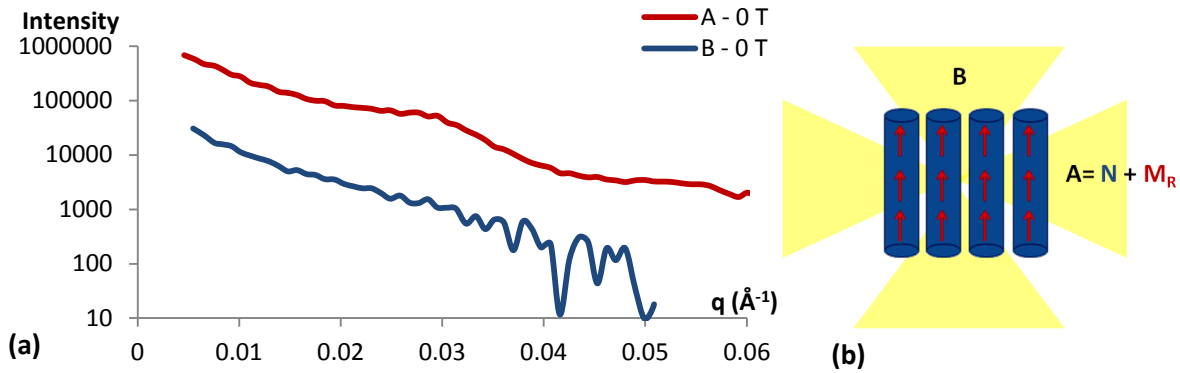

Figure IV- 19 (a) *SANS intensities* $\boldsymbol{A} = \boldsymbol{I}^{\perp}_{\boldsymbol{H}_{\perp}}$ *and* $\boldsymbol{B} = \boldsymbol{I}^{\parallel}_{\boldsymbol{H}_{\perp}}$ *at 0 T;* ***(b)*** *simplified version of the nanorod assembly with the magnetic moments direction at 0 T, where N is the nuclear contribution and* M_R *the magnetic contribution at remanence.*

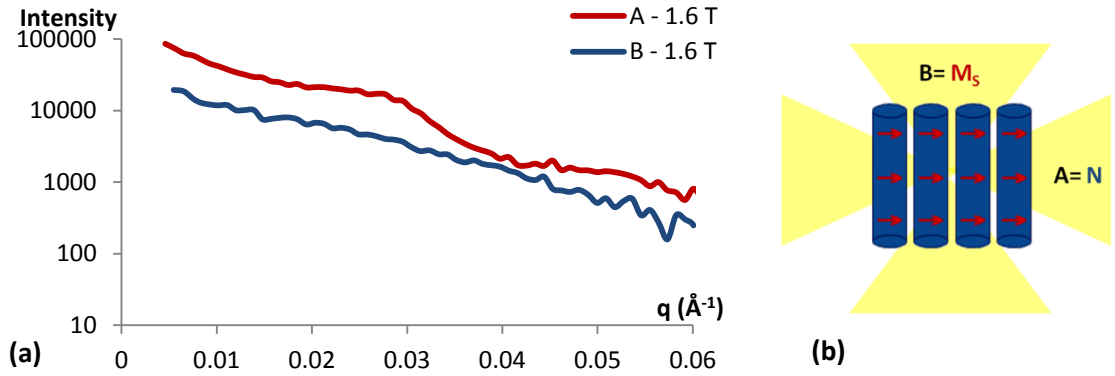

Figure IV- 20 (a) *SANS intensities* $\boldsymbol{A} = \boldsymbol{I}^{\perp}_{\boldsymbol{H}_{\perp}}$ *and* $\boldsymbol{B} = \boldsymbol{I}^{\parallel}_{\boldsymbol{H}_{\perp}}$ *at 1.6 T;* ***(b)*** *simplified version of the nanorod assembly with the magnetic moments direction at 1.6 T, where N is the nuclear contribution and* M_s *the magnetic contribution at saturation.*

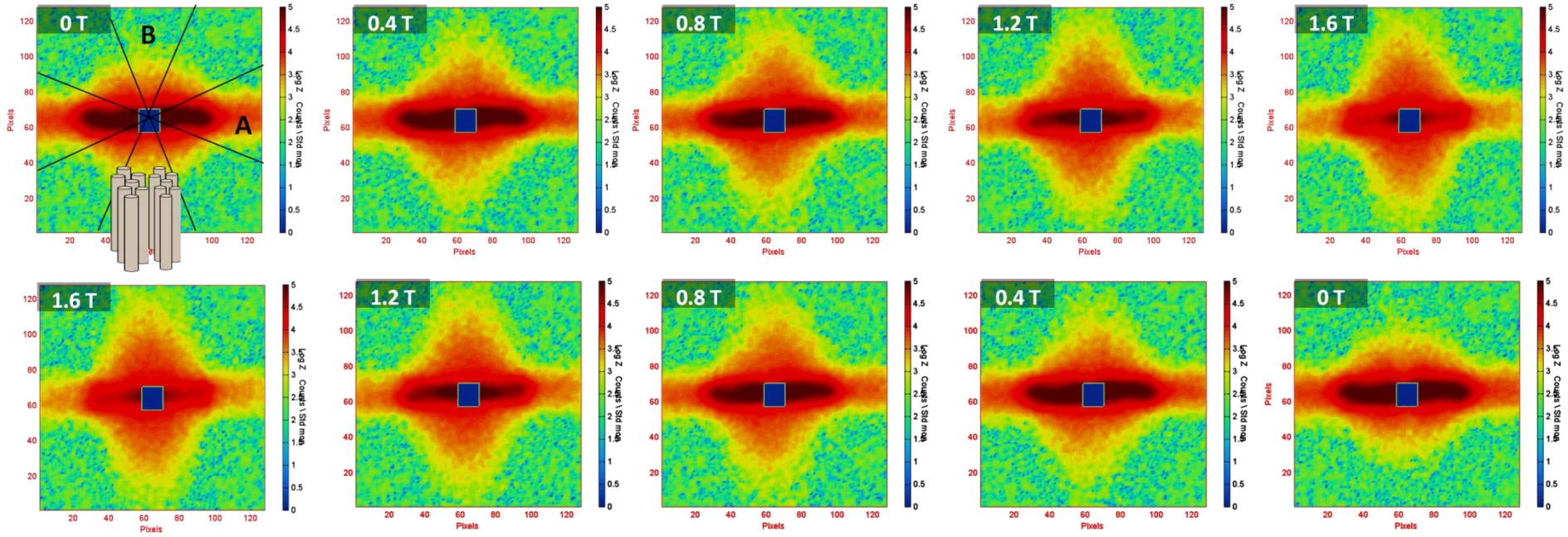

Figure IV- 21 *SANS evolution under magnetic field for the nanorod assembly placed with its alignment axis perpendicular to the applied field. Where* $\boldsymbol{A} = \boldsymbol{I}^{\perp}_{\boldsymbol{H}_{\perp}}$ *and* $\boldsymbol{B} = \boldsymbol{I}^{\parallel}_{\boldsymbol{H}_{\perp}}$.

$\mathbf{A = I_{H_\perp}^{\perp}}$

The intensity A at 1.6 T, corresponding solely to the nuclear contribution of the nanorods to the scattering, is plotted on Figure IV- 22.

At small q, in the range of 0.005 ≤ q ≤ 0.018 Å^{-1}, the curve's slope fits very well with a q^{-1} law, which is characteristic of the scattered intensity by an assembly of 1D objects with a distribution on the long axis orientation. These 1D objects are not the individual rods because a plateau would have been expected at small q owing to the small mean diameter of the rods. These 1D objects are probably rods fibers with a mean diameter higher than the limit of the experiment which is for q= 0.005 Å^{-1} a distance in the direct space of 125 nm. It suggests a fiber texturation of the assembly.

On this curve the correlation peak is less marked than in the patterns reported before, certainly because the magnetic contribution was removed by the magnetic field.

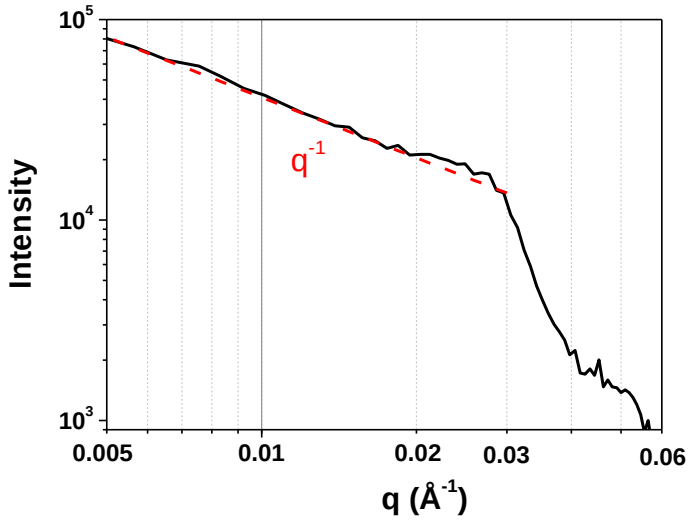

Figure IV- 22 *SANS intensity* $\boldsymbol{A = I_{H_\perp}^{\perp}}$ *at 1.6 T in a log-log scale and its slope for 0.004 ≤ q ≤ 0.018 Å^{-1} (red dashed line).*

As represented schematically on the Figure IV- 23 the subtraction of A(1.6 T) to A(0 T) consists in erasing the nuclear contribution to the perpendicular scattering. Indeed, the intensity profile $[I_{H_\perp}^{\perp}(0T)]$ is due to the nuclear plus the magnetic moment scattering at the remanence while $[I_{H_\perp}^{\perp}(1.6T)]$ is only due to the nuclear scattering. Thus, the difference will give an idea of the magnetic contribution in the remanent state.

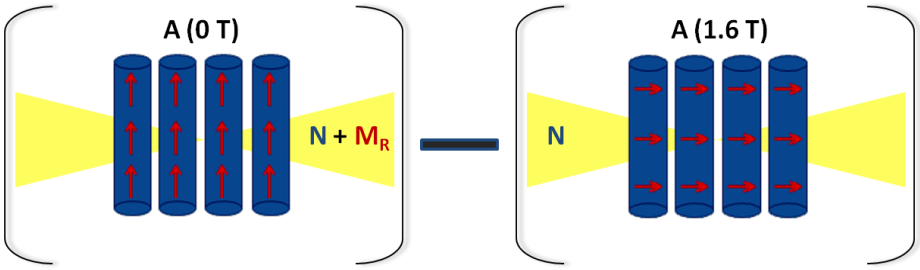

Figure IV- 23 *Simplified scheme of the nanorod assembly showing the direction of the magnetic moments at 0 T and 1.6 T, and the different contribution scattering the neutrons perpendicularly to the rods; N is the nuclear contribution and M_R the magnetic contribution at remanence.*

The intensity profile A(0 T)-A(1.6 T) is plotted on the Figure IV- 24a in a log-log scale. We observe :

- at intermediate q , 7.5E-3 $Å^{-1}$ < q < 2E-2 $Å^{-1}$, the intensity profile fits with a q^{-2} law.
- at very small q , q < 7.5E-3 $Å^{-1}$ a q^{-1} law observed again.

Since the subtraction probes the magnetic contribution, this q^{-2} law may correspond to "aggregates" of magnetic moments, or in other words to magnetic domains. After being saturated at 1.6 T along the hard axis the field was gradually decreased to 0. When the field was switched off, at 0 T the majority of the magnetic moments relaxed along the easy axis. We can imagine that ~50% of the moments are up and ~50% down with the formation of magnetic domains, explaining this q^{-2} law.

The q range, in which the q^{-2} law is observed, corresponds to characteristic length in the direct space between 31 and 85 nm. It may indicate that the domains have a limited extension in the perpendicular direction (domains of a few rods since 85 nm is approximately 4 times the mean diameter) (Figure IV- 24 b). The q^{-1} law observed again at very small q may be due to larger elongated domains that spread in the parallel direction.

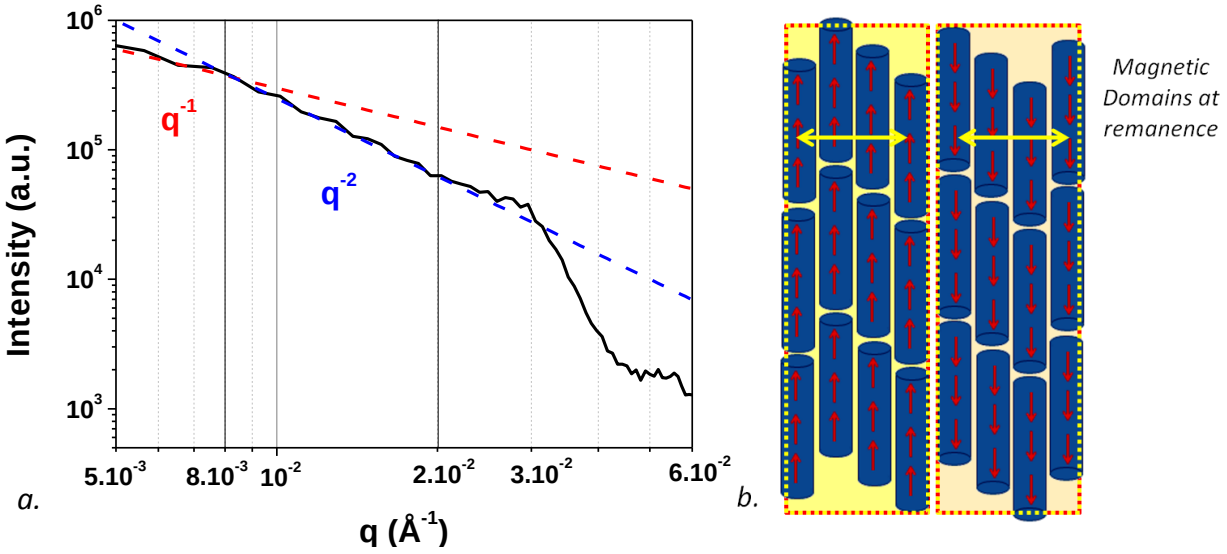

Figure IV- 24 a. *SANS intensity profile* $\boldsymbol{A\,(0\,T) - A(1.6\,T) = I^{\perp}_{H_{\perp}}(0\,T) - I^{\perp}_{H_{\perp}}(1.6\,T)}$ *in a log-log scale;* ***b.*** *Magnetic domains at remanence at the perpendicular direction of width 85 nm.*

$\boldsymbol{B = I^{\parallel}_{H_{\perp}}}$

On the Figure IV- 25a is plotted the intensity scattered parallel to the rods, $B = I^{\parallel}_{H_{\perp}}$, at 0 T and at 1.6 T in log-log scale. We can see that for q < 0.03 Å^{-1} a q^{-2} law fits well the B(0 T) intensity profile while a q^{-1} law fits better the B(1.6 T) intensity profile.

- For the field of 1.6 T the majority of the magnetic moments have tilted perpendicular to the rod long axis. The q^{-1} law suggests the formation of magnetic wires/elongated domains formed by the magnetic moments perpendicular to the rods as in the scheme of Figure IV-25b.
The fact that no correlation peak is observed on the B(1.6 T) profile can be attributed to the lack of correlation between the magnetic moments laying along the hard axis, certainly because we do not have any structural order in the direction parallel to the long axis of the rods (SEM image Figure IV- 16).

- At 0 T, i.e. at the remanence, the magnetic moments are in majority parallel to the long axis and do not scatter the neutrons in the B direction. Nevertheless, the magnetization at the remanence is not exactly zero (see the hysteresis loop on Figure IV- 16). Some magnetic domains perpendicular to the rods and/or some rod aggregates perpendicular to the main orientation of the rods could explain the q^{-2} law followed by B(0 T). These domains or aggregates are however only few because the intensity scattered is very weak.
An intriguing point is that at very small q (q < 0.009 Å^{-1} corresponding to a characteristic length in the direct space > 70 nm) the intensity at the remanence is higher than the intensity at saturation: B(0 T) > B(1.6 T). It suggests the presence of big magnetic objects that scatter the neutron in the direction parallel to the rods. For the moment we do not have a clear interpretation of this observation.

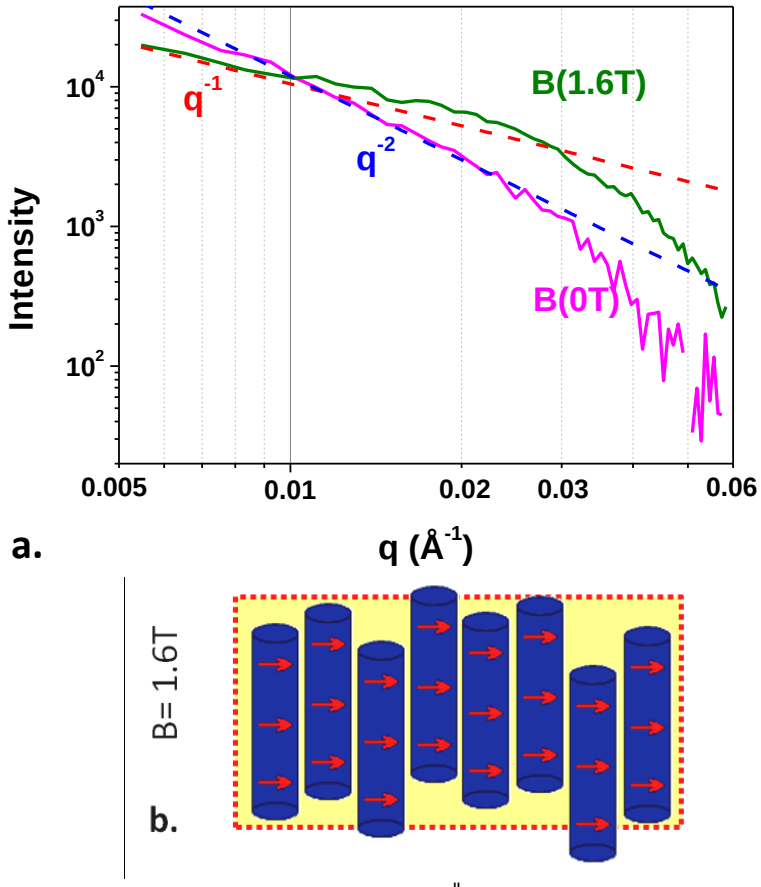

Figure IV- 25 ***a.*** *Magnetic scattering intensity* $\boldsymbol{B = I^{\parallel}_{H_{\perp}}}$ *at 0 and 1.6 T;* ***b.*** *Magnetic wires/domains formed by the magnetic moments alignment perpendicular to the rods at 1.6 T.*

IV.7.3.2 Parallel orientation

In a second set of experiments the same rod assembly was placed with the rod axis parallel to the applied field. The rods were saturated by a magnetic of -1.6 T parallel to the rods. The Figure IV- 28 shows the variation of the normalized 2D scattering intensity, $I_{H_{\parallel}}$, at different magnetic field from 0 to +1.6 T, after saturation at -1.6 T. The corresponding M(H) loop is given on the Figure IV- 16.

For all fields the SANS pattern is anisotropic with the scattering intensity perpendicular to the rods, $C = I^{\perp}_{H_{\parallel}}$, more intense than the parallel one, $D = I^{\parallel}_{H_{\parallel}}$. On the Figure IV- 26 are plotted C(1.6 T) and D(1.6 T) and the schematic representation of the magnetic state of the rod assembly. According to the hysteresis loop (Figure IV- 16), in a field of 1.6 T the saturation magnetization is reached. All the magnetic moments are parallel to the field and to the rods. So, the intensity C(1.6 T) results from both the nuclear and the magnetic moment

contributions. It explains the strong contrast with D(1.6 T) for which neither the nuclear not the magnetic contributions are well oriented.

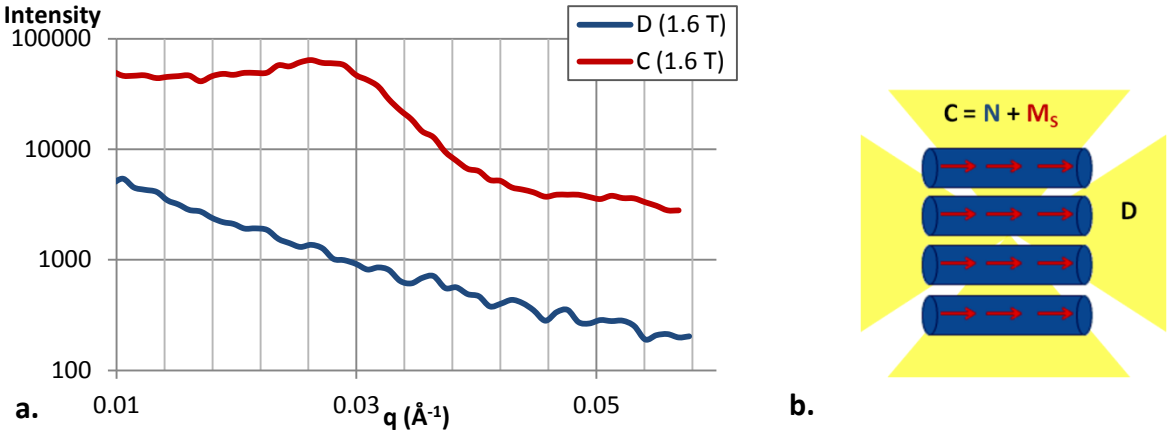

Figure IV- 26 (a) *SANS intensities* $\boldsymbol{C = I^{\perp}_{H_{\parallel}}}$ *and* $\boldsymbol{D = I^{\parallel}_{H_{\parallel}}}$ *at 1.6 T;* ***(b)*** *simplified version of the nanorod assembly with the magnetic moments direction at +1.6 T, where N is the nuclear contribution and* M_S *the magnetic contribution at remanence.*

$\boldsymbol{C = I^{\perp}_{H_{\parallel}}}$

Dealing with the scattering intensity perpendicular to the rods' alignment, $C = I^{\perp}_{H_{\parallel}}$, the Figure IV- 28 clearly evidence two spots corresponding to a correlation peak for H = 0 T and 1.6 T. These spots progressively vanish for an external field H close to the coercive field of the assembly, H_C= 0.47 T (Figure IV- 16 and Table IV-6). The Figure IV- 27 shows the variation of the C profiles with the external field.

Several observations deserve to be commented:

- The profile C(0 T) and C(1.6 T) are almost identical all over the q range (Figure IV- 29 b). It means that the magnetic state at the remanence is very close to the saturation state. This was expected since the M_R/M_S in the parallel configuration was found to be 0.97 (Figure IV- 16; Table IV-6) showing the absence of magnetic modification between the two states (except that the magnetic moment orientation flipped in the opposite direction but the non-polarized neutrons scattering cannot detect this difference, Figure IV- 29).

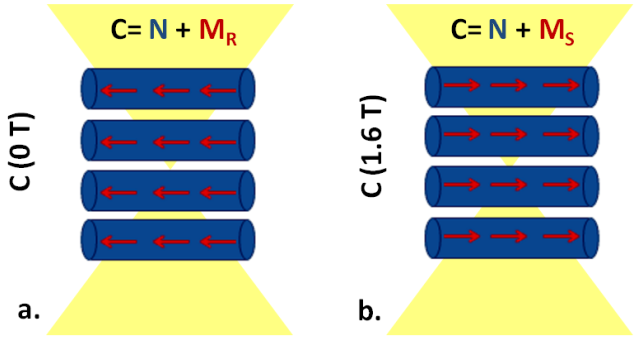

Figure IV- 27 *Simplified version of the nanorod assembly with the magnetic moments direction* ***a.*** *at 0 T (after being saturated at -1.6 T), where N is the nuclear contribution and M_R the magnetic contribution at remanence; b. at +1.6 T, where N is the nuclear contribution and M_s the magnetic contribution at saturation.*

- When the magnetic field was increased from 0 T to a field close to the coercivity, i.e. in the range 0.4-0.47 T, we observe at small q ($q < 0.026$ Å^{-1}) a progressive increase of the intensity (Inset of Figure IV- 29 a) and a progressive decrease of the intensity at high q ($q > 0.026$ Å^{-1});
- When the magnetic field was still increased from 0.47 T to 1.6 T, the intensity decreased at small q and increases at high q to reach again at 1.6 T the same profile than at 0 T.
- The correlation peak, which is clearly marked for magnetic field in the ranges [0-0.35 T] and [0.59-1.6T], fades away for the fields between 0.38 and 0.5 T, i.e. around the coercivity (H_C = 0.47 T).

The strong increasing intensity observed at small q for fields close to the coercivity shows the formation of large magnetic domains scattering the neutrons. On the Figure IV- 29 we have plotted the [C(0.44 T)- A(1.6 T)] in order to examine the perpendicular magnetic contribution at the coercivity, A(1.6 T) corresponding to the nuclear contribution. [C(0.44 T)- A(1.6 T)] is well fitted with a q^{-2} law in the small q range. This observation is also consistent with the formation of domains.

Note that the maximum of intensity at small q is reached for H=0.4 T, a value slightly lower than the coercivity measured on the M(H) loop (H_C= 0.47 T on the M(H) loop). The reason may come from the external shape of the sample measured by SANS and by VSM. The SANS sample was a square platelet but we could not measure the M(H) loop of the whole sample by VSM. Actually, we measured by VSM a smaller assembly of parallel needles. This difference in the external shape may explain a difference on the switching field.

The maximum of intensity of the correlation peak, observed at saturation and remanence, is found for q= 0.028 Å^{-1} which means a mean distance of 22.4 nm. This value is slightly larger than the rod diameter in good agreement with ligands in the inter-rod spacing. The maximm of the correlation peaks will be commented in more details in the next section. The vanishing

of the peak in the field range 0.4 T - 0.5 T (Figure IV- 29) means that around the coercivity the magnetic moment ordering is not so good as in the saturated or remanent state. Magnetic moments have started to flip in the opposite direction and domains are formed. The correlation peak vanishing indicates that the lateral extension of these domains is limited, or in other words the coherence length (perpendicular to the rods) between the magnetic moments inside a domain is small. In the case of very large domains in which a long range order of the magnetic moments would be maintained we should expect a persistence of the correlation peak.

Near the coercivity the global magnetization is zero. But a question arises: how is the spatial organization of the magnetic moments of the rods? The observations described above suggest domains with a small lateral extension like in the schematic representation of the Figure IV- 31 a. The absence of a second correlation peak at smaller q on the C profile near the coercivity (Figure IV- 30) rules out the possibility to have an anti-ferromagnetic order like in the representation of Figure IV- 31b. Complementary information comes from the D profile analysis.

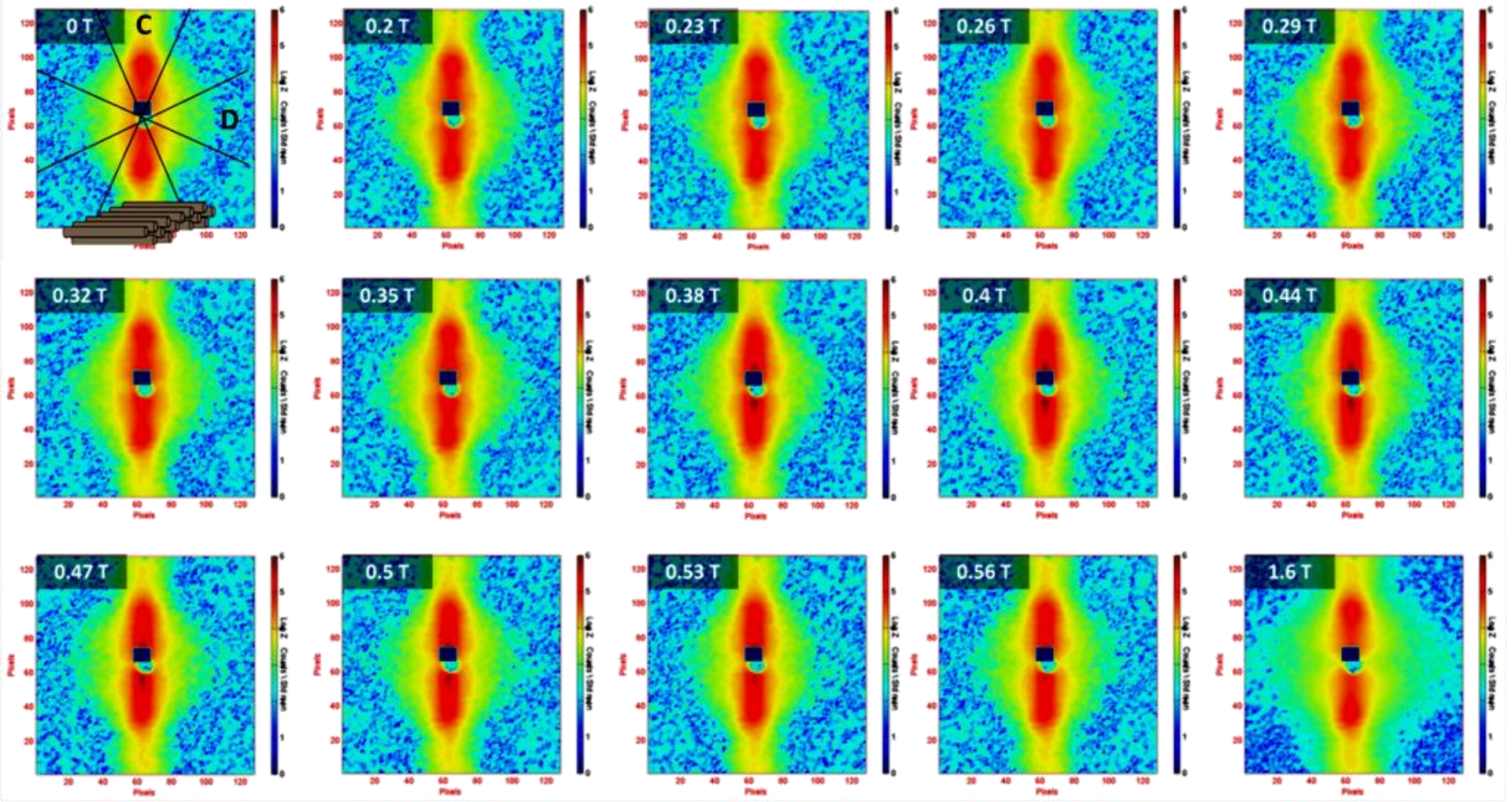

Figure IV- 28 SANS pattern under magnetic field for the nanorod assembly placed with the rod axis parallel to the applied field; $\boldsymbol{C} = \boldsymbol{I}^{\perp}_{\boldsymbol{H}_{\parallel}}$ *and* $\boldsymbol{D} = \boldsymbol{I}^{\parallel}_{\boldsymbol{H}_{\parallel}}$.

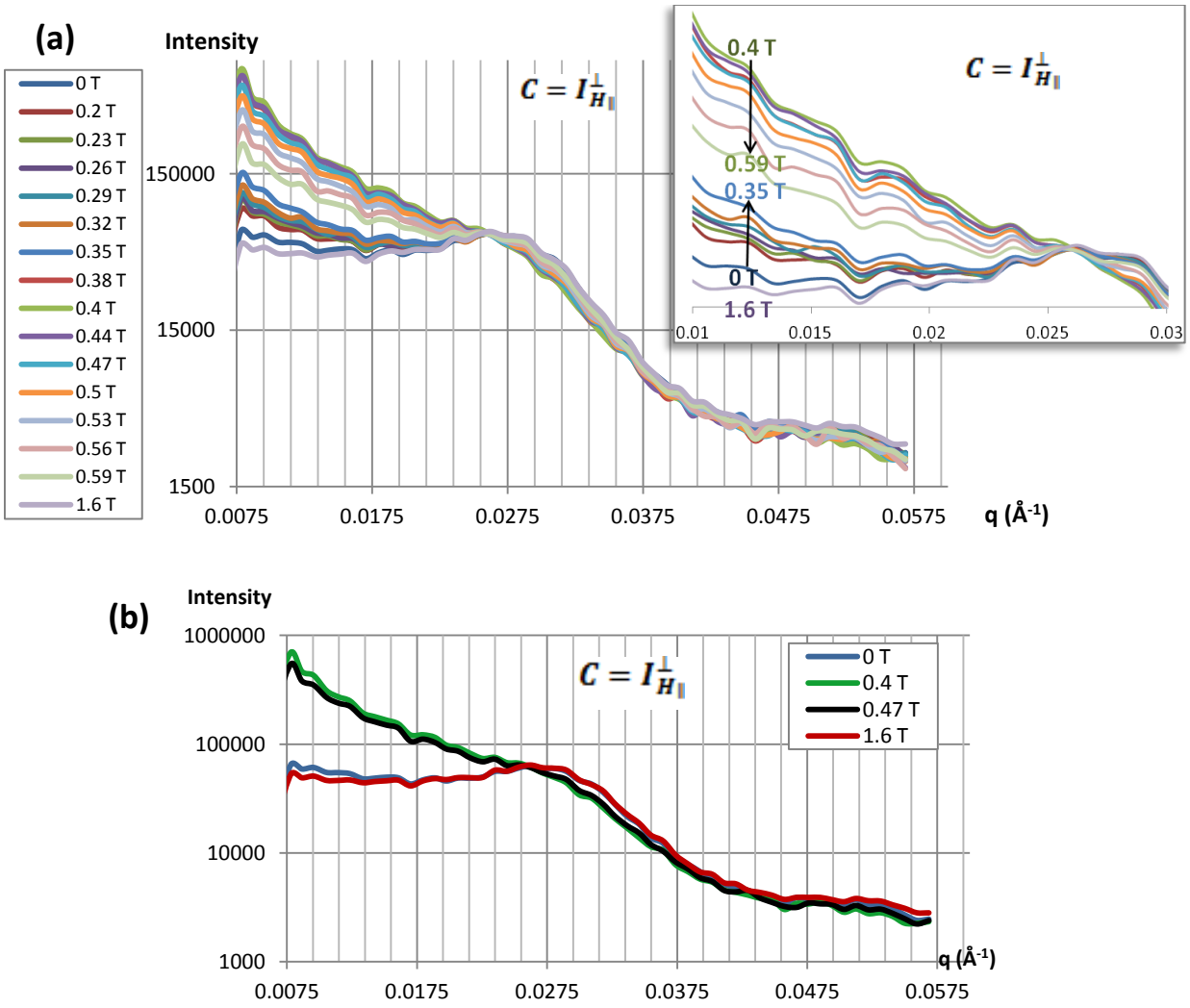

Figure IV- 29 *(a) SANS intensity perpendicular to the rods* $C = I^{\perp}_{H_{\parallel}}$ *with different values of the field applied parallel to the rods. Inset : zoom on the small q range; (b)Selected value of H : 0; 0.4; 0.47 and 1.6 T*

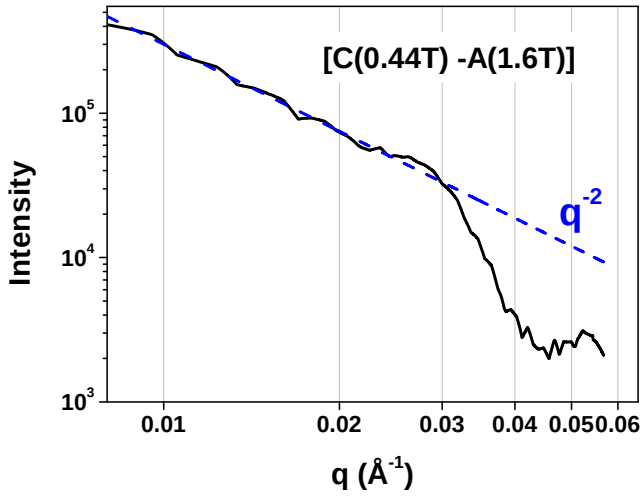

Figure IV- 30 *SANS profile* $C(0.44T) - A(1.6T) = I^{\perp}_{H_{\parallel}}(0.44\,T) - I^{\perp}_{H_{\perp}}(1.6\,T)$ *in log-log scale fitted with a* q^{-2} *law at small q. The nuclear contribution is substracted to the magnetic contribution.*

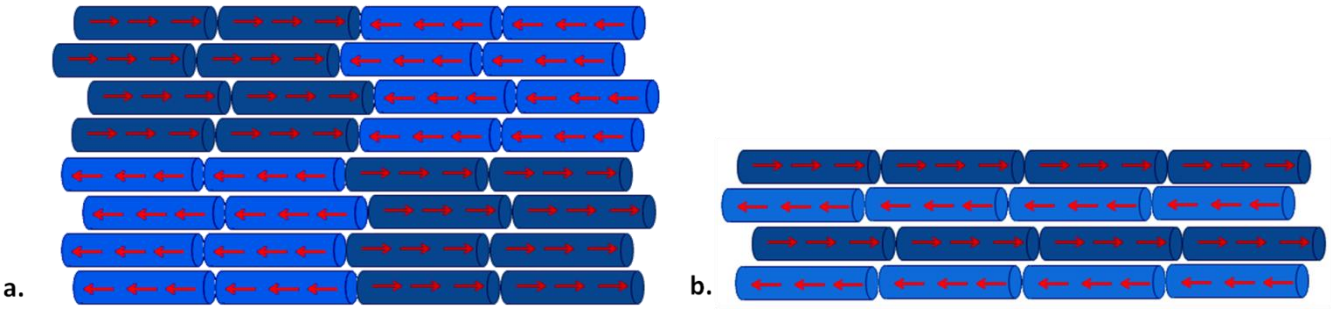

Figure IV- 31 *Schematic representation of* ***a.*** *magnetic domains with the magnetic moment parallel to the easy axis of each rod;* ***b.*** *configuration with an antiferromagnetic order.*

$D = I^{\parallel}_{H_{\parallel}}$

The scattered intensity parallel to the rods' long axis, $D = I^{\parallel}_{H_{\parallel}}$, at different magnetic field values is presented on the Figure IV- 32. The intensity for this direction is always very weak whatever the magnetic field. Moreover, no strong variation of D(H) is observed except at the small q for the field of +1.6 T.

The highest values of D are recorded for H= 0.23-0.26 T and the lowest for H= 1.6 T. The field of 1.6 T aligns all the magnetic moments in the parallel direction explaining the decreasing of the intensity in the direction parallel to the rods.

For the fields in the range 0.23-0.47 T, the D intensity is well fitted by a q^{-2} law at small q (Figure IV- 33) in agreement with the formation of magnetic domains. Nevertheless, the intensity scattered parallel to the rods remains always very low. As we have already seen on Figure IV- 26 there is a strong contrast between C(1.6 T) and D(1.6 T) because at saturation all the scattering contribution is perpendicular to the rods, i.e. along C. Actually the contrast between C(H) and D(H) is very strong for all the H values. The Figure IV- 37 illustrates it at the coercivity (H = 0.47 T). The difference between C(0.47 T) and D(0.47 T) is very similar to the difference between C(1.6 T) and D(1.6 T) shown on Figure IV- 34. It means that there is no strong additional magnetic contribution scattering in the direction of the rods at the coercivity. We can conclude that there is no magnetic domain with the magnetic moments oriented perpendicular to the rods (Figure IV- 35).

The small increase of D close to the coercivity compared to D(1.6 T) may be due to the magnetization reversal at the tips of the rods. But the observation that the highest values of D are recorded for H= 0.23-0.26 T is difficult to comment. According to the M(H) loop nothing should occur in this field range.

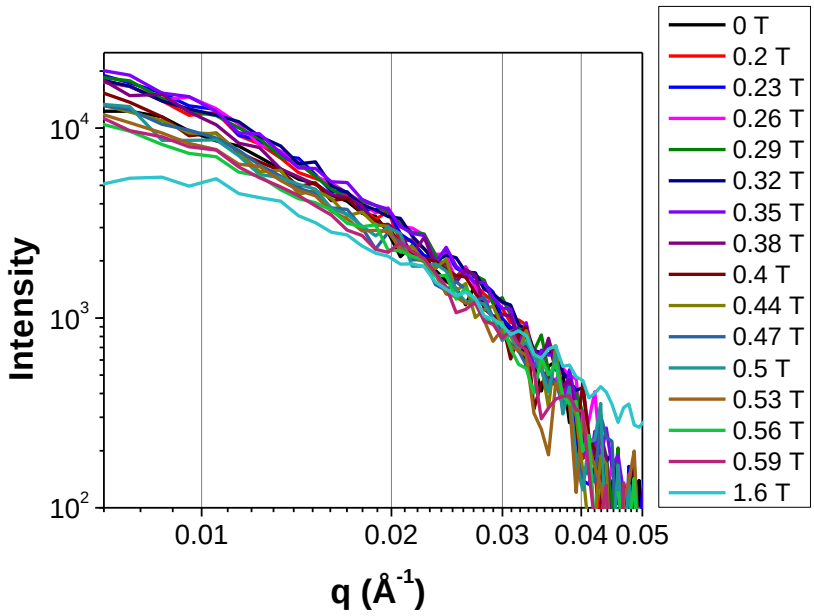

Figure IV- 32 *SANS intensity parallel to the rods,* $\boldsymbol{D = I^{\parallel}_{H_{\parallel}}}$ *, in log-log scale with different applied field parallel to the rods.*

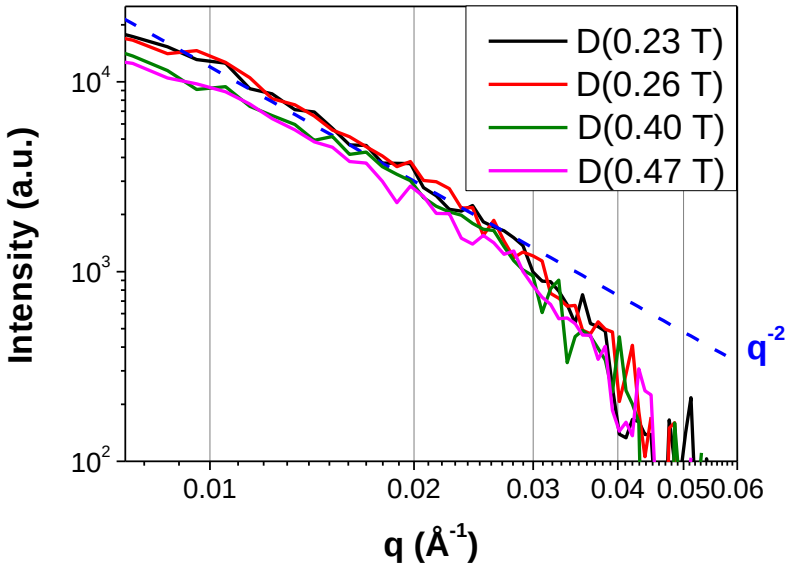

Figure IV- 33 *Variation of the scattering intensity* $\boldsymbol{D = I^{\parallel}_{H_{\parallel}}}$ *for selected fields (0.23, 0.26, 0.40, 0.47 T).*

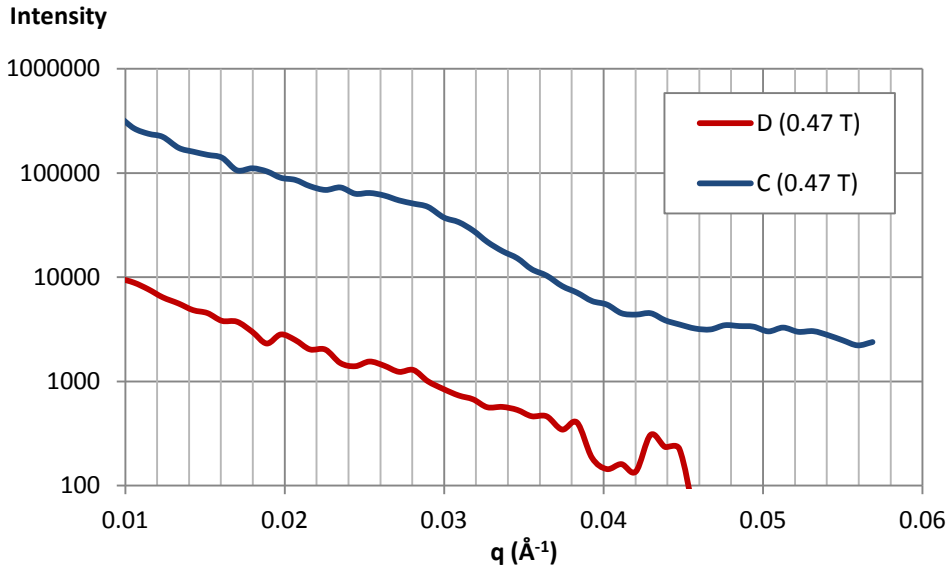

Figure IV- 34 *SANS intensities* $\boldsymbol{C = I^{\perp}_{H_{\parallel}}}$ *and* $\boldsymbol{D = I^{\parallel}_{H_{\parallel}}}$ *at 0.47 T*

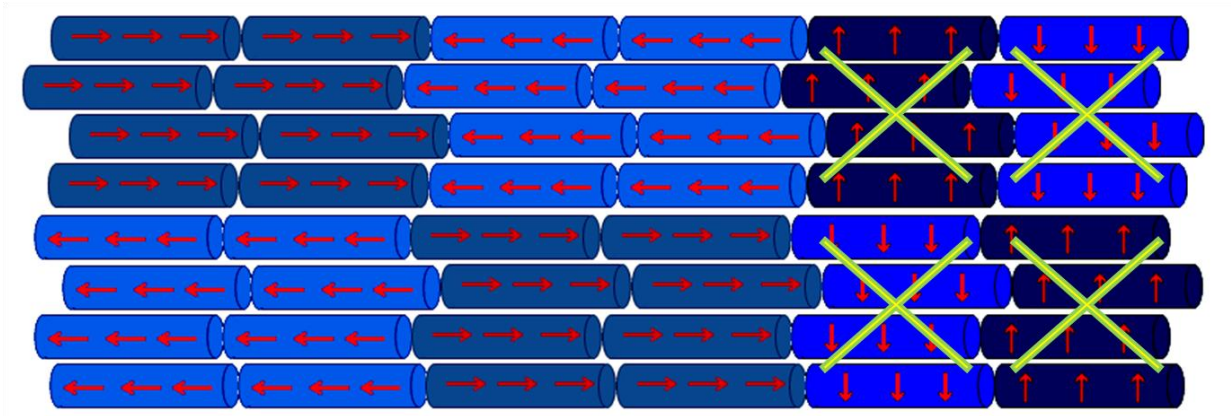

Figure IV- 35 *Schematic representation of the magnetic moments' reversal occurring in parallel to the rods' long axis in opposite directions. We suggest that the magnetization reversal perpendicular to the rods' long axis is difficult due to its high energy cost.*

IV.7.3.3 Correlation peak

A correlation peak is observed in the scattering intensity profile perpendicular to the rods (A or C):

- on the A(1.6 T) profile, corresponding to the nuclear contribution (Figure IV-20a);
- on the [A(0 T)- A(1.6 T)] profile, corresponding to the magnetic contribution at the remanence after being saturated along the hard axis (Figure IV-24a);
- on the C(1.6 T) profile, corresponding to the nuclear and magnetic contributions at saturation (Figure IV-28);

-and, as we will see, also on the [C(1.6 T)- A(1.6 T)] profile corresponding the magnetic scattering at saturation (Figure IV-38).
As a matter of fact, taking into account that C (1.6 T) is due to the nuclear and magnetic scattering of the moments aligned parallel to the rods and that A(1.6 T) is solely due to the nuclear scattering (Figure IV- 20) in [C(1.6 T)- A(1.6 T)] we subtract the nuclear contribution to keep only the scattering contribution of the magnetic moments at saturation. The Figure IV-36 shows a simplified scheme of the corresponding intensities and the result of their subtraction.

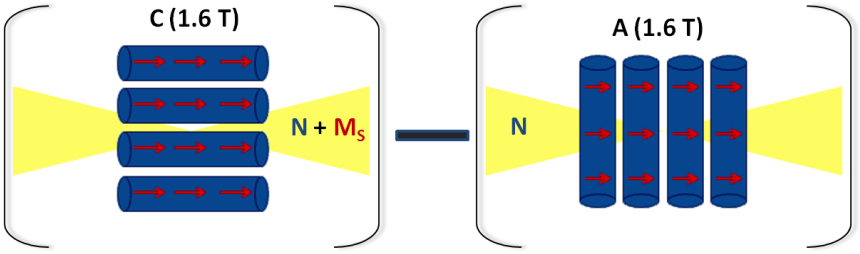

Figure IV- 36 *Simplified schemes of the intensities* $\boldsymbol{C(1.6\,T)}$ *and* $\boldsymbol{A(1.6\,T)}$.

It was interesting to compare the correlation peak for the different configurations. On the Figure IV- 37 are plotted on the same graph:
A(1.6 T) ; [A(0 T)- A(1.6 T)] ; C(1.6 T) ; [C(1.6 T)- A(1.6 T)] in linear scale and in log-lin scale. In both representations we can see that the correlation peak on the A profiles are much less marked than on the C profiles.

The comparison of [A(0 T)- A(1.6 T)] with [C(1.6 T)- A(1.6 T)] suggests that the magnetic order at remanence (after being saturated along the hard axis) is lower than the magnetic order at saturation. This is not surprising because the magnetic configuration corresponding to the [A(0 T)- A(1.6 T)] profile contains magnetic domains with a short lateral extension. Moreover, a slight rod mis-orientation would lead to a loss of magnetic order at the remanence while at saturation the magnetic order is insured by the high magnetic field. A schematic representation of the difference on both configurations is represented on Figure IV- 38.

The comparison of A(1.6 T) with C(1.6 T) and [C(1.6 T)- A(1.6 T)] suggests that the nuclear order is lower than the magnetic order at saturation. Here again a structural disorder may be responsible for this difference. A magnetic scattering length density (SLD) higher than the nuclear SLD may also explain such a difference.

The peak on the [C(1.6 T)- A(1.6 T)] profile is found at q=0.026 $Å^{-1}$ corresponding to a correlation distance of 24.2 nm. The mean distance between the rod is found equal to 3.8 nm.

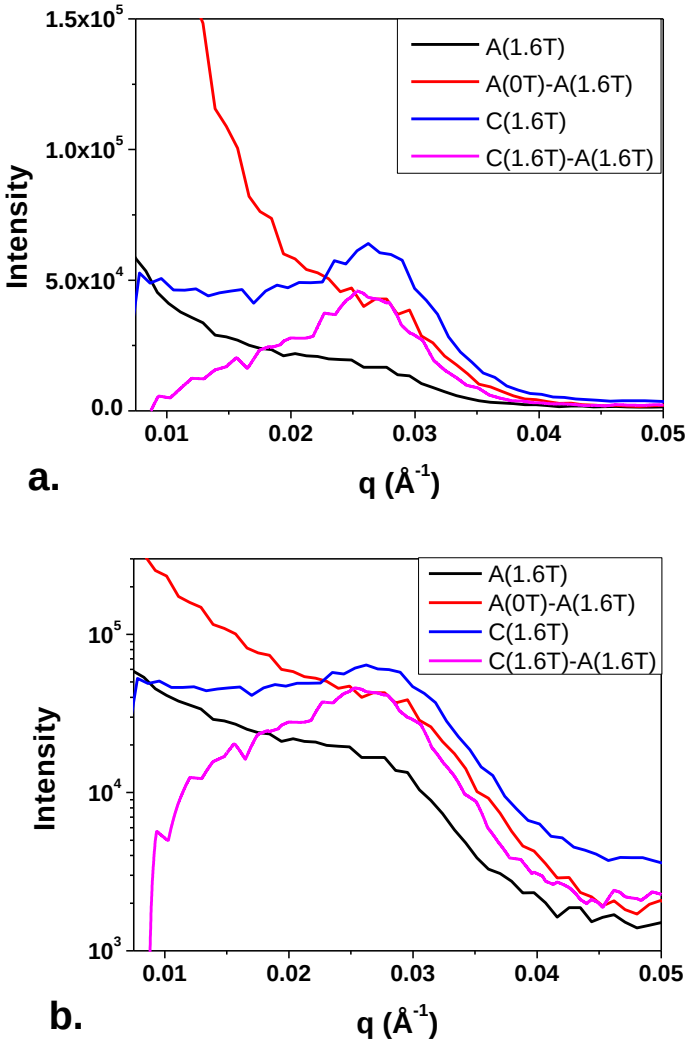

Figure IV- 37 *SANS profiles* A(1.6 T) ; [A(0 T)- A(1.6 T)] ; C(1.6 T) ; [C(1.6 T)- A(1.6 T)] (a) in linear scale –and (b) in log-lin scale..

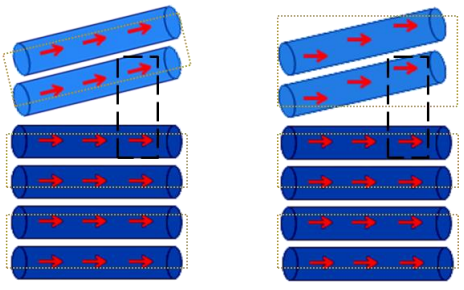

a. M_r (0 T) b. M_s (1.6 T)

Figure IV- 38 *Orientation of magnetic moments at remanence (0 T) and at saturation (1.6 T).*

IV.8 Conclusions

This study is one of the very few SANS studies of magnetic nanorods assemblies with the incident beam perpendicular to the rods. Except the work of Weiqing Fang , most of SANS studies on magnetic nanorods were done on rods grown in alumina membrane with the incident beam perpendicular to the membrane and so parallel to the rod long axis.

We have described first the neutron scattering by dense assemblies of rods in the remanent state after being saturated at 1 T during the rods alignment. The intensity scattered perpendicular to the rods is much more intense than parallel to them thanks to the addition of the nuclear and magnetic scattering. In this study we focused on the correlation peak present in the scattering intensity profile perpendicular to the rods. At a first approximation the q value at the maximum of the peak allow to measure the mean distance between the rods and knowing the rod mean diameter from TEM images to deduce the inter-rod spacing due to ligands. For the three samples analyzed this inter-rod spacing was in the range 3.5 – 4.7 nm and the magnetic volume fraction deduced from the SANS measurements and including a cobalt oxide shell was found very close to the magnetic fraction deduced from the TGA and saturation magnetization measurements. It means, at least locally, that the volume fractions used in the chapter III were reasonable. We observed also a good agreement between the intensity of the correlation peak and the squareness of the M(H) loop of the assemblies. Both are good indicators of the parallel order of the rods in the assemblies.

We have described in the second part of this chapter the variation of the SANS pattern at different magnetic fields. For the same sample, the field was applied successively perpendicular and parallel to the rod alignment and the four intensity profiles: $A = I^{\perp}_{H_{\perp}}$, $B = I^{\parallel}_{H_{\perp}}$, $C = I^{\perp}_{H_{\parallel}}$ and $D = I^{\parallel}_{H_{\parallel}}$ were analyzed. By playing on the configuration it has been possible to extract different contribution to the scattering intensity. We limited ourselves as a first interpretation to consider the magnetic rods as single domain particle with an easy axis and a very high anisotropy.

- The nuclear contribution perpendicular to the rods was deduced from A at 1.6 T. We have evidenced the formation of long fibers of nanorods parallel to the rods in agreement with the fabrication process of the sample that consisted in assembly under a magnetic field.
- When the rods were along the hard magnetic axis, we observed a q^{-1} law on the B(1.6 T) profile suggests the existence of magnetic wires/elongated domains formed by the magnetic moments perpendicular to the rods. It would be interesting to increase the field to see if this signature is persistent at higher fields.
- The intensity at very small q increased a lot for two configurations (i) at the remanence [A(0 T)- A(1.6T)] after being saturated along the hard axis and (ii) at the coercivity after

being saturated along the easy axis C(0.44 T). In both cases the magnetic scattering intensity followed both a q^{-2} law. We have interpreted these two observations as the results of the formation of magnetic domains. In the first case the domains seemed elongated along the rod axis.

- The D profile was very low for all the magnetic fields showing that the magnetization is never along the hard axis. The small increase of D for fields lower than the coercivity could be interpreted as the nucleation of the magnetization reversal in some rods.
- The scattering intensity profiles perpendicular to the rods, A and C, exhibited a peak due to the spatial correlation between the magnetic moments and/or the rods. The comparison of the nuclear correlation in A(1.6 T) with the magnetic correlation [C(1.6 T)-A(1.6T)] showed that the second one is much more marked than the first one. It can be due to a better magnetic order at saturation compared to the nuclear order and/or the a magnetic SLD higher than the nuclear SLD.

Bibliography

[1] S. King, “Small Angle Neutron Scattering”, EPJ Web of Conferences 104, 01004 (2015)

[2] www.neutron.ethz.ch, “Magnetic Small-angle Neutron Scattering”

[3] R. Borsali, R. Pecora, “Soft-Matter Characterization”, Springer, LXXII, 2008.

[4] T. Maurer, F. Zighem, S. Gautrot, F. Ott, G. Chaboussant, L. Cagnon, and O. Fruchart, “Magnetic nanowires investigated by Polarized SANS,” Phys. Procedia, vol. 42, pp. 74–79, 2013.

[5] D. Marchal and B. Demé, “Small-angle neutron scattering by porous alumina membranes made of aligned cylindrical channels", J. Appl. Cryst., 36, pp. 713–717, 2003.

[6] T. Maurer, “Magnetism of anisotropic nano-objects : Magnetic and neutron studies of Co 1-xNi x nanowires,” PhD dissertation, Université Paris XI Orsay, 2009.

[7] B. Hammouda, “Probing nanoscale structures”, www. nist.gov/

[8] www.ill.fr/lss/grasp/.

[9] W. Fang, "Elaboration de matériaux composites nanofils magnétiques / polymères pour la fabrication d' aimants permanents", PhD dissertation, Université Paris XI Orsay, 2013

Chapter V Towards macroscopic magnets: Preliminary results on compaction of cobalt nanorods

In this chapter we will present preliminary results on the consolidation of cobalt nanorods for the fabrication of macroscopic magnets.

Magnets based on consolidation of nanorods can work only if the anisotropic morphology and the small size of the rods are retained after compaction, in other words if the magnetic particles are single domain separated by a thin non magnetic layer. The challenge is to find the good compromise: namely, to compact enough to get a magnet with good mechanical strength and high magnetic volume fraction, but not too much in order to avoid the nanorods' coalescence that would strongly decrease the coercivity. Moreover, in the consolidated material the alignment must be very good. Indeed, we saw in chapter III that a low squareness, due to misalignment, leads to poor $(BH)_{max}$.

In this chapter we will describe the two different approaches followed for the rods' consolidation i.e. compaction of randomly oriented rods under magnetic field and compaction of pre-aligned nanorod assemblies.

All compaction experiments were performed by Dr. Semih Ener in the team of Pr. Oliver Gutfleish at the Technical University of Darmstadt (TUDA).

V.1 Compaction set-ups

Three techniques were used for the densification of the cobalt nanorods into a cohesive structure: cold compaction (C.C), hot compaction (H.C.) and spark plasma sintering (SPS).

- The cold compaction set-up consists of a hydraulic press (with applied forces up to 1.5 GPa) equipped with an electromagnet that provided an external field of 1.6 T. The mechanical load is applied perpendicular to the applied external magnetic field (Figure V- 1 a).
- The hot press set-up combines a hydraulic press reaching forces up to 450 MPa (Figure V- 1 b) with a sample cavity where temperatures in the range 180 - 220°C can be achieved under vacuum, in order to remove the excess of organic entities. The temperature was limited to 220°C because previous studies showed that above this temperature the "naked" cobalt rods undergo coalescence [1]. As this set-up is not equipped with an electromagnet, the powders were pre-aligned in the mould and then loaded in the set-up.
- Spark plasma sintering (SPS) was carried out without magnetic field (Figure V- 1 c). Before starting the sintering process, a 40 MPa pressure was applied to the samples to ensure the good electrical contact. During the sintering, the current was manually controlled to avoid the overheating of the sample ($T < 200^{o}C$).

Depending on the cavity of the three set-ups, thin plates, thicker plates, coined and needle like magnets could be obtained.

The magnetic characterizations of the consolidated samples were performed by Dr. S. Ener with a Metis pulse magnetometer at TUDA.

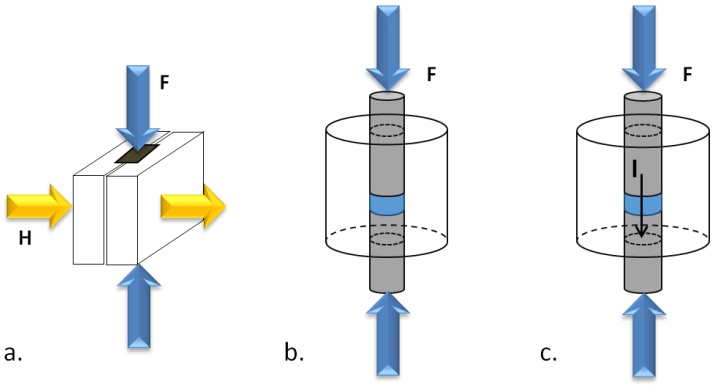

Figure V- 1 a. *Cold compaction;* ***b.*** *Hot compaction and* ***c.*** *SPS set-ups.*

V.2. Compaction of powders

In a first set of experiments rod samples were sent as concentrated suspensions in chloroform after being washed from their mother solution of 1,2-butanediol (twice with ethanol, one time with chloroform, and re-dispersion in chloroform). Before each compaction 1 g of rods was dried into powder in TUDA. Two consolidation experiments have been done by S. Ener.

- Cold consolidation (C.C.) of a bonded magnet: the dried cobalt powder was mixed with epoxy resin (15 w.t. %) and then pressed under a magnetic field of 1.6 T, with a pressure of 150 MPa for 2 min.
- Hot compaction (H.C.) without epoxy resin was carried out in two steps. First the powder was pre-aligned under a field of 1.6 T and then transferred in the compaction machine for densification at 180°C, under a pressure of 40 MPa for 2 min.

In both cases centimeter size magnets were obtained (Figure V- 2 a, b). As we can see the hot compacted magnets exhibited a good mechanical strength despite the relatively low applied pressure. The use of epoxy resin was not necessary to insure cohesion to the compacted powder. The magnetization measurements showed a remanence-to-saturation ratio around 57 % and 61 %, and a coercivity $\mu_0 H_C$ of 0.25 T and 0.28T, for the bonded and hot compacted samples, respectively. The room temperature $(BH)_{max}$ value for the hot compacted Co NRs magnet was calculated at 15.7 kJ/m^3.

The nanorods used for the above experiments were a mixture of three nanorod batches consisting of rods with mean diameter 20 nm and mean length 250 nm (**Error! Reference source not found.**a). Preliminary tries of the nanorods' alignment in a chloroform solution showed that their M_r/M_s ratio could reach a value of 75 % and a coercivity $\mu_0 H_C$ = 0.35 T (**Error! Reference source not found.**b). The M_r/M_s of the compacted magnets were much lower. Thus, we conclude that the rods are better aligned when they are dried under the magnetic field just after their dispersion in the chloroform. During the time when the suspensions were prepared, sent to Darmstadt and dried, the rod agglomerated in random orientations. This agglomeration is irreversible thus rendering impossible any re-align from the dried powder state even with a magnetic field of 1.6 T.

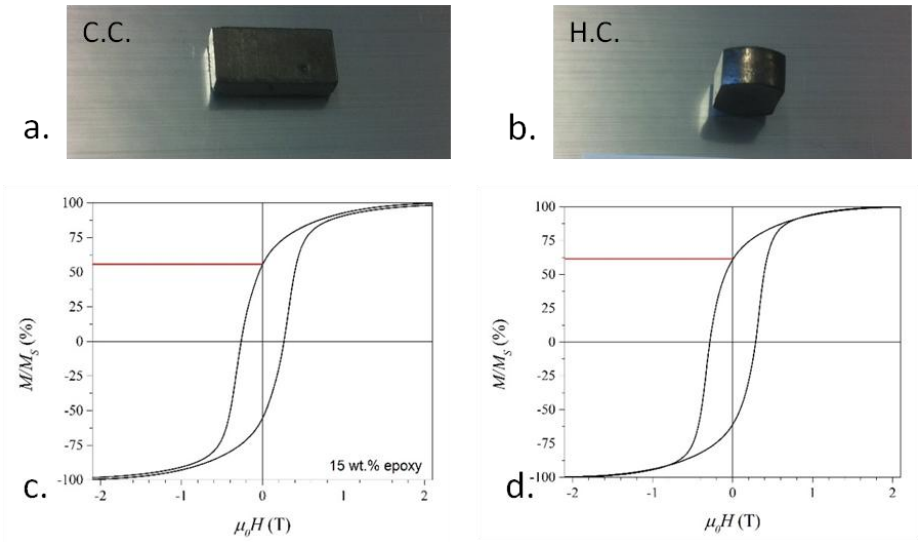

Figure V- 2 a. *Image of a bonded magnet prepared by cold compaction of Co NRs with 15% w.t. of epoxy and* ***c.*** *corresponding normalized M(H) loop;* ***b.*** *image of a magnet prepared by hot compaction of Co NRs and* ***d.*** *corresponding normalized M(H) loop.*

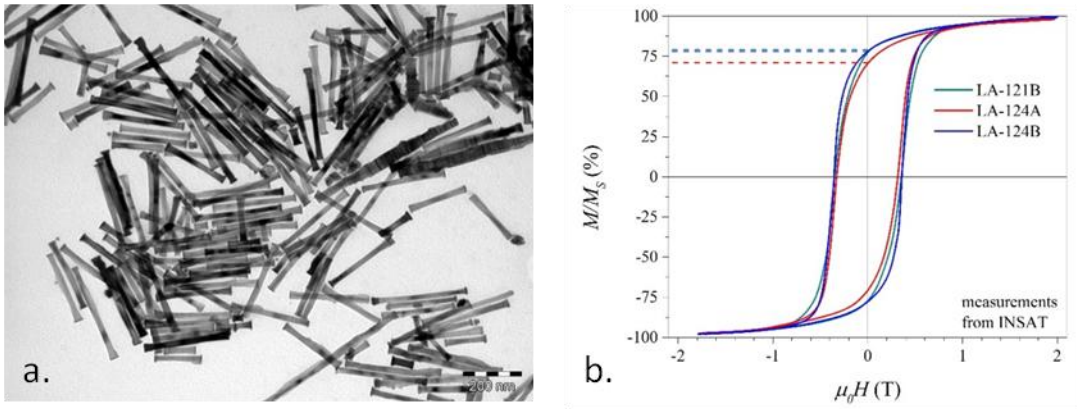

Figure V- 3 a. *TEM image Co nanorods used for the first compaction experiments;* ***b.*** *M(H) loops of the nanorod assemblies aligned from a chloroform suspension.*

Due to the difficulty of the nanorods' alignment in powder we changed the compaction protocol in the following steps. First we aligned the nanorods from a fresh chloroform suspension into macroscopic wafers at INSA and then we transferred them for compaction in TUDA.

V.3. Compaction of pre-aligned nanorods

A second set of consolidation experiments was done on pre-aligned cobalt nanorods (long needles from wafers) provided from INSA to TUDA. The samples consisted of rods with d_m= 18 ± 3 nm and l_m= 320 ± 100 nm, with M_r/M_s= 0.78 and $\mu_0 H_C$= 0.38 T. Two consolidation experiments have been done :

- Cold compaction with 15 wt. % epoxy, 70 MPa pressure and external magnetic field of 1.6 T. The hysteresis loop of the resultant pellet is shown in Figure V- 4.
- Consolidation by SPS. A photograph and the M(H) loop of the consolidated coin are shown in Figure V- 5. Once more, the compacted magnet exhibited a good mechanical strength in absence of any polymer matrix.

The M_r/M_s ratio reached the values of 67 % and 78 % for the cold compacted and SPS sample, respectively. For both samples the M_r/M_s ratio was improved in comparison to the samples described in the previous experiments. Nevertheless the magnetic properties after dispersion in the epoxy matrix are much less satisfactory. The dispersion alters the rod alignment.

The induction per volume, B, was calculated as the ratio of the induction of the sample over the volume of the sample. The magnetic volume fraction V_M was calculated as the ratio of the saturation induction per volume of the sample divided by the bulk saturation induction (1.79 T). The magnetic volume fraction was equal to 39 % and 41 % and the coercivity $\mu_0 H_C$ 0.38 and 0.375 T, for the cold compacted and SPS sample, respectively. The $(BH)_{max}$ value for the SPS sample was measured at 27.5 kJ/m^3 at room temperature.

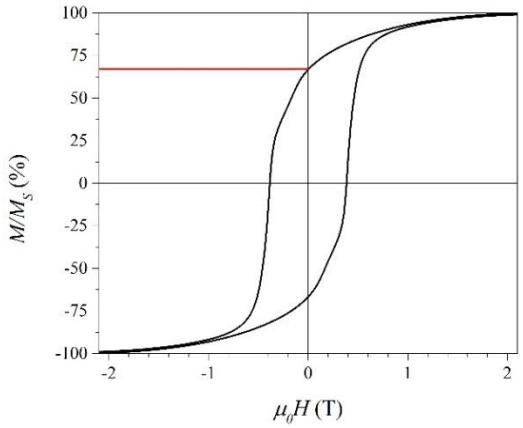

Figure V- 4 *Room temperature pulse magnetometer measurements of polymer bonded pre-aligned Co NRs (needles).*

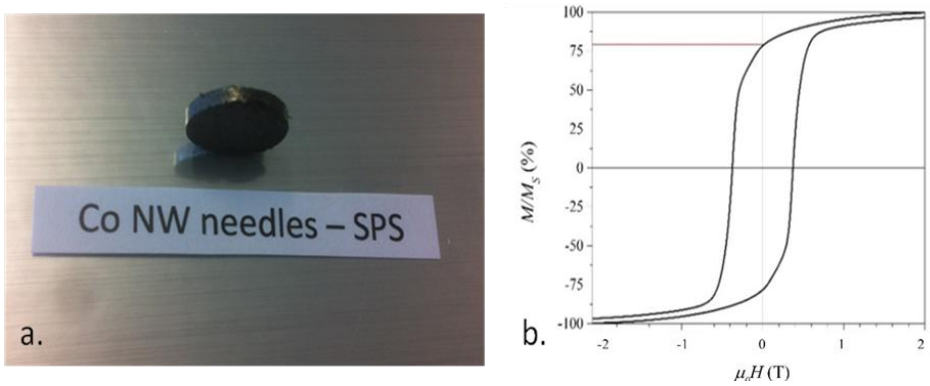

Figure V- 5 a. *Photo of a magnet prepared by SPS consolidation of pre-aligned NRs and* ***b.*** *corresponding M(H) loop measured in room temperature at the pulse magnetometer.*

The conclusions of this study are:

- The new process that consists in the rods' pre-alignment into a dense assembly and its compaction allowed reaching higher M_r/M_s, which means a better rod alignment in the compacted magnet. This is especially true for the SPS sample;
- The use of epoxy resin as binder is detrimental for a good alignment and finally not necessary for a good mechanical strength.- The coercivity of the magnet after compaction was the same as in the pre-aligned wafer's, which means that the rod morphology was not destroyed during the compaction;
- The $(BH)_{max}$ remains quite low due to two reasons: the alignment was still not perfect and the magnetic volume fraction was only of 40 %.

In the following we will only present results obtained from compaction without any addition of epoxy resin.

V.4. Influence of applied pressure in the $(BH)_{max}$

In our attempt to improve the magnets' $(BH)_{max}$ we tested the influence of the applied pressure on the volume fraction.

Nanorod assemblies in the form of rectangular film of thickness ≈1 mm and side 5 mm were used as presented in the Figure V- *6*. The rods' mean diameter and length were 10 ± 1 nm and 200 ± 46 nm, respectively (Figure V- 7 a). The peculiar film shape of the assembly was a result of their alignment in a Teflon parallelepiped mould of side 5 mm (see also Chapter III.2.3). The measured M(H) loop is shown in the Figure V- 7 b. The measured H_{ci}, B_r/B_s, V_M and $(BH)_{max}$ are equal to 486 kA·m^{-1} ($\mu_0 H_{ci}$ = 0.61 T), 0.97, 43 % and 60 kJ·m^{-3}.

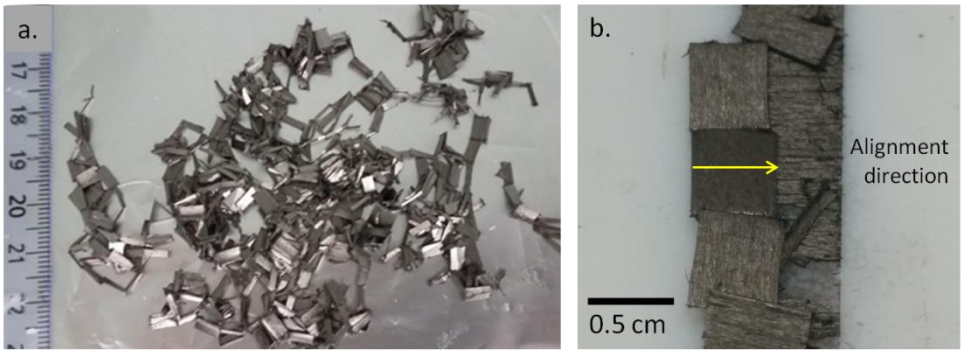

Figure V- 6 a. *Rectangle films of dense arrays of cobalt nanorods aligned in the Teflon parallelepiped of width 0.5 cm;* ***b.*** *rectangle films showing the nanorods' alignment direction.*

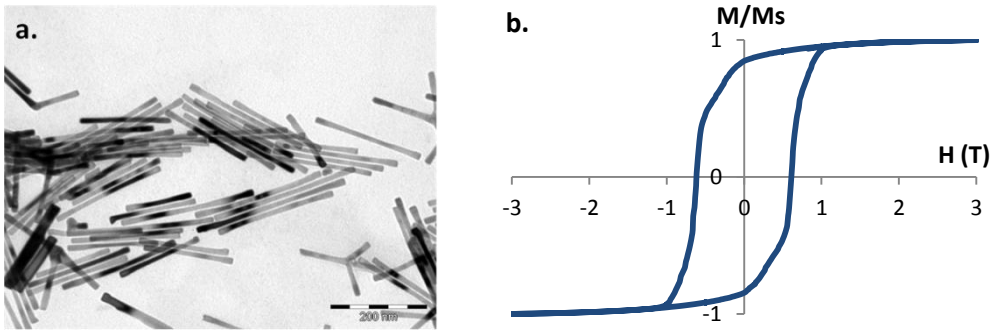

Figure V- 7 a. *TEM image of cobalt nanorods with d_m= 10 ± 1 nm and l_m= 200 ± 46 nm and b. M(H) loop of the nanorod pre-compacted assemblies.*

The films' compaction was performed in two steps by S. Ener.

First the needles were re-aligned in a discoid cavity under 1.6 T, since they were disoriented with respect to each other during their mailing.

The cavity with the aligned needles was then ready to be used for compaction. Two hot and one cold compaction were successively performed according to the following order:

1. Hot compaction under 300 MPa, in relatively stable temperature between 180 – 190°C and with a compaction duration of 2 min.

2 The magnet from the above compaction was consolidated again under higher pressure of 450 MPa and in the same time and temperature conditions.

3 Finally, the previously hot compacted magnet (at 450 MPa) was cold pressed at 1000 MPa, under a field of 1.6 T.

Coin shaped magnets were obtained after each compaction process like the one presented in the Figure V- 8 a. The measured M(H) loops for 300, 450 and 1000 MPa are presented in the Figure V- 8 b.

We can see that the B_s increases with the applied pressure from 0.48 T (300 MPa) to 0.61 T (1000 MPa). On the opposite, the H_{ci} drops from 0.61 T (for 300 MPa) to 0.42 T (for 1000 MPa). The alignment quality of the rods inside the magnet can be calculated from the ratio B_r/B_s. In all cases it is well preserved, but remains lower than the pre-compacted rods. No trend is observed with the applied pressure (Table V- 1).

The magnetic volume fraction was deduced from the calculated B_s and found equal to 26.6 %, 32.5 % and 34.4 % for 300, 450 and 1000 MPa, respectively. This shows that the packing of the rods inside the magnet is increased with the applied pressure. Unfortunately, it did not reach the V_M of the pre-compacted assembly (43 %).
The maximum coercivity loss is observed for the highest applied pressure of 1000 at 31% compared to that of the pre-aligned rods. We assume that under this force the rods coalesce and a part of their shape anisotropy contribution is lost.

As a result of the above, the $(BH)_{max}$ increased at 31 $kJ \cdot m^{-3}$ for the cold compacted magnet (1000 MPa), but did not exceed the 60 $kJ \cdot m^{-3}$ of the pre-compacted rod assemblies. All above results are summarized in the Table V- 1.

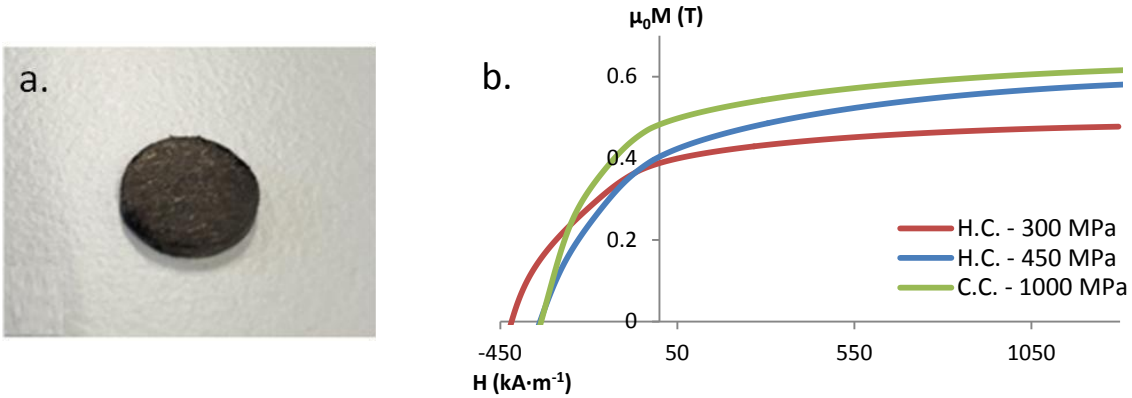

Figure V- 8 a. *Coin shaped magnet;* ***b.*** *B(H) curves of hot compacted (300 and 450 MPa) and cold compacted (1000 MPa) magnets.*

R_{10}	Pressure (MPa)	H_{ci} (T)	H_{ci} ($kA \cdot m^{-1}$)	$\mu_0 M_r$ (T)	$\mu_0 M_S$ (T)	M_r/M_s	V_M %	$(BH)_{max}$ ($kJ \cdot m^{-3}$)
Films	--	0.61	486	0.75	0.77	0.97	43.0	60.0
Magnets	H.C. – 300	0.52	418	0.39	0.48	0.81	26.6	22.5
	H.C. – 450	0.42	337	0.40	0.58	0.69	32.5	21.5
	C.C. – 1000	0.41	334	0.50	0.61	0.82	34.4	31.0

Table V- 1 *Dependence of magnetic properties on the applied pressure. The results correspond to hot (H.C.) and cold (C.C.) compacted magnets. The magnetic properties of the pre-compacted films (R_{10}) are also presented.*

Concluding, the most striking feature of this set of experiments is that the magnetic volume fraction remains very low, even after a pressure of 1000 MPa. Despite the fairly good alignement B_r/B_s = 0.82, the resulting $(BH)_{max}$ is lower than expected. It is likely that the assemblies contain a large amount of organics that cause the formation of large voids in the final compacted magnets.

In our attempt to obtain magnets of high $(BH)_{max}$ we should also take into account their thickness. In the above set of experiments the rods used were particularly thin (d_m= 10 nm), a fact that does not allow reaching high V_M and thus high $(BH)_{max}$ (according to III.9)

V.5. Influence of the rod diameter

The possibility of fabricating magnets with higher $(BH)_{max}$ than their pre-compacted assemblies was examined with the use of thicker rods (d_m= 30 ± 6 nm, l_m= 190 ± 40 nm). We tested their ability to increase their V_M through their hot compaction under 450 MPa, at T= 180 – 190°C, in a rectangular shaped cavity.

The M(H) loop of the pre-compacted assemblies are given in the Figure V- *9*. The measured H_{ci}, B_r/B_s, V_M and $(BH)_{max}$ are equal to 288 $kA \cdot m^{-1}$ ($\mu_0 H_{ci}$= 0.36 T), 0.89, 49 % and 51 $kJ \cdot m^{-3}$.

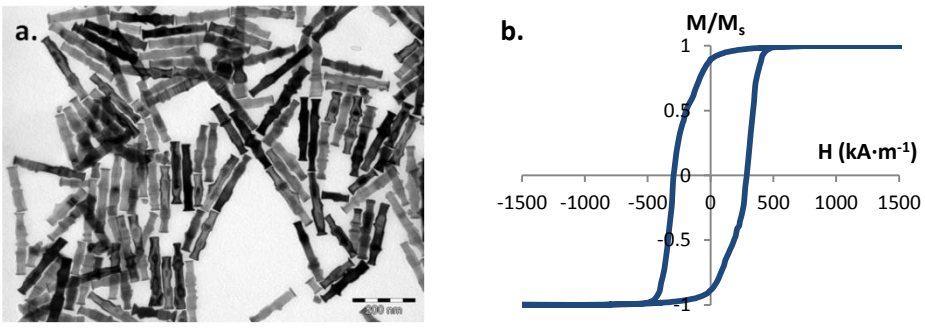

Figure V- 9 a. *TEM image of cobalt nanorods with d_m= 30 ± 6 nm, l_m= 190 ± 40 nm and* ***b.*** *their M(H) loop of their pre-compacted assemblies.*

The compacted needle shaped magnet and its measured B(H) loop is presented in the Figure V- 10. Once more the H_{ci} and B_r/B_s drops to lower values than the pre-aligned assembly at 0.28 T (224 kA·m^{-1}) and 0.67, respectively, an issue that will be examined via small angle neutron scattering measurements. On the other hand, we observe that the B_s rises from 0.87 T to 1.22 T. This shows our successful attempt to pack the rods closer to each other with V_M equal to 64 %. The calculated $(BH)_{max}$ exceeds the initial value of the wafer (51 kJ·m^{-3}) reaching 65 kJ·m^{-3}.

Comparing the hot compaction results under 450 MPa of the samples R_{10} and R_{30} we conclude that the thicker rods yield higher $(BH)_{max}$. This is attributed to their capacity to manage higher V_M values compared to the thinner ones, as simulated in the Chapter III.9.

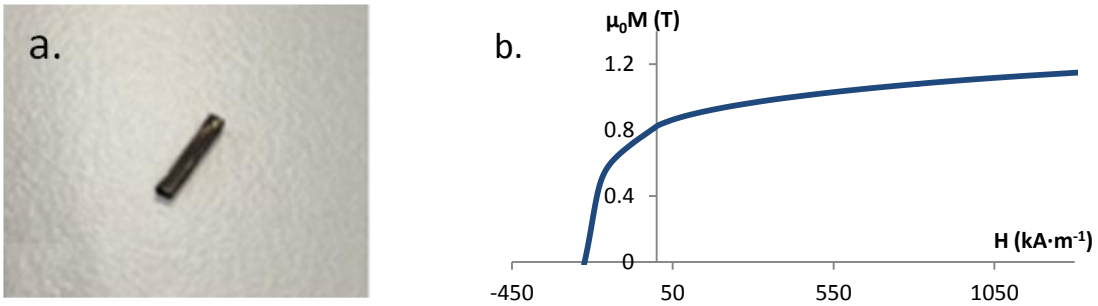

Figure V- 10 a. *Needle shaped magnet;* ***b.*** *Corresponding B(H) curve.*

R_{30}	Pressure (MPa)	H_{ci} (T)	H_{ci} (kA·m^{-1})	$\mu_0 M_r$ (T)	$\mu_0 M_S$ (T)	M_r/M_s	V_M %	$(BH)_{max}$ (kJ·m^{-3})
Films	--	0.36	288	0.78	0.87	0.89	49	51
Magnet	450	0.28	224	0.82	1.22	0.67	64	65

Table V- 2 *Magnetic characteristics of the nanorod assembly R_{30} before and after hot compaction under 450 MPa.*

V.6. SANS of bulk compact permanent magnet

The nanorod film assembly R_{30} was analyzed by SANS under zero magnetic field prior and after its compaction into a bulk magnet. Our objective was to investigate the source of the H_c drop and the alignment quality decrease (B_r/B_s).

The normalized 2D SANS maps of the assembly R_{30} before and after its hot compaction are presented in the Figure V- *11 a.* and *b.*, respectively. Both patterns are anisotropic, with the intensity scattered perpendicularly to the nanorods much more intense than parallel to the alignment. The $I^{//}(q)$ and $I^{\perp}(q)$ curves were obtained by integration in parallel and

perpendicular directions with an angle of 30° and the anisotropic scattering ratio, $I^{\perp}(q)/I^{//}(q)$, versus q was plotted as presented in the Figure V- *11* c.

In both samples the plot of the anisotropic scattering ratio versus q presents two peaks, which are in good agreement with a SANS pattern of an oriented assembly of anisotropic particles. The q_{max} value of the pre-compacted assembly R_{30} was found equal to 0.017 $Å^{-1}$ for the first correlation peak and 0.034 $Å^{-1}$ for the second. The q_{max} of the compacted bulk magnet are shifted to higher values equal to 0.023 $Å^{-1}$ and 0.047 $Å^{-1}$. The corresponding mean nanorod center-to-center distance, D_m, was calculated at 36 nm for the assembly R_{30}, from which the mean spacing between the rods, L_m, was calculated at 6 nm. In the bulk magnet the distance D_m= 26.7 nm is smaller than the rods' mean diameter (30 nm) revealing their coalescence during the compaction process. This leads to the nanorods' shape anisotropy reduction and thus the H_c drop. The above results are summarized in the Table V- *3*.

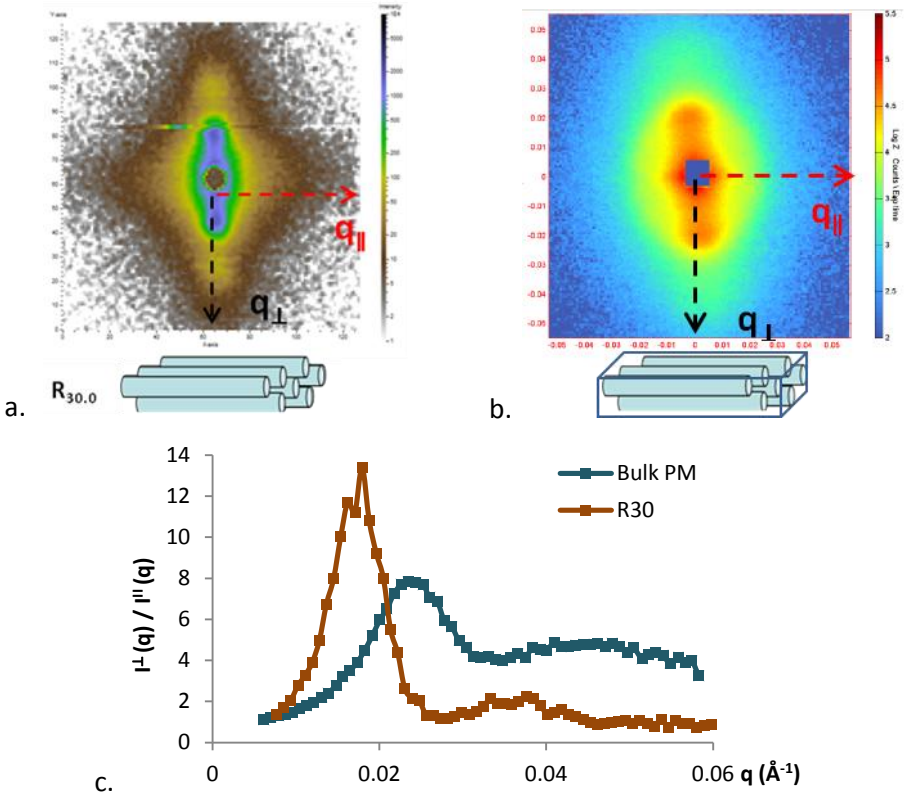

Figure V-11 *Normalized scattering spectra of the dense cobalt nanorod assembly R_{30}* ***a.*** *before and* ***b.*** *after hot compaction; and* ***c.*** *plot of its anisotropic scattering ratio intensity versus the wave vector q.*

Sample	d_m (nm)	q_{max} ($Å^{-1}$)	D_m (nm)	L_m (nm)
R_{30}	30.0 ± 6	0.017	36.0	6
Bulk PM	--	0.023	26.7	0

Table V- 3. *Characteristic lengths of the nanorod assembly R_{30} before and after hot compaction.*

Finally, the maximum of the anisotropic scattering ratio, $[I_{\perp}(q)/I_{\parallel}(q)]_{max}$, varies between the two nanorod assemblies. The highest is observed for the pre-compacted assembly with $[I_{\perp}(q)/I_{\parallel}(q)]_{max}$= 13.4, followed by the bulk magnet at 7.8. This difference explains the alignment quality decrease (B_r/B_s) observed after the compaction.

V.7. Conclusions

A preliminary study on the compaction of cobalt nanorods into bulk macroscopic permanent magnets was presented. We showed that in order to obtain a magnet with high M_r/M_s it is important to align the nanorods from a fresh chloroform suspension prior to their compaction.
No matter the compaction process (hot or cold) we observed the same effect regarding the increase of the applied pressing force: the higher it is, the better the V_M gets.

Nevertheless in order to take full advantage of this condition we suggest that it is preferable to use thick rods (≈30 nm) due to their capacity to achieve high V_M. Indeed, for nanorod assemblies of V_M= 49 % and $(BH)_{max}$= 51 kJ·m^{-3} we managed to increase their volume fraction and performance to 64 % and 65 kJ·m^{-3}, respectively.

Several issues must be addressed in the future to still increase the $(BH)_{max}$ of the consolidated samples:

- Improve the alignment of the rods in the final magnet. Even if a clear improvement was obtained thanks to the pre-alignment the M_r/M_s were far below the maximum values obtained in the pre-alignment;
- Increase the V_M for the magnet prepared with the thinner rods. These rods are more interesting to get higher performance, because of their higher coercivity which will prevent any coercivity limitation of the $(BH)_{max}$.

Bibliography

[1] K. Atmane, F. Zighem, Y. Soumare, M. Ibrahim, R. Boubekri, T. Maurer, J. Margueritat, J.-Y. Piquemal, F. Ott, G. Chaboussant, F. Schoenstein, N. Jouini, and G. Viau, “High temperature structural and magnetic properties of cobalt nanorods,” *J. Solid State Chem.*, vol. 197, pp. 297–303, 2013.

General Conclusions

The main objective of the thesis was the development of a new generation of rare earth free permanent magnet whose energy product, $(BH)_{max}$, would fill the gap between the rare earth magnets like SmCo and the Alnico magnets. The strategy followed consisted in:

1. The exploitation of the shape and magnetocrystalline anisotropy of cobalt nanorods (Co NRs) produced by polyol synthesis, which could be scaled-up at the laboratory scale;
2. Their texturing into macroscopic dense alignments under an external magnetic field, leading to high $(BH)_{max}$;
3. The structural and magnetic characterizations of the dense assemblies;
4. A preliminary study on further compaction into a bulk magnet.

Several hurdles arise from each task such as the fine tuning of the polyol process to yield Co NRs with the ideal ellipsoidal shape, the optimization of the washing and alignment conditions to yield dense assemblies of perfectly aligned rods, and finally the further compaction of pre-aligned needles into bounded magnets without altering the intrinsic Co rods morphology to retain an important shape anisotropy in the nanostructured magnet.

The paragraphs hereafter summarize our approach to these challenges and the most important outcomes of our research. Perspectives for the improvement of the examined systems will be discussed and future perspectives of integration for MEMS applications briefly introduced

- **Synthesis of Co NRs: Up – scaling and shape improvement**

We demonstrated that the scale – up of the polyol process for the synthesis of Co NRs at laboratory scale is possible. The homogeneous heat and mass transfer via controlled stirring, provided by the use of an anchor and a propeller stirrer at 80 rpm, are important features in obtaining monodisperse and single crystalline hcp Co NRs with flat endings.

We showed that the nature of the $RuCl_3$ affects strongly the rods' morphology and dimensions. Three compounds were evaluated and yield, after reduction, to a controlled nucleation step due to their reactivity difference. For instance, the $RuCl_3 \cdot xH_2O$, with ref. Sigma Aldrich 84050, leads to few Ru seeds, resulting in longer NRs of l_m< 200 nm and d_m= 10 – 25 nm. On the opposite, the anhydrous $RuCl_3$ reduction at high heating rates (>

50°C·min^{-1}) yields smaller NRs (l_m< 70 nm, d_m= 8 nm) combined with spheres (d_m= 11 nm). This anhydrous $RuCl_3$ yields NRs with rounded tips, fairly closed to the optimized ellipsoidal morphology shape predicted by micromagnetic simulation, and exhibiting high coercivity. However efforts should be pursued to ensure a better size control and reduced the shape polydispersity observed.

- **Fabrication of dense Co NR assemblies**

Robust and dense macroscopic assemblies were obtained by magnetic alignment of Co NRs under an external field (1 T). The resulting wafers exhibit robustness along the NRs alignment axis and flexibility perpendicular to it thanks to strong magnetic and Van der Waals interactions. Through a combined analysis of their magnetic and thermogravimetric measurements we assessed their V_M in the range between 45 % and 55 %, depending on the NRs mean diameter and the alignment procedure. We showed that monodisperse Co NRs of smooth surface and flat endings yield the characteristic M(H) loop with high squareness, SQ, and orientation coefficient, M_r/M_s, equal to 0.96 and 0.99, respectively. Such NRs are able to reach high performance up to 167 kJ·m^{-3} when ligands are efficiently removed by successive washing process using chloroform. This is the first proof of concept of nanostructured magnets with properties exceeding Alnico magnets (Figure 1).

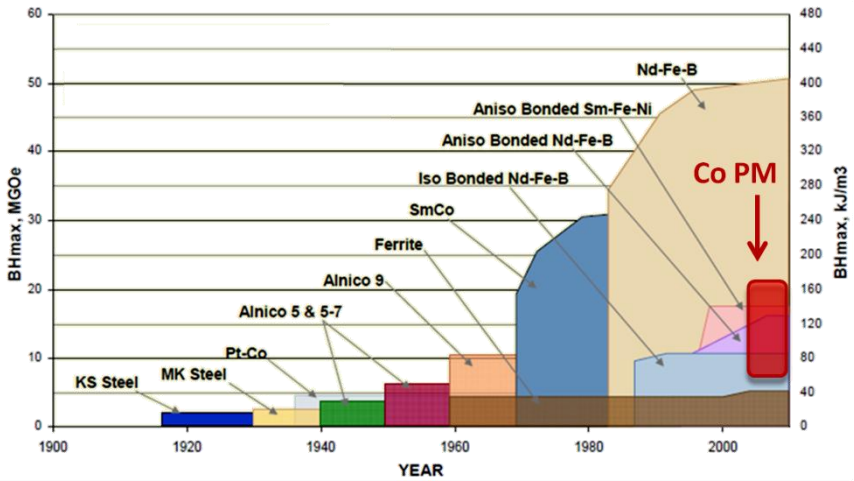

Figure 1. *Comparison of the cobalt nanorod assemblies with the commercial permanent magnets.*

Thanks to a simple model we could evidence that the wafers' coercivity must exceed the critical field limit of $\frac{B_R}{2(1+a)}$, where α being the slope of the M(H) loop at remanence to fully benefit from their magnetic behaviour. The examination of different assemblies show that coercivities higher than 480 kA·m^{-1} can be obtained from NRs with mean diameter lower than 10 nm, due to the higher difficulty of their magnetization reversal to nucleate at their tips.

The road map for the $(BH)_{max}$ improvement is now clear. The next goal will be to increase the V_M, while maintaining a NR mean diameter between 15 nm and 20 nm in order to keep high H_{ci}. To do so, the inter-rod spacing should be decreased and the oxidation prevented. For NRs with d_m in the range of 15 nm and 20 nm, V_M ranging from 60 – 75 % and $(BH)_{max}$ from 230 – 360 $kJ \cdot m^{-3}$are expected. Our preliminary study on alignment protocol under controlled atmosphere proves that such dense non-oxidized macroscopic NR assemblies with V_M= 59 % (for NRs of d_m= 17 nm) could be obtained.

- **Compaction of Co NR assemblies**

First compaction experiments were performed and revealed the key importance of prealignment of Co NRs. As expected, V_M increases with the pressing force applied, however at some point the coercivity drastically decreases due probably to sintering. Thicker rods (≈30 nm) are so far the only one which could benefit from compaction, but these results should be extended to small rods to allow reaching high H_{ci}.

- **Small Angle Neutron Scattering by Co NR assemblies**

SANS studies were performed to have better structural and magnetic characterizations of the cobalt nanorod assemblies. Thanks to the existence of a correlation peak in the perpendicular scattering intensity we were able to measure a mean inter-rod distance and to verify that the magnetic volume fractions deduced from indirect characterizations (TGA and VSM) were consistent.

The SANS patterns under magnetic field are very rich in information. We limited ourselves as a first interpretation to consider the magnetic rods as single domain particles with an easy axis and a very high anisotropy. The magnetization reversal in the assemblies followed by SANS seems in agreement with this simple model but deeper analysis will be done in the future.

- **Perspective of this work**

Our efforts will be pursued in collaboration with the NanoBioSystem team in LAAS (Laboratoire d'Analyse et d'Architecture des Systèmes, Toulouse). The project will explore the integration of Co NRs assembly to tackle the design of new nanostructured magnets with submillimeter sizes, controlled induction orientation and high energy products (above

160 kJ.m^{-3}) and thus open perspective for **Micro-Electro-Mechanical Systems (MEMS) applications.**

Two micromachined biosensor demonstrators will be evaluated to demonstrate the efficiency of **dense assemblies of Co nanorods**, chemically grown : a microcantilever resonator electromagnetically actuated for micro RNA detection and 2D micromagnetic arrays for immunoassay applications (Figure 2).

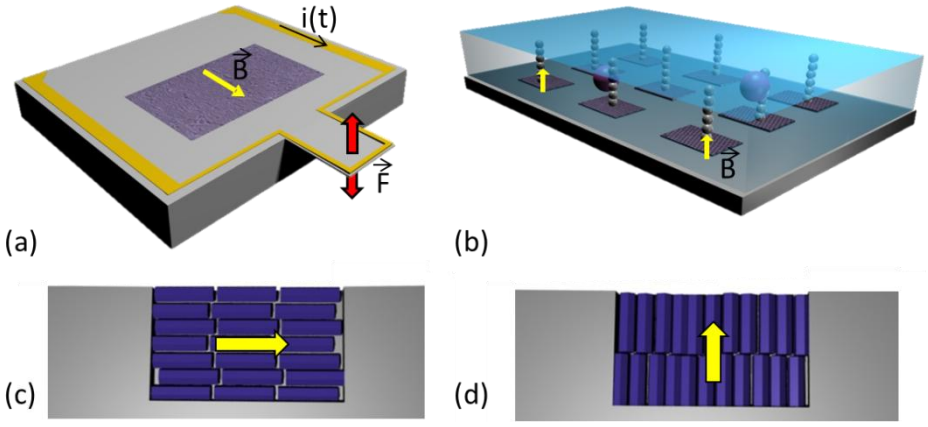

Figure 2. *Schematic view of (a) the Si microcantilever and (b) the microfluidic device. Purple spheres represent CTC trapped on superparamagnetic beads columns. Side views of (c) planar and (d) perpendicular induction magnets obtained by Co NRs assembly for (a) and (b) prototypes respectively.*